AFOSR-TR- 84-0911

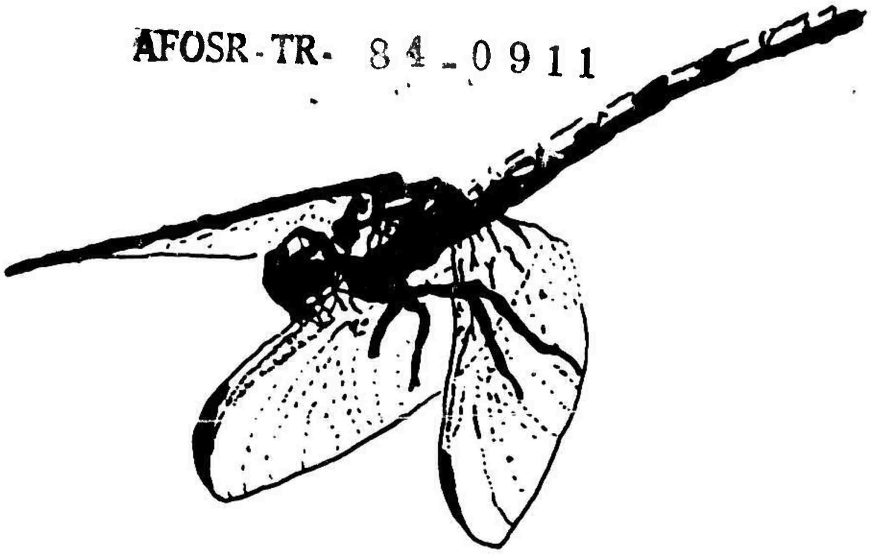

3

WORKSHOP ON

UNSTEADY SEPARATED FLOW

AD-A148 249

UNITED STATES AIR FORCE ACADEMY
AUGUST 10-11, 1983

SPONSORED BY: AFOSR
FJSRL
U. COLORADO

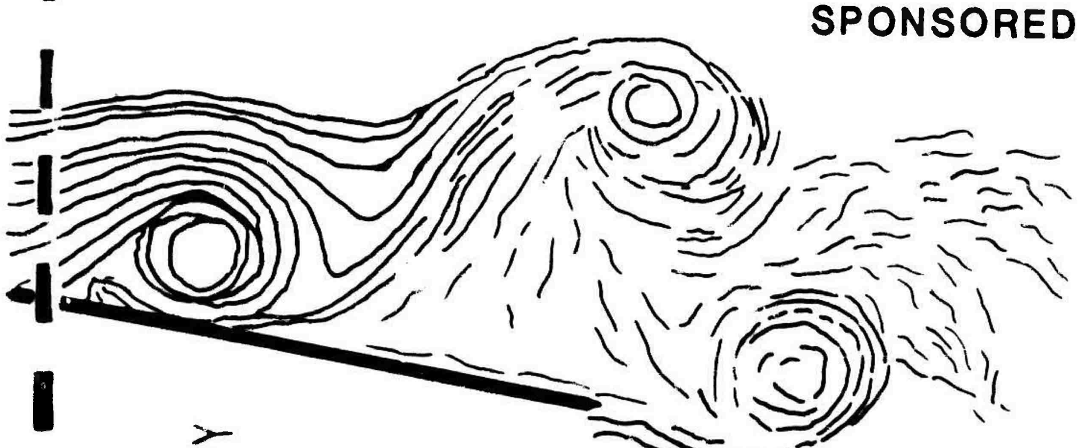

DTIC
ELECTE
NOV 16 1984
S D
A

DTIC FILE COPY

FRANCIS & LUTTGES (EDS.)

1984

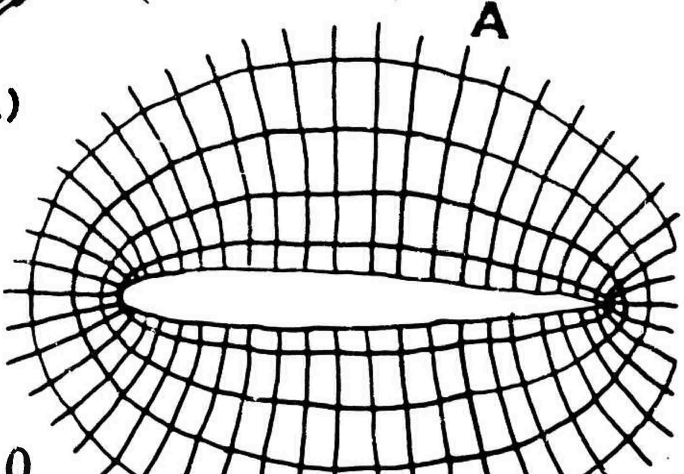

Approved for public release;
distribution unlimited.

84 10 23 320

DISCLAIMER NOTICE

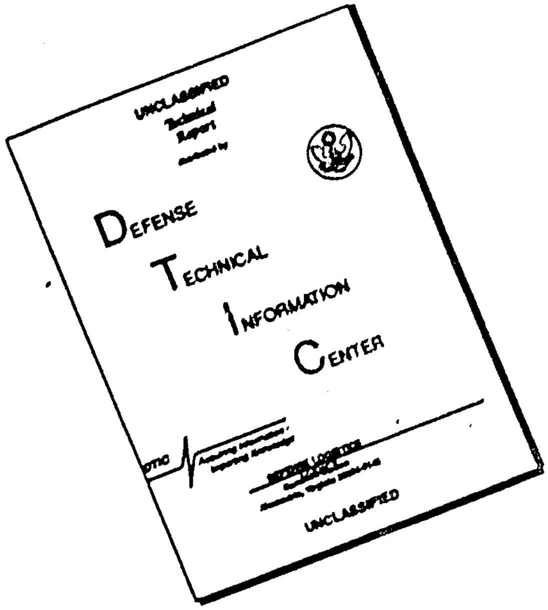

THIS DOCUMENT IS BEST QUALITY AVAILABLE. THE COPY FURNISHED TO DTIC CONTAINED A SIGNIFICANT NUMBER OF PAGES WHICH DO NOT REPRODUCE LEGIBLY.

UNCLASSIFIED
SECURITY CLASSIFICATION OF THIS PAGE

REPORT DOCUMENTATION PAGE

1a. REPORT SECURITY CLASSIFICATION: UNCLASSIFIED

1b. RESTRICTIVE MARKINGS:

2a. SECURITY CLASSIFICATION AUTHORITY:

2b. DECLASSIFICATION/DOWNGRADING SCHEDULE:

3. DISTRIBUTION/AVAILABILITY OF REPORT: Approved for Public Release; Distribution Unlimited.

4. PERFORMING ORGANIZATION REPORT NUMBER(S):

5. MONITORING ORGANIZATION REPORT NUMBER(S): AFOSR-TR- 84-0911

6a. NAME OF PERFORMING ORGANIZATION: AIR FORCE OFFICE OF SCIENTIFIC RESEARCH

6b. OFFICE SYMBOL (If applicable): AFOSR

7a. NAME OF MONITORING ORGANIZATION: AFOSR/NA

6c. ADDRESS (City, State and ZIP Code): DIRECTORATE OF AEROSPACE SCIENCES, BOLLING AFB, DC 20332

7b. ADDRESS (City, State and ZIP Code): Bolling AFB DC 20332

8a. NAME OF FUNDING/SPONSORING ORGANIZATION: AIR FORCE OFFICE OF SCIENTIFIC RESEARCH

8b. OFFICE SYMBOL (If applicable): AFOSR/NA

9. PROCUREMENT INSTRUMENT IDENTIFICATION NUMBER: IN-HOUSE

8c. ADDRESS (City, State and ZIP Code): BOLLING AFB, DC 20332

10. SOURCE OF FUNDING NOS.

PROGRAM ELEMENT NO.	PROJECT NO.	TASK NO.	WORK UNIT NO.

11. TITLE (Include Security Classification): WORKSHOP ON UNSTEADY SEPARATED FLOW

12. PERSONAL AUTHOR(S): MAJOR MICHAEL S FRANCIS   MARVIN W LUTTGES

13a. TYPE OF REPORT: INTERIM

13b. TIME COVERED: FROM ______ TO ______

14. DATE OF REPORT (Yr., Mo., Day): 1984, May

15. PAGE COUNT: 194

16. SUPPLEMENTARY NOTATION: Proceedings of the Workshop on Unsteady Separated Flow, United States Air Force Academy 10-11 August 1983

17. COSATI CODES

FIELD	GROUP	SUB. GR.

18. SUBJECT TERMS (Continue on reverse if necessary and identify by block number): FLUID MECHANICS; TIME-DEPENDENT FLOWS; MANEUVERING FLIGHT; AERODYNAMICS; SEPARATED FLOWS; UNSTEADY FLOWS; AERODYNAMIC MANEUVERING

19. ABSTRACT (Continue on reverse if necessary and identify by block number)

This report documents the proceedings of a "Workshop on Unsteady Flow Separation" held at the US Air Force Academy on 10-11 August 1983. This two day program was comprised of 27 presentations on a wide variety of topics ranging from fundamental concepts to potential applications. Flows with time dependent boundary conditions leading to global separated flow structures were highlighted.

20. DISTRIBUTION/AVAILABILITY OF ABSTRACT: UNCLASSIFIED/UNLIMITED ☒ SAME AS RPT. ☐ DTIC USERS ☐

21. ABSTRACT SECURITY CLASSIFICATION: UNCLASSIFIED

22a. NAME OF RESPONSIBLE INDIVIDUAL: Major Michael S Francis

22b. TELEPHONE NUMBER (Include Area Code): 202/767-4935

22c. OFFICE SYMBOL: AFOSR/NA

DD FORM 1473, 83 APR   EDITION OF 1 JAN 73 IS OBSOLETE

UNCLASSIFIED
SECURITY CLASSIFICATION OF THIS PAGE

COMPONENT PART NOTICE

THIS PAPER IS A COMPONENT PART OF THE FOLLOWING COMPILATION REPORT:

(TITLE): Proceedings of the Workshop on Unsteady Separated Flow Held at the United States Air Force Academy on A ugust 10 11, 1983.

(SOURCE): Air Force Office of Scientific Research, Bolling AFB, DC. Directorate of Aerospace Sciences.

TO ORDER THE COMPLETE COMPILATION REPORT USE AD-A148 249.

THE COMPONENT PART IS PROVIDED HERE TO ALLOW USERS ACCESS TO INDIVIDUALLY AUTHORED SECTIONS OF PROCEEDINGS, ANNALS, SYMPOSIA, ETC. HOWEVER, THE COMPONENT SHOULD BE CONSIDERED WITHIN THE CONTEXT OF THE OVERALL COMPILATION REPORT AND NOT AS A STAND-ALONE TECHNICAL REPORT.

THE FOLLOWING COMPONENT PART NUMBERS COMPRISE THE COMPILATION REPORT:

AD#:	TITLE:
AD P004 153	Supermaneuverability.
AD-P004 154	Wing Rock Flow Phenomena.
AD-P004 155	Potential Applications of Forced Unsteady Flows.
AD-P004 156	Unsteady Stall Penetration of an Oscillating Swept Wing.
AD-P004 157	Simultaneous Flow Visualization and Unsteady Lift Measurement on an Oscillating Lifting Surface.
AD-P004 158	A Visual Study of a Delta Wing in Steady and Unsteady Motion.
AD-P004 159	Comparative Visualization of Accelerating Flow around Various Bodies, Starting from Rest.
AD-P004 160	Prediction of Dynamic Stall Characteristics Using Advanced Nonlinear Panel Methods.
AD-P004 161	Numerical Solution of the Navier-Stokes Equations for Unsteady Separated Flows.
AD-P004 162	Unsteady Aerodynamic Loading of an Airfoil due to Vortices Released Intermittently from Its Upper Surface.
AD-P004 163	A Navier-Stokes Calculation of the Airfoil Dynamic Stall Process.
AD-P004 164	Some Structural Features of Unsteady Separating Turbulent Shear Flows.
AD-P004 165	Can the Singularity Be Removed in Time-Dependent Flows?
AD-P004 166	On the Shedding of Vorticity at Separation.
AD-P004 167	Unsteady Separated Flows. Forced and Common Vorticity about Oscillating Airfoils.
AD-P004 168	Unsteady Separated Flows. Generation and Use by Insects.
AD-P004 169	Theoretical Study of Non-Linear Unsteady Aerodynamics of a Non-Rigid Lifting Body.

DTIC
S DEC 1 4 1984
A

This document has been approved for public release and sale; its distribution is unlimited.

Distribution/
Availability Codes
Dist | Avail and/or Special

COMPONENT PART NOTICE (CON'T)

AD#:	TITLE:
AD-P004 170	Theoretical Investigation of Dynamic Stall Using a Momentum Integral Method.
AD-P004 171	Preliminary Results from the Unsteady Airfoil Model USTAR2.
AD-P004 172	Experiments on Controlled, Unsteady, Separated Turbulent Boundary Layers.
AD-P004 173	Genesis of Unsteady Separation.
AD-P004 174	Flow Separation Induced by Periodic Aerodynamic Interference.
AD-P004 175	Leading Edge Separation Criterion for an Oscillating Airfoil.
AD-P004 176	Natural Unsteadiness of a Separation Bubble behind a Backward-Facing Step.

AFOSR/FJSRL/U. COLORADO

WORKSHOP ON UNSTEADY SEPARATED FLOWS

Organizer: Capt. Michael S. Francis, Ph.D.
AFOSR/NA
Bolling AFB, DC 20332

Coordination and Documents: Marvin W. Luttges, Ph.D.
Professor and Acting Chairman
Aerospace Engineering Sciences, Box 429
University of Colorado
Boulder, Colorado 80309

Coordination and Arrangements: Lt. Hank Helin
Frank J. Seiler Research Laboratory
U.S. Air Force Academy
Colorado Springs, Colorado 80840

Technical Assistance Acknowledgements

Michael C. Robinson
Laurie Beeman
Nancy Searby
Randy Jones
JoAnne Button
Terri MacGregor

Preparation of Final Publication

JoAnne Button
Erika Shuck

Dist Special

Luttges © 1984

LIST OF ATTENDEES

Professor Holt Ashley
Dept. of Aeronautics & Astronautics
Durand 369
Stanford University
Palo Alto, CA 94305
(415) 497-4136

Dr. Robert Bass
P.O. Drawer 28510
6220 Culebra Road
Southwest Research Institute
San Antonio, TX 78284
(512) 684-5111 Ext. 2326

Dr. Dale Berg
Sandia National Laboratory, Div. 1636
P.O. Box 5800
Albuquerque, NM 87185
516-52-2054
(505) 844-1030

Dr. Lawrence Carr
NASA - Ames Research Center
Mail Stop 227-8
Moffett Field, CA 94035

Dr. Frank Carta
United Technologies Research Ctr.
Silver Lane
East Hartford, CT 06108
(203) 727-7355

Dr. Tuncer Cebeci
McDonnel Douglas Aircraft Co.
3855 Lakewood Blvd.
Long Beach, CA 90846
(213) 593-8322

Dr. David Chou
Dept. of Mechanical Engineering
University of New Mexico
Albuquerque, NM 87106

Dr. C.-Y. Chow
Aerospace Engineering Sciences
University of Colorado
Campus Box 429
Boulder, CO 80309
(303) 492-7907

Mr. Morton Cooper
Flow Research Company
1320 Fenwick Lane, Suite 401
Silver Spring, MD 20910
(301) 589-5780

Dr. Eugene Covert
Dept. of Aeronautics & Astronautics
Massachusetts Institute of Technology
Cambridge, MA 02139

Dr. Steven Crow
Poseidon Research
1299 Ocean Avenue, Suite 821
Santa Monica, CA 90401

Dr. Atlee Cunningham
General Dynamics - Ft. Worth Division
P.O. Box 748
Fort Worth, TX 76101
(817) 732-4811 Ext. 4418

Dr. Frank A. Dvorak
Analytical Methods Inc.
2047 - 152nd Avenue, N.E.
Redmond, WA 98052
(206) 643-9090

Dr. John Eaton
Dept. of Mechanical Engineering
Stanford University
Palo Alto, CA 94305
(415) 497-1971

Dr. Lars Ericsson
Lockheed Missiles & Space Co.
D/81-10, Bldg. 157
Sunnyvale, CA 94088
(408) 756-1396

Dr. Hermann Fasel
Dept. of Aerospace & Mechanical Engin
University of Arizona
Tucson, AZ 85721
(602) 621-6119

Professor Peter Freymuth
Aerospace Engineering Sciences
University of Colorado
Campus Box 429
Boulder, CO 80309
(303) 492-7611

Dr. Mohamed Gad-El-Hak
Flow Industries, Inc.
21414 - 68th Avenue South
Kenth, WA 98032
(206) 872-8500

Dr. Wilbur Hankey
AFWAL/FIMM
Wright-Patterson AFB, OH 45433
(513) 255-2455

Lt. H. Helin
FJSRL/NH
USAF Academy, CO 80840
(303) 472-3122

Dr. W.B. Herbst
MBB-Flugzeuge (GMBH)
Military Aircraft Division
Postfach 80 11 60
800 Munchen 80, FRG (Germany)
89 - 60005581

Dr. C.M. Ho
Dept. of Aerospace Engineering
University of Southern California
Los Angeles, CA
(213) 743-6560

Dr. Ed James
Vehicle Research Corporation
650 Sierra Madre Villa, Suite 100
Pasadena, CA 91107
(213) 351-4202

Mr. James B. Johnson
Southwest Research Institute
San Antonio, TX 78284
465-70-7845

Major Eric Jumper
Dept. of Aeronautics & Astronautics
Air Force Institute of Technology
Wright-Patterson AFB, OH 45433
(513) 255-2998

Dr. Donald A. Kennedy
Aerospace Engineering Sciences
University of Colorado
Campus Box 429
Boulder, CO 80309
(303) 492-7633

Mr. Dennis Koga
Dept. of Mechanics & Mechanical Engin.
Illinois Institute of Technology
Chicago, IL 60616
(312) 567-3213

Mr. Peter Lorber
Dept. of Aeronautics & Astronautics
Massachusetts Institute of Technology
Cambridge, MA 02139

Dr. Marvin W. Luttges
Aerospace Engineering Sciences
University of Colorado
Campus Box 429
Boulder, CO 80309
(303) 492-7613

Dr. Brian Maskew
Analytical Methods, Inc.
2047 - 152nd Avenue, N.E.
P.O. Box 3786
Redmond, WA 98052
(206) 643-9090

Dr. Ken McAlister
NASA - Ames Research Center
Mail Stop 215-1
Aeromechanics Laboratory
Moffett Field, CA 94035
(415) 965-5892

Dr. Dean Mook
Office of Naval Research - Code 432F
800 N. Quincy Street
Arlington, VA 22217
(202) 696-4305

Mr. Dieter Multhopt
AFWAL/FIGG
Wright-Patterson AFB, OH 45433
(513) 255-6764

Dr. Hassan Nagib
Mechanics & Mechanical Engineering
Illinois Institute of Technology
Chicago, IL 60616
(312) 567-3213

Mr. William Palmer
Rockwell International Corp.
4300 E. 5th Avenue
Columbus, OH 43216
231-50-2554
(614) 239-3342

Dr. Helen Reed
Dept. of Mechanical Engineering
Stanford University
Stanford, CA 94305

Captain Robert Reilman
AFIT/Georgia Tech
664 Continental Drive
Lawrenceville, GA 30245
253-82-7879
(404) 972-3645

Dr. W.C. Reynolds
Dept. of Mechanical Engineering
Stanford University
Stanford, CA 94305

Mr. Michael Robinson
Aerospace Engineering Sciences
University of Colorado
Campus Box 429
Boulder, CO 80309
(303) 492-6416

Dr. H.L. Sankar
School of Aerospace Engineering
Georgia Institute of Technology
Atlanta, GA 30332
(404) 894-3014

Lt. Col. T. Saito
FJSRL/CC
USAF Academy, CO 80840
(303) 472-3120

Dr. William Saric
Dept. of Engin. Science & Mechanics
Virginia Polytechnic Inst. & State Univ.
Blacksburg, VA 24061
(703) 961-6871

Dr. Stephen J. Shamroth
Scientific Research Associates, Inc.
P.O. Box 798
Glastonbury, CT 06033
(203) 659-0511

Dr. Roger Simpson
Professor of Mechanical Engineering
Southern Methodist University
Dallas, TX 75275
(214) 962-3096

Captain Francis L. Smith
Air Force Weapons Laboratory
Kirkland AFB, NM 87117
418-78-0006
(505) 844-9831

Dr. James Strickland
Dept. of Mechanical Engineering
Texas Tech University - Box 4289
Lubbock, TX 79409
(806) 742-3563

Mr. Charles Suchomel
AFWAL/FIGG
Wright-Patterson AFB, OH 45433
358-28-8380
(513) 476-2096

Dr. Demetri Telionis
Dept. of Engin. Science & Mechanics
Virginia Polytechnic Inst. & State Univ.
Blacksburg, VA 24061
(703) 961-7492

Dr. Hermann Viets
College of Engineering, Rm. 151
P.O. Box 6101
West Virginia University
Morgantown, WV 26506
(304) 293-4821

Mr. Robert Woodcock
AFWAL/FIGG
Wright-Patterson AFB, OH 45433
317-22-7393
(513) 476-2076

Major John Walker
FJSRL/NH
USAF Academy, CO 80840
(303) 472-3122

Dr. James C. Wu
School of Aerospace Engineering
Georgia Institute of Technology
Atlanta, GA 30332
(404) 894-3028

Dr. Robert Whitehead
Office of Naval Research, Code 432F
800 No. Quincy Street
Arlington, VA 22217
(202) 696-4404

Dr. John Yates
Aeronautical Research Assoc. of Princeton
P.O. Box 2229
Princeton, NJ 08540
(609) 452-2950 Ext. 244

Dr. James D. Wilson
AFOSR/NA
Bolling AFB, DC 20332
(202) 767-4935

AFOSR/FJSRL/U. COLORADO

WORKSHOP ON UNSTEADY SEPARATED FLOWS

- PROGRAM -

Wednesday, 10 August 1983

8:00 AM	Welcome Introductory Remarks
	SESSION 1 - APPLICATIONS
8:15 AM	"Supermaneuverability," W. Herbst (Invited Presentation)
9:15	"Wing Rock Flow Phenomena," L. Ericsson
9:45	Coffee Break
10:00	"Aerodynamic Agility Resulting from Energetic Separated Flows," D. A. Kennedy
10:30	"Potential Applications of Forced Unsteady Flows," H. Viets, G. M. Palmer, R. J. Bethke
	SESSION 2 - AERODYNAMIC CHARACTERISTICS OF TIME DEPENDENT MOTIONS - I
11:00	"Unsteady Stall Penetration of an Oscillating Swept Wing," F. Carta
11:30	Lunch (NCO Club - buses leave at front of building)
1:00 PM	"Correlation of Lift and Boundary-Layer Activity on an Oscillating Lifting Surface," R. Bass, J. Johnson, and J. Unruh
1:30	"A Visual Study of a Delta Wing in Steady and Unsteady Motion," Mohamed Gad-el-Hak, C.-M. Ho, and R. Blackwelder
2:00	"Comparative Visualization of Accelerating Flows around Various Bodies, Starting from Rest," P. Freymuth, M. Palmer, and W. Bank
2:30	Coffee Break
	SESSION 3 - ANALYTICAL AND NUMERICAL MODELS - I
2:45	"Prediction of Dynamic Stall Characteristics Using Advanced Non-linear Panel Methods," F. Dvorak and B. Maskew
3:15	"Numerical Solutions of the Navier-Stokes Equations for Unsteady Separated Flows," W. L. Hankey
3:45	"Unsteady Aerodynamic Loading on an Airfoil due to Vortices Released Intermittently from its Upper Surface," C.-Y. Chow and C.-S. Chiu
4:15	"Calculations of Oscillating Airfoil Flow Fields via the Navier-Stokes Equations," S. J. Shamroth
	SESSION 4 - UNSTEADY BOUNDARY LAYER SEPARATION - I
4:45	"Some Structural Features of Unsteady Separating Turbulent Shear Flows," R. Simpson
5:15	"Can the Singularity be Removed in Time-Dependent Flows?" T. Cebeci, A. Khattab, and S. M. Schimke

Session 4 (Continued)

5:45	"On the Shedding of Vorticity at Separation," D. Telionis, D. Mathioulakis, and M. S. Cramer
6:15	Return to Motels (buses leave front of building)

Thursday, 11 August 1983

8:30 AM	"Unsteady Separated Flow: Forced and Common Vorticity about Oscillating Airfoils," M. Robinson and M. W. Luttges
9:00	"Passive and Active Device-Controlled Unsteady Separated Flowfields," H. Nagib, D. Koga, and P. Reisenthel
9:30	"Unsteady Separated Flows: Generation and Use by Insects," M. W. Luttges, C. Somps, M. Kliss, and M. Robinson
10:00	Coffee Break

SESSION 5 - ANALYTICAL AND NUMERICAL MODELS - II

10:15	"Studies of Two Non-Linear Unsteady Flow Problems," J. C. Wu, N. L. Sankar, H. Hu Chen, and T. M. Hsu
10:45	"A Study of Dynamic Stall in Constant - α Gusts using an Unsteady Karman-Pohlhausen Method," E. J. Jumper, R. G. Docken, and J. E. Hitchcock
11:15	"Preliminary Results from the Unsteady Airfoil Model USTAR2," J. Strickland, J. W. Oler and B. J. Im
11:45	Lunch (NCO Club - buses leave at front of building)

SESSION 6 - UNSTEADY BOUNDARY LAYER SEPARATION - II

1:15 PM	"Experiments on Controlled, Unsteady, Separated Turbulent Boundary Layers," W. C. Reynolds and L. W. Carr
1:45	"Genesis of Unsteady Separation," C.-M. Ho
2:15	"Flow Separation Induced by Periodic Aerodynamic Interference," E. E. Covert, P. F. Lorber, and C. M. Viezy
2:45	"Unsteady Leading Edge Separation," E. C. James
3:15	Coffee Break
3:30	"Natural Unsteadiness of a Separation Bubble Behind a Backward Facing Step," J. K. Eaton and A. E. Alving
4:00	"Spectral Determination of Unsteady Flow Phenomena by the Maximum-Entropy Method," H. Nagib, D. Koga, P. Reisenthel, and T. Corke
4:30	Open Discussion Closing Remarks

AD-P004 153

Supermaneuverability

Dr. W. B. Herbst
MESSERSCHMITT-BOLKOW-BLOHM GMBH
Munich, Germany

Abstract:

Supermaneuverability is defined as the capability of a fighter aircraft to execute tactical maneuvers with controlled side slipping and at angles of attack beyond maximum lift. This paper deals particularly with post stall maneuverability at zero side slipping since this element of supermaneuverability is relatively unknown. The analysis is based on optimum control calculation of simplified maneuver elements and on extensive manned and computerized close air combat simulation. This analysis explains the tactical advantage observed during combat simulations and leads to the definition of a typical maneuver duty cycle which is consistant with conventional air combat maneuvers with all aspect weapons. Reference is made to earlier studies about maneuvers with thrust vectoring and thrust reversal. Finally, requirements are given for the necessary level of thrust-to-weight ratios and control power including indications of technical solutions.

1. Introduction

There are three different concepts (fig. 1) of improving maneuverability by means of tilting engine thrust:

a) Inflight thrust reversal
b) Thrust vectoring
c) Post Stall maneuvering (PST)

(a) has been considered as a deceleration device [1] which permits to slow the aircraft down rapidly into a speed regime of better turn performance, however, it does not directly contribute to maneuver performance in terms of improving a change of the direction of flight.

(b) has been discussed [2] in conjunction with configurations, such as the BAe Harrier. Thrust vectoring offers an additional degree of freedom to establish a maneuver state. However, it requires engine exit momentum to point at the aircraft c.g. over the vectoring range, which is fairly incompatible with afterburner installation. A noticeable improvement of air combat capability has been demonstrated.

(c) is the subject of this paper. The engine is fixed to the aircraft fuselage and thus exit momentum is always in line with the c.g. The only difference to a conventional aircraft is the requirement for large angles of attack in excess of maximum lift angle of attack. Post Stall flight conditions have already been demonstrated, however, tactical PST-maneuvers require a level of controllability far beyond that of contemporary aircraft. Also, the tactical advantage was unknown.

There is similarity between the concepts (b) and (c). For both concepts the gain in sustained turn performance is small and limited to extreme flight conditions. The tactical advantage is based on short term and highly instantaneous maneuvers and the achievement of small radii of turn. (b) could even include (c) if the aircraft were allowed to exceed the stall limits. In a PST-maneuver, however, the advantage of thrust vectoring is marginal and may not justify the overall design penalties.

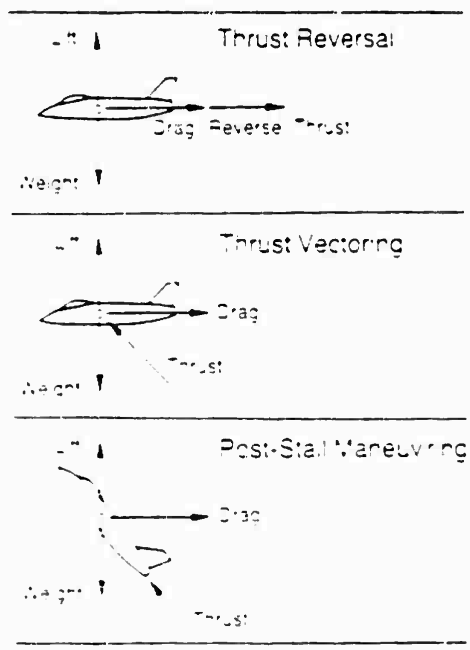

Fig. 1 Schemes of using thrust deflection for maneuver enhancement.

The tactical advantage of PST-maneuvering in short range air combat depends on the weapons used. There is a change in combat maneuver characteristics [3] caused by the all aspect capability of new weapons In head-on situations particularly instantaneous turn performance combined with small turn radii has been found decisive. The new weapons - including radar controlled guns in combination with sideslipping flight modes - will inhibit further improvements of air combat capability by means of further improved energy - maneuverability [3]. New maneuver modes - such as PST-maneuvering - may be the only way of achieving substantial improvements in close combat effectiveness.

2. Tactical results of air combat simulations

PST maneuvering has been the subject of manned and computerized dual and multiple combat simulations [4] - [7]. Significant observations are the following maneuver characteristics:

- o 5 sec average duration of a PST maneuver
- o 10% of total engagement time in PST
- o lower g-level by about 1 Δ g
- o lower average maneuvering speed by about 0.1 Δ M

and tactical advantages:

- o quicker into firing position maneuvering
- o longer a firing position maintaining
- o more first shoot opportunities
- o less counter hits
- o easier and quicker to switch alternate targets
- o dictating tactics throughout entire speed regime
- o more missiles deployable

As an overall result it was found:

- exchange ratio in dual combat with equal weapons against an opponent of equal conventional maneuver performance is about 2:1

- exchange ratio in multiple combat remains to be largely dependent on the numbers ratio, however, can be significantly improved. For example in [4] a single PST-capable fighter was able to neutralize two conventional opponents. Computer simulations [7] involving larger numbers of opponents are showing an increase of the relative advantage of PST-maneuvering (fig. 2).

A large amount of tactical data has been gathered in more than 3000 simulated engagements of 3 different manned combat simulators flown by 15 operational pilots of three airforces. Still, it remained somewhat difficult to precisely understand the advantage. Sometimes the advantage is attributed to fuselage pointing over the larger α-range. Actually, only a relatively small number of gun shots have been observed during PST-maneuvers and a missile firing limitation to α = 30° did not lead to any significant degradation of tactical success [5].

The majority of firing opportunities occurred right after finishing a PST-maneuver and returning to the conventional flight regime. PST capability, therefore, must be interpreted as a maneuvering scheme rather than a gimbaling device.

In general, the pay-off is based on a trade of loss of energy versus positional and time advantage. A proper PST-maneuver preceeding ahead-on engagement provides a decisive time advantage at a momentary expense of energy. In multiple engagements the loss of energy seems to be compensated by a roll-rate advantage, according to [4]. In order to convert from a right hand turn to a left hand turn against an alternate target a conventional aircraft would have to unload, roll and re-load. With PST capability an aircraft could roll around the velocity vector at constant - very high - angle of attack. This capability was developed during

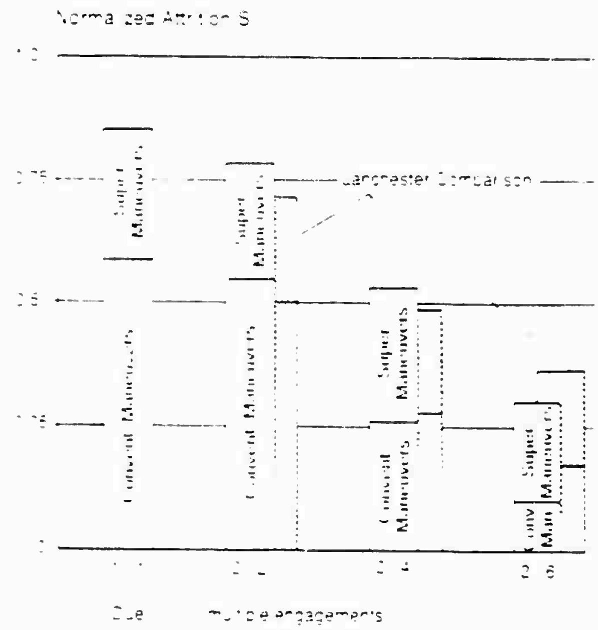

Fig. 2 Evaluation of Supermaneuverability in dual and multiple air combat with all aspect weapons. Results of computer simulations. S = 0.5 means a patt situation.

manned simulations (slicing maneuvers).

As a result, the aircraft with PST-capability was able to dictate the tactical course of the engagement. Missile capability did not allow the conventional opponent(s) to disengage. Overall speed and loadfactor was observed to be lower than in conventional air combat. In particular, there was less time at limit g-loadings.

3. Maneuver analysis

For any flight condition (aircraft attitude, velocity vector, power setting, altitude) the maneuver state (longitudinal and lateral acceleration) is a function of the sum of all forces, aerodynamic forces, engine inlet and exit momentum. The analysis shall be limited to zero sideslip conditions for PST-maneuvering. Fig. (3) and fig. (4) are results of mass point calculations for a particular aircraft drag polar at a particular altitude and for maximum engine power. Fig. (3) pertains to horizontal flight conditions.

Fig. (4) describes two conditions of a vertical maneuver, the highest and lowest point with the velocity vector pointing horizontally. There is a SEP=0 line distinguishing between accelerated and decelerated maneuver states and there are structural and maximum lift limits. Any combination of turn rates and mach number corresponds to a particular radius of turn. Fig. (3) and (4) are special cases of many such diagrams for an infinite number of flight conditions. An aircraft maneuver would be a sequence of maneuver states at continuously changing flight conditions. Fig. (3) and fig. (4) indicate

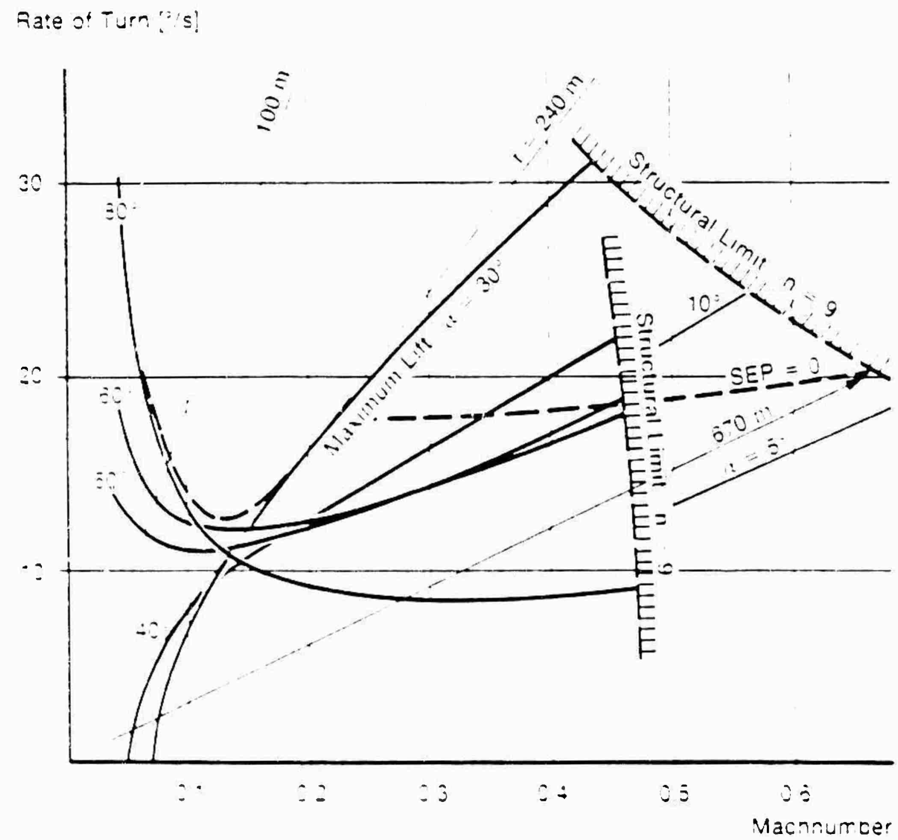

Fig. 3 Maneuver states in a horizontal turn (aircraft dependant).

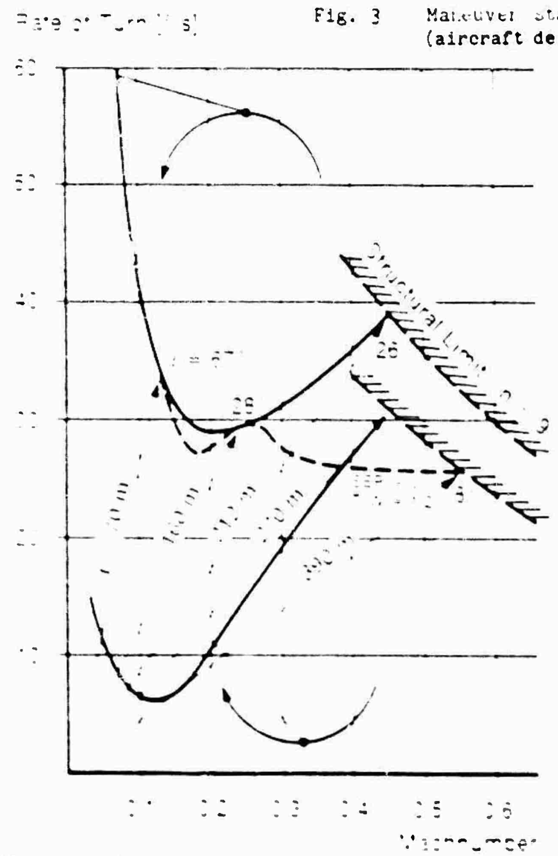

Fig. 4 Maneuver states in a vertical turn (aircraft dependant). Upper curve for top, lower curve for bottom of a vertical maneuver.

- that a turn rate advantage beyond maximum lift angle of attack as compared to "corner speed" can be expected at very low speeds

- that a significant turn radius advantage can be achieved at angles of attack well beyond maximum lift

- that the high angle of attack part of an advantageous PST-maneuver would have to penetrate a relatively low speed regime (0.05>M>0.2)

- that no significant advantage could be expected from PST-maneuvers limited to moderate angles of attack ($\alpha \lesssim 50^{o}$).

Performance of a PST-maneuver is an optimum control problem with angle of attack and bank angles as independent variables (thrust was found to be maximum througnout the maneuver for best results). Pay-off function in real combat would be an earlier firing opportunity and to deny counterfire. In order to get better problem transparency, minimum time maneuvers with defined starting and end conditions have been calculated in [9]. There was an advantage of exceeding maximum lift angle of attack and instantaneous penetration into the PST regime whenever certain geometrical constraints had to be satisfied.

One of the most applicable analytical maneuvers, for example, is that of a 180° change of heading with the additional constraint of returning to

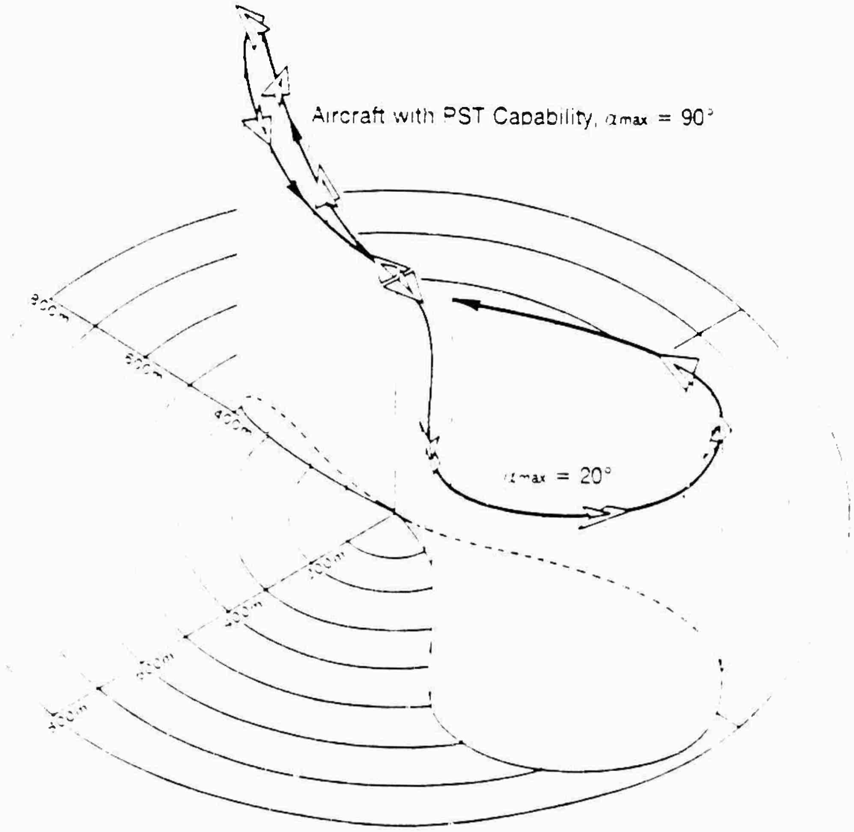

Fig. 5 Comparison of minimum time maneuvers. Result of trajectory optimizations.

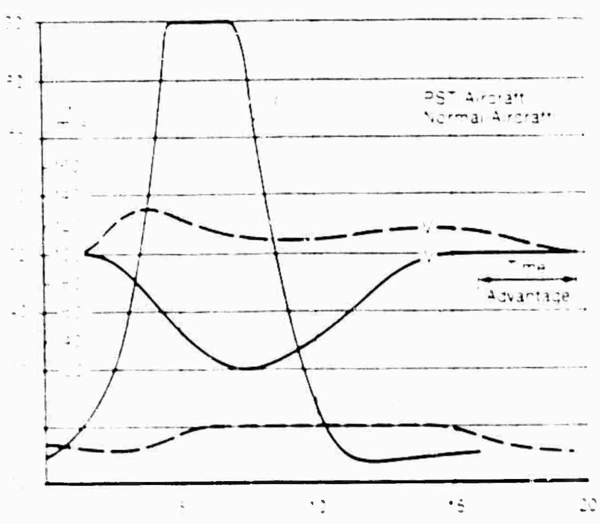

Fig. 6 Time history of minimum time maneuvers. Result of trajectory optimizations.

the point of departure at initial speed and altitude (fig. (5)). The same aircraft, however limited to maximum lift angle of attack would follow a different optimum flight path and need more time. Fig. (6) shows the associated time histories for angle of attack and speed. Typically, the PST-maneuver is characterized by a rapid pitch up to PST-incidences with a fast recovery into the conventional flight regime with only a few seconds of persistence at PST-conditions.

Fig. (7) is a time history of the same analytical minimum time maneuver as shown in fig. (5) an (6), plotted in terms of rate of velocity vector turn vs. speed. It shows the type of PST-maneuver cycle which also has been found in actual combat maneuvers. In comparison with the α -limited optimum maneuver the PST-maneuver features a lower average rate of turn (18°/s against 22°/s) but less total change of headings and a significantly smaller average radius of turn. Fig. (8) shows the energy management of both the conventional and the PST maneuver.

Of course, there is a large variety of maneuver types for which PST-capability can provide an advantage. Mass point trajectory calculation are useful but limited. Actual PST-maneuver performance will depend upon available control power and dynamic response. Fig. 9 is a summary of simulator trials with actual aerodynamic and mass data of a fighter aircraft design, for which a suitable control system was designed incorporating low speed control enhancement by means of ±10° [illegible] efflux deflection in pitch and yaw.

For certain repeatable maneuver types and for a given limitation in angle of attack (abscissa in fig. 9) pilots were trying to

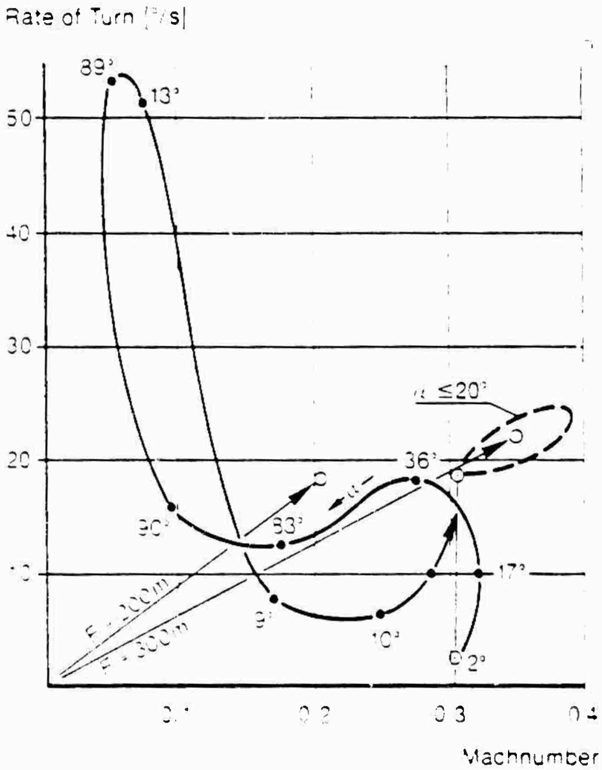

Fig. 7 Comparison of maneuver cycles for minimum time maneuvers. Results of trajectory optimizations.

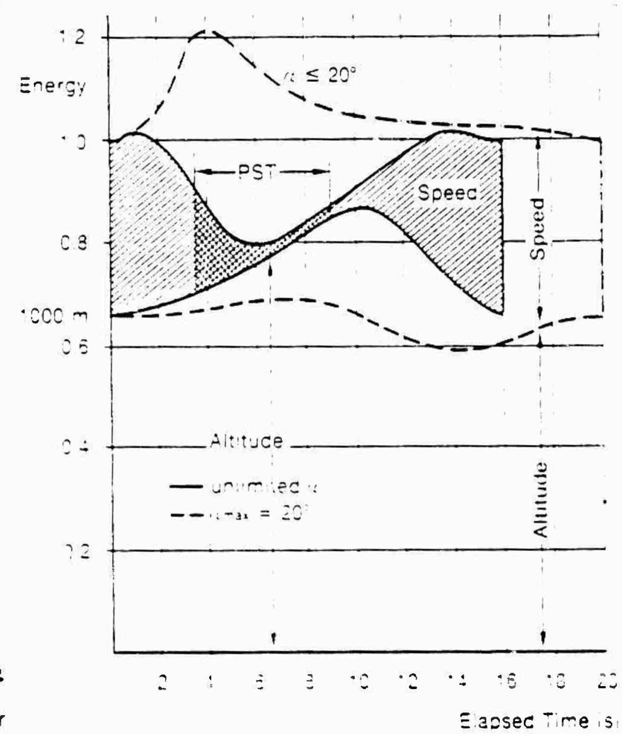

Fig. 8 Energy management comparison for minimum time maneuvers. Results of trajectory optimizations.

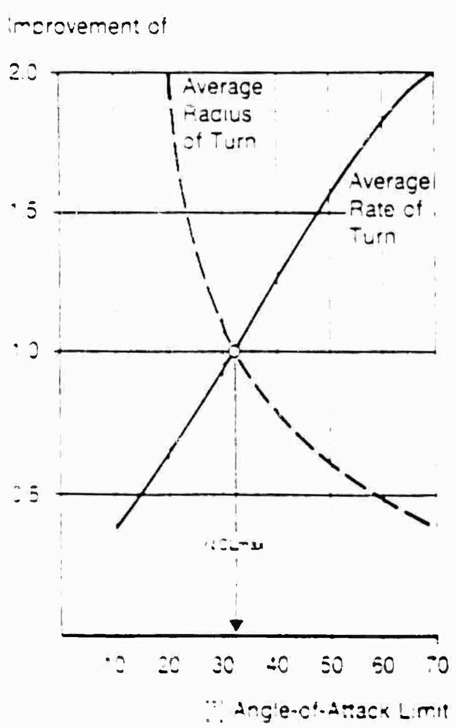

Fig. 9 Results of manned simulations representing real aircraft and control dynamics. Standardized PST maneuver with 180° change of heading. Control augmentation by means of a ±10° vectored nozzle in pitch and yaw.

minimize the time to accomplish the maneuver. Average rate of turn and average radius of turn improvement throughout each maneuver is shown in fig. 9.

Simulated air combat engagements (both manned and computer simulations) have been investigated with regard to common characteristics of PST-maneuvers. Fig. (10) shows trajectories of a typical initial phase engagement of two opponents with equal conventional performance. Aircraft 1 is limited to maximum lift, aircraft 2 has PST-capability up to 70° angle of attack including certain control power in pitch and yaw. Both aircraft are equipped with the same all aspect weapon. The associated time history of turn rate vs. speed and angle of attack is plotted in fig. (11) and fig. (12). Starting at high speed, same altitude, and a typical positional offset opponents are pulling maximum g and then slow down to best instantaneous turn rate by means of gaining altitude. At the same time a smaller radius of turn would help to get the opponent into own weapon off-boresight cone and to keep the opponent from achieving the same objective. A properly scheduled penetration into the PST-regime enhances both the slow down and the minimum radius part of the combat maneuver without a significant loss of turn rate.

As a result aircraft 2 achieves its firing opportunity at a time still outside of aircraft 1 firing cone. It is important to note that this firing opportunity occurs shortly after the aircraft has returned into the normal

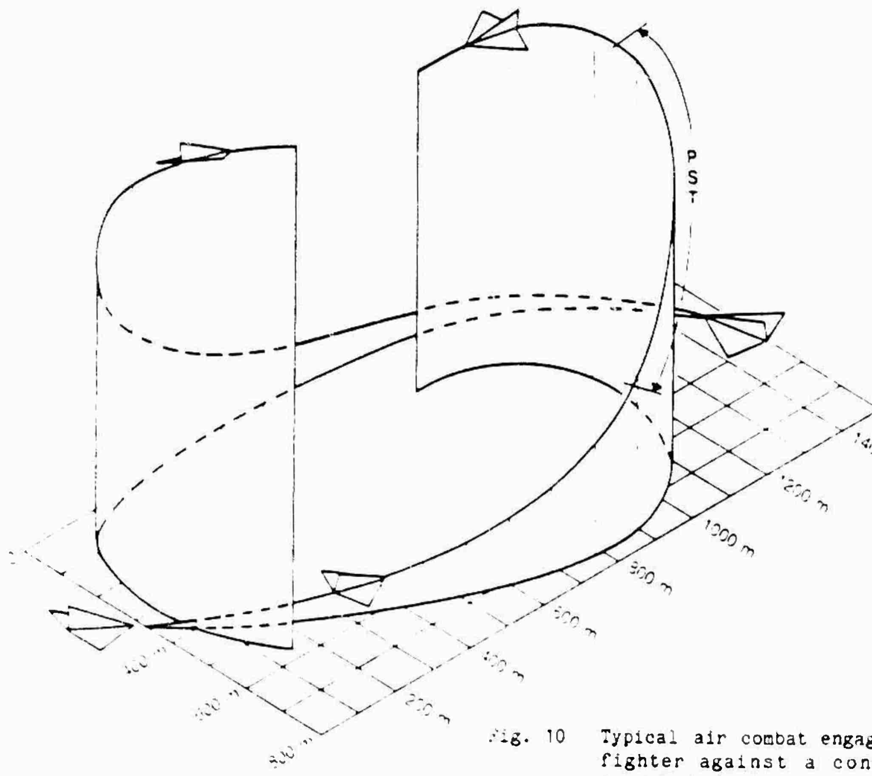

Fig. 10 Typical air combat engagement of a PST fighter against a conventional - limited fighter with all aspect weapons. Result of computer simulations.

flight regime. During the PST-maneuver the weapon was even pointing away from the target.

Fig. (13) is another representation of the

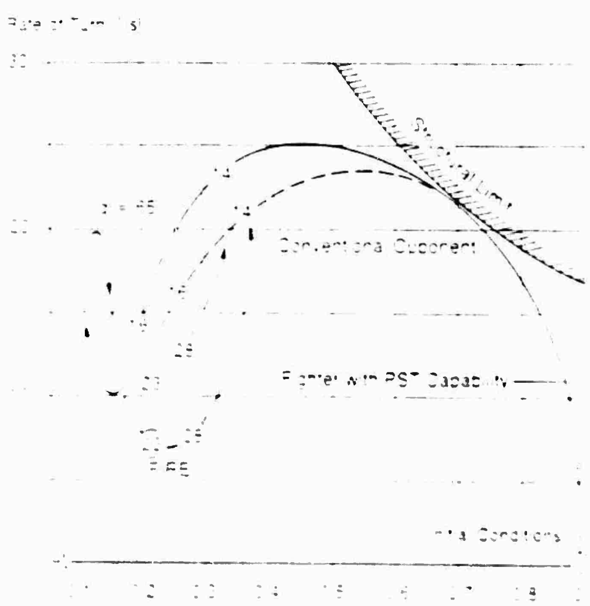

Fig. 11 Maneuver characteristics of a typical air combat engagement. Elapsing time in sec. Result of computer simulations.

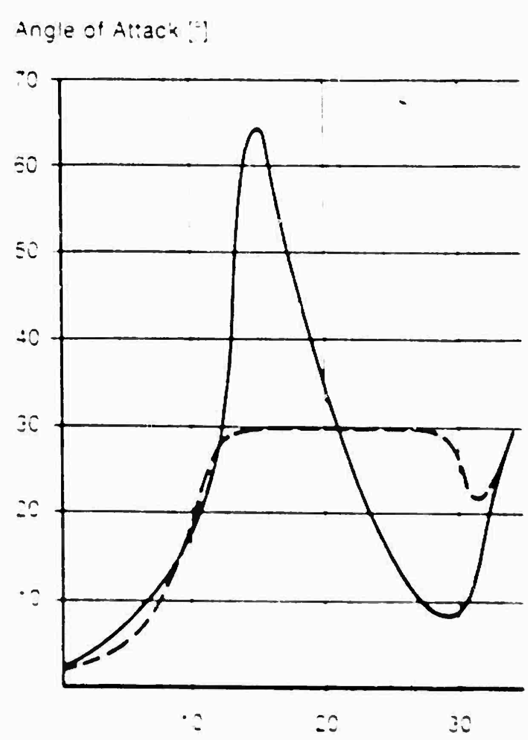

Fig. 12 Angle-of-Attack during a typical air combat engagement. Result of computer simulations.

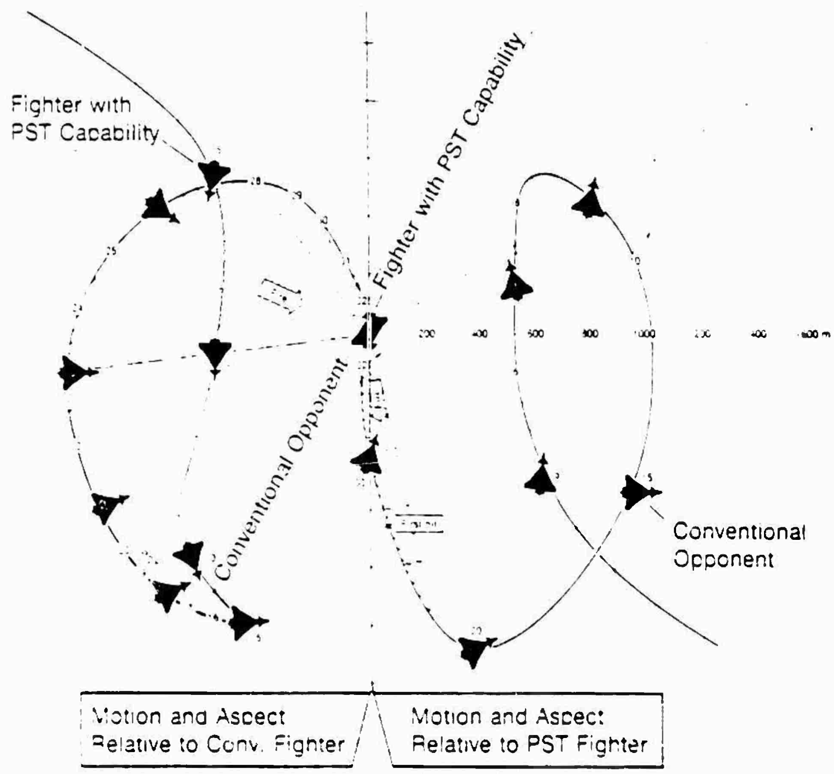

Fig. 13 Typical air combat engagement. Relative positions of opponents and their aspects and firing opportunities Time intervals in sec. Result of computer simulations.

same engagement. It shows how the pilots in aircraft 2 (left hand side of fig. (13)) and in aircraft 1 (right hand side of fig. (13)) would view their opponents as they look outside their cockpit windows. Aircraft symbols in fig. (13) represent the actual aspect relative to the opponent at the indicated time intervals. The figure, therefore, also shows convergence into a firing position and the time in firing position for a given weapon cone.

Aircraft 2 performs the PST-section of the maneuver (second 8 - 15) far outside aircraft 1 weapon range in its backward look angle sector and is getting a first firing opportunity in the 23. second being in a safe beam position relative to the target. There is active firing time without counterfire for several seconds until the opponent would pass each other almost head on. The pilot of aircraft 2 is never looking into his opponent firing cone until his first missile hits the target. He recovered the energy lost during the PST-maneuver right after the attack against aircraft 1 (fig. 14). Average speed of the PST-aircraft observed throughout many simulated dual and multiple combat engagements is only 5 - 10% lower as compared to the conventional opponents. Obviously, the aircraft is vulnerable during the high angle of attack phase of a PST-maneuver, however, the pilot has always the option to restrain if the momentary loss of speed constitutes a tactical disadvantage (provided conventional performance does not suffer too much from its incorporation into the overall design).

PST-maneuvers are consistent with the general dynamic characteristics of air combat with all aspect weapons [10]. There is the same

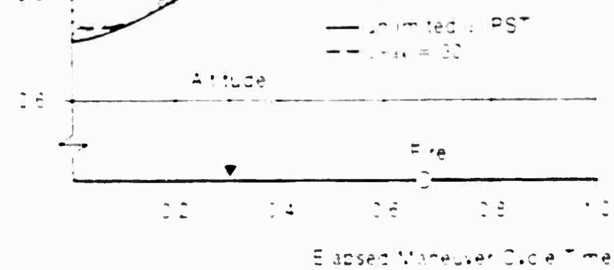

Fig. 14 Energy management in a typical air combat engagement. Result of computer simulations.

overall left hand maneuver cycle of the turn rate vs. speed time history with the addition of a short term right hand cycle excursion into the PST-regime.

4. PST regime and requirements

Limits are given by controleability, engine power and structural constraints (fig. 15). Actual usage, however, is dictated by tactical advantages. For high performance aircraft (thrust-to-weight > 1.0) there is a low speed regime of possible sustained maneuver. In combat, however, there are no sustained maneuvers (constant maneuver states); excess thrust is always used to re-accelerate or to gain altitude. As a general rule PST-capability requires

- sufficient control power in pitch, roll and yaw at mach numbers as low as 0.1 and incidence up to 70°.

- High angle of attack compatibility up to 70° at machnumbers as high as 0.6 (4000 m altitude) for example with regard to aircraft stability or air intake flow.

- Thrust/weight ration > 1.0 fig. (16) shows the time advantage of the optimized PST-maneuver (fig. 5) at different thrust-to-weight ratios. With decreasing engine power the observed maximum values of angle to attack are becoming smaller. At thrust-to-weight rations of less than 0.6 there is no tactical advantage in exceeding maximum lift even if the capability is available.

- Sufficient control power, particularly in pitch and yaw.

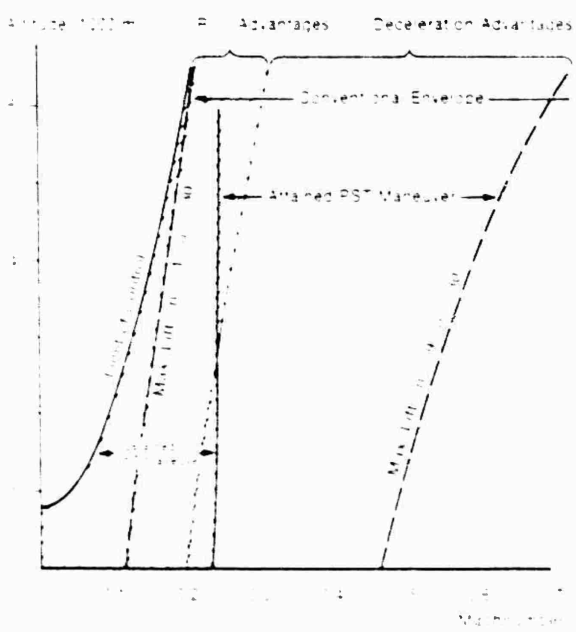

Fig. 15 The PST flight regime (aircraft dependent).

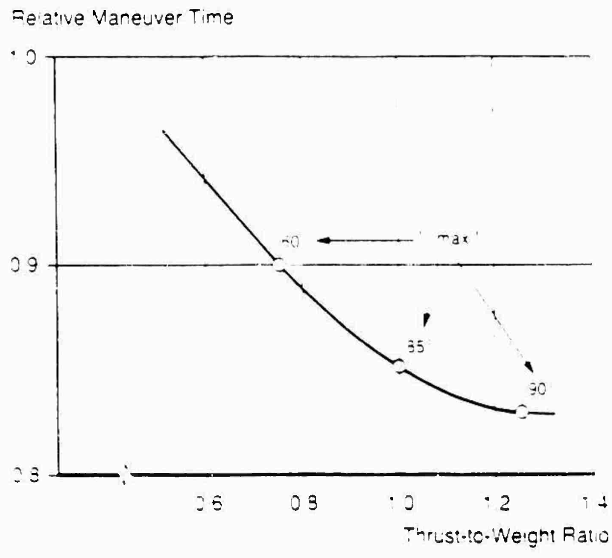

Fig. 16 Thrust dependance of the time advantage in a minimum time maneuver with limited PST capability. Results of trajectory optimizations.

PST-maneuvers are characterized by high pitch rates and rotation in yaw and roll at the same time. Coordinated flight with zero sideslip requires rotation around the velocity vector. Since the pilot does not recognize the velocity vector the control system has to be mechanized accordingly. A lateral stick input would have to produce more yaw and less roll at increasing angle of attack. This caused some confusion with pilots during simulated combat, because a pilot tends to use body axis as reference.

As a result of manned combat simulations a requirement for velocity vector roll acceleration was developed. It is plotted in fig. (17) as a function of angle of attack for a speed of M = 0.2 at 6000 m altitude. A translation in body axis motion shows that for a conventional aircraft the demand for roll could marginally be satisfied with aerodynamic controls, however, for pitch and yaw a control augmentation would be required. For example, a 10° conical deflection of the jet exhaust would suffice if the nozzle actuation meets certain dynamic requirements. Such a nozzle would have to be integrated in the aircraft control system. It was found that nozzle control is an enhancement of handling characteristics and thus combat effectiveness even in the conventional flight regime beyond 10° angle of attack.

5. Summary

The capability of exceeding maximum lift angle of attack - Post Stall (PST) maneuvering - can improve future close air combat effectiveness to a degree unachievable by conventional performance. The tactical advantage is attributed to a combination of fairly high turn rates and small turn radii at PST flight conditions in all aspect weapon environment. PST maneuvers are short period and highly instantaneous and constitute a trade of short term loss of energy against positional

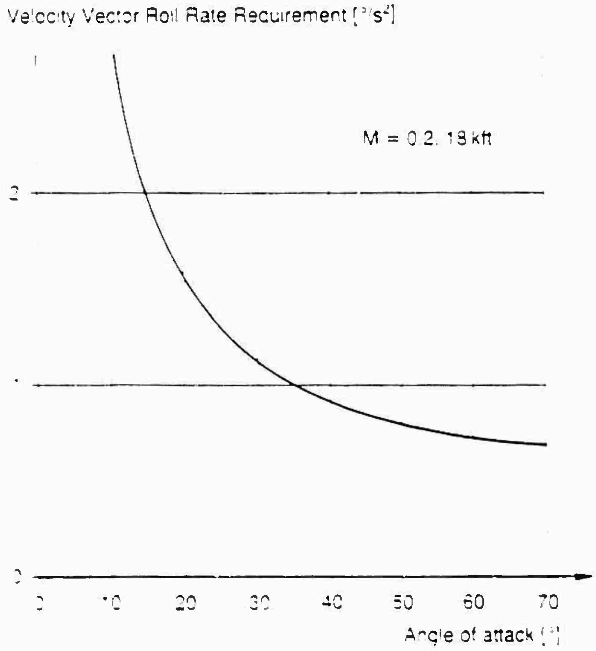

Fig. 17 Control power requirements at PST conditions. Statistical results of manned combat simulations.

advantage. PST maneuvers are an extension of conventional combat maneuvers. PST maneuverability requires an aircraft to be compatible with angles of attack up to 70^{o} at Mach numbers up to M = 0.6, a thrust-to-weight ratio of at least 1.0 and a level of control power at Mach-numbers as low as M = 0.1 which can not be achieved by aerodynamic means alone.

6. References

[1] Minimum time turns with thrust reversal
L. Johnson, J.E. Rader

[2] IDA Paper P-520
John Attinello, October 1969

[3] Design for air combat 1990
AGARD FMP Conference on fighter maneuverability, Florence, Oct. 5-8, 1981. Paper-Nr. AGARD CP-319 (Supp.), page 8-1 to 8-15.
Dr. W. B. Herbst

[4] Simulation analysis of unorthodox control control force fighter aircraft. McDonnel Douglas Technical Report
AFWAL-TR-80-3036, 1980
A.R. Mitchell, T.A. Halley, J.M. Roeder

[5] Bemannte Simulation 1979
MBB-Report
MBB/FE1/TKF/STY/0071/0/14.07.80
R. Haiplik, D. Eberle

[6] Einfluß von Waffenleistung und Supermanovrierfahigkeit im 1:1 Luftkampf
MBB-TN-BT13-88-22/79
W. Frenzl, Dr. R. Polis

[7] Untersuchung des Nutzens von Supermanovriebarkeit in Mehrfachluftgefechten
MBB-TN-BT13-88-23/80
Dr. R. Polis, W. Frenzl, G. Wimbersky

[8] Dynamics of Air Combat
Journal of Aircraft 1982
Dr. W.B. Herbst

[9] Optimale dreidimensionale Steuerung von Hochleistungsflugzeugen mit PST-Eigenschaften DFVLR, IBA 552-78/2, 1978 Kraft, Shan, Dr. Well, Berger

AD-P004 154

WING ROCK FLOW PHENOMENA

L. E. Ericsson
Lockheed Missiles & Space Company, Inc.
Sunnyvale, California

ABSTRACT

Flow mechanisms that can generate wing-rock type oscillations are described. It is shown that the slender wing rock phenomenon, the limit cycle oscillation in roll observed for very slender delta wings, is caused by asymmetric leading edge vortices and that vortex breakdown can never be the cause of it as it has a damping effect. For that reason slender wing rock is only realized for delta wings with more than 74 leading edge sweep for which asymmetric vortex shedding occurs before vortex breakdown. For straight or moderately swept wings the flow mechanism causing wing rock is two-dimensional in nature, closely related to the dynamic stall phenomenon. Pointed forebodies provide a third flow mechanism, asymmetric vortex shedding sensitive to body motion, which can generate a rocking motion of a slender vehicle unless it is completely axisymmetric.

INTRODUCTION

The steadily increasing demands on performance expose present day aerospace vehicles to unsteady flow fields which generate highly nonlinear aerodynamics that exhibit significant coupling between longitudinal and lateral degrees of freedom[1-3]. The complex vehicle dynamics are caused by separated flow effects of various types, which have largely eluded theoretical description. Consequently, the designer is to a large extent dependent upon existing experimental capabilities for dynamic testing[4], where dynamic support interference[5] adds complexity to the already complicated separated flow characteristics. Thus, it can be rather difficult to obtain a true description of non-linear pitch-yaw-roll coupling phenomena such as wing rock and nose slice. In the present paper existing experimental results are examined to obtain a description of the underlying fluid mechanics.

DISCUSSION

Recent systematic experiments performed by Nguyen et al[6] provide the information needed to fully describe the fluid mechanic phenomenon leading to slender wing rock. The phenomenon is similar in many aspects to the limit cycle oscillation in pitch observed on blunt cylinder-flare bodies[7,8]. Thus, the roll oscillations of an 80° delta wing are self-excited and build up to a limit cycle amplitude[6] (Fig. 1), an oscillatory behavior very similar to that observed for blunt-nosed cylinder-flare bodies[7,8]. The roll oscillation, $\phi = \Delta\phi \sin \omega t$ in Fig. 1, induces the following effective angles of attack and sideslip (on each half of the delta wing).

$$\alpha_{EFF} = \arctan (\tan\alpha \ \cos\phi) \qquad (1)$$

$$\beta_{EFF} = \arctan (\tan\alpha \ \sin\phi) \qquad (2)$$

It can be seen that the main effect is the induced sideslip. Thus, one can compare the $C_l(\beta)$-characteristics for a slender delta wing[9] (Fig. 2a) with the $C_m(\alpha)$-characteristics for a cylinder-flare body[8] (Fig. 2b). In both cases the characteristics change in a discontinuous fashion, and are likely to be associated with hysteresis, both phenomena typical for the effects of separated flow. The aerodynamic stiffness, C_{l_β} in Fig. 2a and C_{m_α} in Fig. 2b, increases dramatically when the discontinuity is encountered, (with or without associated hysteresis). Both discontinuous changes of the aerodynamic characteristics are associated with convective time lag effects[7,8,10]. This causes the statically stabilizing effects to become dynamically destabilizing, as is illustrated in Fig. 3 for the cylinder-flare body. The separated shear layer impacting on the flare at time t, when $\alpha(t) = 0$, was generated by the nose at a time increment Δt earlier, when the angle of attack was $\alpha(t-\Delta t) > 0$. Thus, a residual flare force exists at $\alpha(t) = 0$, which drives the motion, and consequently, is undamping.

Thus, the statically stabilizing separation-induced flare force is dynamically destabilizing. It is shown in Refs. 7 and 8 how the unsteady aerodynamics measured for large amplitude oscillations ($\Delta\theta$) around $\alpha = 0$ can be predicted from static aerodynamic characteristics when accounting for the convective time lag effect (Fig. 4).

A sudden change of the leading edge vortex on a delta wing is also associated with convected time lag effects, as is illustrated by the experimentally observed formation of the leading edge vortex[10] (Fig. 5). Accounting for this time lag provided good prediction of the vortex-induced unsteady aerodynamics of slender delta wings at high angles of attack[11,12], and should also permit the effect of the discontinuous aerodynamics associated with the vortex asymmetry to be predicted.

Two types of separation-induced discontinuities occur for the slender delta wing. One is caused by the breakdown of the leading edge vortices. It is the three-dimensional equivalent to airfoil stall. For very slender delta wings another discontinuous change of the aerodynamics can occur before vortex breakdown due to asymmetric leading edge vortices. The asymmetric vortex phenomenon has been studied extensively in the case of slender bodies of revolution[13,14] and has been observed also on slender delta wings[15] (Fig. 6). Vortex asymmetry occurs before vortex breakdown only for very slender delta wings, $\theta_A < 16°$ according to experiments[16] (Fig. 7). In order to use Fig. 7 to explore the effects of sideslip, β, and roll angle, ϕ, an effective apex half-angle is formulated as follows (for small angles, $\theta_A < 15°$, $\beta < 15°$).

$$\bar{\theta}_A = \theta_A + \Delta\theta_A \qquad (3a)$$

$$\Delta\theta_A = \tan\alpha \sin\phi \qquad (3b)$$

$$\Delta\theta_A = \beta/\cos\alpha \qquad (3c)$$

The $C_{l\beta}$ evaluated from static measurements for a 70° delta wing[17] shows the effects of both vortex burst and vortex asymmetry (Fig. 8). The first break in the $C_{l\beta}$-characteristics, at $\alpha \approx 20°$, is caused by vortex burst on the windward wing half (Fig. 9). Eqs. (3a) and (3b) give $\bar{\theta}_A = 24.3°$ for $\alpha = 20°$, $\beta = 4°$ ($C_{l\beta}$ evaluated for $\beta = \pm 4°$). The loss of lift due to vortex burst on the right wing-half causes the observed decrease of the derivative magnitude $|C_{l\beta}|$ (Fig. 8). At $\alpha \approx 35°$ one obtains $\bar{\theta}_A = 15.1°$ for $\beta = -4°$, giving vortex lift-off on the leeward wing half (Fig. 9). This causes a loss of lift which results in an increase of the magnitude of the rolling moment derivative, $|C_{l\beta}|$, in agreement with the experimental results (Fig. 8). Even more erratic $C_{l\beta}$-characteristics have been measured on an 86.5° swept delta wing[9] (Fig. 10a). The expected behavior, following that for the 82.5° swept delta wing, ($\theta_A = 7.5°$) is indicated by a solid line. The zig-zag behavior of the dotted line connecting the experimental results can be understood if one studies the $C_l(\beta)$-characteristics (Fig. 10b). It appears that between $\beta = 0$ and $\beta = 5°$ the vortex asymmetry switched several times, with vortex lift-off alternating between the two wing halves. A static hysteresis of $\beta = \pm 5°$ is indicated.

Experimental results[6] demonstrate that wing rock starts before vortex breakdown (Fig. 11), and that wing rock is associated with a loss of the time-average lift[6,15] (Figs. 11 and 12). It is, of course, to be expected that the "lift-off" of one of the leading edge vortices[15] (Fig. 6) will cause a loss of lift. Thus, wing rock is caused by the vortex-asymmetry and not be the vortex breakdown. Figures 13 and 14 illustrate the fluid mechanical reasons for this. At an $\alpha - \theta_A$ combination where vortex asymmetry occurs, the wing half with the lifted-off vortex loses lift and "dips down", rotating around the roll axis (Fig. 13). As a result of the increasing roll angle ϕ the effective apex angle $\bar{\theta}_A$ is increased, Eqs. (3a) and (3b), and the vortex attaches again. This produces a restoring rolling moment, the positive aerodynamic spring needed for the rigid body oscillation in roll (Fig. 1). Due to the convective time lag effect discussed earlier the wing is dynamically unstable in roll until the amplitude has reached the limit cycle magnitude, at which the damping on both sides of the discontinuity suffices to balance the undamping induced by it, as is illustrated by the cylinder-flare results in Fig. 4. According to Fig. 13 wing rock should start occuring for an 80° delta wing ($\theta_A = 10°$) at $\alpha > 27°$, which is in excellent agreement with experimental results[6].

Thus, the discontinuity introduced by the vortex asymmetry has all the characteristics needed for the limit cycle oscillation in roll. Figure 14 demonstrates that vortex breakdown is lacking these characteristics. If for some reason, due to external disturbances for example, the vortex burst becomes asymmetric, as is sketched in Fig. 14, the resulting net loss of lift on one wing half will cause it to "dip down". This increases ϕ and thereby $\bar{\theta}_A$, Eqs. (3a) and (3b), causing this wing half to penetrate further into the vortex burst region, and no switch to a restoring moment occurs. The opposite wing half gets out of the vortex burst region, generating increased lift that adds to the statically destabilizing rolling moment. Thus, no restoring moment, no positive aerodynamic spring, is generated and no rigid body ϕ-oscillation is possible. If the positive spring is provided by the structure, as in the case of elastic vehicle dynamics, the dynamic effect of the vortex breakdown would be dynamically stabilizing, damping, as the vortex burst is also associated with time lag effects. Thus, vortex breakdown has aerodynamic characteristics completely opposite to those needed to cause slender wing rock.

Although vortex burst cannot cause wing rock, it is involved in the cases of wing rock observed for very high angles of attack[6,18], $\alpha > 35°$ (Fig. 9). Figure 15 illustrates the fluid mechanics for $\alpha = 42°$ and $\theta_A = 10°$, for which a limit cycle amplitude of $\Delta\phi = 32°$ has been measured[6]. At $\phi = 0$, $\bar{\theta}_A = \theta_A = 10°$, asymmetric vortex burst exists. The wing half with the largest lift loss dips down, increasing ϕ and $\bar{\theta}_A$. When $\bar{\theta}_A < 0$ for $\phi < -11°$ and the vortex-induced lift on the opposite leeside wing half is reduced dramatically or lost completely, a restoring rolling moment is generated. Because of the integrated damping effects discussed earlier in connection with Fig. 13 the amplitude $\Delta\phi$ has to exceed $\Delta\phi = 11°$ substantially before net zero damping is reached and the limit cycle oscillation called wing rock is established.

Whereas Nguyen et al[6] measured no wing rock for their 80° delta wing below $\alpha = 27°$ Levin and Katz[18] measured wing rock already at $\alpha = 20°$ for the same leading edge sweep (Fig. 16). This early wing rock occurance is probably, as the authors suggest , caused by the centerbody used on their model (see inset in Fig. 16). The smaller limit cycle amplitude, $\Delta\phi \approx 12°$ (Fig. 18) compared to $\Delta\phi = 34°$, which was the limit cycle amplitude measured by the Nguyen et al at $\alpha = 27°$, is probably due to the lesser vortex-induced loads existing at the lower angle of attack[18].

Nguyen et al[6] showed that the oscillations in roll damped down to zero amplitude if the 80° delta wing ($\theta_A = 10°$) was yawed to $\beta = 10°$ at $\alpha = 27°$ (Fig. 17). This is, of course, to be expected as the windward wing half has $\bar{\theta}_A > 15°$, Eqs. (2), (3a) and (3c), leaving it outside of the boundary for asymmetric vortex shedding (Fig. 13), whereas the leeward wing half with $\bar{\theta}_A < 5°$ remains inside the region for vortex-asymmetry. Thus, neither wing half crosses the boundary, and the wing-rock-inducing discontinuity is never encountered. Correspondingly, oscillations in yaw around $\beta = 0$ are damped for $|\beta| = 10°$ according to the experimental results[6] (Fig. 18).

It was noted by the authors in Ref. 18 that the normal force measured during wing rock was below that measured in static tests. Thus, at $\alpha = 20°$ the mean or time average normal force is $C_{NOR} = 0.64$ for $\Delta\phi_{LIM} = 14°$ (Fig. 16) whereas the static data showed C_{NOR} to vary from $C_{NOR} = 0.80$ to $C_{NOR} = 0.65$ when ϕ increased from 0 to 15°. As the static data show no rolling moment at $\beta = \phi = 0$ for $\alpha < 32°$, it is obvious that the vortices stayed symmetric in the static case, whereas in the dynamic test vortex-asymmetry must have been present to cause the wing rock. The likely reason for this anomaly is the large centerbody. Whereas a thin splitter plate of similar height has been found to trigger early vortex asymmetry also in static tests by forcing asymmetric stagnation flow conditions on the topside[20], the lateral extent of the center body in Ref. 18 apparently allowed symmetric vortex formation in the static test. As a matter of fact the wing rock motion was not self-induced at $\alpha = 20°$ but had to be started at a higher angle of attack, in which case it would persist when the angle of attack was reduced to $\alpha = 20°$. Even at $\alpha = 35°$ the vortices remained symmetric for 15 seconds (Fig. 12). This cannot, however, explain the big difference observed at $\alpha = 30°$, where in the dynamic test with $\Delta\phi_{LIM} = 30°$ C_{NOR} varied between $C_{NOR} = 0.86$ and $C_{NOR} = 0.5$ whereas the static test gave $C_{NOR} = 1.28$ and $C_{NOR} = 0.8$ for $\phi = 0$ and $\phi = 30°$ respectively. In this case it is the early vortex burst observed in the dynamic test[18] that is the likely reason for the additional lift loss.

In regard to the usage of the results in Fig. 7, which are obtained for symmetric flow conditions, $\beta = \phi = 0$, for the asymmetric flow conditions discussed in Figs. 9, 13, 14, and 15, the following needs to be said. Whereas vortex burst is relatively unaffected by the presence or absence of the vortex on the opposite wing-half, the asymmetric vortex shedding is very dependent upon the "crowding" of the companion vortex. It is the strength of the vortex, represented by α in Fig. 7, and the closeness of the opposite vortex, represented by θ_A in Fig. 7, which together determine whether or not "lift-off" of the vortex will occur. In a first approximation the effect of side slip on the "closeness parameter" can be neglected. That is

$$(\theta_A)_{EFF} = \left[(\theta_A)_L + (\theta_A)_R\right]/2 \qquad (4)$$

It is shown in Ref. 19 that the vortex strength and associated aerodynamic loads are determined by the parameter α/θ_A rather than by α alone. Consequently, the indicated changes of θ_A in Fig. 13 should be substituted by changes of $(\alpha/\theta_A)_{EFF}$. That is, the changes would occur in the vertical rather than in the horizontal plane. The conclusions would, however, be the same in regard to the effects of roll angle ϕ.

In Ref. 21 a simple analytic method is presented, which can predict the limit cycle amplitude for the wing rock oscillations measured by Nguyen et al.[16].

WING ROCK OF NON-SLENDER WINGS

A completely different flow mechanism is the cause of wing rock of straight or moderately swept wings. It is closely related to dynamic stall. The experimental results[22] in Fig. 14 illustrate that plunging oscillations of an airfoil can be undamped in the stall region. It is shown in Ref. 23 that this will be the case if the stall is associated with a significant loss of lift. It is the "leading-edge jet", the moving wall/wall jet analogy discussed in Ref. 24 (Fig. 15), that produces the negative aerodynamic damping in plunge[22] shown in Fig. 14.

If an aircraft is perturbed when flying close to stall, the down-rolling wing half will experience the upstream moving wall effect illustrated for the down-stroke in Fig. 15. As it promotes separation, the loss of lift is increased beyond the static lift loss, more the higher the plunging rate $|\dot{Z}|$ is. This generates a rolling moment that drives the motion, i.e., it is undamping. The delayed stall due to downstream moving wall effects on the opposite wing (upstroke in Fig. 15) will add to the undamping rolling moment.

Thus, the induced effects of the local plunging velocity $\dot{Z}$ will drive the wing in roll. What stops the wing rolling motion to produce wing rock? Eq. (1) and Fig. 14 give the answer. When the roll angle ϕ has been increased enough to cause α_{EFF} to decrease below α_{STALL} on the down-going wing half, the flow will reattach to generate the lift needed to produce a restoring rolling moment; the aerodynamic spring needed for wing rock, as was described earlier. The flow reattachment is associated with time lag effects[25], creating negative aerodynamic damping to be added to the "leading edge jet" effect discussed earlier. Thus, the condition for wing rock exists also for a conventional wing.

Associated with wing-rock is the oscillation in yaw called nose slice. The down-rolling wing half will move back due to the stall-induced drag increase. The increased leading edge sweep angle will promote flow reattachment, thus reinforcing the aerodynamic spring of the wing rock. For a straight or moderately swept wing, the side slip due to nose slice will dominate over the roll-induced side slip, β_{EFF} in Eq. (2), as α is small. The opposite is true for a slender delta wing where the drag increase due to nose slice is small and β_{EFF} is the dominant side slip component (α is large in Eq. (2)). Thus, one expects the coupling between wing rock and nose slice to be weak for highly swept wings and strong for straight or moderately swept wings.

BODY ROCK

That a pointed forebody can provide a third mechanism for wing rock, or body-rock, was demonstrated recently[26]. Wings and tail surfaces could be removed from the model of an advanced aircraft without stopping the rocking motion. Obviously, it must be the vortices shed from the pointed forebody that supplied the driving mechanism for this body rock motion. It has been established that the formation of asymmetric body vortices can be dominated by the body motion[27], and that the vortex that is not lifted off moves inboard to remain very close to the surface near the centerline of the body[28, 29] (Fig. 16). Placing the cockpit in the inset sketch of Fig. 16 and considering the data by Fidler[30] (Fig. 17), one starts to see what this third flow mechanism is.

It is shown in Ref. 31 that at a critical Reynolds number negative Magnus lift of large magnitude will be generated at very modest rotation rate on a circular cylinder. It is described in Ref. 27 how this flow phenomenon, which is caused by moving wall effects on boundary layer transition, can explain the results in Fig. 17. That is, the direction of even a very slow rotation determines the direction of the vortex asymmetry. Based upon these results, one obtains the picture sketched in Fig. 18 for the vortex-induced effects on the cockpit.

At $t = t_1$ the body receives a rotational perturbation as indicated. The upstream moving wall effect causes transition to move ahead of flow separation, thereby changing the separation from subcritical to the supercritical type indicated in Fig. 18. The downsteam asymmetric vortex close to the body generates suction on the cockpit, thereby driving the rolling motion. At $t = t_2$, the cockpit has rotated to a position where it interferes with the flow separation, triggering a change from supercritical to subcritical type separation. This generates a restoring rolling moment, which will reverse the roll direction at some time between $t = t_2$ and $t = t_3$. At $t \approx t_3$ the roll rate is large enough to cause transition, changing the flow separation from subcritical to supercritical and generating a driving rolling moment at $\Theta = 0$, as is indicated for $t = t_3$. The situation is somewhat similar to that for slender wing rock discussed earlier. That is, a switch of vortex asymmetry generates the aerodynamic spring, and the associated time lag generates negative aerodynamic damping. The difference is that in the present case of body rock the undamping is amplified by moving wall effects.

The experimentally observed body rock[26] was obtained on a model that only had the roll degree-of-freedom (DOF). For an aircraft in free flight the asymmetry will generate the largest effect in the yaw DOF. That is, the motion will be nose-slice-dominated with relatively weak feedback from the roll DOF illustrated in Fig. 18. However, for vortex interaction with an aft fin[illegible] this third flow mechanism may become much more significant in regard to its impact on pitch-yaw-roll coupling.

It should be noted that the third flow mechanism exists only in a limited range of α and Re. Of course, the critical Reynolds number range may be relatively wide, as the transition induced separation asymmetry moves towards the nose tip on a pointed ogive or cone as the Reynolds number is increased[illegible] (Fig. 19).

CONCLUSIONS

An analysis of wing rock phenomena has shown the following:

- o Slender wing rock is caused by asymmetric leading edge vortices.
- o Vortex breakdown has a damping effect on the roll oscillations and can never cause wing rock.
- o Thus, slender wing rock will only occur for delta wings with more than 74° leading edge sweep.
- o Wing rock of a conventional wing can occur at stall if the stall causes an abrupt lift loss.
- o Body rock can be generated on body alone by asymmetric vortex shedding from a slender nose if the body is not completely axisymmetric.

REFERENCES

1. Many authors, "Dynamic Stability Parameters", AGARD CP-235, Nov. 1978.

2. Ericsson, L. E., "Technical Evaluation Report on the Fluid Dynamics Panel Symposium on Dynamic Stability Parameters", AGARD-AR-137, April 1978.

3. Ericsson, L. E., "A Summary of AGARD FDP Meeting on Dynamic Stability Parameters", Paper 2, AGARD CP-260, Sept. 1978.

4. Orlik-Ruckeman, K.J. "Aerodynamic Aspects of Aircraft Dynamics at High Angles of Attack", AIAA Paper 82-1363, August 1982.

5. Ericsson, L. E. and Reding, J. P., "Review of Support Interference in Dynamic Tests", Accepted for publication in the AIAA Journal. (Also AIAA Paper 82-0594).

6. Nguyen, L. T., Yip, L. P., and Chambers, J. R., "Self-Induced Wing Rock of Slender Delta Wings", AIAA Paper No. 81-1883, August, 1981.

7. Ericsson, L. E., "Unsteady Aerodynamics of Separating and Reattaching Flow on Unsteady Boundary Layers", Vol. 1, IUTAM Symposium, Laval University, Quebec, May 24-28, 1971, pp. 575-586.

8. Ericsson, L. E., "Separated Flow Effects on the Static and Dynamic Stability of Blunt Nosed Cylinder Flare Bodies", NASA CR-76919, December 1965.

9. Letko, W., "Experimental Determination at Subsonic Speeds of the Oscillatory and Static Lateral Stability Derivatives of a Series of Delta Wings with Leading-Edge Sweep from 30° to 86.5°", NACA RM L57A30, April 1957.

10. Lambourne, N. C., Bryer, D. W., and Maybrey, J. F. M., "The Behavior of

the Leading-Edge Vortices over a Delta Wing Following a Sudden Change of Incidence", R & M No. 3645, Aer. Res. Council, Great Britain, March 1969.

11. Ericsson, L. E. and Reding, J. P., "Unsteady Aerodynamics of Slender Delta Wings at Large Angles of Attack", J. Aircraft, Vol. 12, No. 9, Sept. 1975. pp. 721-729.

12. Ericsson, L. E. and Reding, J. P., "Unsteady Aerodynamic Analysis of Space Shuttle Vehicles, Part II: Steady and Unsteady Aerodynamics of Sharp-Edged Delta Wings", NASA CR-124423, August 1973.

13. Ericsson, L. E. and Reding, J. P., "Review of Vortex-Induced Asymmetric Loads-Part I", Z. Flugwiss, Weltraumforsch., 5 (1981), Heft 3, pp. 162-174.

14. Ericsson, L. E. and Reding, J. P., "Review of Vortice-Induced Asymmetric Loads-Part II", Z. Flugwiss, Weltraumforsch., 5 (1981), Heft 6, pp. 349-366.

15. Bird, J. D., "Tuft-Grid Surveys at Low Speeds for Delta Wings", NASA TND-5045, February 1969.

16. Polhamus, E. C., "Predictions of Vortex-Lift Characteristics by a Leading-Edge Suction Analogy", J. Aircraft, Vol. 8, No. 4, April 1971, pp. 193-199.

17. Johnson, J. L. Jr., Grafton, S. B., and Yip, L. P., "Exploratory Investigation of Vortex Bursting on the High-Angle-of-Attack Lateral-Directional Stability Characteristics of Highly-Swept Wings", AIAA Paper 80-0463, March 1980.

18. Levin, D. and Katz, J., "Dynamic Load Measurements with Delta Wings Undergoing Self-Induced Roll-Oscillations", AIAA Paper No. 82-1320, August 1982.

19. Maltby, R. L., et al, "Low Speed Flow Studies of the Vortex Patterns Above Inclined Slender Bodies Using a New Smoke Technique", RAE-TN-AERC-2482, Nov. 1957.

20. Reding, J. P. and Ericsson, L. E., "Review of Delta Wing Space Shuttle Vehicle Dynamics", Vol. III, Proceedings Space Shuttle Aerothermodynamics Conference, NASA Ames R.C., Moffett Field, Calif., Dec. 1971, pp. 861-931 (NASA TMX-2506).

21. Ericsson, L.E., "The Fluid Mechanics of Slender Wing Rock", AIAA Paper 83-1810, July 1983.

22. Liiva, J., Davenport, F.J., Gray, L., and Walton, I.C., "Two-Dimensional Tests of Airfoils Oscillating Near Stall", USA AVLABS TR 68-13, April 1968.

23. Ericsson, L.E., and Reding, J.P., "Unsteady Flow Modules for Dynamic Stall Analysis, a Critical Review", AIAA Paper 82-1324, August 1982.

24. Ericsson, L.E. and Reding, J.P., "Stall Flutter Analysis", J. Aircraft, Vol. 10, No. 1, January 1973, pp. 5-13.

25. Ericsson, L.E., and Reding, J.P., "Dynamic Stall Analysis in Light of Recent Numerical and Experimental Results", J. Aircraft, Vol. 13, No. 4, April 1976, pp. 248-255.

26. Chambers, J.R., Film clip shown at the Specialists Meeting on Aerodynamics and Dynamics of Aircraft and Missiles at High Angles of Attack, Flight Dynamics Laboratory, Wright Patterson AFB, Ohio, July 15-16, 1982.

27. Ericsson, L.E. and Reding, J.P., "Steady and Unsteady Vortex - Induced Loads on Slender Vehicles", J. Spacecraft and Rockets, Vol. 18 No. 2, March-April 1981, pp. 97-109.

28. Ericsson, L.E., and Reding, J.P., "Dynamics of Forebody Flow Separation and Associated Vortices", AIAA Paper No. 83-2118, August 1983.

29. Keener, E.R., Chapman, G.T., Cohen, L., and Teleghani, J., "Side Forces on Forebodies at High Angles of Attack at Mach Numbers from 0.1 to 0.7. Two Tangent Ogives, Paraboloid and Cone", NASA TMX-3438, February 1977.

30. Fidler, J. E., "Active Control of Asymmetric Vortex Effects", J. Aircraft, Vol. 18, No. 4, April 1981, pp. 267-272.

31. Ericsson, L.E., "Karman Vortex Shedding and the Effect of Body Motion", AIAA Journal, Vol. 18, No. 8, August 1980, pp. 335-344.

32. Orlik - Ruckemann, K. J., Film clip shown at the Specialists Meeting on Aerodynamics and Dynamics of Aircraft and Missiles at High Angles of Attack, Flight Dynamics Laboratory, Wright Patterson AFB, Ohio July 15, 16, 1982.

33. Keener, E.R., "Oil-Flow Separation Patterns on an Ogive Forebody", AIAA Journal, Vol. 21, No. 4, April [illegible], pp. 550-556.

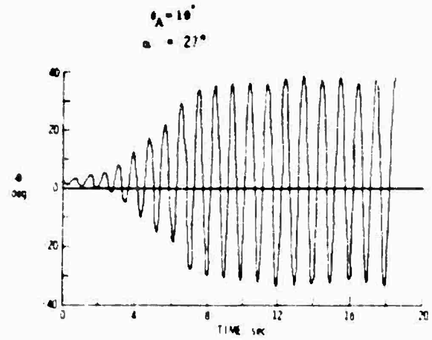

Fig. 1 Time History of Wing Rock at α = 27° for an 80° Delta Wing (Ref. 6)

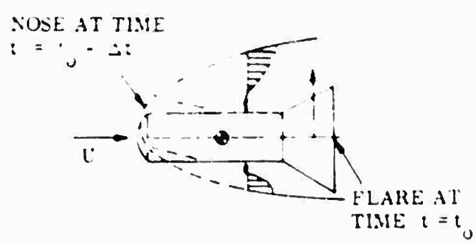

Fig. 3 Effect of Time Lag

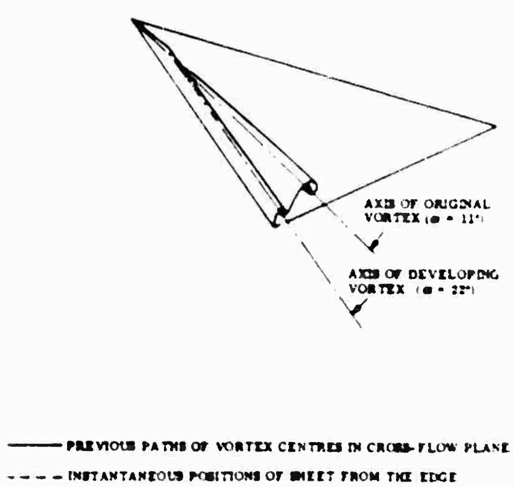

Fig. 5 Leading Edge Vortex Development on a Delta Wing (Ref. 1[illegible])

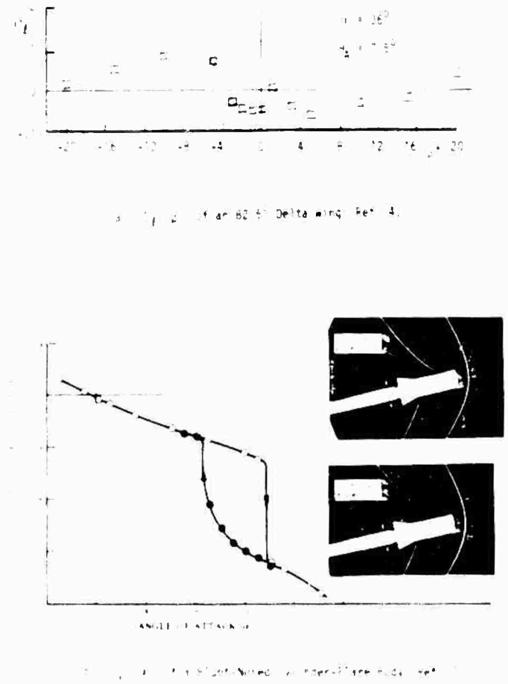

Fig. 2 Nonlinear Aerodynamic Characteristics

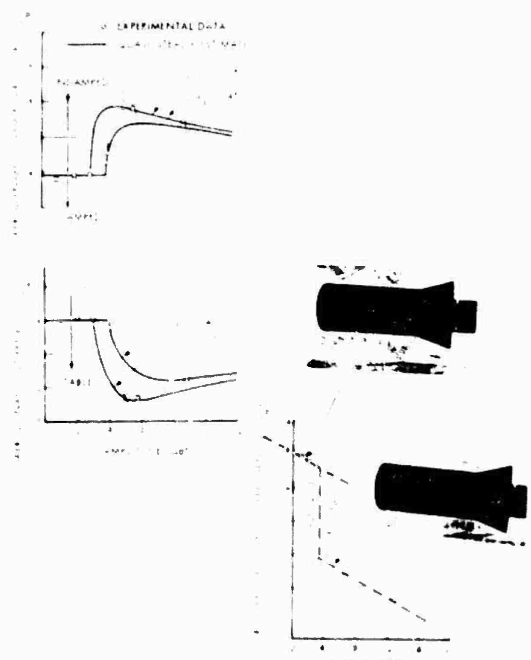

Fig. 4 Nonlinear Aerodynamics of a Blunt Cylinder - Flare - Body (Ref. [illegible])

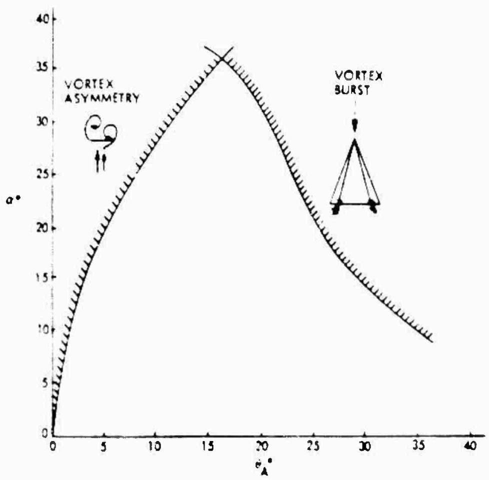

Fig. 6 $\alpha - \theta_A$ Boundaries for Vortex Asymmetry and Vortex Burst (Ref. 16)

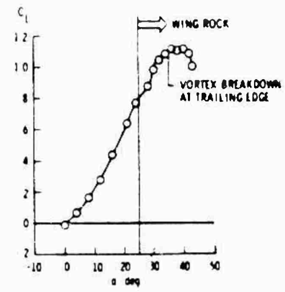

Fig. 7 Effect of Wing Rock on Lift (Ref. 6)

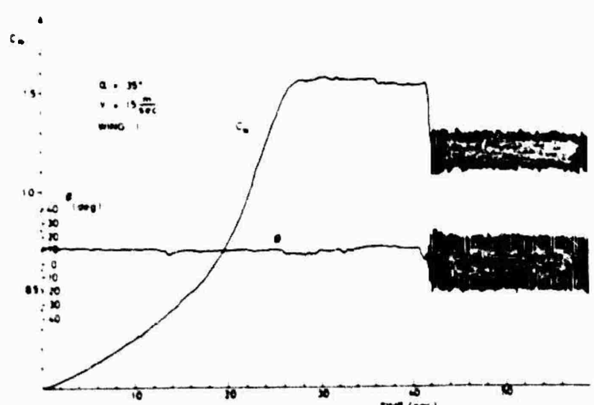

Fig. 8 Development of Wing Rock for an 80° Delta Wing (Ref. 18)

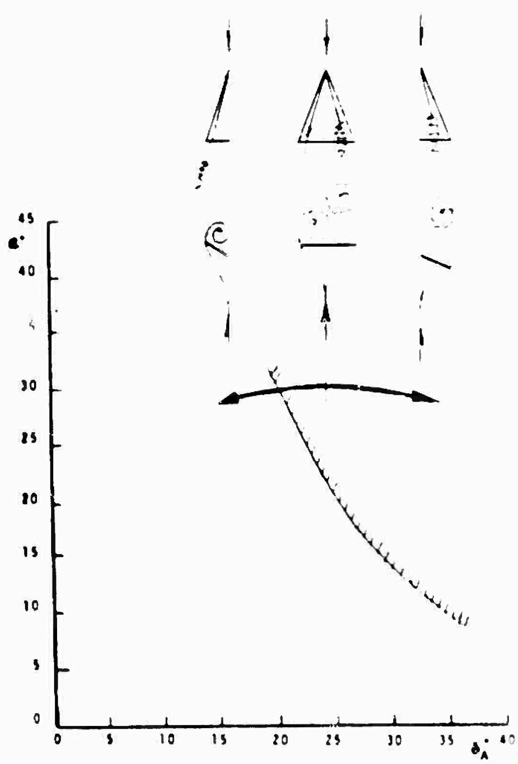

Fig. 9 Wing Rock Caused by Asymmetric Vortices.

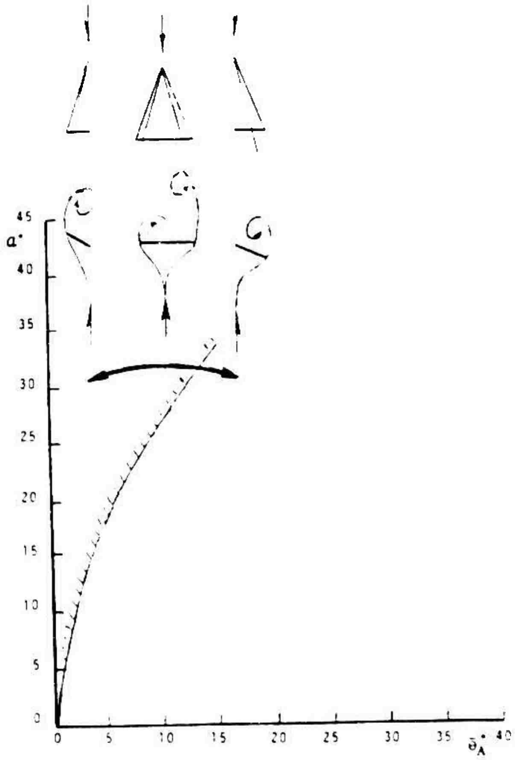

Fig. 10 Effect of Vortex Burst on Lateral Stability.

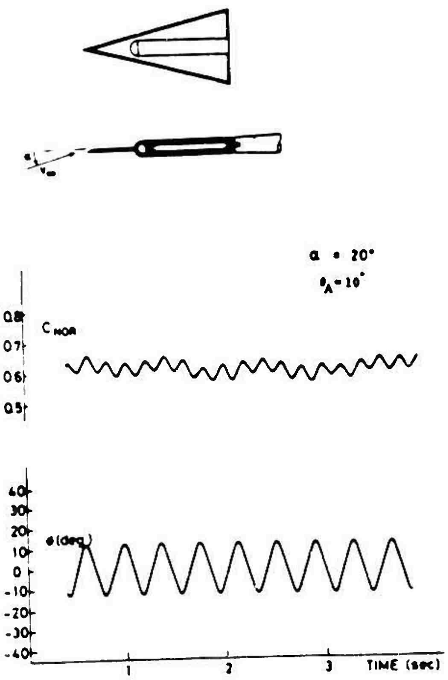

Fig. 11 Time History of Wing Rock, $\Lambda = 80^0$ and $\alpha = 20^0$ (Ref. 18)

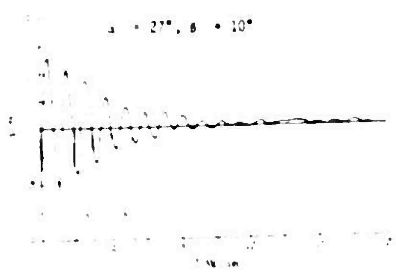

Fig. 12 Roll Response of an 80^0 Delta Wing at $\alpha = 27°$, $\beta = 10°$ (Ref. 6)

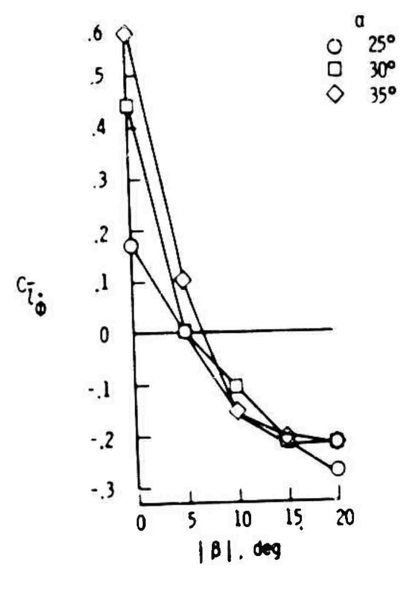

Fig. 13 Effect of Sideslip on Roll Damping of an 80^0 Delta Wing (Ref. 6)

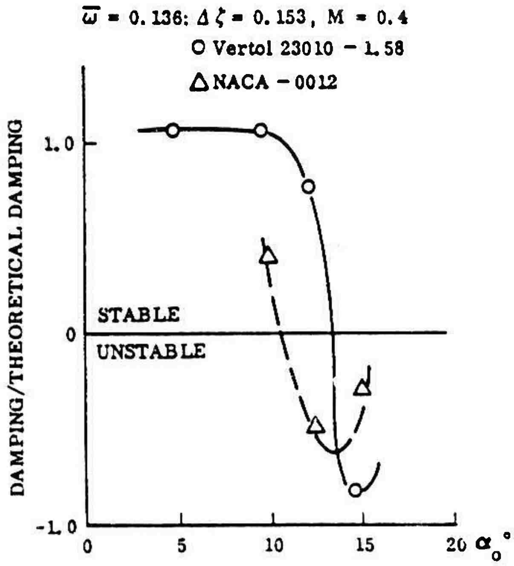

Fig. 14 Airfoil Damping in Plunging Oscillations (Ref. 22)

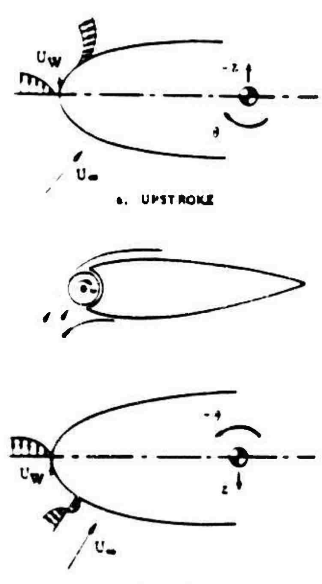

Fig. 15 "Leading Edge Jet" Effect

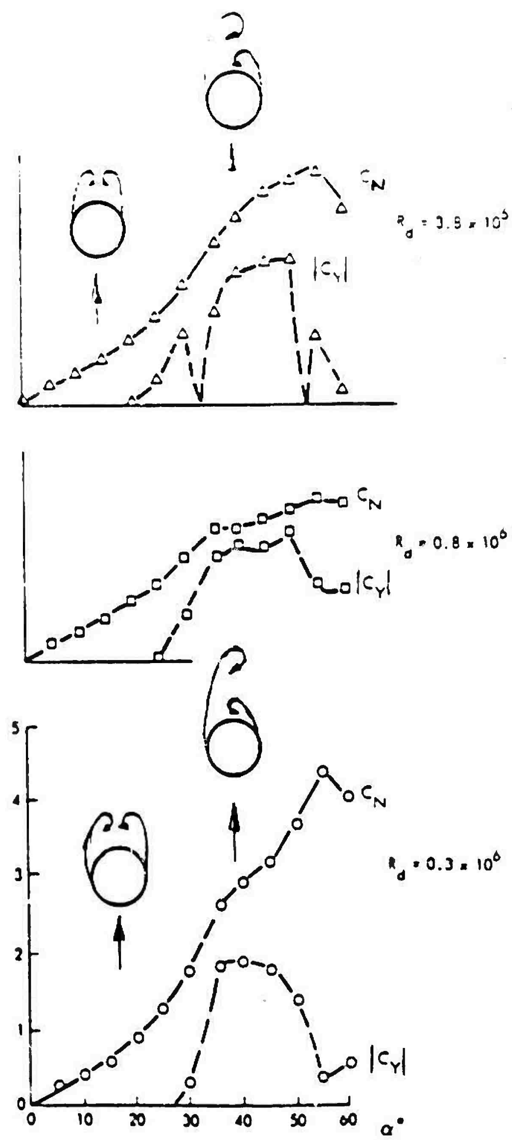

Fig. 16 Effect of Asymmetric Vortex Shedding on Side Force and Normal Force

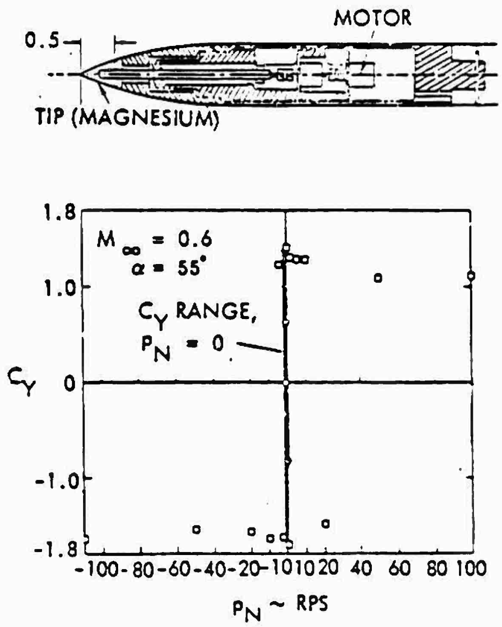

Fig. 17 Effect of Spinning Nose Tip on Vortex-Induced Side Force (Ref. 30)

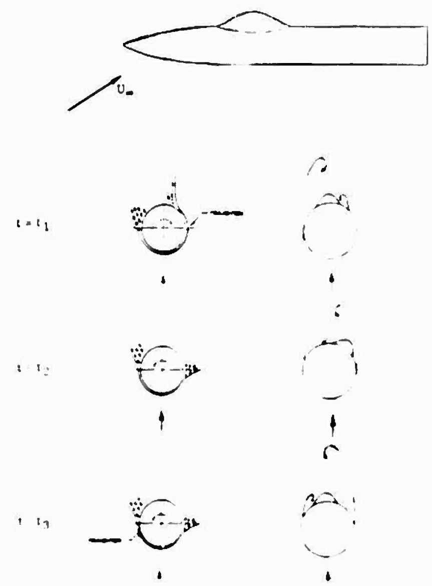

Fig. 18 Vortex-Induced Load on Aircraft Cockpit

Fig. 19 [illegible] Flow Pictures of Pointed Ogive at [illegible] 20° (Ref. 33)

POTENTIAL APPLICATIONS OF FORCED UNSTEADY FLOWS*

Hermann Viets** and G. Michael Palmer***
West Virginia University
Morgantown, West Virginia 26506

Richard J. Bethke***
Wright State University
Dayton, Ohio 45435

AD-P004 155

Abstract

Forced unsteady flows are examined from the point of view of potential application of new devices which are made possible by the improved understanding of these flows. In particular, flows are examined which require no external driver but obtain their energy from the free-stream velocity. Other flows require no moving parts at all to generate the unsteadiness.

Introduction

Unsteady separated flows may appear as a consequence of the motion of the surface of the body or as a result of the unsteadiness in the flow over that surface. In many cases, when confronted by such flows, the objective is to eliminate or at least control the separation.

The current research program has taken a somewhat different perspective. The objective of the program is to examine the dynamics of flows which are forced to become unsteady and to specifically consider the possibilities for the application of such flows as well as determining their basic structure. In addition to the question of identifying devices which can drive a flow unsteady in a suitable way, it is necessary to determine the composition and dynamics of the large scale structures created in the periodic flow. The latter point has led to techniques which have some utility in determining the vortex structure of quasi-steady three dimensional flows.

When considering possible techniques to produce an unsteady periodic flow from a nominally steady flow, two basic requirements are apparent:

a. The device must be mechanically simple and easy to build;
b. If possible, the device should not require external power to drive it.

Past Efforts[1-7]

Under the present research program, two devices have been employed to generate the time dependence. The first is a series of purely fluidically controlled jet nozzles which satisfies both of the requirements cited above. Such a nozzle produces a jet which oscillates from side to side and results in large scale structures (shown in the flow visualization results of Figure 1) which have an important effect on the flowfield. Although these nozzles can be employed to control boundary layers, most of the effort has been applied to free jets. The jet is controlled by the fluidic feedback system wrapped around the body of the jet nozzle in Figure 2. An alternate version employing a different fluidic feedback has been found to be capable of producing an unsteady jet even if the phase of the jet flow is different from that of the surroundings.

Figure 1. Smoke flow visualization of a fluidically oscillating jet.

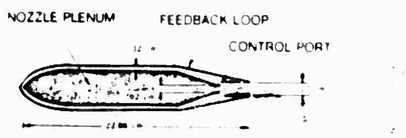

Figure 2. Schematic of the fluidically oscillating jet nozzle.

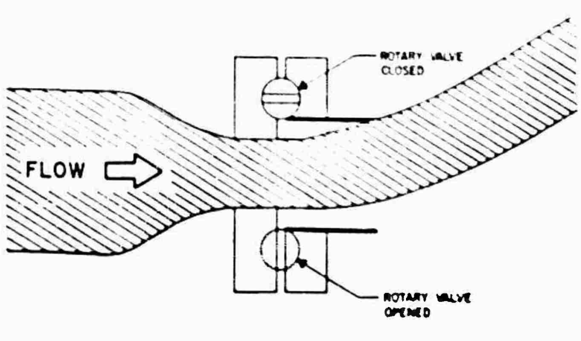

Figure 3. Schematic of the rotary valve system.

* Supported by AFOSR Grant 82-0291, monitored by Capt. (Dr.) Michael S. Francis.
** Professor and Associate Dean; Presently Professor and Dean, College of Engineering, University of Rhode Island, Kingston, Rhode Island, 02881.
***Associate Professor

Another embodiment of a fluidically controlled jet nozzle is shown in Figure 3. In this case the dynamic orientation of the jet is determined by a pair of rotating valves located on either side of the nozzle exit. Since the jet is always inclined toward the closed valve, this nozzle has the advantage that the phase position can be controlled in addition to the frequency. A disadvantage is that the control valves must be externally driven.

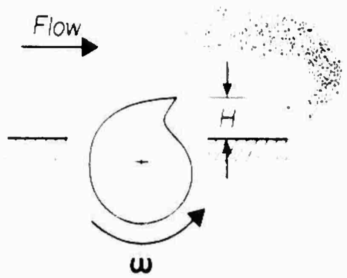

Figure 4. Schematic of the rotor vortex generator.

The second device is a cam shaped rotor shown in Figure 4. As the rotor turns, and as long as the freestream velocity is greater than the tip speed of the rotor, the appearance of the rotor tip will result in the production of a vortex behind the rotor. The flowfield thereby produced has been proved and found to have application to controlling flows on aircraft wings (Figure 5a), helping reattachment on rearward facing ramps (Figure 5b), improving mixing in a dump combustor (Figure 5c), and controlling the flow in a diffuser (Figure 5d).

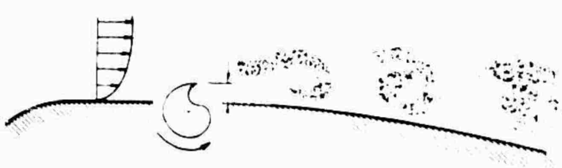

Figure 5a. Schematic of vortex generation on the upper surface of an airfoil.

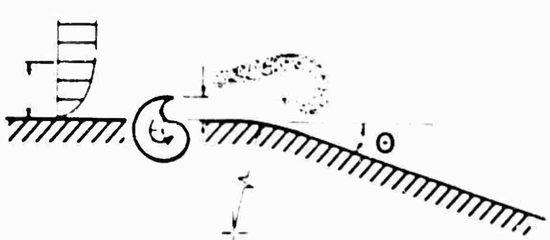

Figure 5b. Schematic of the vortex generator applied to a rearward facing ramp.

[illegible]

leads to an improved mixing rate between the fuel and oxidizer. The presence of the unsteady flow in the diffuser (Figure 5d) has resulted in cases where the diffusion is more effective, especially at larger angles.

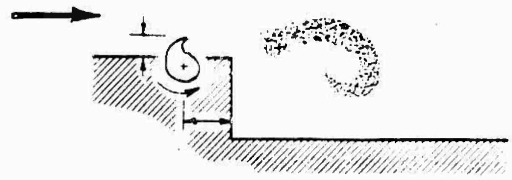

Figure 5c. Schematic of the vortex generator applied to a dump combustor geometry.

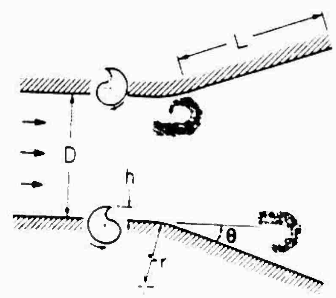

Figure 5d. Schematic of the vortex generator applied to a diffuser geometry.

Current Efforts[8-10]

The design embodied by the unsteady diffuser experiment (Figure 5d) can be adapted to the rotor jet experiment shown in Figure 6. The rotors are located at both sides of the nozzle exit and can be operated in any phase relationship to each other to produce different jet flows. Operated in an in-phase condition, the rotor tips appear simultaneously and the resulting flow is a pulsing jet. Operating the rotors in an out-of-phase condition results in a jet which flaps from side to side in a manner similar to that of the fluidically oscillating jet (Figures 1 and 2). In this case the jet vortex structure downstream is even stronger since it is created by the rotors. The results of Figure 6 show such a jet flowfield. The vortex structure of the field can be shown by transforming to a moving coordinate system, by methods to be discussed in the following sections. The results of such a transformation are shown in Figure [illegible], where the centers of the resulting vortex structures can be clearly identified.

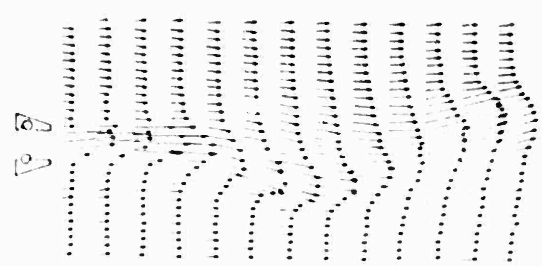

[illegible]

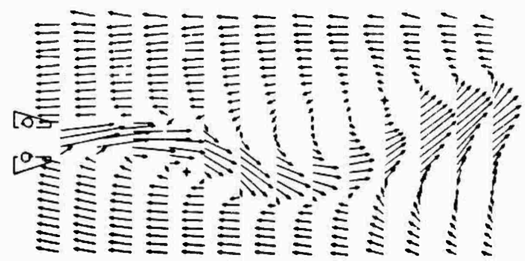

Figure 7. Rotor jet flowfield seen in a moving coordinate system.

Another problem of current interest is the application of the rotor vortex generator to reduce the drag of a bluff body vehicle. An example is a van in which the objective is to reduce the drag but to affect the volume of the van in a minimal way. Thus, simply streamlining the van has severe limitations. The method proposed is to employ the rotor to enable the flow to turn through a larger angle and thus only require a small loss of van volume due to eliminating the rear corner as shown in Figure 8. In this figure, the transformation to a coordinate frame structure dominates the flow and should lead to a drag reduction since it substantially reduces the size of the wake behind the vehicle.

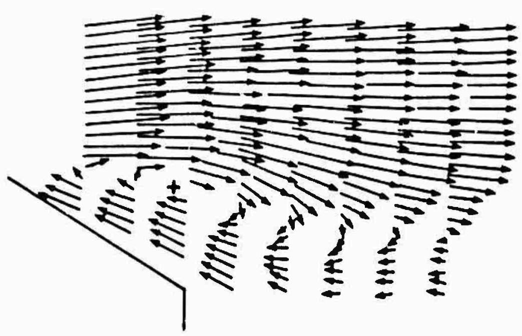

Figure 8. Flowfield produced by the rotor when applied to the wake of a van.

A third area of current interest is the dynamics of an initially rectilinear vortex structure near a wall generated by the rotor device shown in Figure 4. A schematic of the dynamics which such structure undergoes is shown in Figure 9. From the point of view of application, such a flow condition can arise behind very rapidly changed aerodynamic control surfaces. The data acquisition system described in the following section has been developed specifically for this investigation and some typical results will be shown in that section. The results with and without a shear flow profile near the wall are discussed in References 12 and 10 respectively.

Instrumentation and Data Acquisition for Forced Unsteady Flows

The instrumentation system has been designed to measure the instantaneous velocities of the convected coherent flow structures induced by the rotor motion as shown in Figure 4. The velocity (two components) is measured by an "x-wire," hot-wire anemometer and recorded by a [illegible]

through an analog to digital converter. The probe positioning has been automated in one direction and is driven by the microcomputer.

The velocity of the air at any given point in the flowfield is continuously measured by the hot-wire probe. Since the structure of the flowfield generated by the rotor of Figure 4 is coherent and synchronously varying with respect to the position of the rotor upstream, the velocity is sampled with respect to the position of the rotor. Thus a complete "time picture" of the structure is obtained as it passes the probe. In addition, the coherency of the flow structures allows the signals from several successive rotations to be averaged to improve the signal to noise ratio and reduce the effects of turbulence on the measurements. The signals from the hot wire are processed and recorded by the microcomputer through an analog to digital converter.

The shaft of the rotor in Figure 4 has been fitted with a light chopper disk of two tracks. One track has a single hole used to indicate the start of the rotor orbit and the second track has thirty-six equally spaced holes (every 10^{0}) used to indicate the position of the rotor in its orbit. These two tracks are "read" by light emitting diodes (LED), photo transistor pickups. The resulting signals are passed through an interface which provides signal conditioning to prepare the signals for the microcomputer.

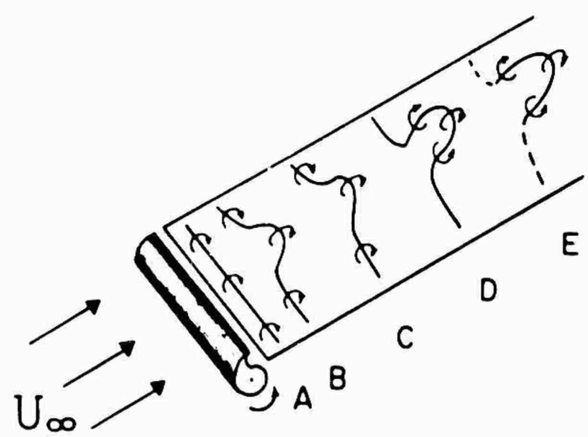

Figure 9. Schematic of the deformation of an initially rectilinear vortex.

The position of the hot-wire probe in the flowfield is partially computer controlled. The streamwise and sidewise positions of the probe are manually set while the height of the probe from the tunnel floor is computer controlled. The probe is driven up or down by a DC motor attached to a lead screw with a [illegible] turn-per-inch pitch. The bottom end of the lead screw is fitted with a light chopper disk with two holes. The holes are read by a LED-phototransistor pickup. The bottom end of the travel of the probe is detected by another LED-phototransistor pickup connected to a spring-loaded probe placed downstream of the hot-wire probe. The signals from the photo pickups are passed through the interface electronics to the microcomputer.

The hot-wire probe is positioned in the flow [illegible] screw. The position accuracy of the system has been found to be within ± ½ turn of the lead screw or about 0.020 inches. The bottom indicator has a reproductibility of better than 0.010 inches.

A computer program to record, process, and store the data from the hot-wire probe has been written and tested. The program takes 100 samples of each of the two wires in the probe for each of the 36 positions of the rotor. This data is averaged and reflected through the calibration curves for the hot wires to yield 36 two component velocities for two wires. The data is displayed on the computer console and stored as a disk file for further analysis. The procedure above is then repeated for each probe position. In this manner, the complete time profile of the convected structure is obtained along the probe path. The probe step size in the right direction is programmable.

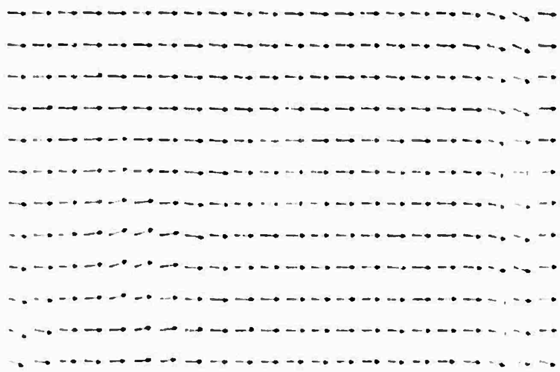

Figure 10a. Flowfield produced by the rotor in Figure 4.

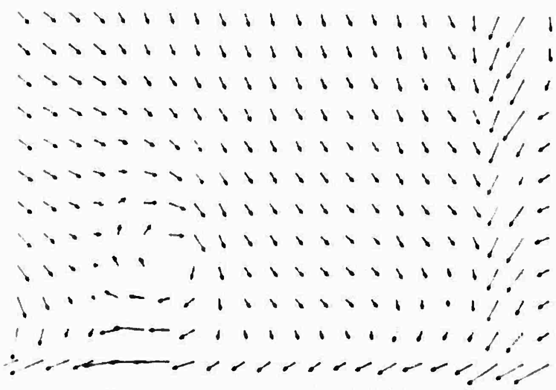

Figure 10b. Flowfield produced by the rotor in Figure 4 seen in a moving coordinate frame.

A typical result obtained by this system is shown in Figure 10a for the flowfield produced by the rotor in an instantaneous position rotated 1/3 revolution in the clockwise direction from that shown in Figure 4. No vortex is evident in the data until it is transformed into a moving coordinate system. The transformed data is shown in Figure 10b and the presence of the vortex structure is clear. The determination of the transformed plane can be by trial and error (guided by experience) or by mathematical techniques discussed in Reference [illegible]. The results corresponding to the [illegible] shown in Figure 4 are presented in Reference [illegible] for the case of a uniform velocity profile above the wall. The vortex distortion in the case of a shear [illegible] velocity profile above the wall is shown in Reference [illegible].

The remainder of this paper will concern itself with the fact that an external driver or power source is not needed to turn the rotor shown in Figure 4. This result improves the utility of the rotor and additional potential applications are discussed.

The Self-Powered Rotor

The results and potential applications of the rotor device cited in the sections concerned with past and current efforts were based on a rotor requiring an external source of power to turn and generate the vorticity. With proper design, however, the rotor motion can be self induced with the required power being drawn directly from the freestream velocity. Perhaps more interesting than the fact that the motion is self induced is the direction of rotation. As shown in Figure 4, the self induced direction of rotation is counterclockwise. Therefore, an increase in the rotational speed will also increase the strength of the resulting vortices.

The basic mechanism which drives the rotor in a direction which opposes the freestream velocity is shown schematically in Figure 11a. The relative pressure distribution is shown on the exposed portion of the rotor for the given configuration. Although there is a stagnation pressure effect near the upstream side of the rotor, the remainder of the upper surface is dominated by a low pressure distribution. One might say that the rotor "flies" in the freestream. From the distribution, it is clear that an integration yielding the moment about the axis of the rotor will result in a counterclockwise moment.

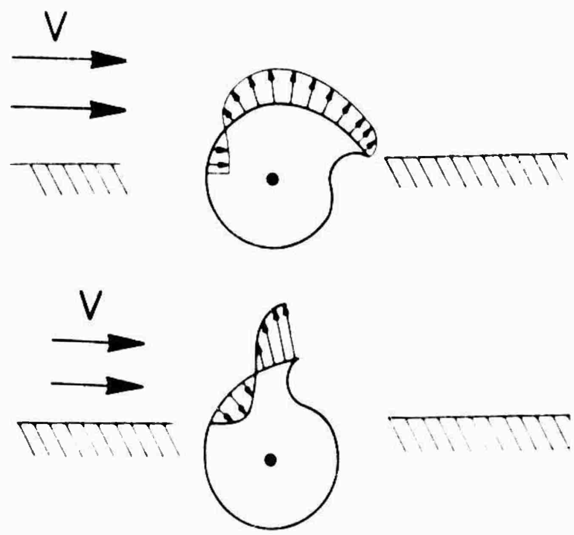

Figure 11. Schematic of the pressure distribution on the rotor surface in two orientations.

A similar conclusion is reached upon examination of the rotor orientation shown in Figure 11b. As shown, the resultant pressure distribution in this orientation with the maximum extension of the rotor again produces a counterclockwise moment. Thus the resultant rotation is in a direction which maximizes the velocity difference between the freestream velocity and the tip speed of the [illegible] shape on the rotor.

The startup operation of the unpowered rotor device is as follows: Even if the rotor is well balanced and relatively free to turn (i.e. low frictional resistance), at low freestream velocities the rotor remains in a static orientation. As the freestream velocity is increased, the rotor assumes the position shown in Figure 11b with the cusp shape directly above the shaft. A further increase in the freestream velocity results in an oscillation or rocking of the rotor about this position. The amplitude of the oscillations increase with freestream velocity until the rotor begins to turn in the counterclockwise direction. The rotor was never observed to turn in the clockwise direction.

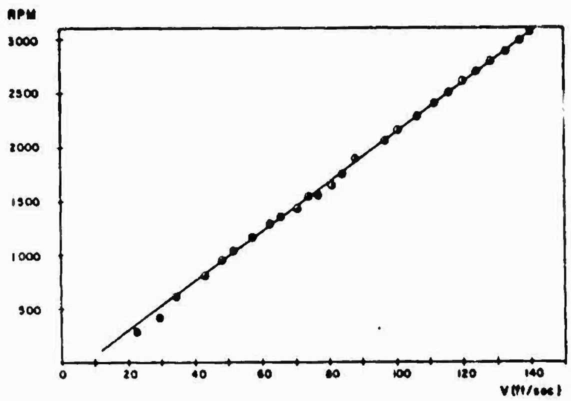

Figure 12a. Self driven rotor speed as a function of freestream velocity.

The particular rotor discussed in Reference 10 has been examined in detail to determine the relationship between the freestream velocity and rotational speed it produces. The results, shown in Figure 12a, are well represented by a linear dependence. This result is emphasized by the non-dimensional results of Figure 12b where the rotational speed is reduced by V/H; the freestream velocity exposed rotor height. Except for low freestream velocities (where both the velocities and the rotational speeds are less accurate), the reduced rotational speed is nearly constant.

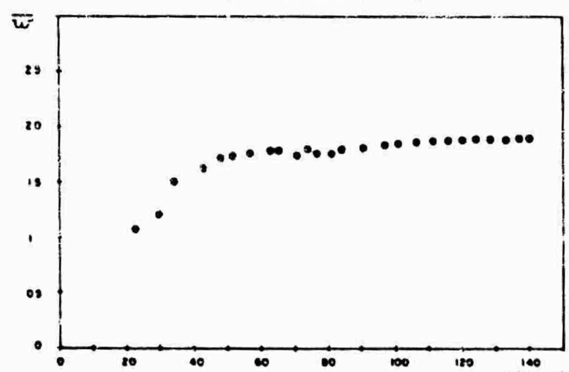

Figure 12b. Self driven rotor speed non-dimensionalized with V/H; freestream velocity extended rotor height.

It should be emphasized that the results of Figures 12a and b are singular results for this particular rotor shape and for the frictional resistance of this bearing configuration. A change in the rotor shape or the frictional resistance would change the value of the curve but is not expected to affect the functional dependence.

From the point of view of potential application, the fact that the rotor can be employed without the need for an external driver is significant. It will allow more widespread use of the concept behind the device, namely the potential use of unsteady flows to achieve results superior to those found with nominally steady flows. All of the rotor based devices discussed in the preceding sections will be positively affected, from the point of view of application, by the possibility of self induced rotation.

Other Potential Applications

A wide range of potential applications exists for unsteady flow devices. Since an external driver is unnecessary to power the rotor vortex generator, the potential applications for this particular technique have improved. The following examples are all related to flow control near a solid wall and are not meant to be at all inclusive. Many other embodiments of these concepts will appear in the future.

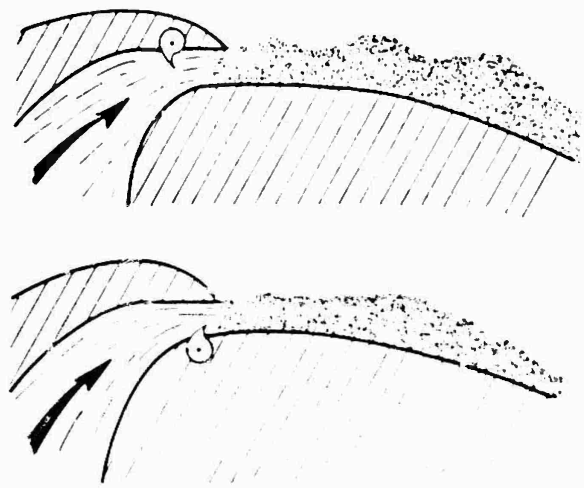

Figure 13. Two schematic embodiments of the rotor applied to a wall jet.

For the rotor concept, a wall jet version of the device is shown in Figures 13a and b where the rotor has been placed on opposite sides of a wall jet exit. In either case, the large scale vortices produced in the jet will allow the flow to remain attached to the wall in situations where it otherwise may separate. Of course, the rotor could be applied on both sides of the jet simultaneously, but it is likely that this will be unnecessary to achieve the desired [illegible].

From the point of view of the influence on the flow, the concept suggested in Figure 13a is likely to be superior. However, supporting the required structure within the geometrical constraints of the nozzle may become difficult. From that point of view, the suggestion of Figure 13b may be more easily achieved.

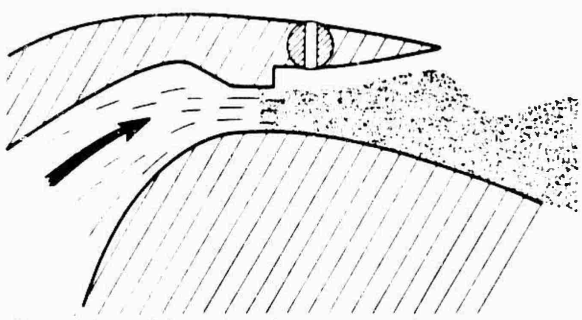

Figure 14. Schematic of a rotary valve geometry applied to a wall jet.

Another mechanical concept which allows the control of the phase angle in addition to the frequency is shown in Figure 14 and is related to the jet nozzle shown in Figure 3. In this case, the nozzle must be designed such that the flow remains attached to the wall when the rotary valve is in the open position shown. Upon closing the rotary valve, the jet detaches from the wall and attaches to the upper lip of the nozzle. The result is a wall jet which flaps up and down and produces an intermittent flow at the surface. Although the phase angle is controllable, the rotary valve must be externally driven.

An alternate embodiment of the fluidically controlled jet shown in Figure 2 is applied to a wall jet configuration in Figure 15. A feedback loop connectes control ports A and B. The resultant flow is an an intermittent flapping wall jet similar to that produced by the concepts in Figures 13 and 14. The advantage of the fully fluidic device is the elimination of all moving parts. The disadvantage is the loss of simple frequency control and a reduced amount of vortex generation.

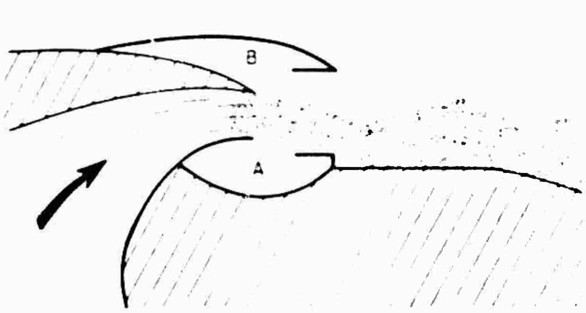

Figure 15. Schematic of a fluidically controlled wall jet.

Another purely fluidic concept as shown in Figure 16 [illegible]

cease. The flow will reattach to the wall and the process will repeat itself. The net result will be an intermittent fluid "flap" without the need for moving parts.

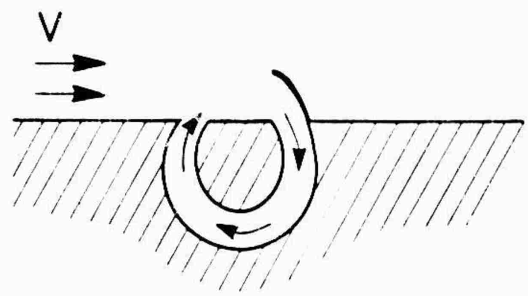

Figure 16. Schematic of a fluidic device to produce an intermittent flapping.

Analyses

In order to determine the effect of the unsteady flow on the field, the coherent vortex structures need to be identified. This will then allow the trajectories of the structures to be found and thus link the structures to the time averaged effects. Two techniques have been developed and examined in detail. The first depends upon a Fourier transformation of the entire flowfield. More recently, another analysis has been based upon decomposing the flow velocities into various components including rotation, translation, expansion and shear as shown in Figure 17. The rotational component has proven to be very useful in locating the vortex structures because it yields a definite pattern when these structures are in the field. An example is shown in Figure 18, where two vortex structures were found in the field behind the vortex generator of Figure 4. The closed regions indicate a vortex in the lower left and upper right portions of the field and correspond well to the results of flow visualization.

Current efforts are underway to extend the analysis into three dimensions, either three space dimensions or two space dimensions and time. These efforts are based on the same orthogonality conditions discussed in Reference [illegible]. However, the improved analysis will include sums and differences of results in different planes in order to generate the structural identifications in three dimensions.

Conclusions

[illegible]

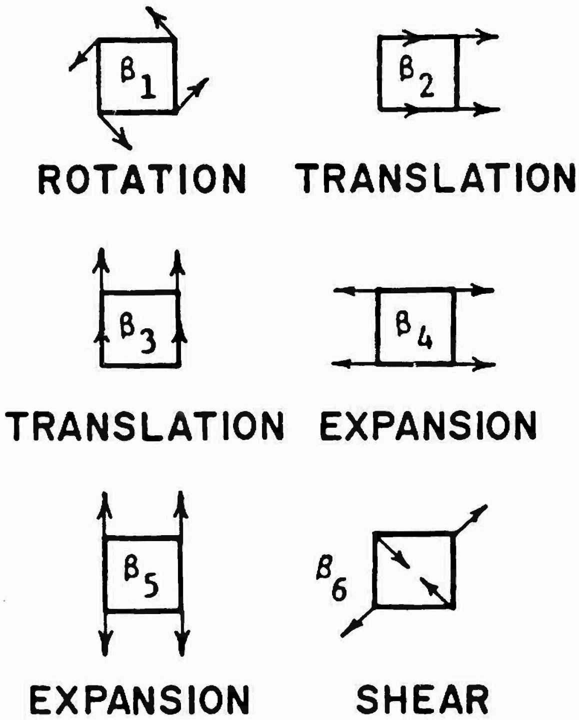

Figure 17. Orthogonal descriptors employed in the vortex identification analysis.

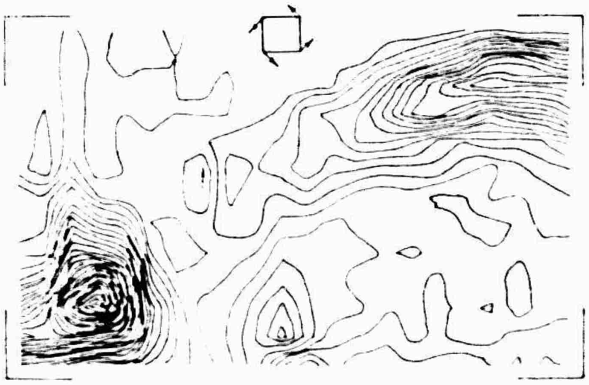

Figure 18. [illegible]

Acknowledgement

[illegible]

References

1. [illegible]

2. [illegible]

3. [illegible]

4. Viets, H., Piatt, M. and Ball, M., "Unsteady Wing Boundary Layer Energization", AIAA Paper No. 79-1631, Aug. 1979.

5. Viets, H., Piatt, M., and Ball, M., "Boundary Layer Control by Unsteady Vortex Generation", Wind Eng. and Ind. Aero., Vol. 7, 1981, pp. 135-144.

6. Viets, H. and Piatt, M., "Induced Unsteady Flow in a Dump Combustor", AIAA Progress in Astro. and Aero., Vol. 76, 1981, pp. 611-624.

7. Viets, H., Ball, M. and Bougine D., "Performance of Forced Unsteady Diffusers" - AIAA Paper No. 0154, Aerospace Sciences Meeting, St. Louis, Mo., Jan. 1981.

8. Viets, H. and Smith, [illegible], "The Rotor Jet", in preparation.

9. Viets, H., Catalano, [illegible] and Bougine D., "Drag Reduction by Means of Vortex Generation", in preparation.

10. Viets, H., Bethke, R. J. and Bougine, D., "Three Dimensional Vortex Dynamics Near a Wall" Fourth International Symposium on Turbulent Shear Flows, Karlsruhe, Germany, Sept. [illegible].

11. Bethke, R. J. and Viets, H., "Orthogonal Decomposition Techniques to Identify Unsteady Flow Structures", AIAA Paper [illegible], [illegible].

12. Viets, H.; [illegible] and Bethke, R. J., "Vortex Dynamics in a Shear Layer Near a Wall", in preparation.

13. Bethke, R. J. and Viets, H., "[illegible] Dimensional Analysis of Vortex Identification", in preparation.

UNSTEADY STALL PENETRATION OF AN OSCILLATING SWEPT WING

Franklin O. Carta
United Technologies Research Center
East Hartford, CT 06108

AD-P004 156

ABSTRACT

Recent unsteady tests on a full scale, oscillating tunnel-spanning wing have shown that the dynamic stall phenomenon for a swept wing model is significantly different from that for an unswept wing. Several critical measurements and calculations relative to the behavior of the stalling flow were made, including chordwise wave speed of the stalling vortex, the degree of pitch rate dependence of the vortex inception angle, and the validity of the cosine law for sweep to correlate unsteady post-stall behavior, even after [illegible] occurs.

The vortex chordwise wave speed was found to be sensitive to sweep angle over the forward [illegible] region. It was approximately half as large [illegible] for a sweep angle of [illegible] deg, [illegible] unswept wing. It was also found that the vortex inception angle (which can be [illegible] with dynamic stall inception) was [illegible] changes in sweep angle. [illegible]

[illegible]

C_M moment coefficient

$C_p(x,t)$ pressure coefficient distribution, Eq. (3)

f airfoil pitching frequency, Hz, Eq. (2)

k_c chordwise reduced frequency, Eq. (2)

M_c chordwise Mach number, Eq. (1)

M_∞ free stream Mach number, Eq. (1)

slope, Eq. [illegible]

$p(x,t)$ chordwise pressure distribution, newton/m², Eq. (3)

q dynamic pressure based on chordwise velocity, newton/m², Eq. [illegible]

T period, sec

t time, sec

t_v vortex inception time, sec

U chordwise velocity, [illegible]

U_∞ free stream velocity, [illegible]

$\bar{V}$ average nondimensional wave speed, [illegible]

$\bar{V}_{w_{ij}}$ average nondimensional wave speed between stations i and j

α airfoil angle of attack, deg, [illegible]

α_0 mean angle of attack, deg, [illegible]

α_{ss} steady state stall angle, deg

α_v vortex inception angle, deg, [illegible]

[illegible]

DESCRIPTION OF THE DATA BASE

The data base for the present study was obtained from aerodynamic experiments performed on an oscillating tunnel-spanning wing (TSW) in both unswept and 30 deg swept configurations in the United Technologies Research Center (UTRC) Main Wind Tunnel. The chordwise profile taken normal to the wing leading edge is a NACA 0012 airfoil. A detailed description of the test program can be found in Ref. 1, and an amplification of the material discussed here is presented in Ref. 2. The parameters for this test were the wing sweep angle, Λ, the amplitude of pitching motion, α, the mean angle of attack, α_M, the pitching frequency, f, and the approach Mach number, M_∞. The effect of sweep was accounted for in the normalization process by referring all data to the component of Mach number, M_c, normal to the wing span,

$$M_c = M_\infty \cos \Lambda \tag{1}$$

where subscript c denotes the chordwise direction. [illegible] pressure data were obtained for sinusoidal pitching about the quarter chord axis at two values of M_c [illegible] for each value of Λ (= 0 deg and 30 deg), and two values of α (6 deg and 10 deg) [illegible] mean angles of attack α_M = [illegible], 12 and 15 deg. All angles were measured in a plane perpendicular to the span axis. Tests were conducted over a range of frequencies such that the chordwise reduced frequency

$$k_c = \frac{\pi c f}{a_\infty M_c} \tag{2}$$

[illegible] several [illegible] at both sweep angles.

[illegible]

[illegible] Analysis

[illegible] pressure coefficient is [illegible]

$$C_p(x,t) = -p(x,t)/q\cos^2\Lambda \tag{3}$$

[illegible] dimensionless position along the [illegible] This nondimensionalization [illegible] a steady-state sweep analysis [illegible] potential and the [illegible] on the wing to be determined [illegible] of the normal velocity [illegible]. The pressure coefficient is [illegible] pressure [illegible] relating [illegible] integrated [illegible]

[illegible] it was shown that plots of unsteady [illegible] and chordwise position [illegible] quantitative information [illegible] pressure waves. [illegible] applied herein, and [illegible] the data are restricted to the [illegible] the unsteady pressure [illegible] steady-state [illegible] location of the pressure [illegible]

Λ = 0° $\bar{\alpha}$ = 0° α_M = 9° f = 10 Hz

M_∞ = 0.30 k_c = .125

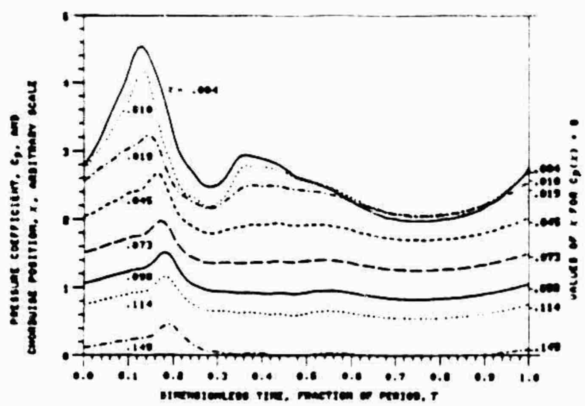

FIG. 1(a) PRESSURE CARPET PLOT, LEADING EDGE REGION

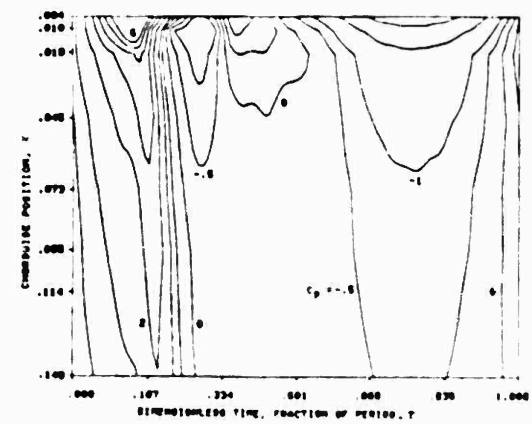

FIG. 1(b) PRESSURE CONTOUR MAP, LEADING EDGE REGION

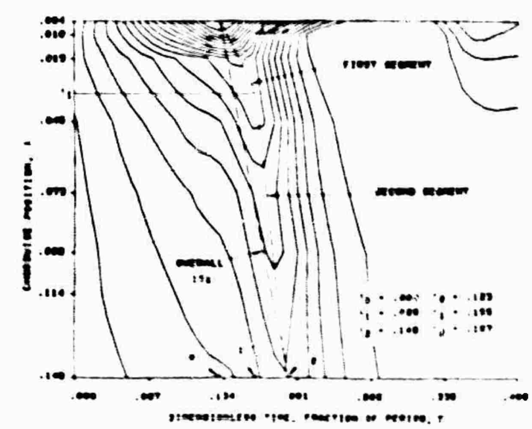

[illegible]

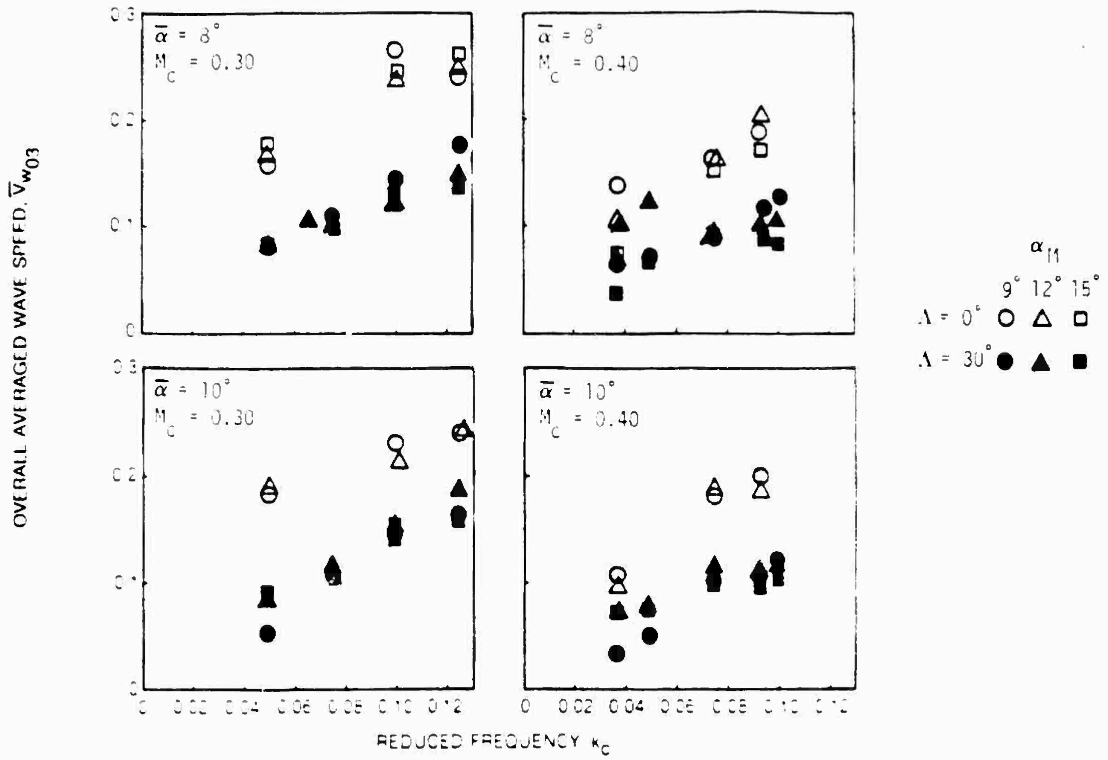

FIG. 2 EFFECT OF SWEEP ANGLE ON OVERALL WAVE SPEED

[illegible] and use the left scale to measure the pressure relative to its zero level. The precipitous drop in C_p in the vicinity of τ = 0.17 [illegible] is customarily associated with dynamic stall and is usually ascribed to the formation and [illegible] passage of a stall cell or vortex.

For this carpet plot a set of constant pressure contours (isobars) was constructed in the [illegible] plane as shown in Fig. 13. The numbers that are appended to each contour are values of unsteady C_p. As shown in Ref. 3, the direction of the [illegible] of contour extremes identifies the direction of wave propagation, and a simple estimate of the slope yields the wave speed.

Figure 1[illegible] concentrates on the first four [illegible] of the period, [illegible]. The connection [illegible] the contour extremum at the leading edge [illegible] extremum at the 15 percent chord location [illegible] line labeled "overall 15%") is used for calculating the wave speed over the forward 15 percent of the blade chord. This set of contour [illegible] toward increasing time as the chord is traversed from front to rear. The dimensionless wave speed was shown in Ref. 3 to be related to the ratio of chord extent to elapsed time by the [illegible]

$$\bar{V}_w = \frac{c\,\Delta x}{V_c\,\Delta t} = \frac{k_c}{\pi}\cdot\frac{\Delta x}{\Delta \tau} \qquad (4)$$

[illegible], and k_c [illegible].

In general, the locus of contour extremes is [illegible] linear [illegible] represented by straight line segments of different slopes. The end points of the first segment are denoted by (x_0, τ_0) and (x_1, τ_1) and those of the second segment by (x_1, τ_1) and (x_2, τ_2). Hence, there are actually two distinct regions within the first 15 percent of the chord that have different wave speeds. For this particular example, these values are (x_0, x_1, x_2) = (0.004, 0.028, 0.149), (τ_0, τ_1, τ_2) = (0.123, 0.155, 0.187), and with k_c = 0.125, application of the wave speed Eq. (4) yields $\bar{V}_{w01}$ = 0.033 (first segment), $\bar{V}_{w12}$ = 0.146 (second segment), and $\bar{V}_{w02}$ = 0.090 (overall, 15%), where the wave speed subscripts match the subscripts of the initial and end-point coordinates of the segment in question. Furthermore, Fig. 14 of Ref. 2 for the entire chord shows that another discontinuity can be defined at the 15 percent chord station, separating the forward region from the aft region of the chord, implying additional speed changes along the chord. This last coordinate point is given by (x_3, τ_3) = ([illegible].471, [illegible].254), and two additional wave speeds can be defined, $\bar{V}_{w23}$ = [illegible] (third segment), and $\bar{V}_{w03}$ = [illegible] (overall, 100%). It is seen that the wave is slowest in the region of high pressure gradient near the leading edge ($\bar{V}_{w01}$). This is the region characterized by the dense array of constant level contour lines in Fig. 13. Conversely, the wave travels more rapidly over the second segment ($\bar{V}_{w12}$) where the chordwise pressure gradient is lower, and attains its highest speed over the last segment ($\bar{V}_{w23}$) where pressure gradient is minimal.

A study was performed to examine the effect of [illegible] of the test parameters on wave speed and the results are illustrated in Fig. [illegible], in which the overall wave speed, $\bar{V}_{w03}$, is plotted versus reduced frequency, k_c. [illegible]

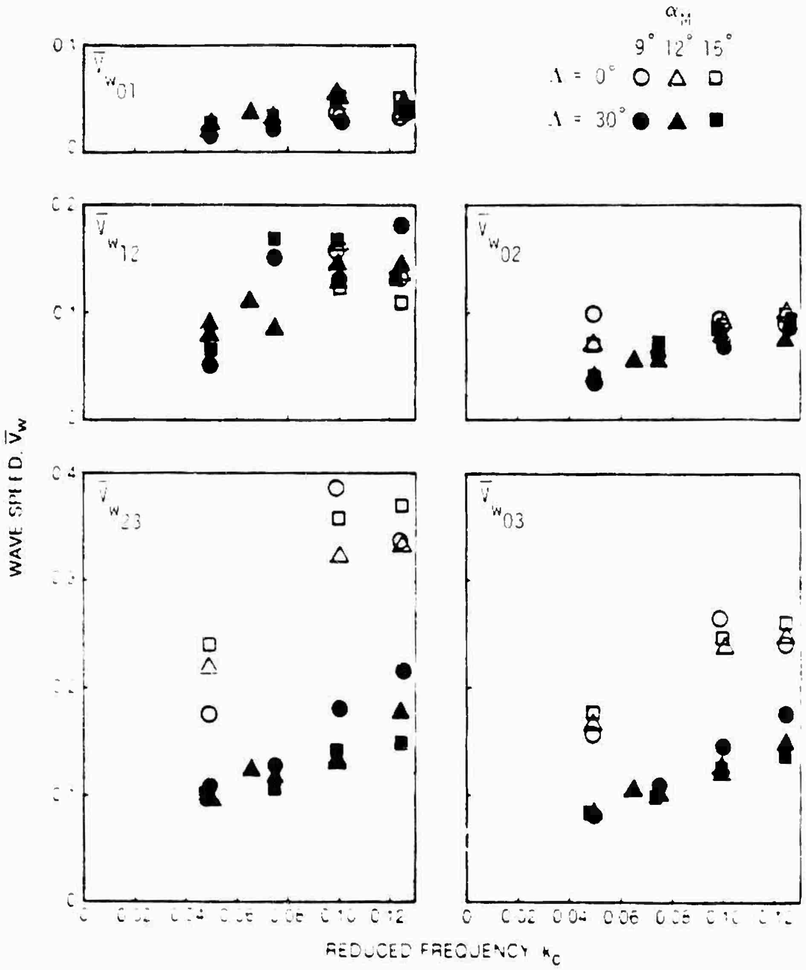

FIG. 3 EFFECT OF SWEEP ANGLE ON WAVE SPEED AT SEVERAL CHORDWISE LOCATIONS FOR M_c = 0.30 AND $\bar{\alpha}$ = [illegible]

[illegible] by the three symbols used (circle, triangle, and square) and the variation of the parameter of primary interest for each figure is indicated by the contrast between open and solid symbols. A comparison of the upper and lower panels (for effect of amplitude) shows a negligible difference, and comparison of the left and right panels (for Mach number) shows a small difference, [illegible]. [illegible] indicates that the effect of M_c on [illegible] is inconsequential.

[illegible], the parameter that has the greatest effect on $\bar{V}_w$ is the sweep angle. In all four panels the overall wave speed for the unswept wing (open symbols) is consistently and significantly greater than that for the swept wing (solid symbols) by a factor of 1.[illegible] to 2.[illegible]. This phenomenon of lower chordwise wave speed in swept wings has not been predicted by any previous analysis or observed in any previous experiment.

In an effort to examine these trends more closely, wave speeds of the several segments defined earlier were computed and are displayed in Fig. [illegible] for M_c = [illegible]. The three left hand panels [illegible] local wave speeds $\bar{V}_{w01}$, $\bar{V}_{w12}$, and $\bar{V}_{w23}$ [illegible]. The two right hand panels are the two average wave speeds, $\bar{V}_{w02}$ over the first 15 percent of the chord, and $\bar{V}_{w03}$ over the entire chord. (The latter is repeated from the upper left panel of Fig. 2.) It is clear that there is substantially no effect of sweep angle on the local wave speed over the forward 15 percent of the chord, either by examination of the panels for $\bar{V}_{w01}$ and $\bar{V}_{w12}$, or from the results for $\bar{V}_{w02}$. Virtually all of the sweep effect is perceived to occur in the aft portion of the chord (lower left panel), with factors of as much as 2 observed in unswept wing wave speed versus that for the swept wing. This result is representative of all cases examined. If the pressure wave is associated with the formation and chordwise transport of a vortex, these results would imply that the vortex motion along the chord is independent of sweep over the first 15 percent region of the chord, and is strongly dependent on sweep thereafter.

Vortex Formation Angle Variation

[illegible]

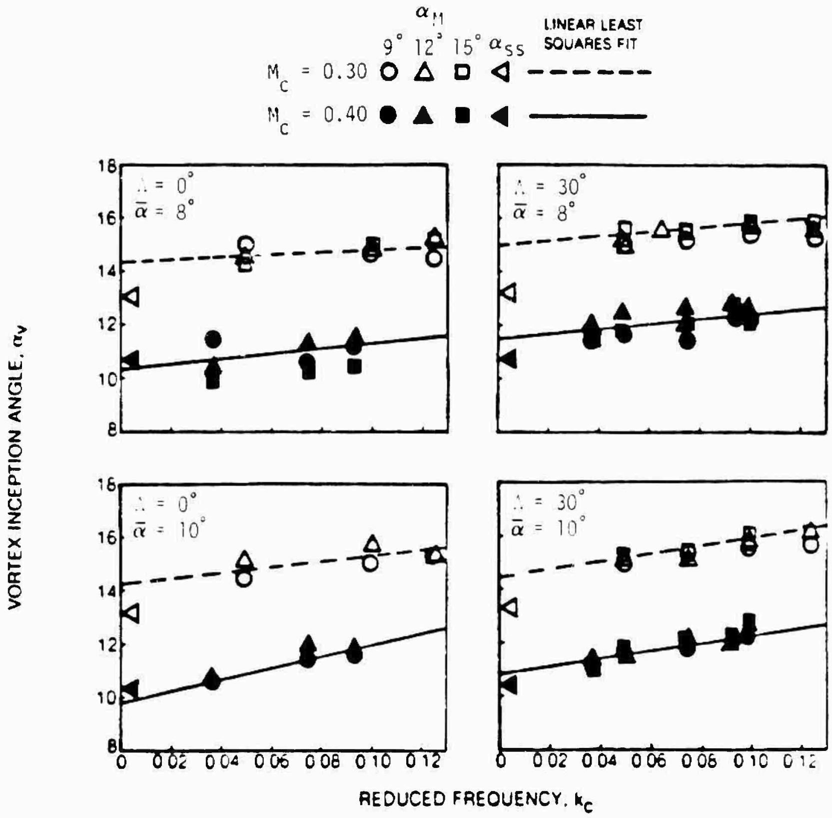

FIG. 4 EFFECT OF MACH NUMBER ON VORTEX INCEPTION ANGLE BASED ON INITIAL WAVE PROPAGATION

vortex inception angle, α_V. A direct computation of α_V can be made by substituting the dimensionless inception time, $\tau_0 = \omega t_0/2\pi$ (cf. Fig. 1b), into the equation for instantaneous angular position.

$$\alpha = \alpha_M + \bar{\alpha} \sin \omega t = \alpha_M + \bar{\alpha} \sin 2\pi\tau_0 = \alpha_V \tag{5}$$

The results are shown in Fig. 4 as plots of vortex inception angle versus reduced frequency. These plots also contain information on the steady state stall angle (triangular symbols on the left ordinate) and on the best linear fit to the data. The latter were obtained by a least squares procedure for each data group, and the former by [illegible] the steady state angle of attack at [illegible] α_M [illegible] in Figs. 14 through 17 in Ref. 1.

The vortex inception angle, α_V, varies linearly with k_c, as indicated by the good correlation of the linear least squares line

$$\alpha_V = \alpha_{VO} + mk_c \tag{6}$$

[illegible] the measured data, and the narrow scatter [illegible] for each data set. (In this equation, α_{V0} is the zero frequency intercept and m is the slope.)

A comparison of the left and right panels of Fig. 4 shows that sweep has a tendency to delay vortex inception, but this delay is less than two degrees overall, and less than one degree in the [illegible]. In contrast to this result, the [illegible] a substantial [illegible], [illegible] vortex angle [illegible] as M_c varies from 0.3 to 0.4. The steady state stall angle based on zero moment slope, α_{SS}, is unaffected by sweep angle changes. (However, Figs. 14 through 17 of Ref. 1 show that the shape of the lift curve changes signficantly in the direction of lift stall delay with increasing sweep, consistent with Fig. 3 of Ref. 4 which is based on the data of Ref. 5.) A comparison of the steady state stall angle with the zero frequency intercept of the least squares vortex inception line shows a two degree difference at $M_c = 0.3$, and a reasonably good correlation at $M_c = 0.4$.

A careful study of Fig. 4 reveals little or no effect of mean angle of attack on the incipient vortex angle. Specifically, at any constant value of k there is no discernable trend of α_V with α_M; there is only scatter. This is an observation that is directly concerned with the effect of pitch rate on α_V, which is addressed next.

A case to be considered in detail is represented by the open symbols at k_c = [illegible] in the lower right panel of Fig. 4 for $M_c = 0.3$, $\bar{\alpha}$ = 10 deg, and Λ = 30 deg. In this instance the vortex inception angle is very nearly 16 deg for all three values of α_M. This is demonstrated in Fig. 5 which depicts three motion time histories for α_M = 9, 12, and 15 deg versus dimensionless time, τ. A horizontal line at α_V = 16 deg represents the observed insensitivity of the vortex inception angle to changes in α_M, and [illegible] [illegible]

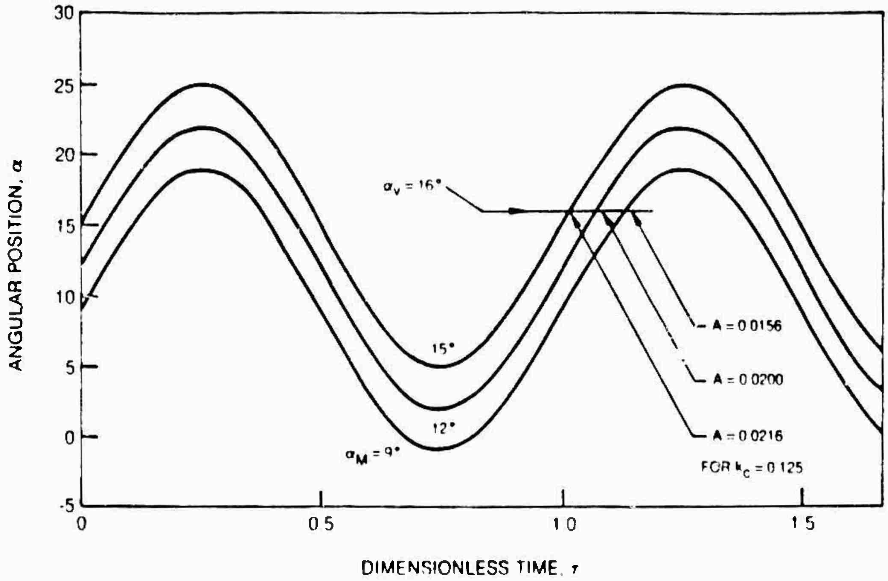

FIG. 5 TYPICAL MOTION TIME HISTORIES FOR THREE MEAN ANGLES OF ATTACK

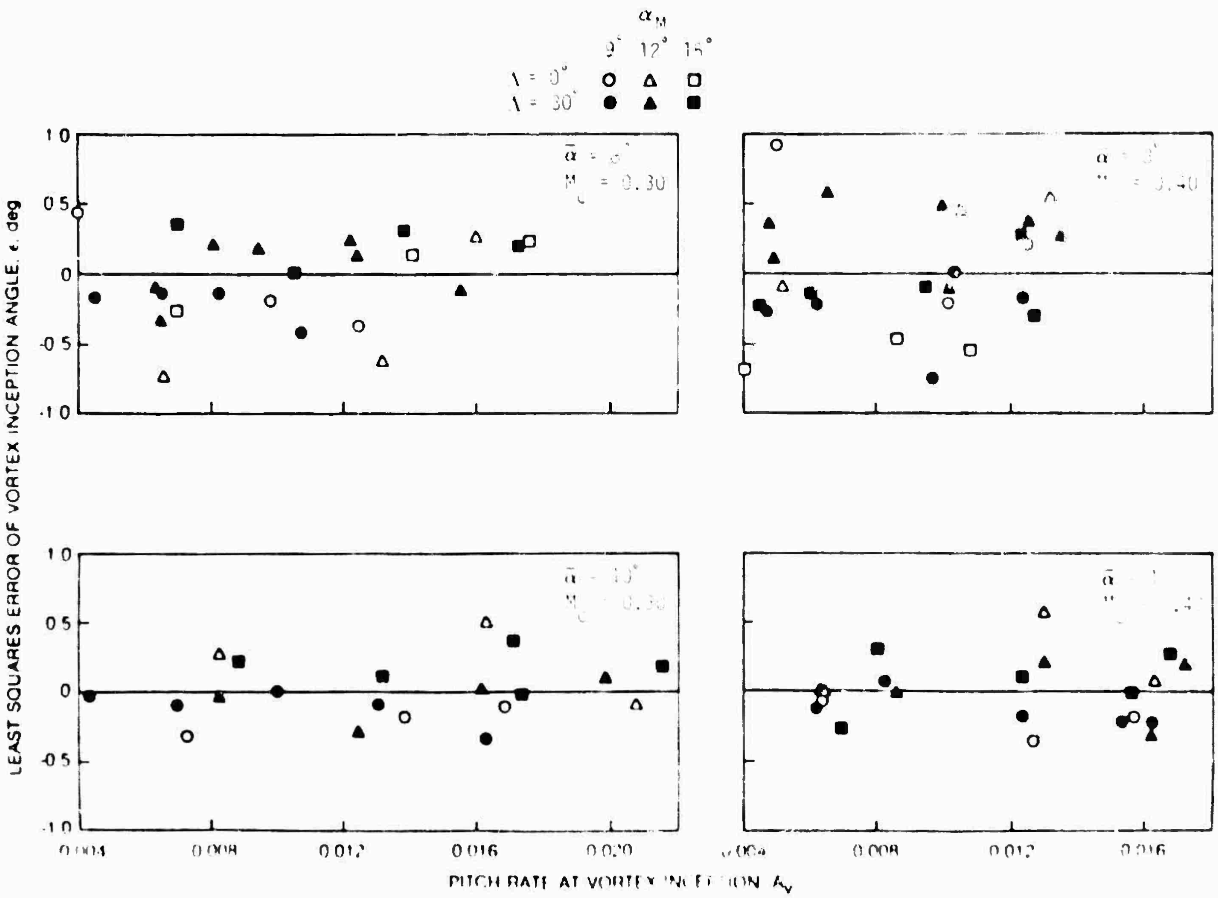

[illegible]

derivative of Eq. (5),

$$\dot{\alpha} = \omega\bar{\alpha}\cos\omega t = \omega\bar{\alpha}\sqrt{1-\sin^2\omega t} \tag{7}$$

A combination of Eqs. (5) and (7) yields

$$\dot{\alpha} = \omega\sqrt{\bar{\alpha}^2 - (\alpha-\alpha_M)^2} \tag{8}$$

which can be converted to [illegible] dimensionless pitch rate, A, by the formula (cf. Ref. 6)

$$A = \frac{c\,\dot{\alpha}}{2a_\infty M_c} = k_c\sqrt{\bar{\alpha}^2 - (\alpha-\alpha_M)^2} \tag{9}$$

The values of A for the intersections of the α_V = 16 deg line with the three motion curves in Fig. 5 are noted on the figure and are seen to vary from 0.0156 to 0.0216.

A direct examination of the effect of mean angle of attack variations on α_V with reduced frequency effects excluded is afforded by a return to the linear least squares fit of Eq. (6). The scatter of individual data points may be quantitatively evaluated by rewriting the equation in the form

$$\varepsilon = \alpha_V - \alpha_{V0} - mk_c \tag{10}$$

where $\varepsilon = 0$ for an exact linear fit. In Fig. 6 a plot of this error function, ε, versus A_V emphasizes the irregularity of the scatter, and leads directly to the observation that the vortex inception angle is independent of the pitch rate when k_c is fixed. With the exception of a few isolated points the error, ε, is generally bounded by $|\varepsilon| \leq 0.5$ deg, and never exceeds ±1.0 deg.

A question must be raised at this point on the possible relationship of the vortex inception angle, α_V, to the various dynamic stall angle concepts that have been cited in the literature. As far back as Halfman's 1951 report (Ref. 7) several authors have shown that the dynamic stall angle increases with both increasing reduced frequency and pitch rate. One of the more complete evaluations is that of Gormont (Ref. 8). Here it is shown that the dynamic moment stall angle, based on α_M [illegible] dynamic)/α = 0), varies linearly with the square root of the pitch rate, and, for the thick V[illegible] airfoil, approaches the steady state stall angle as the zero pitch rate limit is reached.

To permit a comparison of Gormont's linear fit [illegible] earlier dynamic stall angle results with the present data, the steady-state stall angle was removed from the vortex inception angle results of the present experiment, $\alpha_V - \alpha_{ss}$, and then plotted versus A in Fig. 7. The M_c = 0.4 linear fit to Gormont's thick airfoil moment stall results (lower left panel of Fig. 11 in Ref. 8) is shown plotted as dashed lines. Although there is considerable scatter of the present data, a linear trend is discernable for $\bar{\alpha}$ = 10 deg. Gormont's linear fit for moment stall angle starts from the origin and lies roughly parallel to, and significantly above, the α_V data in the lower panel. If these data were linearly extrapolated to zero pitch rate, the [illegible] would [illegible] deg [illegible] the steady state stall angle, which is in [illegible] contradiction to the results [illegible] for M_c [illegible]

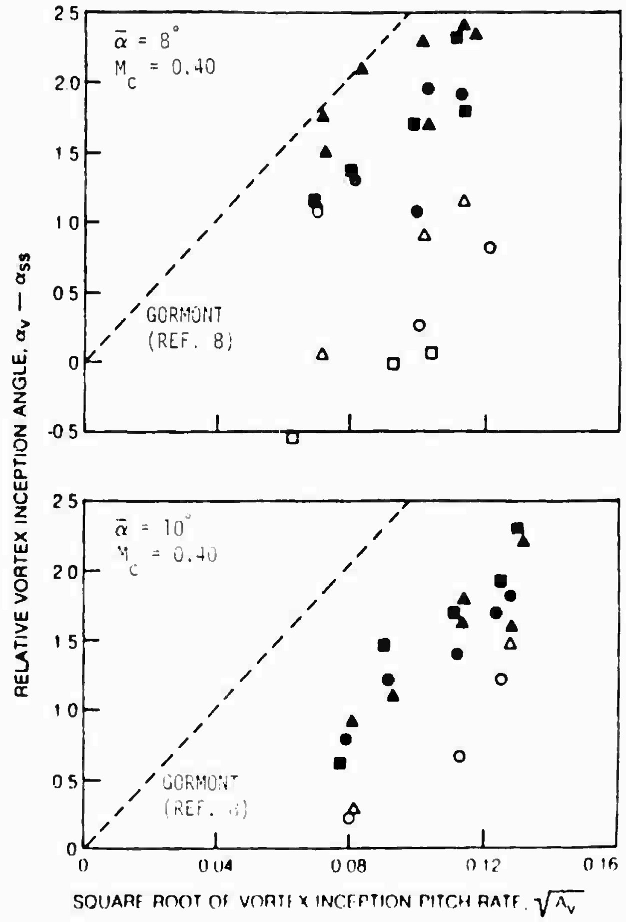

FIG. 7 CORRELATION OF RELATIVE VORTEX INCEPTION ANGLE WITH $\sqrt{A_V}$

0.4 in the lower right panel of Fig. 4. This can be resolved by noting that a linear behavior of the data is observed for $\alpha_V - \alpha_{SS}$ plotted versus A in Fig. 7 or versus A in Fig. 8. The data are now more in keeping with the results in Fig. 4, and the original Gormont linear data fit is now a parabola. The apparent inconsistency lies in the lack of data at low pitch rates (or reduced frequency).

[illegible]

The integrated load results (lift, drag, and moment) reported in Ref. 1 were computed and hysteresis loop comparisons were made therein to show the effects of sweep on the unsteady lift, drag and moment components of the total force response. An unexplained feature in the results is the substantial displacement in the lift curve below stall between the unswept and swept wing results, especially at high mean angles of attack. A perspective on this displacement can be obtained from Figs. [illegible] and [illegible]. Figure [illegible] shows that the normalized steady-state lift curves of the unswept and swept [illegible] airfoils are nearly coalesced below stall. This is not the case when [illegible] [illegible]

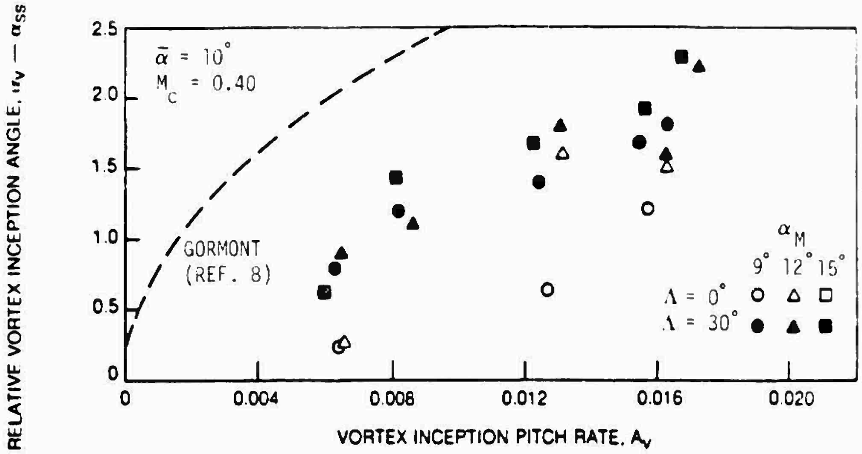

FIG. 8 CORRELATION OF RELATIVE VORTEX INCEPTION ANGLE WITH A_V

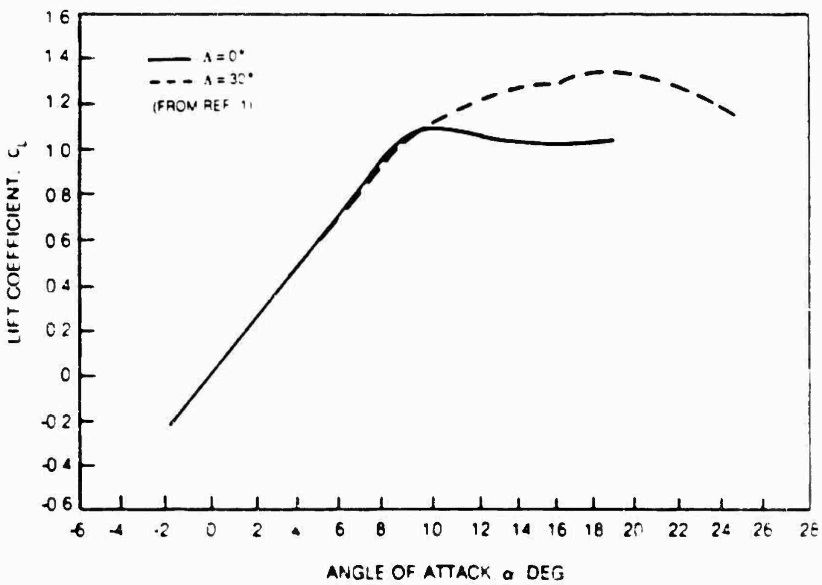

FIG. 9 STEADY-STATE LIFT COEFFICIENT FOR NACA 0012 AIRFOIL AT M_∞ = 0.40

displaced from one another as α_M increases.

It has been found that this displacement of the lift response is mainly associated with the first harmonic component. The time mean component of the lift response was removed in an attempt to bring the loops to closer alignment than shown in Fig. 10. The result is shown in the top row of Fig. 11 for the 15 degree mean angle of attack case where plot 11a is repeated from Fig. 10 and plot 11b is stripped of the time mean component. The resultant lack of change in the relative positioning of these loops indicates that the entire displacement is a sweep-induced unsteady phenomenon. A harmonic analysis of these loops was performed and it was found that the ultimate shape, displacement, and rotation of the lift loops of Fig. 11a are primarily governed by the first harmonic component ellipse. This is clearly illustrated in plot 11c where the distortion [illegible] the [illegible] displacement is accounted for. The remaining comparison in Fig. 11 (plots d through f) show how the addition of higher harmonic terms contributes in evolving the complete unsteady response without significant influence on the C_L displacement at the midpoint of the upstroke.

SUMMARY OF RESULTS

- Mean angle of attack has little or no effect on wave speed, which in all cases increases uniformly with reduced frequency. Motion amplitude also has little or no effect on wave speed. Mach number has a small but consistent effect on wave speed, with higher Mach numbers yielding slightly smaller wave speeds.

- Sweep angle has a significant effect on wave speed. The overall wave speed for the swept wing is consistently greater than that for the unswept

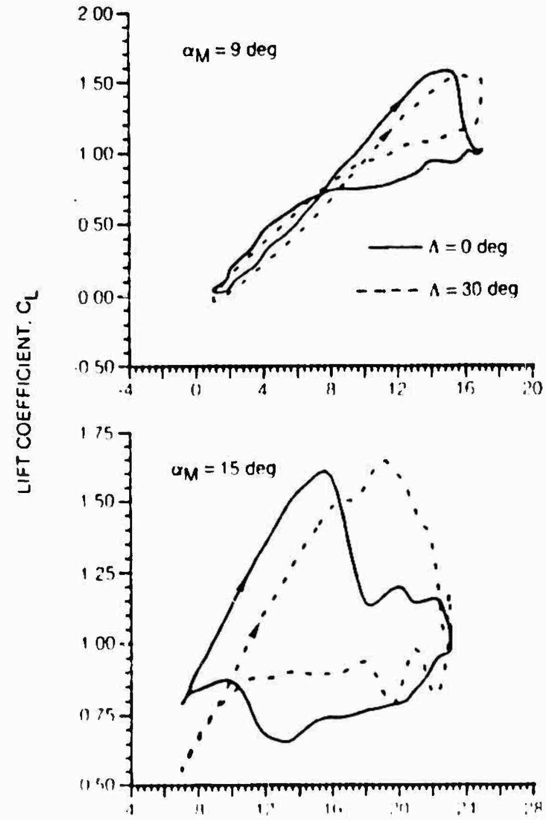

FIG. 10 EFFECT OF MEAN ANGLE OF ATTACK AND SWEEP ON THE LIFT RESPONSE AT k_c = 0.075 (f = 8Hz, M_c = 0.40), AND $\overline{\alpha}$ = 8 DEG

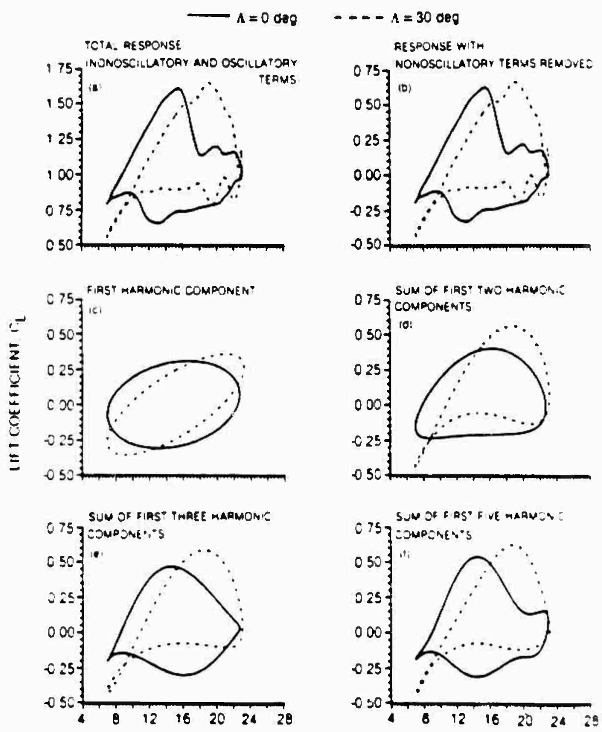

FIG. 11 HARMONIC ANALYSIS OF THE SWEEP EFFECT ON THE LIFT RESPONSE AT α_M = 15 DEG, k_c = 0.075 (f = 8Hz, M_c = 0.40), AND $\overline{\alpha}$ = 8 DEG

rise by a factor of 1.5 to 2.0. This represents a major failure above stall for the cosine law normalization which has been shown to be consistently valid below stall.

- Mach number has a dominant effect on vortex inception angle and static stall angle, with a decrease in both angles as M_c increases.
- Vortex inception is substantially independent of amplitude of motion and of mean angle of attack.
- Local wave speed differences associated with sweep are confined to the region of the blade aft of the 15 percent chord. Wave speeds are substantially the same for both sweep angles forward of this chord location.
- The vortex inception angle is independent of pitch rate when reduced frequency is fixed.
- The [illegible] influence of sweep on the total integrated lift response is very strongly determined by the first harmonic term.

REFERENCES

1. St. Hilaire, A. O., F. O. Carta, M. R. Fink and W. D. Jepson: The Influence of Sweep on the Aerodynamic Loading of an Oscillating NACA 0012 Airfoil. Volume I - Technical Report. NASA CR-3092, 1979.

2. St. Hilaire, A. O. and F. O. Carta: Analysis of Unswept and Swept Wing Chordwise Pressure Data from an Oscillating NACA 0012 Airfoil Experiment. Volume I - Technical Report. NASA Contractor Report [illegible], March, [illegible].

3. Carta, F. O.: Analysis of Oscillatory Pressure Data Including Dynamic Stall Effects. NASA CR-2394, May, 1974.

4. Harris, F. D.: Preliminary Study of Radial Flow Effects on Rotor Blades. Journal of the American Helicopter Society. Vol. 11, No. 3, July, 1966.

5. Purser, P. E. and M. L. Spearman: Wind Tunnel Tests at Low Speed of Swept and Yawed Wings Having Various Plan Forms. NACA Technical Note [illegible], December, [illegible].

6. Carta, F. O., G. L. Commerford, R. G. Carlson and R. H. Blackwell: Investigation of Airfoil Dynamic Stall and Its Influence on Helicopter Control Loads. USAAMRDL Technical Report 72-51, September, 1972.

7. Halfman, R. L., H. C. Johnson and S. M. Haley: Evaluation of High-Angle-of-Attack Aerodynamic-Derivative Data and Stall-Flutter Prediction Techniques. NACA Technical Note 2533, November, 1951.

8. Gormont, R. E.: A Mathematical Model of Unsteady Aerodynamics and Radial Flow for Application to Helicopter Rotors. USAAMRDL Technical Report 72-67, May, 1973.

SIMULTANEOUS FLOW VISUALIZATION AND UNSTEADY LIFT MEASUREMENT ON AN OSCILLATING LIFTING SURFACE

AD-P004 157

Robert L. Bass*,
James E. Johnson**,
and
James F. Unruh†

Abstract

Boundary layer and trailing edge flow activities were recorded using hydrogen bubble flow visualization techniques on an oscillating lifting surface in a two-dimensional water tunnel. Simultaneous with flow documentation, unsteady lift was measured over a range of reduced frequencies from 0.5 to 10. Unsteady loads using classical, inviscid theories were predicted for the experimental conditions investigated. Reduced frequency bands exhibiting poor agreement between experiment and theory were identified and a correlation to observed flow phenomena was accomplished. The results support the utilization of a separate viscous model near the trailing edge coupled with an inviscid flow field model to predict unsteady loads. The results further show that for certain reduced frequency bands, classical inviscid solutions may be applicable and adequate.

Nomenclature

b	1/2 chord length
c	Chord length
$C(k)$	Theodorsen function
$C_{L_{\bar{\alpha}_{os}}}$	Oscillatory lift coefficient
$C_{L_{\alpha_0}}$	Two-dimensional steady state lift curve slope
f	Oscillation frequency
k	Reduced frequency ($\omega b/V$)
t	Time
V	Free stream velocity
x	Distance along chord from leading edge
α	Instantaneous angle of attack
$\bar{\alpha}$	Oscillatory angle of attack amplitude
α_0	Mean angle of attack
δ	Boundary layer thickness
δ^*	Boundary layer displacement thickness
[illegible]	Width of lifting surface
ν	Fluid kinematic viscosity
ω	Circular frequency
ρ	Fluid density
ϕ	Phase shift in Theodorsen's function

Introduction

The dynamics of the boundary layer (viscous effects) have an important bearing on lifting surface unsteady aero and hydrodynamic behavior. Inviscid theories are not adequate in many practical applications in their prediction of unsteady loads or flutter inception.

Improved theories of lifting surface dynamic performance which account for real fluid effects are required to advance the state of unsteady aero- and hydrodynamics. This realization has led numerous researchers[1-9] to re-evaluate assumptions used in inviscid unsteady aerodynamic theories. Both analytical and experimental efforts have been undertaken. Most studies have evaluated the applicability of the Kutta condition in unsteady flows. Significant experimental activity has been undertaken to study trailing-edge loading and flow patterns on oscillating lifting surfaces. Theoretical efforts have also been initiated to include viscous corrections to inviscid solutions to allow better prediction of oscillatory loads. These research efforts have been accomplished primarily in 1974-1980.

In the composite, these efforts, which are discussed in Reference 10, represent both analytical and experimental research investigating the effects of viscosity on unsteady loads on oscillating lifting surfaces. The experimental efforts show that for many cases, viscous (real fluid) effects drastically alter the trailing-edge conditions on oscillating lifting surfaces and, thus, the classical Kutta condition is not maintained. The experimental work represents measurements of trailing-edge pressures and flowfield patterns under various oscillatory conditions. In some cases low reduced frequencies have been utilized and in other cases high reduced frequencies. Theoretical work has replaced the Kutta condition with auxiliary conditions which appear appropriate relative to the viscous flow phenomena at the trailing edge and which alter the associated circulation.

In recent years, unsteady fluid dynamics has received considerable attention as it relates to unsteady separated flows, and there is a wealth of literature in high Reynolds number dynamic stall and unsteady viscous-inviscid interaction on oscillatory airfoils.[11-18] Current interest in high angle of attack supermaneuverability aircraft has emphasized the need to advance the state of knowledge in unsteady separated flows. Also recent interest in low speed (Reynolds number) drone aerodynamics[19-21] has required a re-evaluation of unsteady separated flow activity at conditions where viscous effects on separation phenomena and associated loads can result in significantly different lifting surface response than would be encountered at the Reynolds numbers associated with conventional or high speed aircraft. Regardless of the application, the projected operation of advanced lifting surfaces with active load controls in separated flow environments requires a significant advancement in unsteady separated flow technology.

Objective

The objective of this study is to expand the state of knowledge about the effects of unsteady boundary layer activity (viscous effects) on the loads of oscillating lifting surfaces. These objectives were accomplished through visualizing the boundary layer activity on a NACA-16-012 lifting surface harmonically pitching about the 1/4 chord in a two-dimensional water tunnel. Simultaneous with boundary layer observation and documentation, unsteady lift was measured for a wide range of reduced frequencies (0.5 [illegible] 10). These measurements were undertaken with the [illegible]

*Director, Department of Mechanical Sciences.
**Manager, Fluid Systems and Instrumentation, Department of Mechanical Sciences, Member AIAA.
†Staff Engineer, Department of Engineering Mechanics, Member AIAA.

- o evaluating the applicability of the Kutta condition over a wide range of reduced frequencies, and

- o establishing flow regimes where poor agreement exists between classical unsteady loads theory and experiment.

Experiments were undertaken in a two-dimensional water tunnel since higher Reynolds numbers could be achieved than with models in a wind tunnel, and hydrogen bubble techniques could be utilized to visualize the unsteady boundary layer activity. This work provides data whereby total oscillatory lift was recorded simultaneously with the recording of unsteady boundary layer activity.

Experimental Apparatus

Flow Tunnel and Instrumentation

Figure 1 shows the water tunnel contraction, test section and diffuser used in this study.

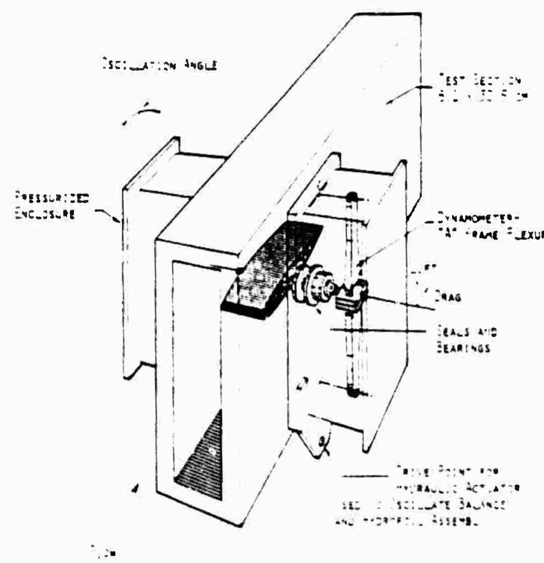

Fig. 1 Test section with balance and hydrofoil

A rectangular two-dimensional test section of 6.1 x 30.5 cm provided a test section aspect ratio of 5. The test section length is 61 cm with a 45.7 x 30.5 cm high viewing area. A 1600 watt quartz lamp placed over a plexiglass window 1.27 cm wide by 45.7 cm long located on the top surface provided light at 90° to the viewing angle and provided illumination for flow visualization. The water tunnel test section shown in Figure 1 was part of a continuous water tunnel flow loop where 5.08 cm pipe was used for the return line. A 1.22 cm section of 35.6 cm pipe was placed upstream of the convergent section to form a stagnation chamber. A fixed speed pump and throttling valve was used for flow control. Flow velocity was determined by measuring the time of a flight of a tracer along a known distance in addition to inferring average velocity from a 5.08 cm turbine flow meter.

Flow Visualization Equipment

Hydrogen bubbles were utilized to provide flow visualization for this study. A grid of platinum wire was placed upstream of the test model to provide visualization of the stream lines. In addition, hydrogen bubble generators were imbedded at different locations on the model surface to allow direct injection of tracers into the oscillating foil boundary layer. Photography of the hydrogen bubble tracers was successfully accomplished with a 16mm high-speed motion picture camera with zoom lens. The water tunnel test section viewing window was marked with a vertical line for a tracer reference point. The developed film was analyzed frame-by-frame on a Vanguard Motion Analyzer where flight trajectories of hydrogen bubbles were easily determined. The film analyzer was configured to computerize the coordinates of motion of the flow tracers. The computerized space-time histories of individual bubbles were used to establish flow separation and reattachment locations and reverse flow activity during a foil oscillation cycle. These data were used for recording qualitative information on boundary layer activity and were not used for load determination.

Dynamometer Design

A dynamometer, based upon the work of Epperson and Pengelley[22], was used for measuring the dynamic lift coefficient on the oscillating model. The dynamometer, shown in Figure 1 is classified as an external dynamic balance which can resolve two forces (vertical and horizontal) and one moment about a given axis perpendicular to the plane containing the two forces. Electric resistance strain gages attached to the structural elements of the A-frame flexures mounted back-to-back were incorporated in a Wheatstone bridge circuit in such a manner that the bridge output was proportional to the applied external moment.

The airfoil section was supported by a shaft connected to an external dynamometer unit located on each side of the tunnel test section. The dynamometer units were attached to a clevis that was allowed to rotate upon shaft bearings mounted on the tunnel side walls. Oscillatory motion was imparted by a hydraulic servo cylinder located on the lower structure of the test section. A unique pressure balanced seal was fabricated which absorbs no load but inhibits the flow of liquid from the test section to the surroundings.

Model Design

A NACA 16-012 airfoil section molded of Resolin compound in two halves with a chord 15.2 cm long was used for the model. An oscillation shaft was positioned at the quarter chord point. The shaft was hollow and carried electrical wires from the surface hydrogen bubble generators to the power source. Surface generators were made of gold plated aluminum chips, 0.159 cm by 0.635 cm imbedded flush in the surface of the hydrofoil. Figure 2 shows the model cross-section with the bubble generator locations and surface coordinates.

Flow Visualization Results

Table 1 summarizes the test conditions investigated. Flow visualization was obtained while varying four parameters, (1) free-stream velocity,

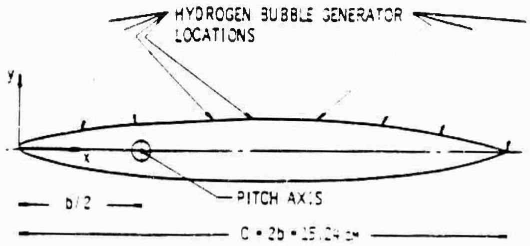

(A) MODEL CROSS-SECTION

SURFACE COORDINATES x PERCENT C	y PERCENT C	BUBBLE GENERATOR LOCATION (x) PERCENT C
0	0	
1.25	1.292	
2.5	1.80[illegible]	
5.0	2.509	
7.5	3.032	
10	3.457	10.3
15	4.135	
20	4.664	23.3
30	5.417	33.5
40	5.855	47.5
50	6.000	
60	5.835	
70	5.233	61.[illegible]
		[illegible]
80	4.199	
90	[illegible]	78.[illegible]
95	1.425	
100	0.120	100

LEADING EDGE RADIUS [illegible] PERCENT C

B) SURFACE COORDINATES NACA16-012

Fig. 2 NACA 16-012 model surface and hydrogen bubble generator coordinates

(2) oscillation frequency, (3) mean angle of attack, and (4) pitch amplitude. In each test set (Table 1), one parameter was varied with the others held constant. For the velocity and frequency variation test, the mean angle of attack was held at approximately 5.8 degrees with a pitch amplitude of ± 1 degree. Using 5.8 degrees for the mean angle of attack, allowed a sufficient boundary layer growth to be observed during a full oscillation cycle while maintaining a relatively small angle of attack. All oscillatory tests were performed with harmonic pitching about 1/4 chord.

Initial tests were performed without oscillation to visualize and record steady-state boundary layer activity as a function of angle of attack. The results showed that the boundary layer separated at X/2b = .88, .84, and .75 for α = 1.4, [illegible], and 5.[illegible], respectively. This separation near the trailing edge results from the rapid change in slope of the foil surface at X/2b = 0.75. Aerodynamic C_L data for this profile (NACA 16-012) indicates the stall angle of attack occurs at α_s = 8°. With the exception of test runs $H\alpha_0$-3 and $H\alpha$-3a, all test cases were performed with the maximum angle of attack below the stall angle.

The flow visualization studies revealed that boundary layer activity varied significantly depending on reduced frequency, k. In general, a more pronounced degree of boundary layer activity and instability was observed at k < 1. At all test conditions for 1 < k < 10 reduced boundary layer activity was observed, and at k > 10, a distinct boundary layer and wake flow regime developed. Table [illegible]

summarizes the important boundary layer observations for the test conditions of major interest. Figure 3 shows trailing edge flow patterns during a pitch oscillation cycle at k = 0.81. This general trailing edge flow activity was observed at all test cases with k < 10. Figure 4 shows instantaneous trailing edge flow patterns from the movie frames for k < 10 and k > 10. A description of the boundary layer activity as a function of reduced frequency follows:

- At the lowest frequency tested (k = .45), the boundary layer remained attached to the foil until approximately the 3/4 chord where the boundary layer separated from the foil surface. During an oscillation cycle fluid was pumped into the separation zone along the foil trailing edge as the angle of attack increased to the maximum value of 6.8°. As the foil reversed direction and proceeded to lower angles of attack, fluid was pumped out of the separation zone into the wake until the minimum angle of attack of 4.8° was reached.

- Increasing reduced frequency to k = .55, resulted in leading edge separation at X/2b = .17. The boundary layer reattached at approximately 40% of the chord and separated again at about 56% of the chord. Activity in the separation zone at the trailing edge of the foil was similar to the k = .45 case.

- Increasing k to .65 resulted in leading edge separation at X/2b ≅ .125 with a slight oscillation of the leading edge separation point during a foil pitching cycle. The boundary layer reattached at approximately 50% of the chord with reseparation oscillating between .625 < X/2b < .77 during a pitch oscillation cycle.

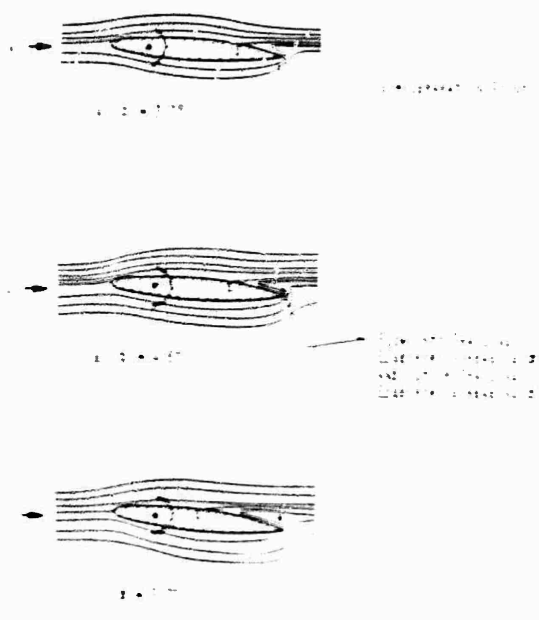

Fig. [illegible] Trailing edge flow patterns [illegible] at [illegible]

Table 1 Model test conditions

Run	Freestream velocity, V, cm/s	Oscillation frequency, f, Hz	Reduced frequency, $k = 2\pi fb/V$	Reduced velocity, $1/k$	Angle of attack, deg $\alpha(t) = \alpha_0 + \hat{\alpha}\sin 2\pi ft$	Reynolds No.,[a] $Re = 2Vb/\nu$	Re^* = [illegible]
			1) Velocity variation				
HV-1	9.82	0.132	0.648	1.54	$5.85 + 0.95 \sin 0.83t$	16,105	219
HV-2	3.90	0.147	1.80	0.55	$5.825 + 1.025 \sin 0.925t$	6,390	138
HV-3	16.23	0.151	0.445	2.25	$5.775 + 1.025 \sin 0.947t$	26,620	282
HV-4	12.51	0.144	0.552	1.81	$5.80 + 1.0 \sin 0.905t$	20,650	247
			2) Frequency variation				
HW-1	4.33	0.387	4.28	0.234	$5.9 + 0.9 \sin 2.43t$	7,105	146
HW-2	4.18	0.329	3.76	0.266	$6.05 + 0.95 \sin 2.07t$	6,865	143
HW-3	4.07	0.836	9.84	0.102	$6.05 + 0.95 \sin 5.26t$	6,70	141
HW-4	3.69	0.241	3.13	0.319	$6.05 + 0.95 \sin 1.51t$	6,060	135
			3) Mean angle-of-attack variation				
Hα_0-1	3.99	0.436	5.24	0.191	$1.95 + 1.05 \sin 2.74t$	6,545	140
Hα_0-2	4.18	0.602	6.89	0.145	$5.60 + 1 \sin 3.78t$	6,860	143
Hα_0-3	4.56	0.575	6.04	0.166	$7.65 + 1.15 \sin 3.61t$	7,485	150
Hα_0-4	4.34	0.633	6.98	0.143	$-1.55 + 1.05 \sin 3.98t$	7,125	146
Hα_0-5	4.50	0.649	6.90	0.145	$-5.25 + 1.05 \sin 4.08t$	7,385	149
			4) Pitch amplitude variation				
H$\hat{\alpha}$-1a	5.89	0.503	4.09	0.244	$4.25 + 1.55 \sin 3.16t$	9,655	170
H$\hat{\alpha}$-2a	5.76	0.47	3.91	0.256	$4.25 + 2.45 \sin 2.95t$	9,450	168
H$\hat{\alpha}$-3a	5.78	0.446	3.69	0.271	$4.20 + 4.8 \sin 2.80t$	9,475	168

[a] δ^* – based on theoretical value for an equivalent flat plate of chord $2b$.

Table 2 Model boundary-layer observations

Flow regime ident	Run	k	$1/k$	V, cm/s	f, Hz	Observed boundary-layer activity[a]
A	HV-3	0.45	2.2	16.2	0.15	BL separation at $X/2b \cong 0.75$
						Fluid flows into separation zone at TE at $\alpha_{max} = 6.8$ deg
						Fluid pumped out of separation zone at TE at $\alpha_{min} = 4.8$ deg
	HV-4	0.55	1.8	12.5	0.14	LE separation at $X/2b \cong 0.17$
						Reattached BL at $X/2b \cong 0.4$
						TE separation at $X/2b \cong 0.56$
						Separation zone activity similar to HV-3
B	HV-1	0.65	1.5	9.8	0.13	LE separation at $X/b \cong 0.125$ with slight oscillation of separation point during foil pitching cycle
						Reattached BL at $X/2b \cong 0.48$
						TE separation at $0.625 \leq X/2b \leq 0.77$ (TE separation zone oscillates during foil cycle)
C	HW-1a	0.81	1.2	8.5	0.15	On verge of LE separation at $X/2b \cong 0.18$
						TE separation at $0.5 \leq X/2b \leq 0.75$ (TE separation zone oscillates during foil cycle)
D	HV-2	1.8	0.56	4.0	0.15	BL separation at $X/2b \cong 0.25$ (reverse flow oscillates in separation zone during foil cycle)
E	HW-4	3.1	0.32	3.7	0.24	Identical to HV-2
	HW-2	3.8	0.26	4.3	0.33	
	HW-1	4.3	0.23	4.3	0.39	
	HW-3	9.8	0.10	4.0	0.84	
F	–	10.9	0.09	4.9	1.10	Vortex shedding at TE at $k > 10$

[a] Nomenclature: BL – boundary layer; TE – trailing edge; LE – leading edge; and b – semichord (c/2).

c. Increasing k to .81, resulted in near elimination of leading edge separation. For this case it appeared that leading edge separation was on the verge of occurring at X/2b = .18 although no distinct leading edge separation could be discerned. Trailing edge separation occurred between the .50 and .75 point with the separation location oscillating during a foil oscillation cycle.

d. Increasing k to 1.8 and at all higher values up to k = 10, resulted in the boundary layer separating at approximately the quarter chord as compared to separation at X/2b = .2[illegible] for steady state flow at an equivalent [illegible].

e. At k > 10, a distinct vortex shedding from the foil trailing edge was observed with the vortex shedding frequency equal to the pitch oscillation frequency.

f. During an oscillation cycle, flow activity in the separation region for any k value was identical to that described for k = .45. Increasing mean foil angle of attack resulted in a wider separation region and more pronounced activity in the separation zone.

The observed boundary layer activity on the oscillating model is noteworthy in the region of reduced frequencies between .7 and 1.4. Data of Reference 13 indicates that experimental unsteady load data on hydrofoils are in good agreement with

(a) k > 10

(b) k < 10

Fig. 4 Trailing edge flow activity at high and low k

the ... for k < 1. The flow visualization results indicate a transition in boundary layer behavior in this region. In addition, the results of the flow visualization studies presented above reveal that the Kutta condition appears to be violated, with the flow phenomena at the trailing edge being dependent on k. This observation implies that relaxing the Kutta condition is a valid approach to providing more realistic predictions of hydrofoil performance. Also, the unstable boundary layer activity observed at k values < 1 implies that incorporating boundary layer stability theory in a hydrofoil loads analysis should be a reasonable attempt to improving current theoretical methods.

[illegible] Loads to Observed Boundary Layer Activity

[illegible]

unsteady lift measurements were made. Figure 5 shows a comparison of theory and experiment for oscillatory lift coefficients $C_{L_{\bar{\alpha}_{os}}}$ versus reduced velocity (1/k). Also shown on this figure are the various flow regimes (see Table 2) where different distinct boundary layer activity was observed during the flow visualization.

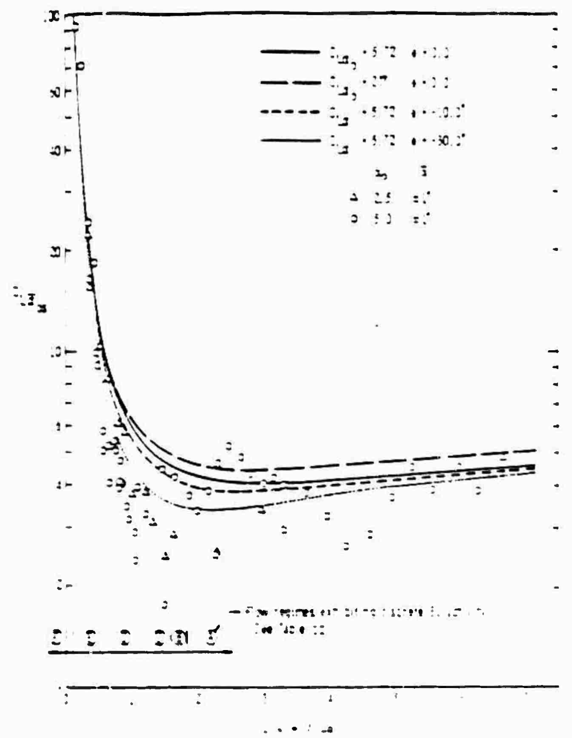

Fig. 5 Comparison of theory and experiment for oscillatory lift coefficient $C_{L_{\bar{\alpha}_{os}}}$ vs. 1/k

Theoretical oscillatory lift coefficients were predicted using the classical predictions of Theodorsen[24] and the modified strip theory approach of E. C. Yates[25] wherein the actual two-dimensional lift curve slope for the experimental model ($C_{L_{\alpha_0}}$ = 5.72 /rad) was employed. The measured steady state two-dimensional lift curve slope of 5.72 per radian is in good agreement with the expected value for these sections[6]. The oscillatory lift coefficient for pitch about the 1/4 chord as a function of reduced frequency is given by

$$C_{L_{\bar{\alpha}_{os}}} = \left\{ -\left[ik - \frac{k^2}{2} \right] + C_{L_{\alpha_0}} C(k) \left[1 + ik \right] \right\}$$

where $C_{L_{\bar{\alpha}_{os}}}$ is defined as

$$C_{L_{\bar{\alpha}_{os}}} = \frac{L}{[illegible]}$$

[illegible]

$$C(k)' = C(k)e^{i\theta} \, . \tag{3}$$

A phase shift between the virtual mass and oscillatory lift contributions to $C_{L\bar{\alpha}_{os}}$ was introduced to synthesize changes in the Kutta condition.

From the data shown in Figure 5, it can be seen that agreement between theory and experiment is good in those regions where boundary layer activity was well behaved. For $1/k < 0.75$ ($k > 1.33$) good agreement between theory and experiment is noted. Also, for $1/k > 2$ ($k < 0.5$), reasonable agreement is noted. However, at the knee of the theoretical curves ($0.75 < 1/k < 2.0$), significant deviation between measured and predicted oscillatory lift coefficient is noted. This flow regime represents conditions where the greatest degree of boundary layer activity is recorded wherein significant separation and reattachment of the boundary layer was observed. Also, the flow near the trailing edge was separated with flow alternating around the trailing edge region as the foil oscillated through its maximum and minimum angle of incidence. Since such trailing edge flow conditions will significantly affect the circulation around the oscillating foil in comparison to that predicted from classical inviscid theory, lift predictions were also carried out for various values of θ. As noted in Figure 5, a 30° phase lag in C(k) provides improved agreement between theory and experiment.

Conclusions and Recommendations

The presented simultaneous unsteady loads measurements and boundary layer flow visualization provide additional insight into the effects of viscosity on unsteady loads on oscillating lifting surfaces, and additional insight into the flow conditions which occur in different reduced frequency bands. The results in this paper show that:

- The Kutta condition, based on qualitative flow visualization, was violated for many of the observed oscillating foil test conditions.

- Observed boundary layer phenomena supports the hypothesis that unsteady boundary layer activity is responsible for poor agreement between current theoretical predictions and experimental data used for predicting hydrofoil unsteady loads and flutter.

- The largest disagreement between unsteady load theory and experiment occurs in the reduced frequency range, $0.5 \leq 1/k \leq 2$, which corresponds with the most pronounced boundary layer activity (i.e., flow separation, flow around the trailing edge, etc.).

- Introducing a phase lag in the circulation function provides better agreement between theory and experiment.

The experimental work presented in this report supports the utilization of a separate viscous model on the trailing edge of an oscillating lifting surface which can be coupled with an inviscid flow field model to provide unsteady load predictions. The results of this study should be compared to the analytical predictions of References [illegible] and [illegible]. The results further show that for certain reduced frequency bands classical inviscid solutions may be applicable and adequate.

Acknowledgements

The authors of this paper wish to express their appreciation to Dr. H. Norman Abramson who first suggested this work. Also, we want to express our gratitude to Mr. C. M. Wood for his dedicated work in conducting the experiments, Mr. Victoriano Hernandez for his skillful art work on the figures, and Mrs. Adeline K. Raeke for typing the text.

References

[1] Gostelow, J. P., "Trailing Edge Flows Over Turbomachine Blades and the Kutta-Joukowski Condition," ASME Paper 75-GT-94, Dec. 1974.

[2] Archibald, F. S., "Unsteady Kutta Condition at High Values of the Reduced Frequency Parameter," Journal of Aircraft, Vol. 12, June 1975, pp. 545-550.

[3] Brown, S. N. and Daniels, P. G., "On the Viscous Flow About the Trailing Edge of a Rapidly Oscillating Plate," Journal of Fluid Mechanics, Vol 67, Pt. 4, 1975, pp 743-761.

[4] Sears, W. R., "Unsteady Motion of Airfoils with Boundary-Layer Separation," AIAA Journal, Vol. 14, Feb. 1976, pp. 216-220.

[5] Basu, B. C. and Hancock, G. J., "The Unsteady Motion of a Two-Dimensional Aerofoil in Incompressible Inviscid Flow," Journal of Fluid Mechanics, Vol 87, Pt. 1, 1978, pp. 159-178.

[6] Daniels, P. G., "On the Unsteady Kutta Condition," Quarterly Journal of Mechanics and Applied Mathematics, Vol. XXXXI, Pt. 1, Feb. 1978, pp. 49-75.

[7] Satyanarayana, B. and Davis, S., "Experimental Studies of Unsteady Trailing-Edge Conditions," AIAA Journal, Vol. 16, Feb. 1978, pp. 125-129.

[8] Fleeter, S., "Trailing Edge Conditions for Unsteady Flows at High Reduced Frequency," AIAA Journal, Vol 18, May 1980, pp 497-503.

[9] Yates, J. E., "Viscous Thin Airfoil Theory," ARAP Rept. 413, Contract N00014-77-C-0616, Feb. 1980.

[10] Bass, R. L., Johnson, J. E., and Unruh, J. F., "Correlation of Lift and Boundary-Layer Activity on an Oscillating Lifting Surface," AIAA Journal, Vol 20, Aug. 1982, pp. 1051-1056.

[11] McCroskey, W. J., "Some Current Research in Unsteady Fluid Dynamics - The 1976 Freeman Scholar Lecture," Journal of Fluids Engineering, 99: 8-39 (1977).

[12] Francis, M. S., Keese, J. E., Lang, J. D., Sparks, G. W., Jr., and Sisson, G. E., "Aerodynamic Characteristics of an Unsteady Separated Flow," AIAA Journal, 17: 1332-1339 (1979).

[13] McCroskey, W. J. and Pucci, S. L., "Viscous-Inviscid Interaction on Oscillating Airfoils in Subsonic Flow," AIAA Journal, 20: 167-174 (1982).

[14] McCroskey, W. J., "The Phenomenon of Dynamic Stall," presented to von Karman Institute Lecture Series on Unsteady Airloads and Aeroelastic Problems in Separated and Transonic Flows, Rhode-Saint-Genese, Belgium, March 1981.

[15]Katz, J. and Weihs, D., "Wake Rollup and the Kutta Condition for Airfoils Oscillating at High Frequency," AIAA Journal, 19: 1604-1606 (1981).

[16]McCroskey, W. J., "The Challenge of Unsteady Separating Flows," Journal of the Engineering Mechanics Division, ASCE, 107: 547-563 (1981).

[17]Robinson, M. C. and Luttges, M. W., "Unsteady Flow Separation and Attachment Induced by Pitching Airfoils," AIAA Paper No. 83-0131, AIAA 21st Aerospace Sciences Meeting, Reno, Nevada, (1983).

[18]McCroskey, W. J., "Unsteady Airfoils," Annual Review of Fluid Mechanics, 14: 285-311 (1982)

[19]Lissaman, P. B. S., "Low-Reynolds-Number Airfoils," Annual Review of Fluid Mechanics, 15: 223-239 (1983).

[20]Telionis, D. P. and Koromilas, C. P., "Flow Visualization of Transient and Oscillatory Separating Laminar Flows," in Nonsteady Fluid Dynamics, edited by D. E. Crow and J. A. Miller (ASME, New York, 1978) pp. 21-32.

[21]Conigliaro, P. E., "An Experimental Investigation of the Low Reynolds Number Performance of the Lissaman 7769 Airfoil," AIAA Paper 83-0647 (1983).

[22]Epperson, T. B. and Pengelley, C. D., "An Electric Resistance Type, Inertia-Cancelling, Dynamic Load Measuring Device," U.S. Air Force Contract AF 33(616)-176.

[23]Abramson, H. N., Chu, W.-H., and Irick, J.T., "Hydroelasticity," Contract Nonr-4830(00)(X), Aug. 1966.

[24]Theodorsen, T., "General Theory of Aerodynamic Instability and the Mechanism of Flutter," NACA Rept. 496, 1935.

[25]Yates, E. C., Jr., "A Modified-Strip-Analysis Method for Predicting Wing Flutter at Subsonic to Hypersonic Speeds," N66-36094(NASA TM-X-54830, 1964).

[26]Abbott, I. H. and Von Doenhoff, A. E., Theory of Wing Sections, Dover Publications, New York, 1959.

A VISUAL STUDY OF A DELTA WING IN STEADY AND UNSTEADY MOTION*

Mohamed Gad-el-Hak
Chih-Ming Ho**
Ron F. Blackwelder**

Flow Research Company
Kent, Washington 98032

AD-P004 158

Abstract

Two delta wings with a leading edge sweep of 45° and 60° were studied in a towing tank at chord Reynolds number up to 3.5×10^5. The wings were pitched about the quarter chord point through typical angles of attack of $15° \pm 15°$, with a reduced frequency in the range of 0 to 3. In the steady state flow, dye visualizations revealed the existence of a shear layer near the leading edge that rolls up and forms discrete vortices parallel to the leading edge. These vortices were observed to pair at least once as they were convected downstream. Similar phenomena were observed in the unsteady case, except that the vortices shed from the leading edge were modulated and altered by the unsteady motion, which was an order of magnitude lower in frequency. In general, the unsteadiness delayed separation and promoted hysteresis similar to results obtained in unsteady two-dimensional airfoils.

Nomenclature

AR	aspect ratio
c	root chord
f	pitching frequency
K	reduced frequency, $\pi fc/U_\infty$
R_c	chord Reynolds number, $U_\infty c/\nu$
s	wing semispan
t	time (sec)
U_∞	towing speed
$\alpha(t)$	angle of attack
β	apex angle
γ	angle between vortex cores
λ	perturbation wavelength
ν	kinematic viscosity

1. Introduction

In a steady flow, a traditional two-dimensional airfoil experiences stall at large angle of attack. The separation on the upper surface reduces the leading edge suction peak and subsequently the lift decreases. The stall angle for most airfoils is around 12°. The aerodynamic characteristics of a delta wing are considerably different. The leading edge suction peaks predicted by potential theory do not exist (Jones and Cohen, 1960). Instead, two smooth suction peaks inbound of the leading edges are detected. The lift is mainly contributed by these two peaks which are produced as the flow separates on the leeward side of the wing and forms a pair of stationary leading edge vortices. Therefore, the lift on a delta wing is created by the separated vortical structures rather than by the attached flow near a convex surface. These vortices exist to angles of attack as large as 30° or more. The lift keeps increasing with α until the vortex breaks down. Hence, a delta wing is a good means to obtain high lift at large angle of attack.

By using air bubbles for visualization in a water channel, Elle (1958) showed that the separation vortices have very concentrated cores. Furthermore, the angle between the two cores, γ, is not a sensitive function of the angle of attack. The ratio between γ and the apex angle, β, is always between 0.6 and 0.7, but the vortex cores lift away from the wing surface with increasing α. Fink and Taylor (1967) investigated the pressure distribution on a wing with $\beta = 20°$. The suction peaks of the spanwise pressure distribution at several chordwise locations always occurred at about 60% of the semispan from the center for all tested angles of attack, $5° < \alpha < 30°$. In other words, the suction peaks were located under the vortex cores. A more detailed visualization (Fink, 1967) showed that there is a counter rotating vortex associated with each primary separation vortex. The existence of the counter rotating vortex could also be inferred from the total head survey.

Under many practical situations, e.g. fast manuevering of an aircraft, the flow is not steady. The unsteady aerodynamic properties are significantly different from those in steady flow. For a two-dimensional airfoil, the lift, drag and moments experience large hysteresis during the execution of one cycle (McAlister and Carr, 1978 & McCroskey, 1982). A large separation vortex develops near the leading edge and convects along the chord. High level surface pressure fluctuations are produced. On the unsteady delta wing the information about the time evolving vortices is very limited (Lambourne et al., 1969). This is one of the main reasons for this work.

2. Experimental Approach

2.1 Models and Test Conditions

Two delta wings with a leading edge sweep of 45° and 60° were used in the present investigation. The root chord of both wings was 25 cm, and the chord Reynolds number varied in the range of 2.5×10^4 to 3.5×10^5. Fig. 1 is a sketch of the 45° delta wing, which had a NACA 0012 profile at each spanwise section. The wing was made of two aluminum pieces with grooves on the inner surface of each for dye passage and storage. The 60° delta wing had a flat surface with a sharp leading edge.

---

*Supported under AFOSR Contract F49620-82-C-0020.

**Permanent Address: Dept. of Aerospace Engineering, University of Southern California, Los Angeles, California 90007.

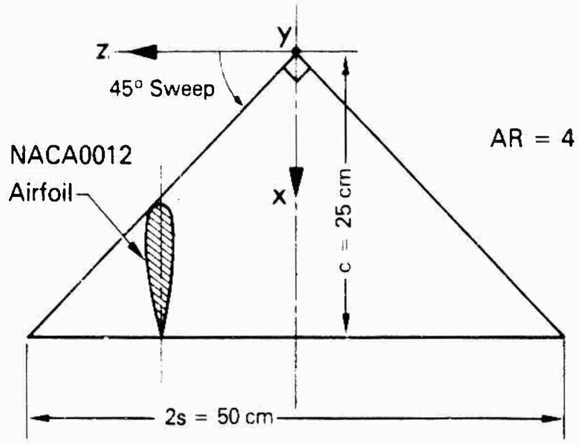

Fig. 1 Schematic of the 45° Delta Wing.

The four-bar mechanism shown in Fig. 2 was used to sting-mount and to pitch the delta wing around the desired position along the chord. In the experiments reported herein the wing was pitched around the 1/4 chord position. The mean angle of attack could be set from 0° to 45°. A Boston Ratiotrol motor derived the four-bar linkages to produce approximately sinusoidal oscillations of amplitude $\pm 5°$, $\pm 10°$ and $\pm 15°$ about a given mean angle of attack. The reduced frequency, $K \equiv \pi fc/U_\infty$, was varied in the range of 0 to 3, and a digital readout displayed the instantaneous angle of attack of the wing.

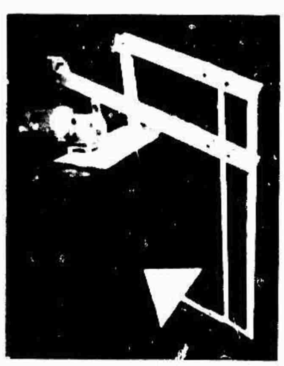

Fig. 2 Photograph of the Pitching Mechanism.

2.2 Towing Tank System

The wings used in the present investigation were towed at speeds in the range of 10 to 100 cm/sec through the water channel described by Gad-el-Hak et al. (1981). The towing tank is 18 m long, 1.2 m wide, and 0.9 m deep. The pitching mechanism was rigidly mounted on a carriage that rides on two tracks mounted on top of the towing system. During towing, the carriage was supported by an oil film which insured a vibrationless tow, having an equivalent free-stream turbulence of about 0.1 percent.

2.3 Flow Visualization

Food color and fluorescent dyes were used in the present investigation. The food color dyes were illuminated with conventional flood lights. The fluorescent dyes were excited with sheets of laser projected in the desired plane. To produce a sheet of light, a 5 watt argon laser (Spectra Physics, Model 164) was used with a mirror mounted on an optical scanner having a 720 Hz natural frequency (General Scanning, Inc.). A sine-wave signal generator, set at a frequency equal to the inverse of the camera shutter speed, derived the optical scanner to produce light sheets approximately 1 mm thick.

Side views of the flow field were obtained using a vertical sheet of laser in the x-y plane at z = 10 cm (40% of the root chord) and a stationary camera outside the tank as shown in Fig. 3. End views were obtained using a vertical sheet of laser in the y-z plane at x = 20 cm (80% of the root chord). The camera was stationary and by necessity outside the towing channel; thus the view was from a 45° oblique angle and the horizontal scale was contracted by about 30 percent.

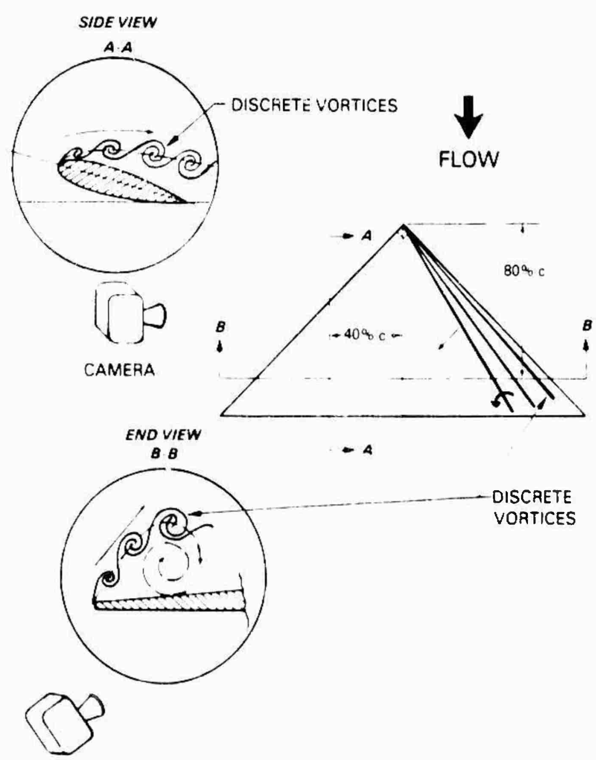

Fig. 3 Definition Sketch

Dye sheets or dye lines were seeped into the boundary layer through a system of slots and holes on the suction side of the wing. The slots were 0.2 mm wide and were milled at a 45° angle to minimize the flow disturbance. The holes were 0.4 mm diameter and were spaced at 1 cm center to center.

Dye was also placed in the flow field by laying several thin, horizontal sheets prior to towing the wing. The dye layers remained thin, about [illegible] mm in thickness, due to the inhibition of vertical motion caused by introducing a weak saline stratification in the tank. The dye layers remained quiescent until disturbed by the flow field on and around the wing. Thus, the boundary layer flow as well as the potential flow could be observed since the dye layers existed in both flow regions.

3. Experimental Results

3.1 Steady State Flow

Dye visualization techniques were used to observe the flow on a delta wing at fixed angle of attack in the range of 0° to 45°. The trailing edge separation could be seen even at zero angle of attack. As α increased above 5°, two stationary vortices occurred near the leading edge as found by other investigators. At the interface between these large primary vortices and the external potential flow, a thin shear layer was formed by the velocity difference between the free stream and the separated region. The shear layer was unstable and small secondary vortices were generated. In the present operating conditions about five small vortices rolled around the primary vortex/potential flow interface. At angles of attack above 10°, the separated region was sufficiently thick that the smaller secondary vortices were at least one diameter removed from the wing. Under these conditions, the secondary vortices merged in a pairing process as they were convected around the edge of the primary vortex, as shown in Fig. 4 . In this side view using a vertical sheet of laser, the 45° delta wing was at angle of attack $\alpha = 10°$, the chord Reynolds number was $R_c = 2.5 \times 10^4$, and the flow was from left to right. The pairing process appeared to be quite similar to the one observed in plane mixing layers (Winant and Browand, 1974). The physical mechanism for generating the small vortices in the delta wing case is believed to be the same as that in a free shear layer (Brown and Roshko, 1974). In the delta wing case, however, the flow field is more complicated because of the complex geometry and the non-planar velocity field.

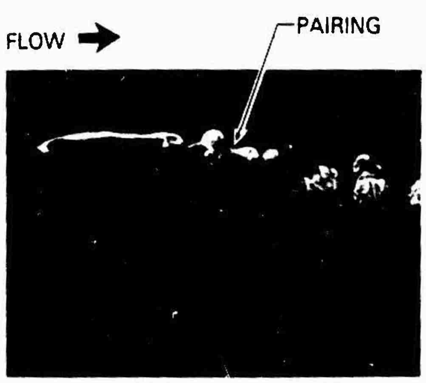

Fig. 4 Side View with Wing Fixed at $\alpha = 10°$.

The discrete vortices were also observed on the 60° sweep, sharp leading edge delta wing as shown in the top view in Fig. 5. Here, $\alpha = 10°$, $R_c = 2.5 \times 10^4$, and the flow is from top to bottom. Four discrete vortices could be distinguished along approximately straight lines emanating from the wing apex. The pairing process was observed on cine films of this run.

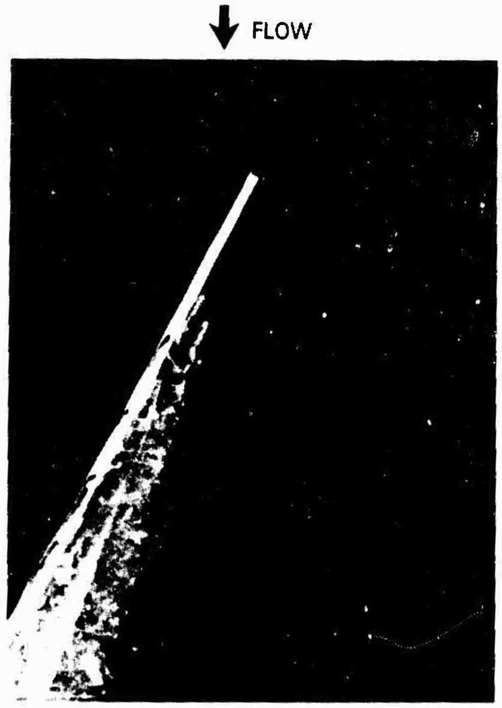

Fig. 5. Top View with the 60° Delta Wing Fixed at $\alpha = 10°$.

At smaller angles of attack, the vortex merging seemed to be inhibited by the presence of the wing surface. At larger attack angles, intense mixing made it more difficult to observe the pairing process. It is not clear from the present experiments whether the primary vortex only caused the secondary vortices by setting up the initial shear layer, or if it was possibly the result of several mergings of the secondary vortices.

Similar vortex formation and pairing were observed in the pitching case. However, the process was modulated by the lower frequency oscillation of the wing as shown in the next section.

3.2 Unsteady Flow

The flow visualization results of the 45° sweep delta wing undergoing a sinusoidal pitching motion are presented in here and in Flow Research Film No. 55 (available on request). On the suction side of the pitching delta wing, the leading edge separation vortices executed a grow-decay cycle during one period. Fig. 6 is a side view of the 45° wing undergoing the pitching motion $\alpha(t)° = 15 + 5 \sin(0.4t)$, at chord Reynolds number $R_c = 2.5 \times 10^4$ and reduced frequency $K = 0.5$. Both the upward and downward motions are shown side by side for the angles of attack of 10°, 12°, 14°, 16°, 18° and 20°. At a particular attack angle, the flow patterns were very different during the upward and downward motions. The hysteresis loop clearly existed. The discrete vortices formation and pairing is more readily observed in the upward part of the pitching cycle, and is modulated by the lower frequency oscillation (f = [illegible] Hz).

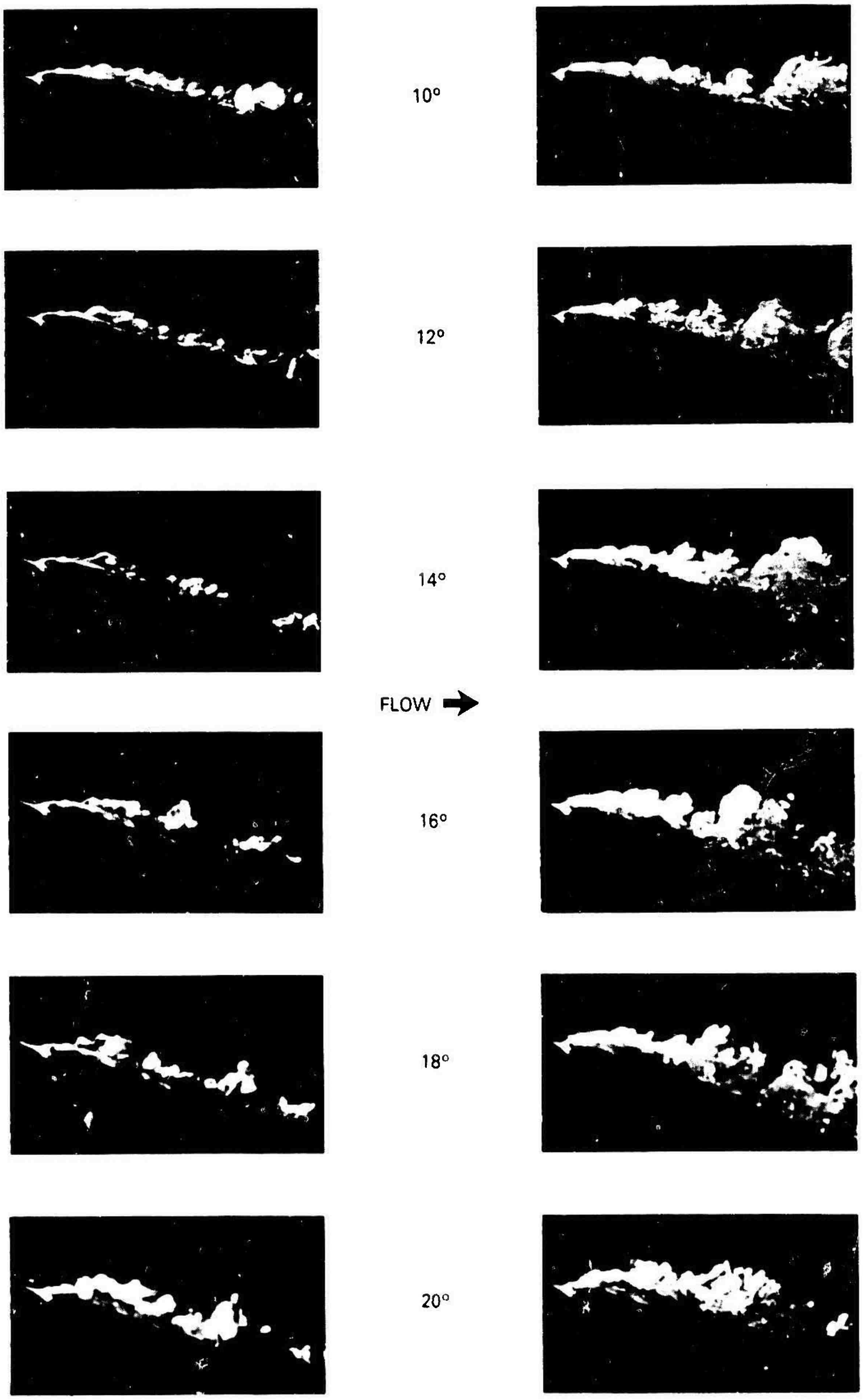

α Increasing

α Decreasing

Fig. 6 Side View of the Pitching Delta Wing

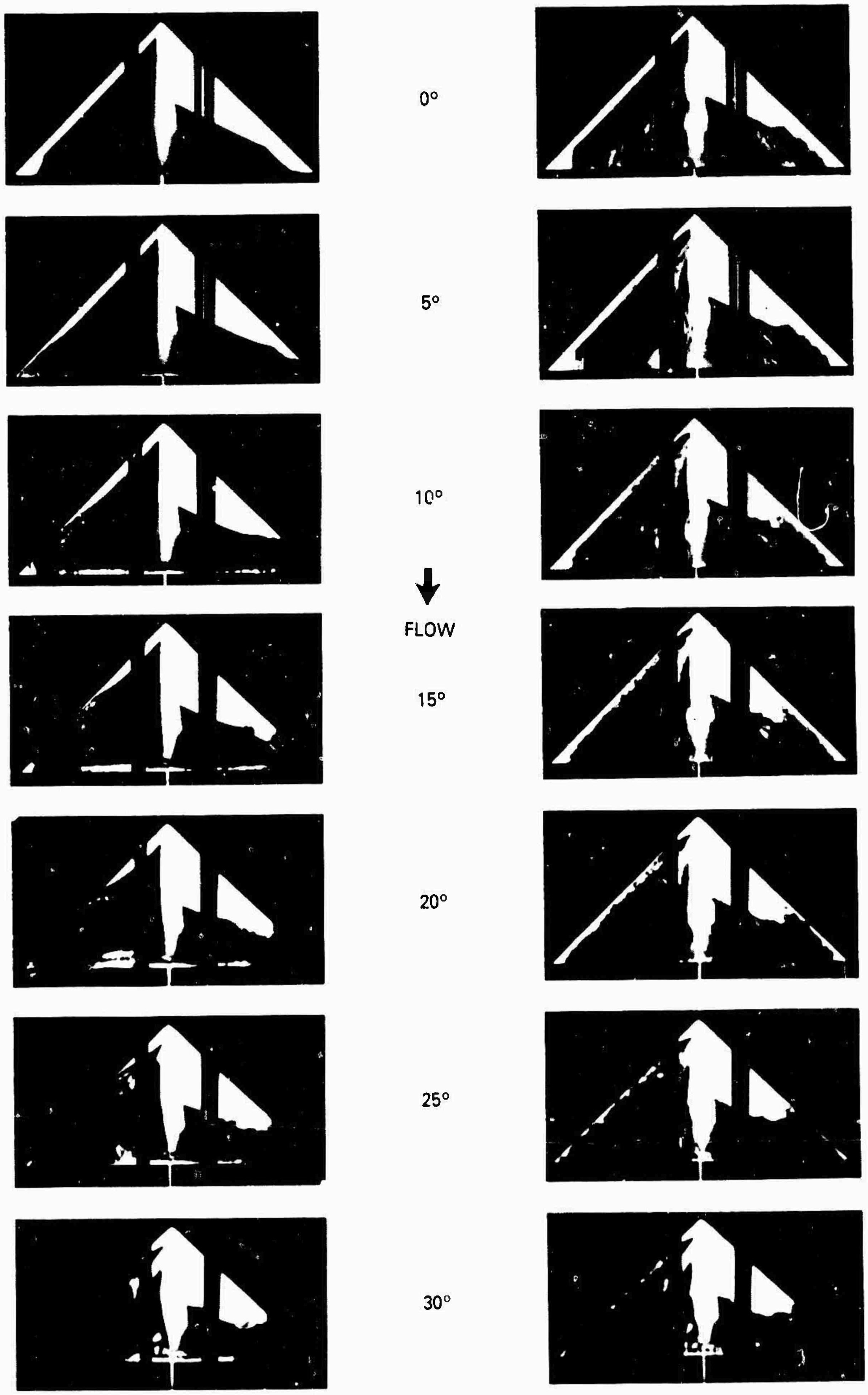

α Increasing

α Decreasing

Fig. 7 Top View of the Pitching Delta Wing.

Fig. 7 shows top view of the wing undergoing the pitching motion $\alpha(t)^\circ = 15 + 15 \sin(0.8t)$, at chord Reynolds number $R_c = 2.5\times10^4$ and reduced frequency $K = 1.0$. Both the upward and downward motions are shown side by side for the attack angles $\alpha = 0°, 5°, 10°, 15°, 20°, 25°$ and $30°$. The three dye slots on the left side of the wing are closer to the leading edge as compared to the ones on the right side. During the up stroke, the separation first started across the whole trailing edge at $\alpha = 2°$. As the angle of attack increased, the separation propagated upstream from the two corners at the trailing edge toward the apex. The propagation speed along the leading edge was approximately equal to the flow speed (10 cm/sec). At $\alpha = 30°$, the separation front reached the apex and the separation vortices were fully developed. During the down stroke, the vortices became smaller and diminished in size at about $\alpha = 10°$, but the flow was still separated near the trailing edge.

Fig. 8 shows an end view of the pitching wing obtained using a vertical sheet of light in the y-z plane at x = 0.8 c. The view is from a 45° oblique angle and the flow is out from the plane of the photograph. In this run the wing underwent the pitching motion $\alpha(t)^\circ = 15 + 10 \sin(0.2t)$, at chord Reynolds number $R_c = 2.5\times10^4$ and reduced frequency $K = 0.25$. The up stroke at the angles of attack $\alpha = 5°, 10°, 15°$ and $20°$ is shown in the figure. The dye was released only from the slots on the left side of the wing. Hence, only one of the leading edge separation vortices is marked. The vortex grows as the angle of attack is increased. In the cine film from which the frames shown in Fig. 8 were obtained, several discrete vortices rolled around the primary vortex and merged in a pairing process as mentioned above.

The dye layers technique was used to visualize the boundary layer flow as well as the potential flow around the wing. The horizontal dye layers were excited with vertical sheets of laser in the x-y and y-z planes. When the wing passed through the quiescent dye layers, the local motion of the fluid could be inferred from the deformation of the layers. In the end views, the dye layers near the center portion of the span moved downward during the up stroke as the separation vortex grew, indicating a strong downwash in that region. During the down stroke a second blob of dye appeared next to the separation vortex and nearer to the center portion of the span. As the angle of attack decreasd, the separation vortex diminished while the second blob of dye grew in size. The nature of this motion is not clear at present, but it could be a separation bubble near the trailing edge similar to the one observed by Winkelmann and Barlow (1980) on a small aspect ratio rectangular wing at constant angle of attack.

[illegible] Effects of the Reduced Frequency

Lower reduced frequencies were also tried in order to check the effect of the pitching frequency on the hysteresis loop. The lowest non-zero reduced frequency achieved in the present study was K = [illegible], and hysteresis could still be detected. Apparently, the "quasi-steady" state is only achieved at even smaller reduced frequency.

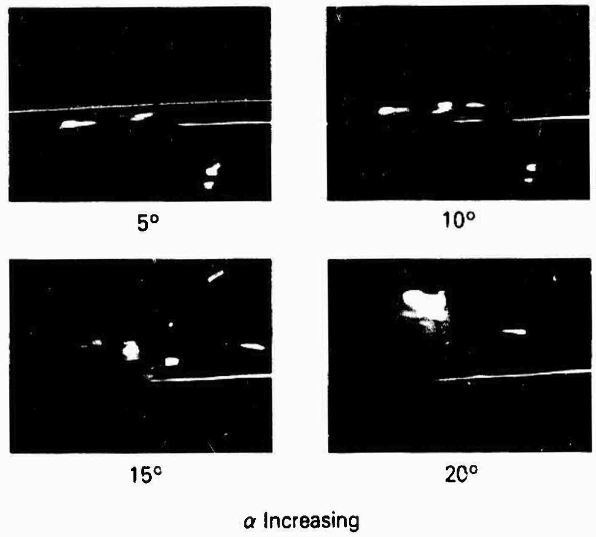

Fig. 8 End View of the Pitching Delta Wing.

In general, the unsteadiness delayed separation and promoted hysteresis similar to results obtained in unsteady two-dimensional airfoils. As the attack angle decreased from its maximum value at least one and often two large separated regions appeared on the wing as a result of the unsteadiness. As the oscillation frequency increased, the formation of the separated region appeared further downstream. At K = 1, the streamlines remained parallel to the wing surface until high attack angles. Significant changes occurred when the reduced frequency was above 3. No large scale separation was then observed on the wing; however, a strong vortex was shed at the trailing edge as α passed through its maximum value. Fig. 9 is a side view of the pitching wing using the dye layers technique. The wing underwent the pitching motion $\alpha(t)^\circ = 15 + 15 \sin(2.6t)$, at chord Reynolds number $R_c = 2.5\times10^4$ and reduced frequency $K = 3.3$. The photograph shows the wing at angle of attack $\alpha = 25°$ during the up stroke. The dye layers in the outer flow regions indicates that the potential flow is following the motion of the wing, and that the separation region is restricted to be very close to the wing surface.

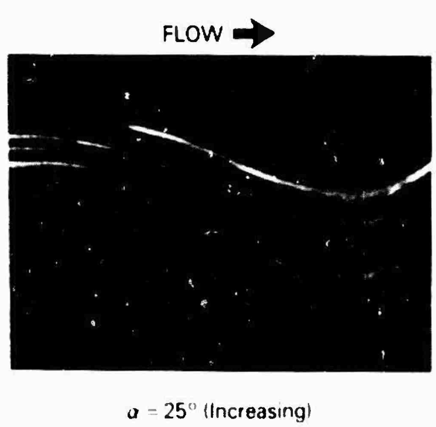

Fig. 9 Side View at High Reduced Frequency

Fig. 10 is an end view at the same run conditions depicted in Fig. 9, but at an attack angle $\alpha = 20°$ during the down stroke. Both the separation vortex and the second blob of dye mentioned in the previous section appear in the photograph.

$\alpha = 20°$ (decreasing)

Fig. 10 End View at High Reduced Frequency.

A tentative explanation for the distinct change at $K \geq 3$ is as follows. The reduced frequency can be viewed as the ratio of the chord to a "perturbation" wavelength: $K = \pi fc/U_\infty = \pi c/\lambda$. In other words, the perturbation wavelength is about equal to the chord length at $K = 3$. As a matter of fact, the reattachment point can be seen near the trailing edge in Fig. 9. After the flow is reattached, a thin shear layer with intense vortices formed and a strong vortex counter rotating with respect to the attached wing circulation was shed from the trailing edge. The induced velocity of this vortex kept the potential flow moving downward with the wing. If the perturbation wavelength was longer than the chord, i.e. $K < \pi$, the wake remained thick. The diffused vortex could not enforce a thin separation region on the wing. Based on these arguments, it appears that a parameter based on the chord length and the perturbation wavelength is more appropriate to describe the flow than the conventional reduced frequency.

4. Conclusions

Two delta wings with a leading edge sweep of 45° and 60° were studied in a towing tank at chord Reynolds number up to 3.5×10^5. The wings were pitched about the quarter chord point with sinusoidal oscillations of amplitude $\pm 5°$, $\pm 10°$ and $\pm 15°$ about a given mean attack angle that varied in the range 0° to 45°. Food color and fluorescent dyes were used to visualize the flow field on and around the wings. Sheets of laser excited the fluorescent dye to yield detailed flow information in the desired plane.

The steady state flow field was studied at angles of attack of 0° to 45°. Separation was observed near the trailing edge on the centerline at small attack angles. As α increased above 5°, leading edge separation occurred forming two large scale stationay vortices approximately parallel to the leading edge as found by previous investigators. In addition, the dyed shear layer near the leading edge was observed to roll up and form discrete vortices along approximately straight lines emanating from the wing apex, similar to the ones commonly observed in free shear layers. These vortices rolled around the primary vortex potential flow interface, and merged in a pairing process much the same as observed in plane mixing layers.

Similar phenomena were observed in the unsteady case, except that the vortices shed from the leading edge were modulated and altered by the unsteady motion which had an order of magnitude lower frequency. The leading edge separation vortices executed a grow-decay cycle during one pitching period. As the angle of attack increased, the first observable separation was along the trailing edge of the wing. As α increased further, the separated region increased by moving from the wing tips along the leading edge toward the apex. At large angle of attack, the potential flow field had a downward component near the center of the span indicating strong downwash in this region. As α decreased from its maximum value, at least one and often two large separated regions appeared on the wing as a result of the unsteadiness. In general, the unsteadiness delayed separation and promoted hysteresis similar to results obtained on unsteady two-dimensional airfoils. As the oscillation frequency increased, the formation of the separated region appeared further downstream. At a reduced frequency $K = 1$, the streamlines remained parallel to the wing surface until high attack angles. At $K = 3$, no large scale separation was observed on the wing; however, a strong vortex was shed at the trailing edge as α passed through its maximum value.

References

Brown, G. L., and Roshko A., "On Density Effects and Large Structure in Turbulent Mixing Layers," J. Fluid Mech. 64, p. 775, 1974.

Elle, B. J., "An Investigation at Low Speed of the Flow Near the Apex of Thin Delta Wings with Sharp Leading Edges," ARC Tech. Rep. R&M No. 3176, 1958.

Fink, P. T., "Some Early Experiments on Vortex Separation. Part III: Further Experiments with 20 Degree Delta Wings," ARC Tech. Rep. R&M No. 3489, 1967.

Fink, P. T., and Taylor J., "Some Early Experiments on Vortex Separation. Part II: Some Low Speed Experiments with 20 Degree Delta Wings," ARC Tech. Rep. R&M No. 3489, 1967.

Gad-el-Hak, M., Blackwelder, R. F., and Riley, J. J., "On the Growth of Turbulent Regions in Laminar Boundary Layers," J. Fluid Mech. 110, p. 73, 1981.

Jones, R. T., and Cohen D., High Speed Wing Theory, Princeton Univ. Press, 1960.

Lambourne, N. C., Bryer, D. W., and Maybrey, J. F. M., "The Behavior of the Leading-Edge Vortices Over a Delta Wing Following a Sudden Change of Incidence," ARC Tech. Rep. R&M No. 3645, 1969.

McAlister, K. W., and Carr, L. W., "Water Tunnel Visualization of Dyanmic Stall," in Nonsteady Fluid Dyanmics, ed. D. E. Crow and J. A. Miller, ASME, p. 103, 1978.

McCroskey, W. J., "Unsteady Airfoils," Ann. Rev. Fluid Mech. 14, p. 285, 1982.

Winant, C. D., and Browand, F. K., "Vortex Pairing, the Mechanism of Turbulent Mixing Layer Growth at Moderate Reynolds Number," J. Fluid Mech. 63, p. 237, 1974.

Winkelmann, A. E., and Barlow, J. B., "Flowfield Model for a Rectangular Planform Wing beyond Stall," AIAA J. 18, p. 1006, 1980.

COMPARATIVE VISUALIZATION OF ACCELERATING FLOW AROUND VARIOUS BODIES, STARTING FROM REST

Peter Freymuth, Mark Palmer and Wolfgang Bank
Department of Aerospace Engineering Sciences
University of Colorado
Boulder, Colorado 80309

AD-P004 159

Abstract

Separation, vortex formation and turbulent decay are visualized for accelerating air flow around various bodies, starting from rest. The bodies investigated were a cylinder, a sphere, a flat plate, a round plate and an NACA 0015 airfoil. All bodies had the same characteristic length (body diameter or chord length) and were subjected to the same flow acceleration resulting in the same Reynolds number and allowing for a meaningful comparison.

Nomenclature

- c — characteristic length (body diameter, chord length)
- a — flow acceleration 2.44 m/sec^2
- ν — kinematic viscosity of the air flow 0.18 cm^2/sec
- R — Reynolds number $a^{1/2}\ c^{3/2}\ \nu^{-1} = 5200$
- α — angle of attack of airfoil or flat plate
- t — time
- t_c — characteristic time scale $c^{1/2}\ a^{-1/2} = 0.25$ sec
- t_i — time between acceleration startup (from rest) and the first movie frame shown in a figure
- Δt — time between shown consecutive movie frames in a figure

Introduction

Visualization of starting flow around plates, cylinders and airfoils goes back to Prandtl (1905, 1927). Starting flow around a sphere was visualized by Honji (1972). More recent visualizations of unsteady flows have been reviewed by Taneda (1977) and most recent visualizations are due to Bouard and Coutanceau (1980) and Izumi (1983). A comparison of starting flow around even a limited number of different bodies is however hardly possible on the basis of past work. There are too widely differing techniques of visualization and photography, differences in flow configuration (water flow, airflow, accelerating and impulsive flow, different body dimensions, Reynolds numbers, time visualized etc.).

We compared some bodies under similar conditions in order to obtain insight into the similarities and differences of various unsteady flow. All bodies had similar dimensions (same diameter or chord length) and were subjected to the same acceleration of airflow. The same flow visualization and photographic techniques were used in all cases.

Experimental Setup

A large, low turbulence, open return wind tunnel was converted to unsteady operation as described by Freymuth, Palmer and Bank (1983). The tunnel started from rest, then maintained a nearly constant acceleration of 2.44 m/sec^2 (25% of gravity) for 5 seconds prior to power shutoff. The tunnel had a test section 0.9 m X 0.9 m across and was 20 m long with Plexiglas front and top walls allowing for photography.

We investigated a cylinder, a sphere, a flat plate, a round plate and an NACA 0015 airfoil. These bodies had the same diameter or chordlength c = 15.2 cm; the Reynolds number was R = 5200.

A strip of liquid titanium tetrachloride ($TiCl_4$) was painted in flow direction on the body surface, releasing dense white fumes. The method is described in detail by Freymuth, Bank and Palmer (1983). Since smoke is released in the regions of vorticity production we assume that smoke patterns reveal vorticity patterns near the body and in the near wake behind the body, where differences in vorticity diffusion and smoke diffusion do not represent a problem. A problem may exist for low Reynolds number flow, far downstream, and when vortices of opposite sign are adjacent to each other (smoke density does not have a distinction in sign).

Smoke patterns were recorded for 3 sec with a 16 mm Bolex movie camera at 64 frames per sec and with a shutter speed of 1/500 sec. Because of space limitations, only a restricted number of frames of an acceleration sequence can be shown in the Figures (additional frames can be obtained upon request from the authors). In the figure captions we denote the time between frames shown as Δt and the time from acceleration start to the first frame shown as t_i.

Interpretation of these pictures can be accomplished by the reader in any desired detail. At the outset we will present some of our interpretations along with the photographs in the next section.

Comparative Flow Visualization

In the figures of this section flow is always from left to right.

Figure 1 compares accelerated flow around a cylinder (left column) and around a sphere (right column), starting with the vorticity separation tongue from which the main vortex forms. Flow is initially quite similar for both cases. A separation tongue forms and develops into a main vortex (first observed by Prandtl in 1905 behind a cylinder in a starting flow) which induces a counterrotating secondary vortex locked in between the main vortex and another weak vortex structure (first observed by Prandtl in 1927 behind an impulsively started cylinder). Subsequently there is a weak tendency of the main vortex to decay into smaller ones prior to turbulent decay. For the sphere the secondary vortex is visible as a vortex ring on the sphere surface.

Upon close examination quantitative differences exist between the two cases. Separation for the sphere occurs later (larger t_1) than for the cylinder but transition to turbulence proceeds faster, resulting in a smaller primary vortex. In the late stages of turbulent decay a turbulent vortex street develops behind the cylinder (first observed by Prandtl 1905) whereas the sphere wake remains rather symmetric and diffuse.

Figure 2 compares accelerated flow around a flat plate (left column), a round plate (middle column) and an NACA 0015 airfoil (right column), all placed perpendicular to the flow. For the round plate only the lower edge is visualized. While vortex development is qualitatively similar for the 3 cases the contrast to Figure 1 is considerable. The separation tongue which previously developed into the main vortex now starts formation of a vortex group consisting of up to ca. 30 small vortices, some of them in a stage of pairing. The 2 vortex groups behind the top and bottom edges of the body then interact while they become turbulent. Secondary flow is not established in these cases except near the round upper edge of the airfoil. Decay into turbulence is slower than in Figure 1 and is slowest for the round airfoil edge.

Figure 3 compares the symmetric NACA 0015 airfoil (left column) with the same airfoil in reverse (sharp leading edge, round trailing edge) and with the flat plate (right column), all at an angle of attack of $\alpha = 20^{\circ}$. In all 3 cases vortex development is similar near the leading edge. As in case of the cylinder (Fig. 1) a triple structure forms consisting of the primary vortex, a secondary counterrotating vortex and a third vortex, which forms a beautiful pattern (second frame, left column). Also a second counterrotating vortex is in evidence near the apex (third frame, left column) along with some faint indication of a small tertiary vortex behind the secondary vortex. The formation of even more elaborate patterns is prevented by turbulent decay with the primary vortex rolling as a turbulent large scale structure over the airfoil. For the reversed airfoil and for the flat plate the separation tongue is nearer the trailing edge than for the regular airfoil and development to turbulence for the former cases is more slowly. For the airfoil, an additional immature vortex seems to form closer to the trailing edge which is swept into the wake. The airfoil surface is shiny and therefore one sees an optical mirror image of the vortex structure in the airfoil in addition to the vortex structure itself. It should be mentioned that we only visualize the upper airfoil surface and flat plate surface because flow along the bottom surface remains attached.

Differences in vortex development are most apparent in Figure 4 where the airfoil, the reversed airfoil and the flat plate are compared to each other at an angle of attack [illegible]. While for the airfoil (left column) separation [illegible]

and vortex development creeps up from the rear of the airfoil, the sharp edged reverse airfoil and flat plate retain vortex formation close to the leading edge, with vortices following each other in rapid succession. These vortices get quickly turbulent, especially for the flat plate.

For the flat plate, the movie was taken at a wider angle of view to show some of the wake downstream of the trailing edge. Details of the wake for the airfoil are reported by Freymuth, Palmer and Bank (1983), showing an unstable shear layer and a subsequent vortex street.

Conclusions

We have compared accelerating flow around a limited number of bodies under similar experimental conditions. Obviously a more general investigation is possible by considering additional body shapes and by changing some experimental conditions simultaneously for all bodies, in particular the Reynolds number.

References

Bouard, R., and Coutanceau, M. 1980. The early stages of development of the wake behind an impulsively started cylinder for $40 < Re < 10^4$ J. Fluid Mech. 101, 583-607.

Freymuth, P., Bank, W. and Palmer, M. 1983. Use of titanium tetrachloride for visualization of accelerating flow around airfoils. Third International Symposium on Flow Visualization. Sept. 6-9, Ann Arbor, Mich. Proceedings.

Freymuth, P., Palmer, M. and Bank W. 1983. Visualization of accelerating flow around an airfoil at angles of attack 0° to 30°. 8th Biannual Symposium on Turbulence, Sept. 26-28, Rolla, Mo. Proceedings.

Honji, H. 1972. Starting flows past spheres and elliptic cylinders. Rep. Res. Inst. Appl. Mech. 19, 271-281.

Izumi, K. Unsteady flow field, lift and drag measurements of impulsively started elliptic cylinders and circular-arc airfoil. 1983. AIAA 16th Fluid and Plasma Dynamics Conference. July 12-14, Danvers, Ma. Paper AIAA- 83-1711.

Prandtl, L. 1905. Über Flüssigkeiten bei sehr kleiner Reibung. Verhandlungen des III. Internationalen Mathematiker-Kongresses, Heidelberg, 1904, Teubner Verlag, Leipzig, 484-491.

Prandtl, L. 1927. The generation of vortices in fluids of small viscosity. Royal Aeronautical Society 31, [illegible].

Taneda, S. 1977. Visual study of unsteady separated flows around bodies. Prog. Aerospace Sci. 17, 287-348.

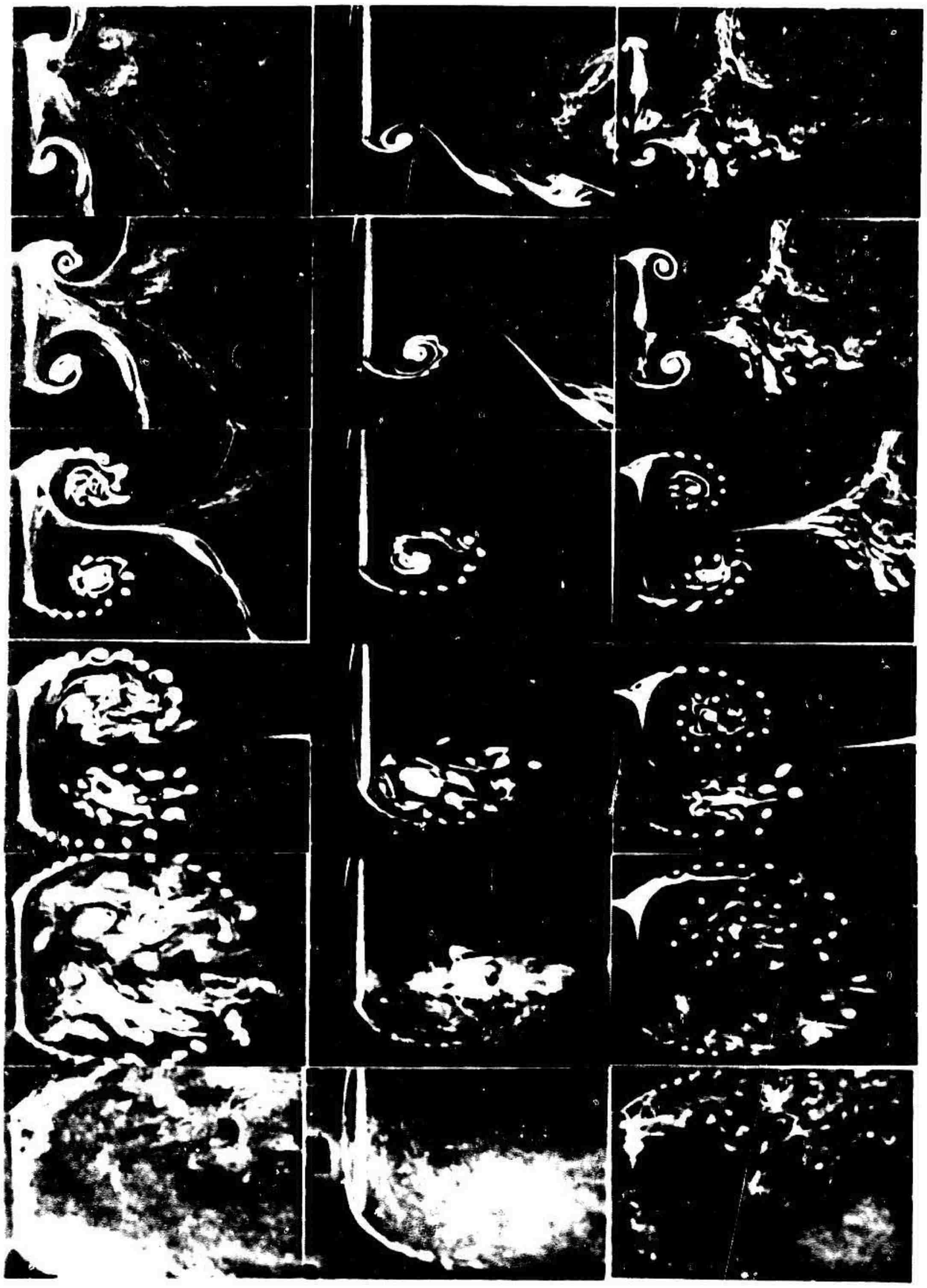

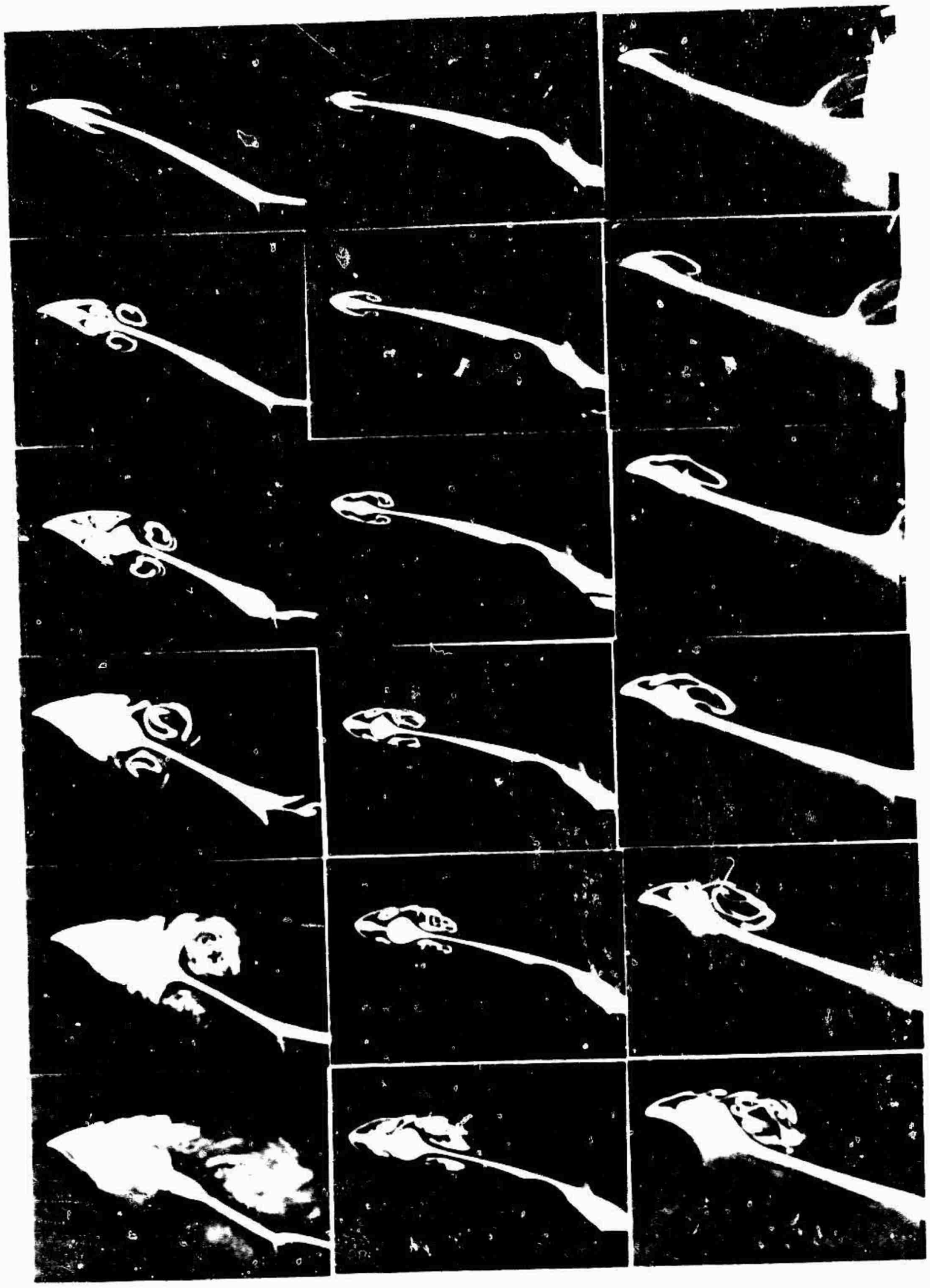

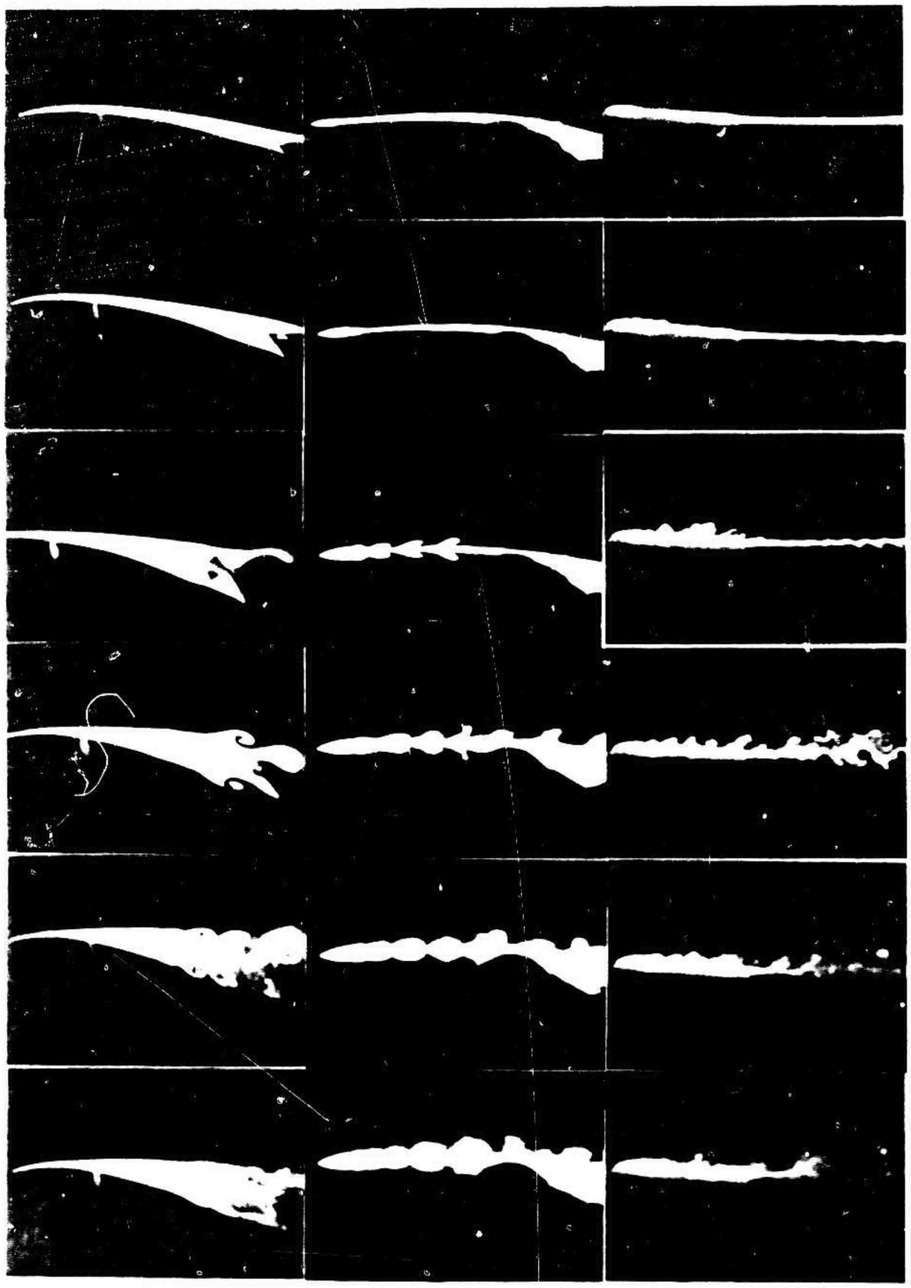

AD-P004 160

PREDICTION OF DYNAMIC STALL CHARACTERISTICS USING ADVANCED NONLINEAR PANEL METHODS+

B. Maskew* and F.A. Dvorak**
Analytical Methods, Inc.
Redmond, Washington

Abstract

This paper presents preliminary results from a program of work in which a surface singularity panel method is being extended for modelling the dynamic interaction between a separated wake and a surface undergoing an unsteady motion. The method combines the capabilities of an unsteady time-stepping code and a technique for modelling extensive separation using free vortex sheets. Routines are being developed for treating the dynamic interaction between the separated wake and the solid boundary in an environment where the separation point is moving with time. The behavior of these routines is being examined in a parallel effort using a two-dimensional pilot version of the three-dimensional code. This allows refinements in the procedures to be quickly developed and tested prior to installation into the main code.

The extended code is being coupled with an unsteady integral boundary layer method to examine the prediction of dynamic stall characteristics. The boundary layer code is accessed during the time-step cycle and provides the separation locations as well as the boundary layer displacement effect--the latter is modelled in the potential flow code using the source transpiration technique.

The preliminary results presented here include basic unsteady test cases for both the potential flow and boundary layer routines. Some exploratory separated flow calculations are included from a series of numerical studies on the stability of the calculation procedure. Correlations with experimental dynamic stall results have yet to be performed.

Introduction

Flow separation on the lifting surfaces of a vehicle at high angle of attack is always complicated by a certain degree of unsteadiness, but, when the vehicle itself is undergoing unsteady motion or deformation, or if it enters a different flow field rapidly, then the complexity of the separated flow is even greater, and culminates in the phenomenon of dynamic stall. If the angle of attack oscillates around the static stall angle, the fluid dynamic forces and moments usually exhibit large amounts of hysteresis and a condition of negative aerodynamic damping often develops during part of the cycle. This can lead to the condition of flutter in a single degree of freedom oscillation rigid body motion. (Normally, in attached flow, flutter only occurs when the body motion includes multiple degrees of freedom, e.g., combined bending and torsion of an aircraft wing.) During a rapid increase in angle of attack, the static stall angle can be greatly exceeded, resulting in excursions in the dynamic force and moment values that are far greater than their static counterparts. The consequences of dynamic stall are far-reaching and lead to such problems as wing drop, yaw (sometimes leading to spin entry), wing rocking and buffeting as well as stall flutter.

Although a great deal has been learned about dynamic stall characteristics--mainly through experimental observation--there is not at this time a completely satisfactory theoretical method (1), (2) for predicting the dynamic stall characteristics for new untested shapes even for the two-dimensional case. Moreover, quantitative comparisons of experimental test data on new geometries can be obscured by the effects of three-dimensional wind-tunnel interactions, wall interference and experimental uncertainties (3). In the present work a possible theoretical approach is examined for predicting dynamic stall characteristics. The approach combines an unsteady time-stepping method (4) with a steady inviscid/viscid iterative code (5) that includes an extensive separation model. The latter has proven very successful in the steady case. Both codes are applicable to general three-dimensional shapes and have been developed from the same basic panel method (6).

Extensive investigations of the dynamic stall characteristics of airfoils oscillating in pitch have been reviewed by McCroskey (1), (2). In practical aerodynamic environments, the unsteadyness can be a combination of several motions. Unsteady motions other than pitching have been investigated by, among others, Liiva et al. (7), Lang (8), Lang and Francis (9), Maresca et al. (10), and Saxena et al. (11). In these references the phenomena of plunging, flap, spoiler and rectilinear oscillations were examined. There are very few theoretical approaches, however, and in a recent review, McCroskey (2) concludes that at the present time the engineer who needs answers should turn to one of the empirical correlation techniques, even though these are not completely satisfactory and only supply broad details of force and moment characteristics. The method of Ericson and Reding is perhaps one of the most comprehensive of these methods. Their latest paper (12) incorporates a number of findings from the systematic experiments of Carr et al. (13).

Early theoretical approaches to dynamic stall addressed the deep stall aspect which is dominates by the passage of vortices shed from the vicinity of the leading edge. Ham (14) used just a thin plane model of the airfoil. Later work by Baudu et al. (15) extended the basic model to thick sections using a panel method. The main drawback with the approach is that crucial assumptions regarding the location and time of vortex shedding have to be made in order to perform the calculations. Also, the results (from (15)) are sensitive to (a) the angle at which the vortex path leaves the surface, (b) the

---

+ Paper presented at the AFOSR/FJSRL Workshop on Unsteady Separated Flows, USAF Academy, Colorado Springs, CO, August 10-11, 1983.

* Vice President Applications

** President

time at which vortex emissions terminate so as to start the reattachment process and (c) the viscous diffusion of the free vortices.

Calculations of the characteristics of the thin boundary layer in the attached flow regions of an oscillating airfoil using unsteady methods (16), (17), have demonstrated good qualitative agreement with experimental observations. However, one feature at least needs further examination in regard to improved modelling: it is reported (18), (19), that when incidence is increasing beyond the static stall angle, the location of zero skin friction in the turbulent boundary layer and the catastrophic separation can occur at different stations, Figure 1. Apparently, a long thin tongue of reversed flow precedes the main separation zone. This is not observed under quasi-steady conditions.

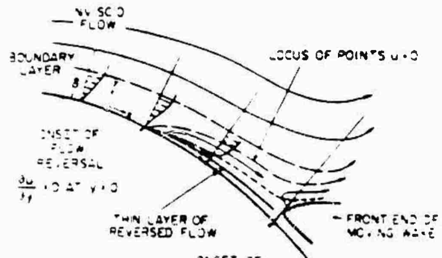

Fig. 1. Model of Sears and Telionis (19) for Upstream-Moving Separation of an Unsteady Boundary Layer.

Crimi and Reeves (20) combined a potential flow method with an unsteady boundary layer analysis in a viscous/inviscid interaction approach. The potential flow model was based on chordline singularities and so excluded modelling of the thick wake. Also, detail of the stagnation point location in relation to the curved leading edge was missing. Emphasis was placed on the details of leading-edge bubble bursting and application to trailing-edge separation was not attempted. Shamroth and Kreskovsky (21) developed a similar technique but with improved treatment of the separated flow region, transition phenomena and potenital flow region. However, the procedure failed to predict the flow field about the stalled airfoil. They concluded that the effect on the outer inviscid solution due to the finite wake displacement must be modelled.

In spite of the shortcomings of the above approaches, the general technique of matching various viscous and inviscid regions remains an attractive alternative to the full Navier-Stokes treatment. Although, in principle, the latter can overcome limitations of the potential flow/boundary layer iterative approach, such treatment is limited at this time to laminar flows at Reynolds numbers much lower than realistic for most practical applications (2). Progress twoards higher Reynolds numbers is being made, but applications to general problems is still a long way away (22).

The present method goes beyond the capabilities of the earlier theoretical approaches in that both trailing-edge and leading-edge stall with vortex passage can be included in principle. The method, developed for the three-dimensional case, is applicable to arbitrary configurations and to general motions; i.e., not just pitch oscillation. In addition, because the basis of the method is a surface singularity panel code, a more reliable and direct coupling between the inviscid and viscous analysis is assured. Moreover, modelling of the separated zone in the trailing-edge region and more detailed treatment of the vortex/surface interaction should make the approach more viable for applications to dynamic separation problems.

Potential Flow Methods

General

Although remarkable advances are being made in flow field calculations using finite-difference and also finite-element methods, the surface integral approach using panel methods coupled with special routines for nonlinear effects still offers distinct advantages for many real flow problems. In particular, panel methods offer greater versatility for practical application to complicated configurations and are considerably more efficient in terms of computing effort. However, the concept of zonal modelling--in which a local Navier-Stokes analysis is coupled with a panel method--should not be overlooked. Ultimately, such a coupling should lead to an improved modelling of vortices (e.g., vortex cores, vortex dissipation and breakdown), thick viscous regions, local separation bubbles, and shock wave/boundary interactions.

Over the past decade, panel methods have seen a trend towards higher-order formulations (23), (25) and (26) At the outset it was argued that compared with the earlier low-order methods the more continuous representation of the surface singularity distribution should allow a reduction in panel density for a given solution accuracy and, hence, should lead to lower computing costs. No such benefits have appeared so far for the general three-dimensional case. In fact, preliminary investigations (27) have indicated that the prediction accuracy for problems with complicated interactions, such as vortex/surface or high curvature situations, depends more on the density of control points where the boundary conditions are enforced; the order of the singularity distribution plays a minor role. In the meantime, further developments of piecewise constant singularity panel methods, e.g., Morino (28) and AMI's Program VSAERO (6), are giving comparable accuracy to the higher-order methods at much lower computing costs.

The low computing cost of Program VSAERO makes it practical to apply the method to nonlinear problems requiring iterative solutions, e.g., wake relaxation for high-lift configurations, multiple-component problems and rotor cases; and viscous/inviscid calculations with coupled boundary layer analyses, including the case with extensive separation (5), and also time-stepping calculations for three-dimensional unsteady problems (4) that are beyond the scope of a harmonic analysis. This method, therefore, offers an attractive basis for a practical tool aimed at predicting the aerodynamic characteristics of dynamic stall problems. At the outset, this code was being developed in two different directions; viz, one was for extensive separation modelling under "steady" conditions, while the other was for unsteady time-stepping calculations. These two capabilities, described in the section below, have now been brought together in one code.

Separated Flow Model

Under essentially steady conditions, the pressure distribution in a trailing-edge separation region is usually characterized by a constant pressure region extending back to the trailing edge followed by a short recompression region (e.g., (29)). A simplification of this characteristic is modelled in the two-dimensional CLMAX program (30), (31) using a pair of constant strength vortex sheets to enclose the separated region, Figure 2. The length of the sheets required a semi-empirical approach and the condition that the sheets be force-free is satisfied in an interative cycle in which segments of the sheet are aligned with calculated local flow directions. The method combines boundary layer and potential flow codes in an outer inviscid/viscid iteration cycle. The potential flow pressure distribution--which includes the influence of the free vortex sheets--is passed to the boundary layer routine which then supplies the separation points and the boundary layer displacement thickness distribution for the next iteration. The boundary layer displacement effect in the attached flow region is modelled by transpiration (i.e., source distribution) rather than by a displacement surface. The main advantage of the transpiration approach is that the matrix of influence coefficients in the panel method remains essentially the same from one iteration to the next; only the wake condition changes.

The thin vortex sheet model of the upper separated shear layer was demonstrated by Young and Hoad (32) to be a reasonable representation of the flow as far back as the trailing edge. For example, a comparison from (32) of a laser-velocimeter flow survey, and a CLMAX program calculation is shown here in Figure 3. Downstream of the trailing edge the vortex sheet model becomes less representative of the flow; however, a later evaluation of a graded vorticity model over the recompression zone showed little effect on the airfoil solution. More detailed modelling of the recompression zone (such as, for example, the approaches used by Gross (33) or Zumwalt (34) would be desirable in cases where the wake interacts closely with a downstream component.

A particular feature of the vortex sheet model enclosing the region of low energy is that pressures can be calculated directly in the separated zone (30). This is an additional advantage over the displacement surface approach of Henderson (35) and over the source outflow model of Jacob (36). The CLMAX method generally gives very close agreement with experimental pressure distributions (30), (31). An initial extension of this method to the unsteady case is reported in (31) where quasi-steady solutions coupled with a phase shift model were used. Extension of the model to the three-dimensional case is reported in (37) for a stripwise model and in (5) for a more general treatment. The separation model has also been successfully installed in a transonic finite-difference code (38).

The same basic model is also applicable for the unsteady case; here, however, the assumption of constant vorticity is no longer valid. In fact, a dynamic wake model is essential and will be discussed below after the description of the unsteady formulation.

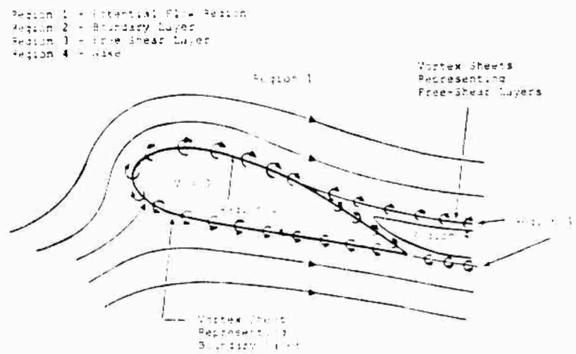

Fig. 2. Mathematical Flow Model (Steady).

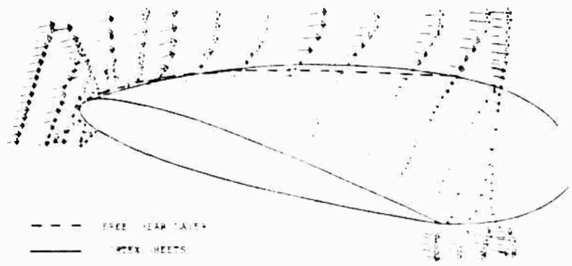

Fig. 3. Location of Experimental Free Shear Layer and CLMAX Calculated Vortex Sheet Centerlines for Low Mach Number Case (from (32)).

Unsteady Method

Formulation. Consider the whole of space divided into two regions by the surface of the configuration and assume the existence of Laplacian velocity potential distributions in the two regions, i.e., ϕ in the flow field and ϕ_i in the blade interior. If we now apply Green's third identity to the two regions, then the total potenital at a point, P, on the inside surface of the boundary can be written:

$$\phi_P = \iint_{S-P} (\phi - \phi_i)\, n \cdot \nabla\left(\frac{1}{r}\right) dS - 2\pi(\phi - \phi_i)_P$$

$$+ \iint_W (\text{[illegible]} - \text{[illegible]})\, n \cdot \nabla\left(\frac{1}{r}\right) dW$$

$$- \iint \frac{1}{r}\,(\text{[illegible]} - \text{[illegible]})\, dS + \text{[illegible]}$$

Here, r is the length of the vector from the surface element to the point, P, and S-P signifies that the point, P, is excluded from the surface integration. Equation (1) includes the contribution from the wake surface, W.

The Dirichlet boundary condition is now applied in the interior region to render a unique distribution. In principle, any potential flow can be applied. However, the flow, $\Phi_i = \Phi_\infty$, implied by Morino (28) and used by Johnson and Rubbert (25), has proven to be very reliable in practice. With this flow, Eq. (1) becomes

$$0 = \iint\limits_{S-P} \phi\,\underline{n}\cdot\nabla\left(\frac{1}{r}\right) dS - 2\pi\phi_P + \iint\limits_{W} \left(\phi_U - \phi_L\right)\underline{n}\cdot\nabla\left(\frac{1}{r}\right) dW - \iint\limits_{S} \frac{1}{r}\,\underline{n}\cdot\nabla\phi\, dS \tag{2}$$

where ϕ, the perturbation potential in the flow field, has been substituted for $\Phi - \Phi_\infty$.

The first two terms in Eq. (2) give the perturbation potential due to a distribution of normal doublets of strength, ϕ, on the configuration surface. Similarly, the third term represents a doublet distribution of strength, $\phi_U - \phi_L$, on the wake and the fourth term represents a source distribution of strength, $\underline{n}\cdot\nabla\phi$, on the configuration surface.

Equation (2) is basically the same as the formulation given by Morino (28), who used a direct application of Green's theorem in the flow field. The present approach to the problem is a special case of a multi-domain formulation which has lead to the more general three-dimensional method in which large regions of separated flow are modelled in a similar way to that in the CLMAX program (5), (30) and (31).

The source term in Eq. (2) can be evaluated directly from the condition of no flow penetration at the surface. The flow velocity relative to the body-fixed frame is at any instant of time

$$\underline{V} = \underline{v} + \underline{V}_\infty - \Omega\,\underline{h} \times \underline{R}, \tag{3}$$

where the perturbation velocity is $\underline{v} = \nabla\phi$, $\underline{h}$ is the axis of rotation, $\underline{V}_\infty$ and Ω are the instantaneous onset flow and angular velocity, respectively, and $\underline{R}$ is the relative position vector between a point on the rotation axis and a point on the surface.

For zero penetration, $\underline{V}\cdot\underline{n} = 0$. Hence,

$$\underline{n}\cdot\nabla\phi = \underline{n}\cdot\underline{V}_\infty - \Omega\,\underline{n}\cdot\underline{h}\times\underline{R},$$

and Eq. (2) becomes

$$0 = \iint\limits_{S-P} \phi\,\underline{n}\cdot\nabla\left(\frac{1}{r}\right) dS - 2\pi\phi_P + \iint\limits_{W} \left(\phi_U - \phi_L\right)\underline{n}\cdot\nabla\left(\frac{1}{r}\right) dW - \iint\limits_{S} \frac{1}{r}\left(\underline{n}\cdot\underline{V}_\infty - \Omega\,\underline{n}\cdot\underline{h}\times\underline{R}\right) dS \tag{4}$$

This is the basic equation of the method. It is solved for the unknown surface perturbation potential, ϕ, or surface doublet distribution, μ, at a number of time steps as the configuration proceeds through the motion. The wake surface is transported at the end of each step using calculated velocities of points on the wake surface. The doublet distribution, $\phi_U - \phi_L$, on each wake surface is known from solutions at earlier time steps. The unsteady Kutta condition

$$\frac{\partial\mu}{\partial t} + V\frac{\partial\mu}{\partial s} = 0 \tag{5}$$

is satisfied at points along each wake separation line at each time step.

At each time step the flow solution is determined with reference to the body-fixed frame. The incompressible pressure coefficient is, therefore, given by

$$C_p = \left(V_s^2 - V^2 + 2\frac{\partial\phi}{\partial t}\right)/V_\infty^2 \tag{6}$$

where $\underline{V}_S = \Omega\underline{h} \times \underline{R} - \underline{V}_\infty$ is the instantaneous velocity of a point on the surface relative to a stationary reference frame, and $\underline{V}$ is given by Eq. (3).

Numerical Procedure. The general arrangement of the configuration is shown in Figure 4. The x, y, z coordinate system with unit vectors, $\underline{i},\underline{j},\underline{k}$ is

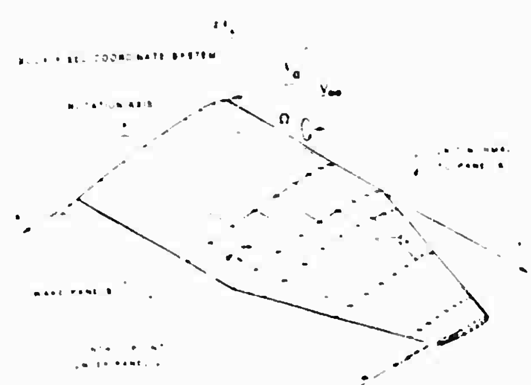

Fig. 4. General Arrangement of the Configuration.

fixed relative to the configuration. For symmetrical applications, the z-x plane is regarded as the plane of symmetry.

A numerical procedure has been assembled in a time-stepping mode to obtain the unsteady pressure distribution and forces and moments. The surface of the wing is represented by planar quadrilateral panels over each of which the doublet and source distributions are assumed constant. With this assumption, the surface integrals in Eq. (4) can be performed in the closed-form for each panel.

Equation (4) is then satisfied simultaneously at a point at the center of each panel. If there are N panels representing the configuration surface, Eq. (4) becomes:

$$\sum_{\substack{K=1\\K\neq J}}^{N} \left\{ \mu_K C_{JK} \right\} - 2\pi\mu_J + E_J = 0; \qquad J=1,N \tag{7}$$

where μ_K is the unknown doublet value on panel K. (Note: $\mu_K = \phi_K/4\pi$.)

$$E_J = \sum_{K=1}^{N_W} \left\{ \mu_{W_K} C_{JK} \right\} + \sigma_{R_J} - \underline{V}_\infty \cdot \underline{\sigma}_{M_J}$$

where N_W, the number of panels in the wake, varies with time and and $\underline{V}_\infty$ take their instantaneous values at each time step.

$$\sigma_{R_J} = \sum_{K=1}^{N} \left\{ \left(\underline{h} \times \underline{R}_K \right) \cdot \underline{n}_K B_{JK} \right\} / 4\pi$$

is the source distribution due to rotation about the axis, $\underline{h}$, and

$$\underline{\sigma}_{M_J} = \sum_{K=1}^{N} \left\{ \underline{n}_K B_{JK} \right\} / 4\pi$$

are the components of a three-part source distribution due to the relative translation of the configuration and the onset flow. (Note: in a symmetrical case the y-component is zero.)

The quantities, B_{JK} and C_{JK}, are the velocity potential influence coefficients for the constant source and doublet distributions, respectively, on panel K acting on the control point on panel J. These include contributions from the image panel in the symmetrical case. Expressions for these influence coefficients have been given by Morino in ([illegible]) based on hyperbolic paraboloidal panels. Slightly different expressions are installed in the VSAERO code based on planar panels.

Equation (7) is solved by a direct method for $N \leq 320$ and by an iterative method for $N > 320$.

The surface pressure distribution is calculated using Eq. (6). The surface gradient of μ is evaluated on each panel by differentiating a two-way parabolic fit through the doublet values on the panel and its four immediate neighbors. At the separation lines a simple differencing is applied for the gradients approaching the separation line.

The gradient of ϕ with respect to time is evaluated by central differencing over two time steps; i.e.,

$$\frac{\partial\phi}{\partial t}^{t-\Delta t} = \left(\phi^{t} - \phi^{t-2\Delta t} \right) / 2\Delta t.$$

For harmonic motions the real and imaginary pressures are obtained by Fourier analysis for the first harmonic based on solutions over a complete cycle. The calculations start with incidence α_0 and a regular (i.e., steady) wake. Two iterations are performed to render the wake force free. An oscillatory doublet component based on a linearized solution is then superimposed along each wake line before starting the time-step model. Time-step calculations proceed over a half cycle before applying the Fourier analysis.

At each time step a new panel is formed at the head of each column of wake panels and all the existing wake panel corner points are convected downstream at the local velocity. Each wake panel keeps the doublet value it received at the time it was formed. This doublet value is based on the conditions at the separation line and satisfies Eq. (5). It is assumed that the shedding occurs at constant vorticity over the time interval, t. In this way the doublet strength, $\mu_W^{t+\Delta t}$, on the new wake panel is related to the strength, μ_W^{t}, of the previous wake panel at the separation line by

$$\mu_W^{t+\Delta t} = 2\mu_T^{t} - \mu_W^{t}.$$

where μ_T^{t} is the resultant doublet value at the separation line.

Unsteady Separated Flow

The combined code for separated flow modelling in the unsteady case requires a more sophisticated treatment of the free-shear layer model than was used for the steady case. Velocities are still calculated at a set of points along each free sheet, but in the unsteady case we now transport these points (and their associated doublet value) along the calculated velocity vectors for a small time interval, Δt. In this way, as time progresses, a dynamic wake model is generated. At each step a new piece of free sheet is shed from the calculated separation point; the strength and size of this new segment is determined by the local upstream velocity condition. The location of the separation--calculated using an unsteady boundary layer code, see the next section--can now move with time.

It is convenient to regard the local vorticity (i.e., doublet gradient) on the free vortex sheets in two components; a streamwise component and a cross-flow component. The streamwise component is already force free and is related to the spanwise rate of shedding of circulation from the wing. The cross-flow vorticity component is associated with direct dumping of bound circulation from the separation line and must be transported with the local flow velocity in order to be force free. This cross-flow vorticity component--which was assumed constant with streamwise distance in the steady case--now varies along each streamline on the free sheets for two reasons: first, the vorticity value being convected onto the free sheet at each separation point is varying in time because of varying onset flow conditions and because of the changing separation locations, secondly, stretching by the entire configuration of solid surfaces and free wake sheets. This stretching of the doublet disbribution carried by the free sheets yields varying vorticity values when the doublet gradient is evaluated. In this way the free sheets can become highly distorted and centers of vortex roll-up may form. Special treatment of the sheets is therefore essential if numerical stability is to be maintained. Two routines are being evaluated in this work but they have not been fully implemented at this time.

(i) Vortex Amalgamation

To cater for vortex roll-up in a reasonable manner it is essential to include a vortex core model in which integrated vorticity is accumulated rather than to follow a detailed calculation of multiple turns of a vortex spiral. An amalgamation scheme similar to that of Moore (39) is being used. When the angle between neighboring segments representing a sheet exceeds a specified angle, the segment end points are merged to a new location at the centroid of their combined circulation. A number of such cores are allowed in the new routine to deal with complex motions. A viscous core expression can be applied to each vortex core when computing the field velocities.

(ii) Redistribution

Having performed the vortex-core amalgamation calculation along each free sheet the points defining the intermediate free sheets are redistributed with equal spacing in a manner similar to Fink and Soh (40) and Sarpkaya and Schoaff (41). Portions of the sheet between amalgamated cores are treated independently here, Figure 5. This treatment, which is applied to both the sheet geometry and its doublet distribution, uses a biquadratic interpolation scheme based on surface distance along the sheet.

This routine should help stabilize the numerical calculations, especially in the initial part of each sheet when the separation location is varying with time. In the three-dimensional case the redistribution scheme is being arranged along the calculated mean streamlines in the wake sheets. This causes some difficulty if amalgamation is not proceeding uniformly along all lines on a sheet.

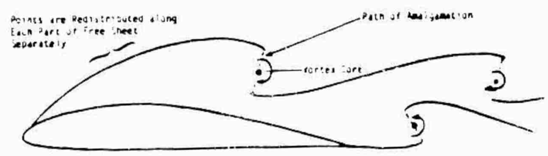

Fig. 5. Illustration of Multiple Vortex Core Amalgamation and Redistribution Scheme.

Calculations

As the routines are being developed, preliminary calculations are being performed to check the basic operation of the code. Figure 6 shows the growth of indicial lift and circulation for a NACA 0012 impulsively started from rest at an angle of attack of .1 rad. The curves are compared with Wagner's function for indicial lift and R.T. Jones indicial circulation for a flat plate. These initial calculations, which used 31 panels around the section, are in good agreement and indicate a slightly higher trend which is consistent with a higher steady state circulation for the thickness case.

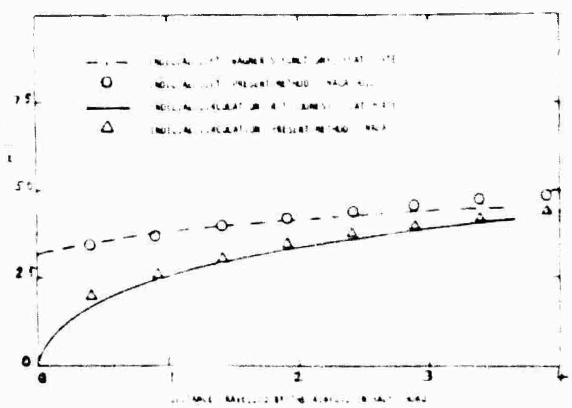

Fig. 6. Indicial Lift and Circulation for an Impulsively Started Two-Dimensional Flat Plate.

Some recent refinements developed in the two-dimensional pilot code have significantly reduced the computing requirement of these time-stepping calculations. For example, Figure 7 shows the effect on indicial lift of varying the number of time steps in the Wagner problem and demonstrates a rapid convergence.

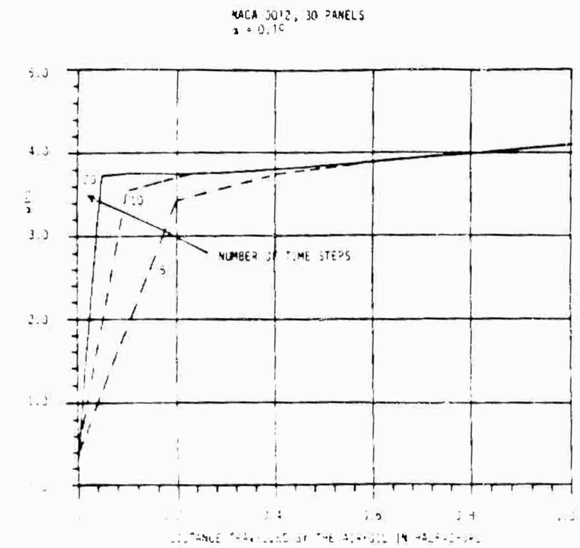

Fig. 7. Computed Indicial Lift for an Impulsively Started NACA 0012 Section--Effect of Number of Time Steps.

The procedure has been tested also for the harmonic oscillation case. Earlier calculations required 80 time steps per cycle for a NACA 0012 oscillating in pitch about the quarter chord. These compared favorably with the Theodorsen flat plate function over a range of reduced frequency, Figure 8. The new calculations are also in good agreement but were performed with only 16 time steps per cycle.

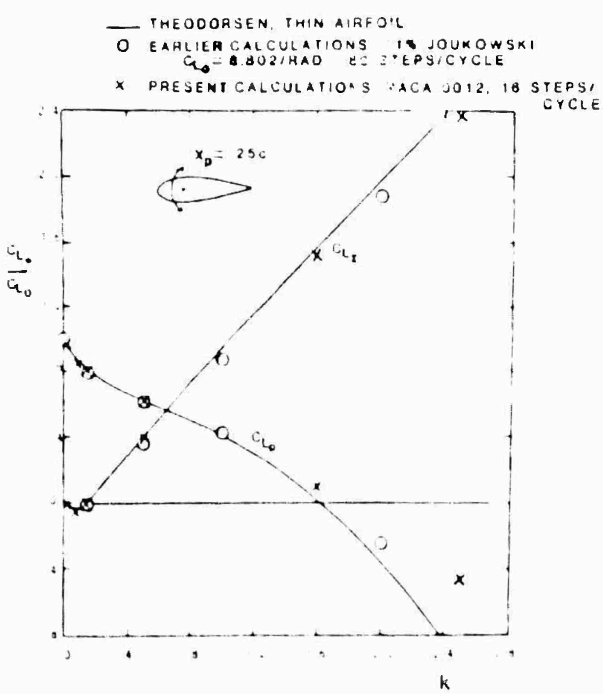

Fig. 8. Comparison of Real and Imaginary Lifts as a Function of Reduced Frequency. α = 1 sin kt.

Figure 9 shows the computed results, C_L versus time, using only 4 time steps per cycle. This is in remarkably good agreement with the 16 and also 32 time-step/cycle solutions, demonstrating an extremely good convergence characteristic.

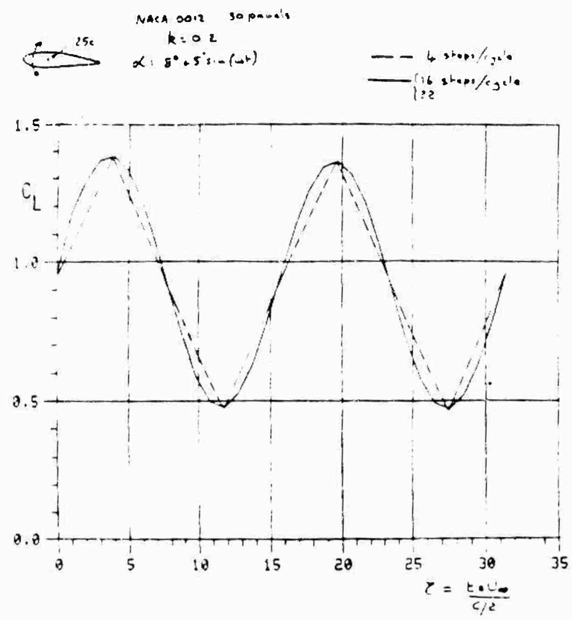

Fig. 9. Computed C_L - τ for a NACA 0012 Section Oscillating in Pitch about the Quarter-Chord.

Time-stepping calculations have also been performed for cases with prescribed extensive separations. The purpose of these calculations was to check the basic unsteady circulation shedding model in the potential flow code. For the first set of tests, the wake panels were simply transported at the onset flow velocity after the initial growth as determined from the surface conditions at separation. Several triangular shapes were considered, each starting impulsively from rest and proceeding forwards over 10 time steps for a total time of $\tau = tU_\infty/h = 3.0$, where h is the triangle base height. Separation was prescribed at the corners. Figure 10(a) shows the computed history of the drag coefficient from pressure integration for a 60° triangle with blunt face forward. A total of 40 panels was used to represent the triangle surface. The calculation was repeated in the presence of wind tunnel walls (also panelled) with a 10% blockage ratio. The indicated blockage correction is somewhat lower than that given by standard techniques. Figure 10(b) compares the computed pressure distributions for this triangle in and out of the tunnel. This "base" pressure has only a small variation and is quite close to experimental measurements. Figure 11 shows a summary of computed drag coefficient versus triangle semi-apex angle. The calculated values are slightly high in relation to the experimental data collected from several sources by Hoerner in Aerodynamic Drag.

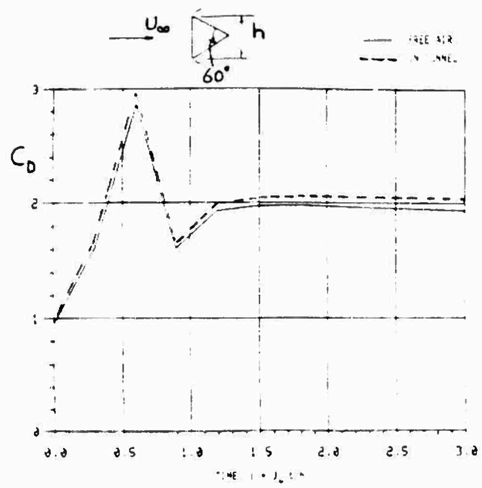

(a) History of Drag.

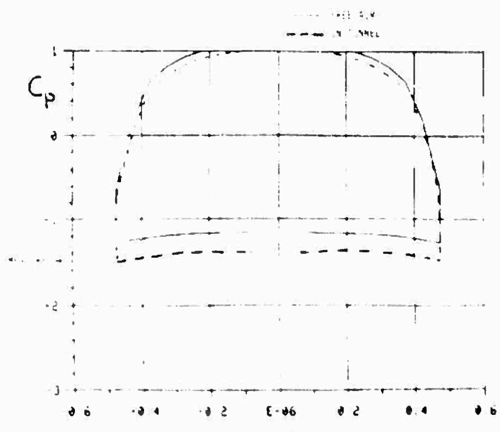

(b) Calculated Pressure Distribution at $\tau = 3.0$.

Fig. 10. Calculations on a Triangular Section Started Impulsively from Rest.

One further case was run for the 60° apex-forward triangle in free air with the full wake velocity calculation routine turned on but without the amalgamation and redistribution schemes at this stage. The calculated C_D for this case falls below the experimental value, Figure 11. A series of computed wake shapes is shown in Figure 12. These are samples from a total of 40 time-step calculations. The total computing time for this case was 195 seconds on a PRIME 550 minicomputer--this is equivalent to less than 2 seconds of CRAY time. The solution should benefit from the numerical damping provided by the amalgamation and redistribution schemes described earlier.

Finally, a test calculation was performed for a NACA 0012 section in a state of pitch from 10° to 30° with $\dot{\alpha}c/2U_\infty = .175$. The calculation used 30 panels and 10 time steps. Separation points were prescribed and the motion was started impulsively

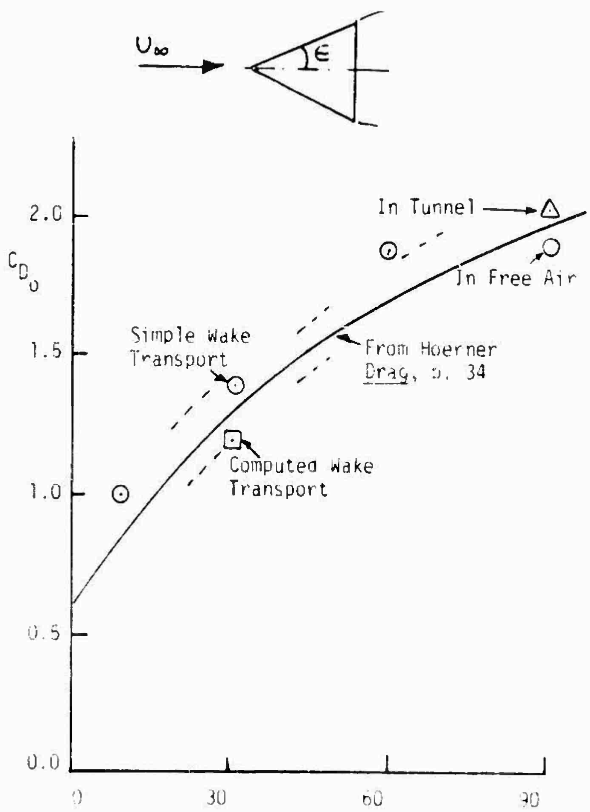

Fig. 11. Calculated Drag Coefficient of Two-Dimensional Wedges as a Function of Apex Angle.

from rest.

Figure 13(a) shows a sample of the computed wake shapes and demonstrates a reasonable numerical behavior. Sample pressure distributions are shown in Figure 13(b). The passage of the leading-edge vortex is clearly shown. This is associated with a local region of reversed flow. These are preliminary test calculations aimed at exploring the numerical behavior of the calculation procedure and potential flow model. Future cases will include the coupled boundary layer calculation for predicting the separation point. At that time the calculated results will be compared with experimental data.

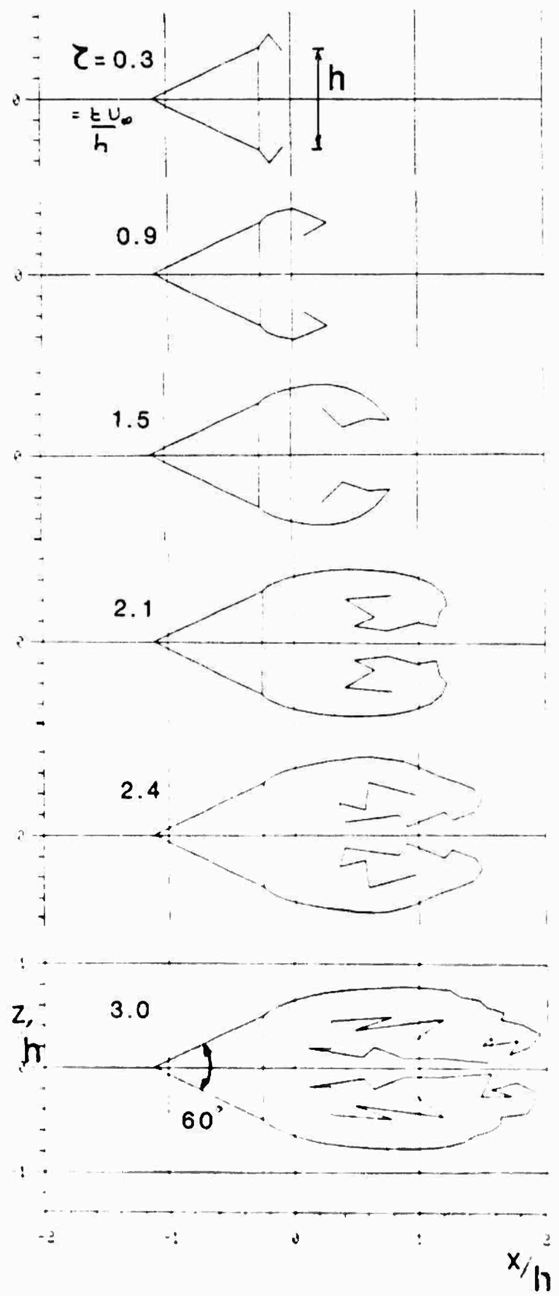

Fig. 12. Computed Wake Shapes for a 60° Wedge Started Impulsively from Rest.

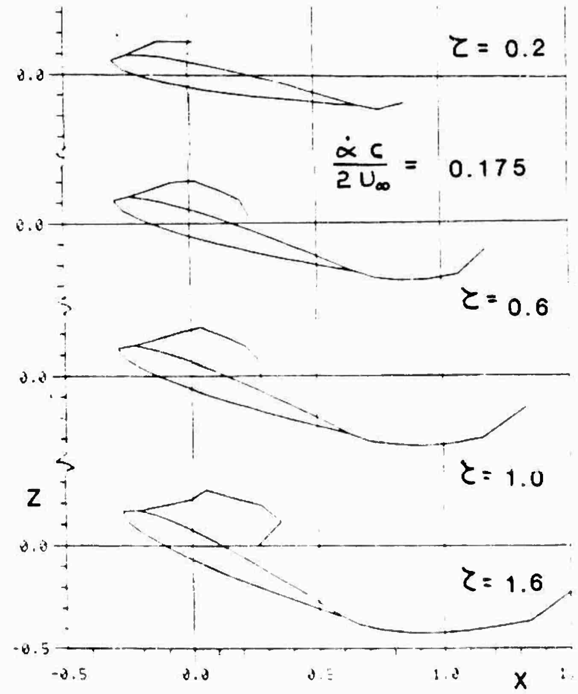

(a) Wake Shapes.

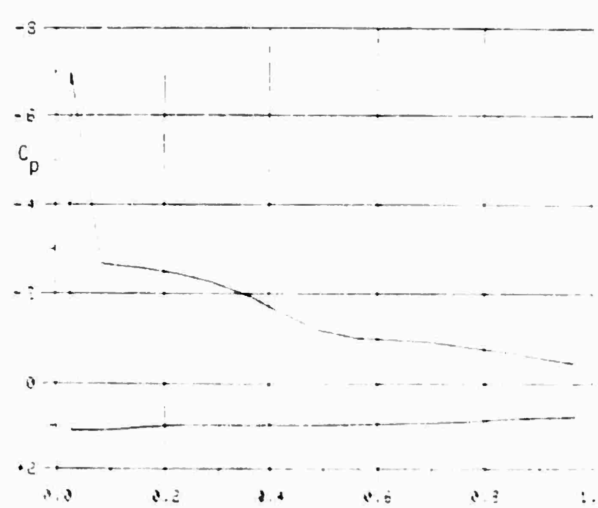

(i) τ = 0.6.

(b) Calculated Pressure Distributions at Two Time Steps.

Fig. 13. Calculated Results for a NACA 0012 Starting Impulsively from Rest and Pitching from 10° to 30° at a Rate $\dot{\alpha}c/2U_\infty = 0.175$.

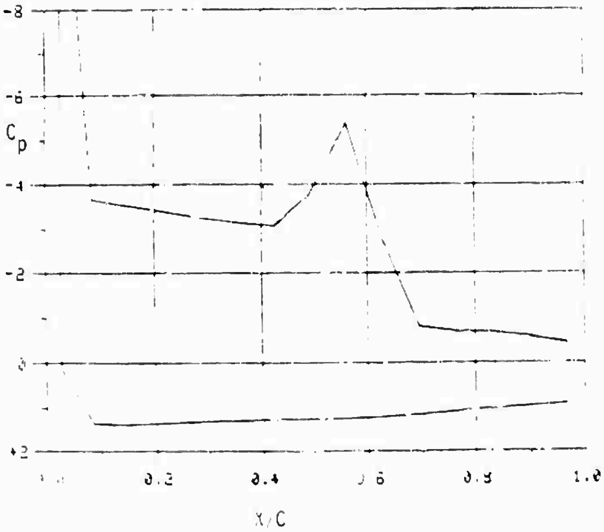

(ii) = 1.6.

(b) Calculated Pressure Distributions at Two Time Steps.

Fig. 15. Concluded.

Boundary Layer Calculation Methods

Curle's original method has been modified to calculate the unsteady boundary layer development. This is achieved by solving the unsteady momentum integral equation using a Runge-Kutta method. The turbulent boundary layer method is based on the unsteady momentum integral equation as in the laminar boundary layer method. Coustei×'s entrainment relationship (43) and Lyrio Ferziger's skin friction relationship (44) are used for closure. The details of the methods are described in the following sections.

Laminar Boundary Layer Method

[illegible]

[illegible] and can be solved [illegible] additional relationships [illegible] are given. [illegible] laminar layer [illegible] closure, these relationships are [illegible]

$$C_f = 2 \cdot \cdot /R \qquad (10)$$

$$L = 2[\cdot - K(H + 2)] \qquad (11)$$

where

$L, \cdot$ = functions of and K

$$K = \cdot^2 / (dU_e/dx) \qquad (12)$$

$$= K^- U_e U_e''/U_e'^2$$

Calculation begins at the stagnation point and K takes the starting value, $K_0 = 0.0855$. The initial momentum thickness, θ_0, is

$$\theta_0 = (0.0855 / (dU_e/dx))^{\frac{1}{2}} \qquad (13)$$

Turbulent Boundary Layer Methods

For unsteady turbulent boundary layers, the momentum integral equation and the entrainment equation are given by:

$$\frac{\partial\theta}{\partial x} + \frac{H+2}{U_e}\frac{\partial U_e}{\partial x} + \frac{1}{U_e^2}\frac{\partial}{\partial t}(\delta^* U_e) = \frac{C_f}{2} \qquad (14)$$

$$\frac{1}{U_e}\frac{\partial}{\partial x}[U_e(\delta - \delta^*)] = C_E \qquad (15)$$

where

$$C_E = \frac{\partial\delta}{\partial x} - \frac{V_e}{U_e}. \qquad (16)$$

Equations (14) and (15) have five unknowns, i.e., C_f, C_E, , , and δ^*, and the system needs additional relationships for closure.

For the skin friction, [illegible] Lyrio et al. (44) is used.

[illegible]

where

[illegible]

$$v_T = \frac{1}{k}\sqrt{\frac{\tau_w}{\rho U_e^2}}\,\mathrm{sgn}(\tau_w) \tag{20}$$

and $k = 0.41$ is the von Karman constant.

The similarity solutions have shown that the entrainment coefficient, C_E, can be expressed as

$$C_E = C_{E_S} - \frac{1}{U_e}\frac{\partial\delta}{\partial t} \tag{21}$$

where C_{E_S} is the entrainment coefficient for the steady case as given by:

$$C_{E_S} = \sqrt{\frac{C_f}{2}}\,(0.074G - 1.0957/G) \tag{22}$$

Substitution of Eq. (21) into Eqs. (14) and (15) and the introduction of $H^* = (\delta - \delta^*)/\theta$ give

$$\frac{1}{U_e}\frac{\partial\delta^*}{\partial t} + \frac{\partial\theta}{\partial x} = B_1 \tag{23}$$

$$H^{*\prime}\frac{\partial\delta^*}{\partial x} + \frac{1+H^{*\prime}}{U_e}\frac{\partial\delta^*}{\partial t} + (H^* - HH^{*\prime})\frac{\partial\theta}{\partial x} + \frac{H^* - HH^{*\prime}}{U_e}\frac{\partial\theta}{\partial t} = B_2 \tag{24}$$

with

$$B_1 = \frac{C_f}{2} - \frac{\theta(H+2)}{U_e}\frac{\partial U_e}{\partial x} - \frac{\delta^*}{U_e^2}\frac{\partial U_e}{\partial t}$$

$$B_2 = C_{E_S} - \frac{[illegible]}{U_e}\frac{\partial U_e}{\partial x}$$

Equations (23) and (24) constitute a system of [illegible] partial differential equations [illegible]. The [illegible] of the second degree for the parameter, $\lambda = \frac{dx}{U_e dt}$:

$$\lambda^2(H^* - HH^{*\prime}) + \lambda[1 - H^* + H^{*\prime}(1 + H)] - H^{*\prime} = 0 \tag{25}$$

Equations (23) and (24) can be solved in various ways. Initial conditions at $t = t_0$ and boundary conditions at the stagnation point ($x = 0$) are sufficient to determine a solution in the region where the flow is attached, i.e., $\tau_w > 0$. In the present paper, the time derivatives are treated as forcing terms and the integration is performed in the x-direction using a Runge-Kutta method.

The boundary layer procedure has been tested against experiments and the calculations of other investigators. The results are shown in Figures 14 and 15. Figure 14(a), (b) and (c) shows the mean quanitites (momentum thickness, skin friction and shape factor) for the experiment conducted by Cousteix (45) on a flat plate. The main free stream velocity is 22 m/sec and the motion is harmonic with respect to time with the frequency of 38 hz. The present calculation (solid line) agrees very well with the calculation by Cousteix and the correlation with experiment is also very good.

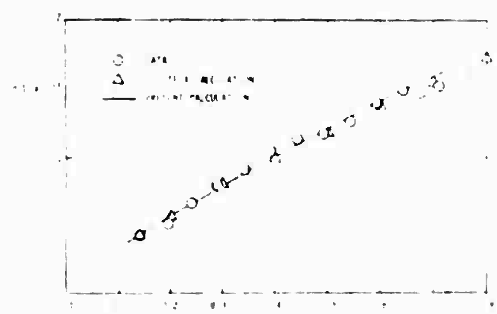

(a) Mean Momentum Thickness, [illegible]

[illegible]

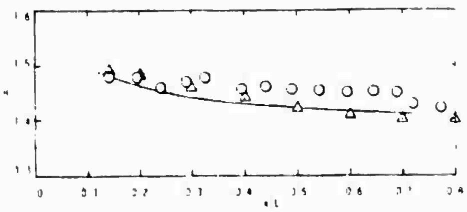

(c) Mean Shape Factor.

Fig. 14. Concluded.

Figure 15 shows the comparison with the calculation of Nash et al. (46) for a monotonically time-varying flow on a flat plate. The present calculation predicts the separation at the end of the plate when wt = 0.682 as in the Nash et al. calculation. The overall results are in good agreement with their calculation.

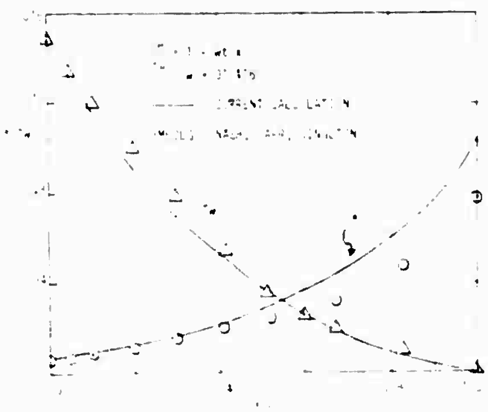

Fig. 15. Wall Shear Stress and Displacement Thickness Distribution at wt = 0.682.

These test calculations have shown that the current boundary layer procedure is capable of predicting the unsteady boundary layer development and it should be adequate for analyzing dynamic stall problems.

Complete Procedure

[illegible]

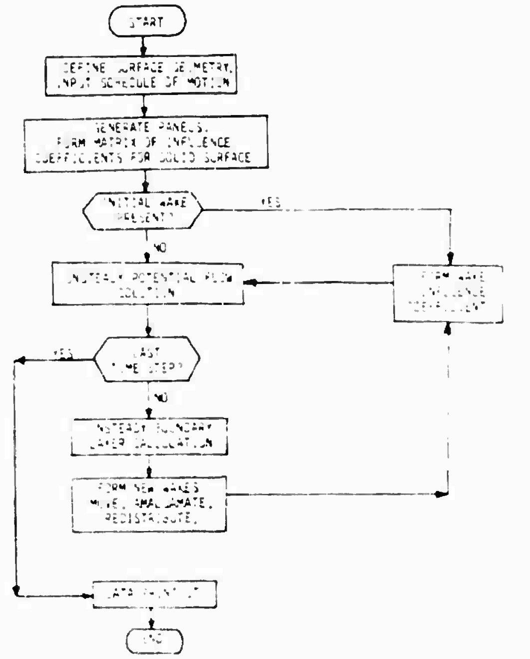

Fig. 16. Flow Diagram for the Combined Code.

A preliminary calculation was performed for a NACA 0012 section oscillating in pitch about the quarter-chord with [illegible]. Figure 17 shows the predicted history of the separation location superimposed [illegible]. The most forward separation reached [illegible] with a phase lag of about [illegible].

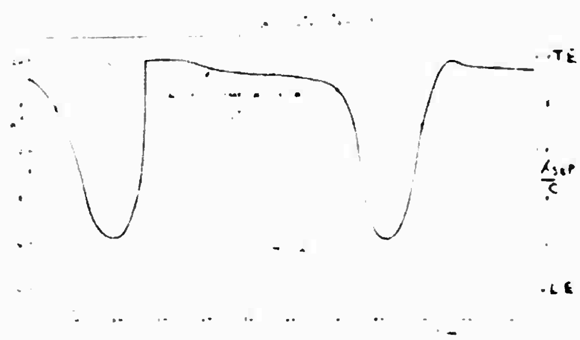

Fig. 17. [illegible]

[illegible]

Finally, an experimental data case from (3) was run and the computed lift variation with α compared with the measured data in Figure 18. The airfoil is a NACA 0012 and is oscillating in pitch about the quarter-chord line with $\alpha = 8.1° + 4.9°$ sin (0.2t); i.e., below the dynamic stall onset. Reynolds number was 4×10^6. This reduced frequency condition is very close to the changeover from a lead to a lag situation and so there is only a small difference between the upswing and downswing curves.

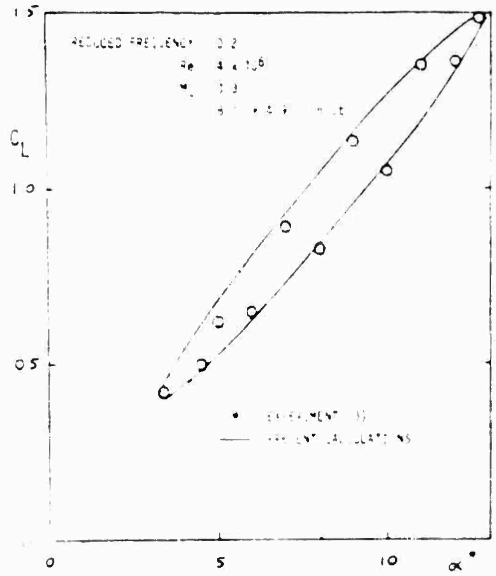

Fig. 18. Comparison of Calculated and Measured Lift on a NACA 0012 Airfoil Oscillating in Pitch about the Quarter-Chord.

Conclusions

A system of routines has been developed to couple an unsteady time-stepping potential flow panel method with an extensive separation model and an unsteady boundary layer code. The routines include treatment of the growth of a multiple sheet [illegible] wake model and also the movement of the separation location with time. Preliminary check-out of the routines using a simplified pilot code show encouraging results for conditions approaching the onset of dynamic stall. Work is now proceeding [illegible] the case of light dynamic stall using the extensive separation model. These test calculations have shown that the current boundary layer procedure is capable of predicting the unsteady boundary layer development and it should be adequate for analyzing dynamic stall.

Acknowledgements

This work is supported by the Air Force Office of Scientific Research [illegible]

References

1. McCroskey, W.J., "Recent Developments in Dynamic Stall", Proc. Symposium on Unsteady Aerodynamics, University of Arizona, Tuscon, Arizona, Vol. I, March 1975, pp. 1-33.

2. McCroskey, W.J., "Prediction of Unsteady Separated Flows on Oscillating Airfoils", AGARD Lecture Series on Three-Dimensional and Unsteady Separated Flow at High Reynolds Numbers, VKI, Belgium, AGARD LS-94, Paper 12, February 1978.

3. McCroskey, W.J., McAlister, K.W., Carr, L.W., Pucci, S.L., Lambert, O. and Indergand, Lt. R.F., "Dynamic Stall on Advanced Airfoil Sections", Paper 80-01 in Proc. 36th Annual Forum of the American Helicopter Society, May 1980.

4. Maskew, B., "Influence of Rotor Blade Tip Shape on Tip Vortex Shedding--An Unsteady Inviscid Analysis", Paper 80-6 in Proc. 36th Annual Forum of the American Helicopter Society, May 1980.

5. Maskew, B., Rao, B.M. and Dvorak, F.A., "Prediction of Aerodynamic Characteristics for Wings with Extensive Separations", Paper No. 31 in Computation of Viscous-Inviscid Interactions, AGARD-CPP-291, September 1980.

6. Maskew, B., "Prediction of Subsonic Aerodynamic Characteristics--A Case for Low-Order Panel Methods", Paper 81-0252, Presented at the AIAA 19th Aerospace Sciences Meeting, St. Louis, MO, January 1981.

7. Liiva, J., et al., "Two-Dimensional Tests of Airfoils Oscillating near Stall", U.S. Army Aviation Material Lab., Ft. Eustis, VA, Technical Report 68-13, April 1968; also J. Aircraft, Vol. 6, No. 1, January [illegible], pp. 46-51.

8. Lang, J.D., "Experimental Results for an Airfoil with Oscillating Spoiler and Flap", Symposium on Unsteady Aerodynamics, Kinney, R.B., ed., Univ. of Arizona, Tuscon, AZ, 1975, pp. 55-[illegible]; also J. Aircraft, Vol. 13, No. 9, September 1976, pp. 687-694.

9. Lang, J.D. and Francis, M.S., "Dynamic Loading on an Airfoil due to [illegible] Separated Flow", Paper 26 in "Prediction of Aerodynamic Loading", AGARD CP-204, 1976.

10. [illegible]

11. [illegible]

12. [illegible]

13. Carr, L.W., McAlister, K.W. and McCroskey, W.J., "Analysis of the Development of Dynamic Stall Based on Oscillating Airfoil Experiments", NASA TN D-8382, January 1977.

14. Ham, N.D., "Aerodynamic Loading on a Two-Dimensional Airfoil During Dynamic Stall", AIAA J., Vol. 6, No. 10, October 1968, pp. 927-1934.

15. Baudu, N., Sanger, M. and Souquet, J., "Modelisation du Décrochage Dynamique d'un Profil Oscillant", AAAF 10th Colloque d'Aérodynamique Appliquée, Lille, France, November 1973.

16. McCroskey, W.J. and Philippe, J.J., "Unsteady Viscous Flow on Oscillating Airfoils", AIAA J., Vol. 13, No. 1, January 1975, pp. 71-79.

17. Scruggs, R.M., Nash, J.F. and Singleton, R.E., "Analysis of Dynamic Stall using Unsteady Boundary Layer Theory", NASA CR-2467, October 1974.

18. McCroskey, W.J., "Introduction to Unsteady Aspects of Separation in Subsonic and Transonic Flow", AGARD Lecture Series on Unsteady Separated Flow at High Reynolds Numbers, [illegible], AGARD LS-94, Paper 5, February 197[illegible].

[illegible]

27. Maskew, B., "Calculation of Two-Dimensional Vortex Surface Interference using Panel Methods", NASA CR-159334, December 1980.

28. Morino, L., Chen, L.-T. and Suci, E.O., "Steady and Oscillatory Subsonic and Supersonic Aerodynamics around Complex Configurations", AIAA J., Vol. 13, No. 3, March 1975.

29. Seetharam, H.C., "Experimental Investigation of Separated Flow Fields on an Airfoil at Subsonic Speeds", Ph.D. Dissertation, Wichita State University, March 1975.

30. Maskew, B. and Dvorak, F.A., "The Prediction of $C_{L_{MAX}}$ Using a Separated Flow Model", J. Am. Hel. Soc., April 1978.

31. Dvorak, F.A., Maskew, B. and Rao, B.M., "An Investigation of Separation Models for the Prediction of $C_{L_{MAX}}$", Final Technical Report Prepared for the U.S. Army Research Office, Research Triangle Park, N.C., 1975-1979.

[illegible]

41. Sarpkaya, T. and Schoaff, R.L., "Inviscid Model of Two-Dimensional Vortex Shedding by a Circular Cylinder", AIAA J., Vol. 17, No. 11, November 1979, pp. 1193-1200.

42. Curle, N., "A Two-Parameter Method for Calculating the Two-Dimensional Incompressible Laminar Boundary Layer", J. R. Aero. Soc., Vol. 71, 1967.

43. Cousteix, J. and Houdeville, R., "Singularities in Three-Dimensional Turbulent Boundary Layer Calculation and Separation Phenomena", AIAA J., Vol. 19, No. 8, August 1981.

44. Lyrio, A.A. and Ferziger, J.H., "A Method of Predicting Unsteady Turbulent Flows and its Application to Diffusers with Unsteady Inlet Conditions", AIAA J., Vol. 21, No. 4, April 1983.

45. Cousteix, J., Private Communication.

46. Nash, J.F., Carr, L.W. and Singleton, R.E., "Unsteady Turbulent Boundary Layers in Two-Dimensional, Incompressible Flow", AIAA J., Vol. 13, No. 2, February 1975.

NUMERICAL SOLUTIONS OF THE NAVIER-STOKES EQUATIONS FOR UNSTEADY SEPARATED FLOWS

Wilbur L. Hankey*
Air Force Wright Aeronautical Laboratories
Wright-Patterson Air Force Base, Ohio 45433

AD-P004 161

Introduction

Advances in computer hardware during the last decade have permitted the numerical solution of the Navier-Stokes equations. Original efforts concentrated on steady flow problems, however, more recently unsteady flows have been addressed. One of the best uses of the Navier-Stokes numerical program is to solve separated flows due to the non-linear character of the problem. (For problems in linear aerodynamics more efficient computer programs exist). However, most separated flows are unsteady due to the fundamental instability of such flows. Rayleigh's second theorem[1] states that a velocity profile with an inflection point (U"=0) is unstable. All separated flows have inflection points and hence have an unstable region. In these flows, small disturbances of a certain wave length are amplified. In simple linear theory these disturbances attain infinite amplitude, however, a "limit cycle" is achieved in nature. The time-dependent Navier-Stokes equations possess the capability to investigate unsteady separated flows. This paper will review some of the progress accomplished over the past few years in this area.

Governing Equations

The time-dependent Navier-Stokes equations in a rotating coordinate system take the following form:

[illegible] $= H$

where

[illegible]

where [illegible] = stress tensor

[illegible]

[illegible] equations are solved by a finite difference [illegible] using MacCormack's explicit algorithm [illegible] on the [illegible] computer.

[illegible]

1. Steady separated flows.
   Supersonic flight with steady boundary conditions.
   a. Missile at moderate angle of attack[1].
   b. Hypersonic cruiser at angle of attack[2].

2. Self-excited oscillations.
   Periodic solutions of unsteady flows with steady boundary conditions.
   a. Buffet of a Cylinder[3] and Airfoil[4].
   b. Weapons Bay Cavity Resonance[5].
   c. Buzz of a Spike[6] and Inlet[7].

3. Forced Oscillations.
   Periodic solutions of unsteady flows with time dependent boundary conditions.
   a. Dynamic lift of an oscillating airfoil[8].
   b. Rotation of a flat plate[9].

Although other categories could also be addressed, these few cases were chosen to demonstrate the versatility of the numerical program and to indicate the present state-of-the-art in solving the Navier-Stokes equations. (See Figures 1-6). These solutions averaged about one hour on a CRAY 1 computer.

Conclusion

By use of the time-dependent Navier-Stokes equations, simplifying assumptions are no longer necessary to investigate many classes of unsteady separated flows. The projected advancement of computer capability over the next few years renders questionable the wisdom of supporting basic research on short-cut approximate methods for analyzing unsteady separated flows.

References

1. Rayleigh, Lord, "On the Stability or Instability of Certain Fluid Motion," Scientific Papers, [illegible] pp. [illegible], Cambridge University Press, [illegible].
2. Hankey, W.L., [illegible], Shang, J.S., "Navier-Stokes Solution [illegible] Slender Body [illegible] at Large Incidence," AIAA Paper 81-[illegible].
3. Shang, J.S., and Hankey, W.L., "Numerical Simulation [illegible] Flows Past a Hypersonic [illegible]," [illegible] Symposium on Numerical and Physical Aspects [illegible] Flows, California State University, Long Beach, 17-20 Jan 1984.
4. Shang, J.S., "Oscillatory Compressible Flow Around a Cylinder," AIAA Paper 82-[illegible], Jan 1982.
5. [illegible]
6. [illegible]
7. [illegible]

8. Newsome, R.W., "Numerical Simulation of Near-Critical and Unsteady Subcritical Inlet Flow Fields," AIAA Paper 83-0175, Jan 1983.
9. Hegna, H., "Numerical Prediction of Dynamic Forces on Arbitrarily Pitched Airfoils in Turbulent Flow," AIAA Paper 82-0092, Jan 1982.
10. Gallaway, C., "Aerodynamic Analysis of a Free Falling Autorotating Plate," PhD Dissertation to be published.

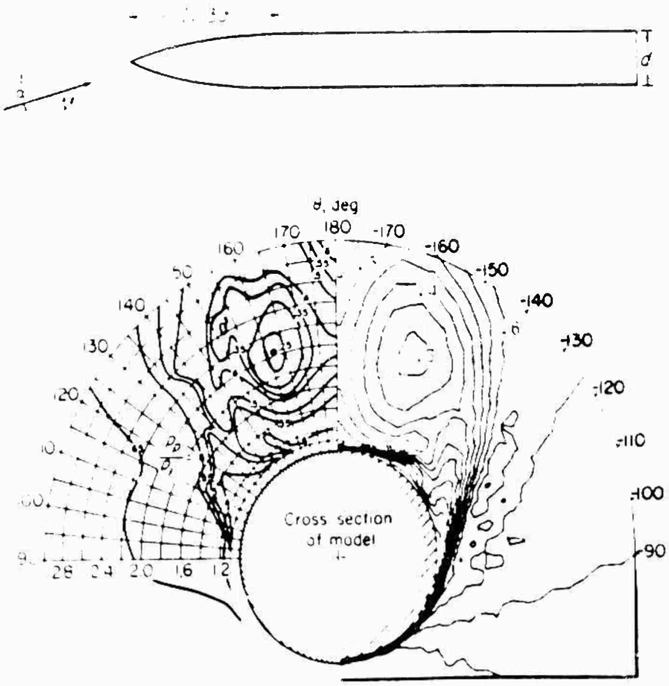

Fig. 1 Missile at Angle of Attack (Ref. 2)

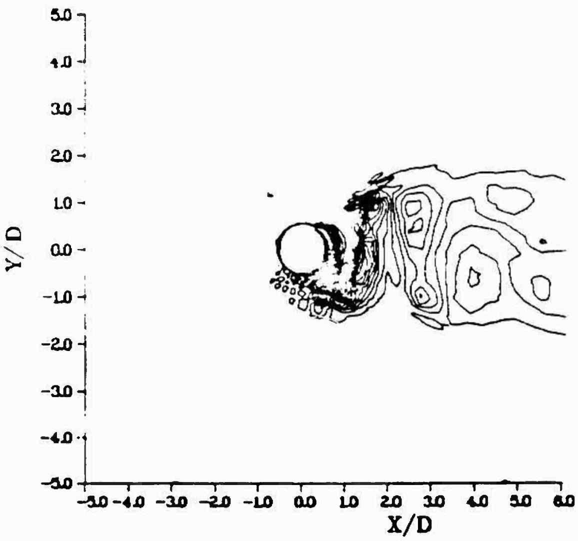

Fig. 3 Flow over an Infinite Cylinder (Ref. 4)

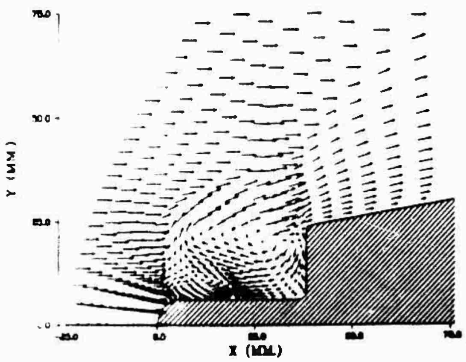

Fig. 4 Spike-Tipped Body Buzz (Ref. 7

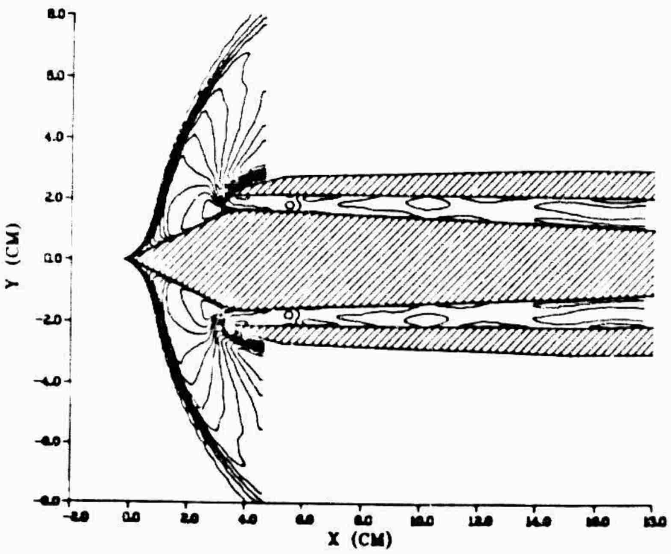

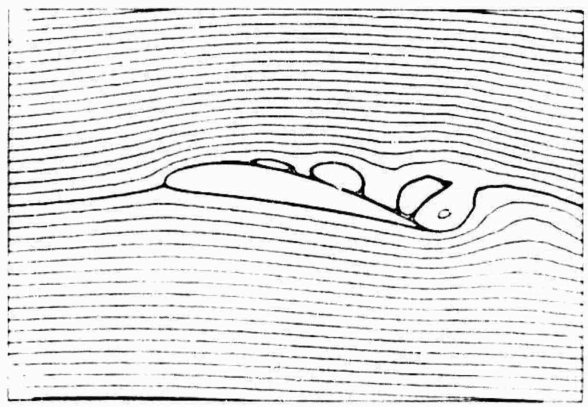

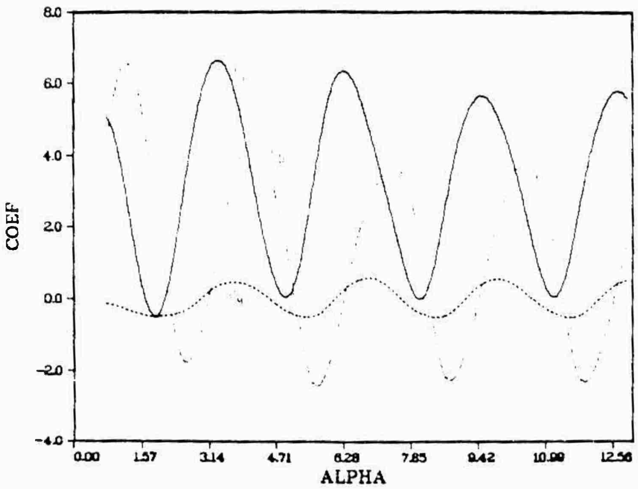

Fig. 6 Computed Aero Characteristics for Rotating Plate (Ref. 10)

UNSTEADY AERODYNAMIC LOADING ON AN AIRFOIL DUE TO VORTICES RELEASED INTERMITTENTLY FROM ITS UPPER SURFACE

Chuen-Yen Chow*
and
Chyn-Shan Chiu**
University of Colorado
Boulder, Colorado 80309

AD-P004 162

Abstract

An unsteady flow analysis is made of the flow past a symmetric airfoil with identical vortices released intermittently from its upper surface. The vortex train is used to simulate the flow observed in the laboratory which was perturbed by an oscillating spoiler or a rotating cam embedded in the airfoil surface. Based on numerical computations, the airfoil lift has a general behavior that it increases oscillatorily with time, and seems to approach an asymptotic value as time increases indefinitely. The asymptotic lift is enhanced with increasing frequency at which vortices are generated, and is only slightly influenced by changing the vortex-releasing position along the chord. The behavior of the drag is similar to that of the lift, but its magnitude is two orders smaller. Our study also indicates that it is more efficient to implement the vortex-augmented unsteady lift at higher angles of attack of the airfoil.

Introduction

Experiments have been conducted at the University of Colorado and elsewhere to study the flow past an airfoil, which was perturbed by an oscillating fence-type spoiler protruding from the upper surface, like the device used by Francis et al., or by a rotating cam-shaped rotor adopted by Viets et al. In these experiments organized vortex structures were observed to form periodically behind the perturbing mechanism and to be carried into the wake by the local streaming fluid motion. [illegible]

---

* [illegible]

** [illegible]

When moving along the airfoil surface, this train of vortices not only makes the flow unsteady but also may cause significant changes in airfoil performance. While empirical data are not yet available for comparison, we are presenting here a theoretical analysis for computing the unsteady lift and drag of the airfoil when vortices are released intermittently from its upper surface.

Despite the fact that vortices observed in the laboratory are most likely formed from rolling up of vortex sheets resulting from boundary layer separation at the sharp tip of the spoiler or rotor as sketched in Fig. 2, they are treated as discrete potential vortices in our formulation based on an inviscid incompressible flow analysis. The symmetric airfoil configuration adopted in our computation is generated from a circle through Joukowski transformation, and the effect of oscillating spoiler or rotating cam is simulated by the intermittent appearance of discrete vortices of the same strength at a given location above the airfoil. In an unsteady flow about airfoil, a vortex sheet is expected to shed continuously from the sharp trailing edge. Strengths of the discretized wake vortices and the instantaneous circulation about the airfoil are determined from requirements that the resultant flow be tangent to the airfoil surface, the Kutta condition be satisfied at all times, and the total circulation in the entire flow field be kept at the initial value. The complex potential for the physical flow about the airfoil is obtained by transformation from that for the flow about the circle, from which the motions of all discrete vortices as well as the lift and drag on the airfoil can be computed at any time instant. The unsteady flow problem is solved [illegible]

[illegible]

[illegible]

As shown in Fig. 1, the transformation

$$z = \frac{1}{2}\left(\zeta + \frac{1}{\zeta}\right) \tag{1}$$

maps a circle of radius a (>1) in the ζ ($= \xi + i\eta$) plane, centered at $\zeta = 1 - a$, into a symmetric Joukowski airfoil in the physical z ($= x + iy$) plane, whose chord is slightly longer than 2. A free-stream velocity of magnitude of one half and at an angle of attack α is mapped without changing its orientation into a uniform stream of unit speed in the physical plane. For the convenience of formulation a ζ' ($= \xi' + i\eta'$) plane is introduced in Fig. 1, whose origin coincides with the center of the circle. The relation

$$\zeta' = \zeta + a - 1 \tag{2}$$

holds for coordinate transformation between ζ and ζ' planes.

A discrete vortex of circulation k_j at a position z_j outside the airfoil is transformed according to Eq. (1) into a vortex of the same strength at ζ'_j outside the circle. To satisfy the boundary condition that the flow be tangent to the circle and to fulfill the requirement that the total circulation be conserved, an image vortex of strength $-k_j$ and another vortex of strength k_j are added at $a^2/\bar{\zeta}'_j$ and the center of the circle, respectively. For each of the discrete vortices in the physical plane, be it the vortex generated by a spoiler or a vortex shed in the wake, a set of three vortices is placed in the transformed plane following the procedure just described. Suppose the initial steady-state circulation about the airfoil is Γ, which is determined by the airfoil angle of attack α. After vortices have been generated by a perturbing mechanism, the total circulation in the entire flow must be kept at its initial value according to the inviscid theory. In other words, no matter how many vortices are present in the flow, the total strength of all vortices situated at the center of the circle in the transformed plane must be Γ at all times. Thus when a vortex appears in the flow, it is sufficient to represent it by a vortex pair across the circle as shown in Fig. 2. The instantaneous circulation around the airfoil is therefore given by

$$\Gamma - \sum_{j=1}^{m} k_j$$

where m represents the total number of discrete vortices in the flow at that instant.

The velocities of the physical flow can be computed from that in the transformed plane, [illegible] at any point ζ' outside [illegible]

[illegible]

in which

$$\frac{dw}{d\zeta'} = \frac{1}{2} e^{-i\alpha}\left(1 - \frac{a^2}{\zeta'^2} e^{2i\alpha}\right) + \frac{i\Gamma}{2\pi\zeta'} + \sum_{j=1}^{m} \frac{ik_j}{2\pi}\left(\frac{1}{\zeta' - \zeta'_j} - \frac{1}{\zeta' - a^2/\bar{\zeta}'_j}\right) \tag{5}$$

$$\frac{dz}{d\zeta} = \frac{\zeta^2 - 1}{2\zeta^2} \tag{6}$$

This expression holds at any point in the physical flow except at the trailing edge of the airfoil and the center of a free vortex.

In the unsteady flow field, a wake vortex is shed at any instant of time. Let this be the mth vortex whose position is ζ'_m in the transformed plane. Its circulation k_m, determined by satisfying the Kutta condition that $\zeta' = a$ be a stagnation point, has the expression

$$k_m = \left[2\pi a \sin\alpha - \Gamma - \sum_{j=1}^{m-1} k_j \frac{a^2 - \zeta'_j\bar{\zeta}'_j}{(a - \zeta'_j)(a - \bar{\zeta}'_j)}\right] \Big/ \frac{a^2 - \zeta'_m\bar{\zeta}'_m}{(a - \zeta'_m)(a - \bar{\zeta}'_m)} \tag{7}$$

This vortex will later move at the local fluid velocity without changing its circulation.

For numerical computations we choose a = 1.15 to obtain a 17% thick symmetric airfoil. The strength of vortices generated by a perturbing device is determined by the size of the device, frequency of oscillation, Reynolds number, and other factors. It can be measured according to a method described by Keesee, Francis, and Lang.[7] However, because of insufficient empirical data corresponding to our concerned conditions, we arbitrarily pick a circulation value of [illegible] for all of the cases that we have examined. This dimensionless strength represents a circulation which, when applied around an airfoil, would produce a lift coefficient of [illegible]. For a given angle of attack and prescribed vortex-releasing [illegible] position and period, the procedure for numerical computation is outlined as follows.

[illegible] ζ_2' [illegible]

z_n, derived after taking a proper limit.

$$(u - iv)_{z_n} = \left(\frac{dw}{dz} - \frac{ik_n}{2\pi}\,\frac{1}{z - z_n}\right)_{\zeta' = \zeta'_n}$$

$$= \frac{\zeta_n}{\zeta_n^2 - 1}\Big[e^{-i\alpha} - \left(\frac{a}{\zeta'_n}\right)^2 e^{i\alpha} + \frac{i\Gamma}{\zeta'_n}$$

$$+ \sum_{j\neq n}^{m} \frac{ik_j}{2\pi}\,\frac{1}{\zeta'_n - \zeta'_j} - \sum_{j=1}^{m} \frac{ik_j}{2\pi}\,\frac{1}{\zeta'_n - a^2/\bar{\zeta}'_j}\Big]$$

$$- \frac{ik_n \zeta_n}{2\pi(\zeta_n^2 - 1)^2} \tag{8}$$

[illegible] lift, L, and drag, D, on the airfoil are computed based on the Blasius theorem for unsteady flow.

$$D + iL = [illegible] - i\rho e^{-i\alpha} \sum_{j=1}^{m} k_j (u + iv)_{z_j} \frac{\zeta_j}{\zeta_j^2 - 1}$$

$$- i\rho e^{-i\alpha} \sum_{j=1}^{m} k_j (u - iv)_{z_j} \left(\frac{a}{\bar{\zeta}'_j}\right)^2 \frac{\bar{\zeta}_j}{\bar{\zeta}_j^2 - 1} \tag{9}$$

Time is advanced by an increment Δt, which is chosen as T/20 so that one cycle of oscillation is completed in 20 time steps. The new position $\vec{R}(t + \Delta t)$ of a vortex, whose previous position vector is $\vec{R}(t)$, is calculated [illegible] a two-step predictor-corrector procedure

$$\vec{R}_p = \vec{R}(t) + \Delta t\, \vec{V}[\vec{R}(t)] \tag{10}$$

$$\vec{R}(t + \Delta t) = \vec{R}(t) + \Delta t\, \{\vec{V}[\vec{R}(t)] + \vec{V}(\vec{R}_p)\}/2 \tag{11}$$

where the velocity vectors are those constructed from the complex-velocity expression [illegible].

[illegible]

sheet rolls into a spiral, which becomes tighter and tighter as time progresses. When distances among vortices become too small, inaccurate results are expected which appear in the form of scattered vortices in the wake. To eliminate this chaotic motion of the wake vortices, we adopt Moore's method[5] to use a concentrated tip vortex to represent the tightly rolled portion of a vortex sheet. More specifically, when the total number of wake vortices exceeds 20 in the computation, the first two vortices at the tip are combined into one situated at their centroid position, whose circulation is the sum of the two individual strengths.

Results

For the 17% thick symmetric airfoil, computations have been made by varying angle of attack, chordwise position of the released vortices, and the period at which they are released.

At zero angle of attack and when vortices of circulation 0.5 are released with a period T = 5 at a height of 0.1 above the upper surface at the midchord position, the behavior of lift coefficient at the early stage is plotted in Fig. 4. The sudden release of a vortex causes a negative lift on the airfoil. Lift increases with time in an oscillatory manner; the mean lift coefficient $(C_L)_m$, averaged within each oscillation, gradually approaches an asymptotic value after more than [illegible] vortices have been released. The variation of lift in one cycle has a shape that is almost identical to that in any other cycle, except that the entire curve is shifted upward after each period.

A representative lift curve within one cycle, for [illegible] ≤ t ≤ [illegible], is blown up and plotted in Fig. [illegible]. At the beginning of that cycle when a vortex is just released at the upper surface, lift has the lowest value. At this instant the vortex released in the previous cycle is in the wake at a distance of about four half-chord lengths from the newly released vortex, as shown in the leftmost of the three insertions in Fig. [illegible]. The shape of the wake vortex sheet is displayed by a group of [illegible] vortices. [illegible] neighboring released vortices and stronger interactions between these vortices and the wake vortex sheet. It is interesting to note that all wake vortices have counterclockwise circulations. Within that period, lift climbs to a maximum and then drops to a minimum, both occurring when a released vortex leaves the trailing edge.

The variation of mean lift coefficient with time is plotted in Fig. 8 for different values of T. Solid lines represent results for the arrangement that vortices are released at the midchord location. The plot reveals that for a shorter T when vortices are released at a higher frequency, a higher average lift can be generated on the airfoil. Each of the higher T curves approaches an asymptotic value, which increases with increasing frequency. The curves for lower values of T seem to have the same behavior, but a tremendous amount of computer time is needed to find their asymptotic lift values. For example to reach t = 200 for the T = 2 curve, the CPU time is 2700 seconds on a Cyber 170-720 computer. No attempt has been made to extend the computation beyond that time. However, it should be pointed out that for T equals 2 or 1, the mean lift coefficient can become greater than 0.5, which is the static lift coefficient if the circulation of a released vortex is applied around the airfoil. For a period equal to or greater than 4, the mean lift cannot exceed this value.

The dashed and the dash-dotted lines in Fig. 8 are used to represent results obtained when the vortex-generating mechanism is at the 1/4-chord and 3/4-chord positions, respectively. In these two cases vortices are still released at the same initial height of 0.1 above the local airfoil surface. The influence of changing chordwise position on lift is not too strong as revealed in the figure. Generally speaking, releasing vortices at the 1/4-chord position causes a decrease in average lift, whereas shifting it rearward to the 3/4-chord position does the opposite for T = [illegible] and T = [illegible].

Plotted in Figs. [illegible] and [illegible] are the initial behavior of drag coefficient for T = 5 and [illegible], respectively. The general pattern of drag variation is similar to that of the lift, but the magnitude is two orders smaller. The mean drag coefficient [illegible], averaged over one period, approaches negative and positive asymptotic values, respectively, for T = [illegible] and [illegible].

The effect of changing airfoil angle of attack on mean lift coefficient is examined. A representative result, obtained for the case vortices are released at the midchord location at T = [illegible], is shown in Fig. [illegible]. Plotted against time in this figure is the mean incremental lift coefficient, defined as [illegible] $- \pi\alpha$. A comparison of the curves for α = [illegible], [illegible], and [illegible] indicates that the vortex-augmented unsteady lift increases with increasing angle of attack.

[illegible]

[illegible]

generated on a wing utilizing a properly designed vortex-triggering device installed on its upper surface. Despite the negligibly small drag shown in the result, it can be expected to be substantial in reality when vortices are generated by moving a spoiler into and out of the airfoil surface.

The strength of the released vortices is arbitrarily assigned in the present analysis. It actually should be determined more realistically from empirical data or from viscous flow computations. The latter approach is being taken by us in an attempt to solve the problem of an unsteady viscous flow past an oscillating spoiler.

Acknowledgment

This work was supported by the U.S. Air Force Office of Scientific Research under Grant No. F49620-83-K-0009. The authors express their appreciation to Lorrie Beeman and Nancy Searby for providing the photograph shown in Fig. 1.

References

[1] Francis, M.S., Keesee, J.E., Lang, J.D., Sparks, G.W., and Sisson, G.E., "Aerodynamic Characteristics of an Unsteady Separated Flow," AIAA Journal, Vol. 17, No. 12, December 1979, pp. 1332-1339.

[2] Viets, H., Piatt, M., and Ball, M., "Unsteady Wing Boundary Layer Energization," AIAA Paper No. 79-1631, August 1979.

[3] Chow, C.-Y. and Huang, M.-K., "Unsteady Flows About a Joukowski Airfoil in the Presence of Moving Vortices," AIAA Paper No. 84-[illegible], January 1984.

[4] Keesee, J.E., Francis, M.S., and Lang, J.D., "Technique for Vorticity Measurement in Unsteady Flow," AIAA Journal, Vol. [illegible], No. 4, April [illegible], pp. [illegible].

[5] Moore, D.W., "A Numerical Study of the Roll-Up of a Finite Vortex Sheet," Journal of Fluid Mechanics, Vol. [illegible], [illegible], pp. [illegible].

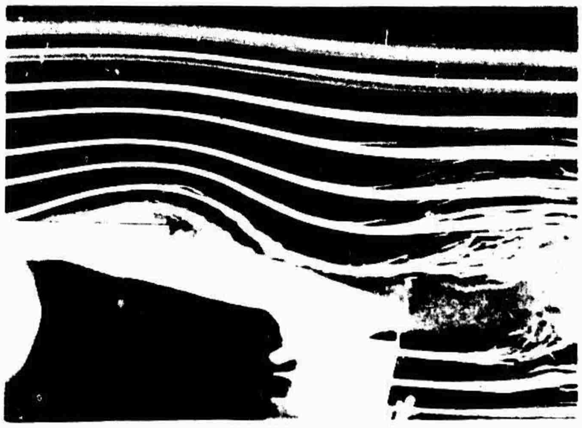

Fig. 1 Flow past a NACA 0015 airfoil with a spoiler at the quarter-chord position on the upper surface. Photograph was taken from the left rear side of the wing. Streak lines were traced out by smoke injected at different heights from a vertical column installed far upstream.

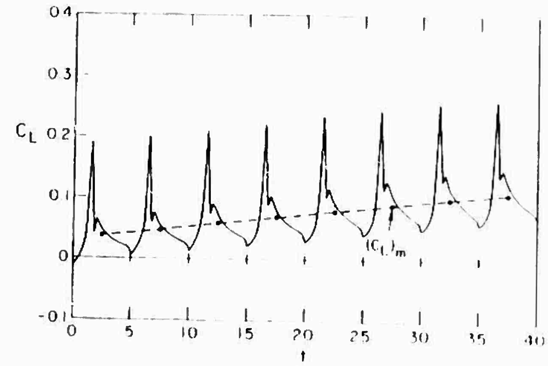

Fig. 4 Initial variation of lift coefficient for $\alpha = 0$ and $T = 5$. Circulation of vortices released at the midchord position is 0.5.

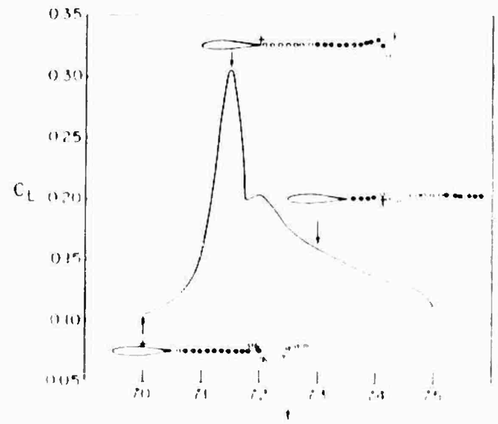

Fig. [illegible] Variation of lift coefficient and vortical configurations in a representative cycle of spoiler oscillation for $\alpha =$ [illegible] and $T = 5$. A cross represents a vortex released from the airfoil surface. The filled and open circles are used to show the positions of wake vortices of clockwise and counter-clockwise [illegible]

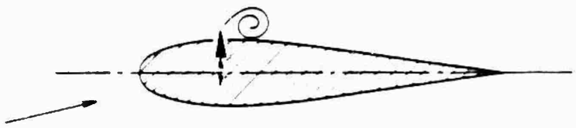

Fig. [illegible] Vortex generated behind an oscillating spoiler.

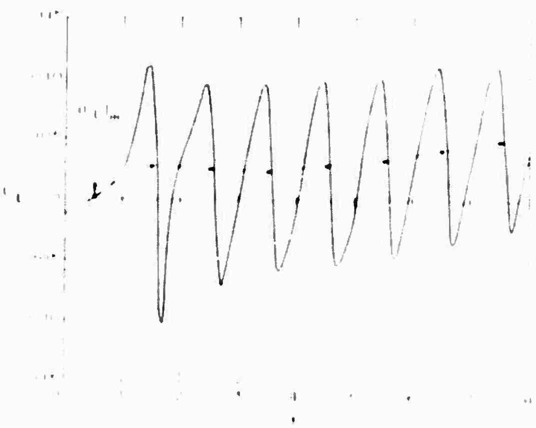

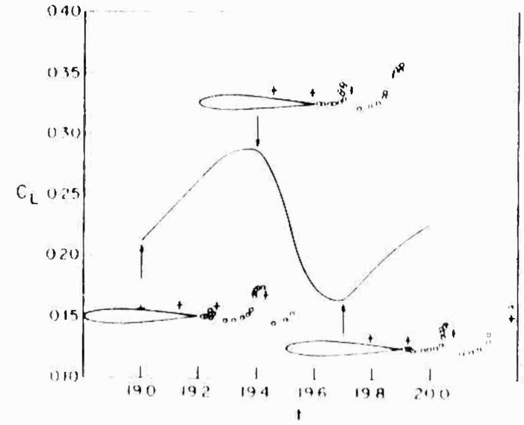

Fig. Variation of lift coefficient and vortical configurations in a representative cycle of spoiler oscillation for α = 0 and T = 1. Meaning of crosses and open circles can be found under Fig.

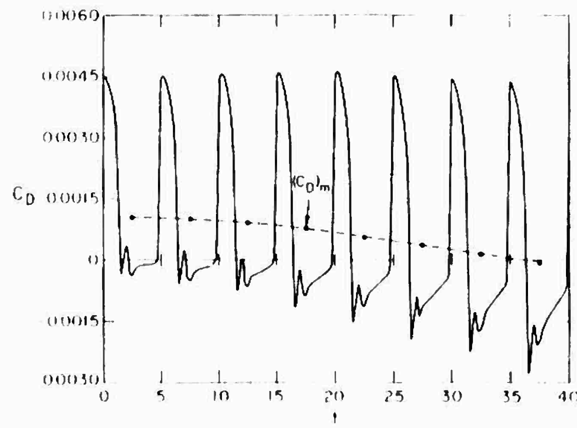

Fig. ...al variation of drag coefficient for α = 0 and T = 5. Circulation of vortices released at the midchord ...tion is ...

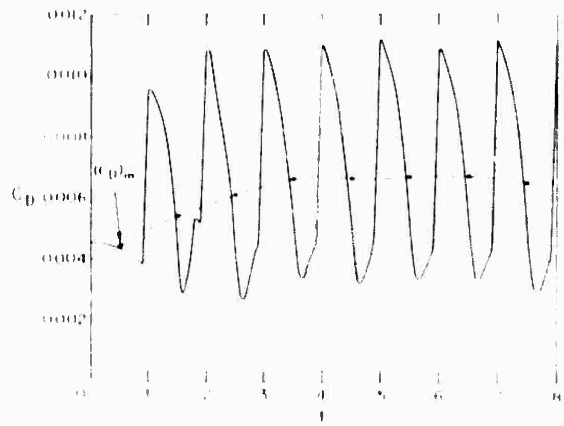

Fig. ... variation of drag coefficient for α = and T = . Circulation of vortices released at the midchord position is ...

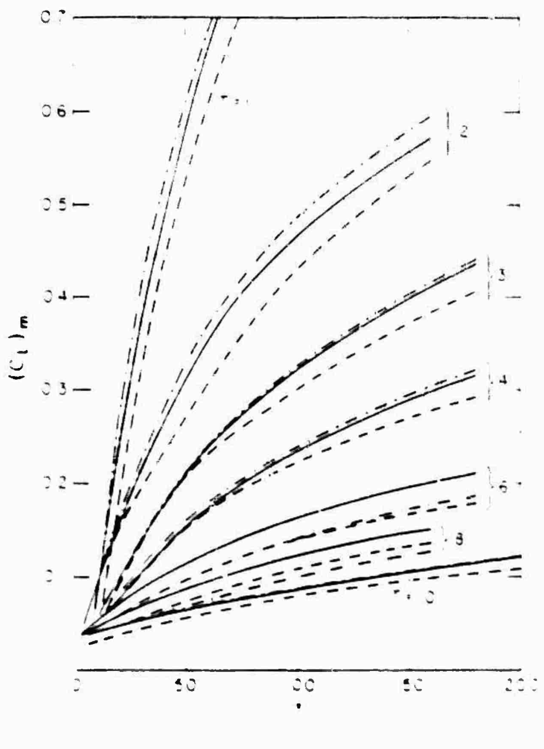

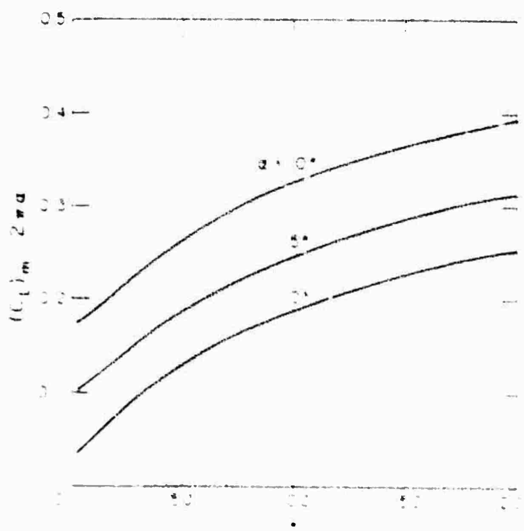

A NAVIER-STOKES CALCULATION OF THE AIRFOIL DYNAMIC STALL PROCESS

AD-P004 163

Stephen J. Shamroth
Scientific Research Associates, Inc.
Glastonbury, Connecticut 06033

Abstract

A time-dependent Navier-Stokes calculation procedure has been applied to the problem of an NACA 0012 airfoil oscillating in pitch in a low Mach number, high Reynolds number environment. The calculated results show many of the known physical features, including sudden suction surface separation, vortices shed at the leading and trailing edges and the return to attached flow at low incidences. Both the lift and moment coefficient curves show the expected features and the calculated wall pressure coefficients show strong correspondence to measured data.

Introduction

The unsteady flow field about an isolated airfoil is an important problem commonly encountered in a number of practical flow situations. These include airfoil flutter, vibration, buffet and gust response, as well as the problem of airfoil dynamic stall. This latter problem, airfoil dynamic stall, is the subject of the present paper. Airfoil dynamic stall occurs in a variety of situations. One important flow which has initiated the present study is the helicopter rotor problem. As the helicopter blade travels through the rotor disc, the blade experiences a varying incidence angle. Over most of the disc the blade will be unstalled (i.e., the flow will not contain any large separated regions leading to a decrease in blade lift or a generation of large blade moment coefficients); however, for example, in forward flight over the retreating portion of the disc large regions of separated flow may appear and over these regions the blade performance will deteriorate. This time history dependence of the problem makes dynamic stall prediction a particularly difficult task.

Despite its complex nature, airfoil dynamic stall has been the subject of a number of theoretical and experimental investigations over the past years. Some recent experiments giving surface pressure data for a variety of flow conditions include those of Carta and St. Hilaire[1-3], McAllister, Pucci, McCroskey and Carr[4] and Fukushima and Dadone[5]. Other investigations have examined the vortex shedding process for both oscillating wings (e.g. McAllister, Carr and McCroskey[6]) and steady wings in stall (e.g. Young, Meyers and Hoad[7]). In regard to analytical approaches to the dynamic stall problem, several early approaches were based upon inviscid and/or semi-empirical analyses. Although useful in certain cases, applications of inviscid or semi-empirical analyses to the dynamic stall problem are limited due to the highly complex nature of the flow and the strong dependence on viscous related phenomena. Likewise, use of inviscid approaches with boundary layer corrections or boundary layer [illegible] strong-interaction approaches are inappropriate due to the presence of strong shed vortices and large separation regions.

[illegible]

flow fields. A recent discussion of much of this work is given by Shamroth and Gibeling[8]. Although most airfoil Navier-Stokes analyses have focused upon either steady airfoils or impulsively started airfoils, some attention has been given to the more complex problem of airfoils oscillating in pitch. For example, Mehta[9] investigated an NACA 0012 airfoil oscillating in pitch in an incompressible laminar environment and Wu, Sampath and Sankar[10] considered a 9% thick Joukowski airfoil, again oscillating in an incompressible, laminar flow environment. In later works Shamroth[11] investigated an NACA 0012 airfoil oscillating in pitch between 0° and 10.5° in a turbulent environment and Tassa and Sankar[12] examined an airfoil oscillating between 0° and 20° in turbulent flow showing dynamic stall loops but no comparison with data was performed. The present paper focuses upon calculations of a high Reynolds, turbulent, 0.3 Mach number flow about an NACA 0012 airfoil oscillating in pitch and compares calculated surface pressures with experimental measurements.

Analysis

The Coordinate System

The presence of bounding surfaces of a computational domain which do not fall upon coordinate lines presents significant difficulties for numerical techniques which solve the Navier-Stokes equations. If a bounding surface (such as the airfoil surface) does not coincide with a coordinate line, serious numerical errors may arise in the application of boundary conditions for the problem and considerable effort may be required to reduce these errors to an acceptable level. Although this problem arises in both viscous and inviscid flows, it is more severe in viscous flows where no-slip conditions on solid walls can combine with boundary condition truncation error to produce numerical solutions which are both qualitatively and quantitatively in error. Thus coordinate systems are sought in which each no-slip surface of the specific problem falls on a coordinate line. Such a system is termed a body-fitted coordinate system. Several approaches are available to form a body-fitted coordinate system. Among the coordinate system candidates are conformal coordinate systems, systems based upon solution of a set of equations, and constructive systems. A comprehensive review of [illegible] papers discussing these [illegible] is given in Ref. 13. The approach [illegible] the present effort is a constructive [illegible] the required airfoil [illegible] coordinate line and in which grid point [illegible] specified by the user. The procedure was developed [illegible] for the isolated airfoil [illegible] Shamroth and Gibeling[8], and [illegible]

[illegible]

The form of the equations expressed in the more common coordinate systems can be found in standard fluid dynamic texts. One possible approach for solving the equations in general nonorthogonal form is the strong conservation approach such as that used by Steger[15]. A second possible approach solves a set of equations in which the metric coefficients do not appear within derivatives. This has been termed the quasi-linear form by Shamroth and Gibeling[8] and the chain rule conservation form by Hindman[16]. Although accurate results have been obtained with both forms of the equations, in cases where the Jacobian of transformation is independent of time the latter form is less sensitive to the precise manner in which the matrices are evaluated[8,15,16]. Therefore, the present effort utilizes the quasi-linear form. Discussion of coordinate systems having time-dependent Jacobians has been given by Thomas and Lombard[17].

If the spatial variables are transformed from the Cartesian coordinates (x,y) to a new set of coordinates (ξ, η) where

$$\xi = \xi(x,y,t) \qquad \eta = \eta(x,y,t) \qquad \tau = t \tag{1}$$

The quasi-linear form of the equations becomes

$$\frac{\partial W}{\partial \tau} + \xi_t \frac{\partial W}{\partial \xi} + \xi_x \frac{\partial F}{\partial \xi} + \xi_y \frac{\partial G}{\partial \xi} + \eta_t \frac{\partial W}{\partial \eta} + \eta_x \frac{\partial F}{\partial \eta} + \eta_y \frac{\partial G}{\partial \eta} = \frac{1}{Re}\left[\xi_x \frac{\partial F_1}{\partial \xi} + \eta_x \frac{\partial F_1}{\partial \eta} + \xi_y \frac{\partial G_1}{\partial \xi} + \eta_y \frac{\partial G_1}{\partial \eta} \right] \tag{2}$$

where

$$W = \begin{pmatrix} \rho \\ \rho u \\ \rho v \end{pmatrix}, \quad F = \begin{pmatrix} \rho u \\ \rho u^2 + p \\ \rho uv \end{pmatrix}, \quad G = \begin{pmatrix} \rho v \\ \rho uv \\ \rho v^2 + p \end{pmatrix}$$
$$F_1 = \begin{pmatrix} 0 \\ \tau_{xx} \\ \tau_{xy} \end{pmatrix} \quad G_1 = \begin{pmatrix} 0 \\ \tau_{xy} \\ \tau_{yy} \end{pmatrix} \tag{3}$$

In Eqs. (2) and (3) ρ is density, u and v are Cartesian velocity components, p is pressure, τ_{ij} is the stress tensor and Re is the Reynolds number. All quantities have been normalized by appropriate reference values. It should be noted that the present formulation assumes a constant total temperature flow field, thus relating the local static temperature to the velocity, [illegible]

$$[illegible] \tag{4}$$

[illegible]

governing equations are replaced by an implicit time difference approximation, optionally a backward difference or Crank-Nicolson scheme. Terms involving nonlinearities at the implicit time level are linearized by Taylor expansion in time about the solution at the known time level, and spatial difference approximations are introduced. The result is a system of multidimensional coupled (but linear) difference equations for the dependent variables at the unknown or implicit time level. To solve these difference equations, the Douglas-Gunn procedure for generating alternating-direction implicit (ADI) schemes as perturbations of fundamental implicit difference schemes is introduced. This technique leads to systems of coupled linear difference equations having narrow block-banded matrix structures which can be solved efficiently by standard block-elimination methods.

The method centers around the use of a formal linearization technique adapted for the integration of initial-value problems. The linearization technique, which requires an implicit solution procedure, permits the solution of coupled nonlinear equations in one space dimension (to the requisite degree of accuracy) by a one-step noniterative scheme. Since no iteration is required to compute the solution for a single time step, and since only moderate effort is required for solution of the implicit difference equations, the method is computationally efficient; this efficiency is retained for multidimensional problems by using ADI techniques. The method is also economical in terms of computer storage, in its present form requiring only two time-levels of storage for each dependent variable. Furthermore, the ADI technique reduces multi-dimensional problems to sequences of calculations which are one-dimensional in the sense that easily-solved narrow block-banded matrices associated with one-dimensional rows of grid points are produced. One problem which must be considered in using the technique to solve time-dependent flows is that of splitting error. The presence of splitting error may limit the allowable time step; however, as will be shown, the results obtained in the [illegible] considered are very promising despite this [illegible] problem. Methods [illegible] splitting error in transient [illegible] are a subject of current investigation at SRA.

Boundary Conditions

Prior experience in solving a variety of [illegible]

[illegible]

tational domain into the problem than can be removed through specification of physical boundary conditions. These additional variables can be removed in a variety of ways; for example, by use of one-sided differencing, by use of equations applied in a one-sided manner at the boundaries or through so-called "extraneous boundary conditions". If extraneous conditions are utilized, they should be chosen to be as reasonable as possible from a physical point of view. The hypothesis is adopted that if a solution can be obtained with the extraneous boundary conditions applied, then any defective influence of these extraneous conditions will result only from the approximations inherent in them, and the solutions should be assessed in this manner.

With these considerations in mind, the following approach was taken in setting boundary conditions for the airfoil flow field problem. The outer boundary was divided into four segments. These were an upstream boundary, a downstream boundary and two boundaries representing the wind tunnel walls. Consistent with a characteristic analysis, two physical boundary conditions are assumed for the upstream boundary and one for the downstream boundary. These represent items which would be set in a wind tunnel experiment and are the upstream stagnation pressure, the upstream flow angle and the downstream static pressure. The "extraneous boundary conditions" chosen were first derivative of density at the upstream boundary and second derivatives of both velocity components. It should be noted that the choice of boundary conditions used, while clearly appropriate for steady flows, may require further investigation in unsteady flows, particularly in regard to minimizing physically unrealistic wave reflections. Non-reflective boundary conditions are the focus of much current research; e.g., Ref. 23, and consideration of non-reflective boundary conditions for airfoils and cascades is under consideration by SRA.

The final boundary conditions concern the solid airfoil surface and wind tunnel walls. No-slip and [illegible] conditions were applied on the airfoil surface leading to a specification of zero velocity on the surface. In regard to the final boundary conditions, two approaches were used. First a one-side differenced transverse momentum equation was applied at the airfoil surface. Second a [illegible] gradient condition was used. Although the former is physically preferable, it had [illegible] whereas no such [illegible] were encountered with the latter. When the former was stable, results obtained with the two [illegible] differences. [illegible]

[illegible]

[illegible]

the boundary layer thickness δ, i.e.,

$$\ell = \kappa y \mathcal{D} \qquad (5)$$
$$[illegible] = .09[illegible]$$

where $\mathcal{D}$ is the van-Driest damping factor, κ is the von-Karman constant and δ is the boundary layer thickness. In the wake region downstream of the airfoil trailing edge δ is taken as 0.2h where h is the wake thickness. It is recognized that an accurate representation of the turbulent viscosity for this very complex flow with multiple shed vortices and large separated zones will require a more general turbulence model. However, in these initial dynamic stall studies the main focus is upon assessing the general level of prediction accuracy for the dynamic stall process, and identifying the sensitive parameters of the problem. Studies with a two equation model are currently in progress.

Artificial Dissipation

The final item to be considered concerns the use of artificial dissipation. Since the calculations were at high Reynolds numbers, it was necessary to add "artificial dissipation" terms to suppress central difference spatial oscillations. Such "artificial dissipation" could be added via the spatial differencing formulation (e.g., one-sided difference approximations for first derivatives) or by explicitly adding an additional dissipative type term. The present author favors the latter approach since when an additional term is explicitly added, the physical approximation being made is usually clearer than when dissipative mechanisms are contained within numerical truncation errors, and further, explicit addition of an artificial dissipation term allows greater control over the amount of non-physical dissipation being added. Obviously, the most desirable technique would add only enough dissipative mechanism to suppress oscillations without deteriorating solution accuracy. Various methods of adding artificial dissipation were investigated in Ref. [illegible] and these were evaluated in the context of a model one-dimensional problem containing a shock with a known analytic solution (one-dimensional flow with heat transfer). The methods which were considered included second-order dissipation, fourth-order dissipation and [illegible] dissipation techniques.

As a result of this investigation it was concluded that a second-order anisotropic artificial dissipation formulation suppressed [illegible]

[illegible]

[illegible]

$$Re_{\Delta x} = |a - \partial b/\partial x| \Delta x/\mu_e \quad (7)$$

where μ_e is the total or effective viscosity including both laminar and turbulent contributions, and Δx is the grid spacing. The dissipation coefficient d_x is non-negative and is chosen as the larger of zero and the local quantity $\mu_e(\sigma_x Re_{\Delta x} - 1)$. The dissipation parameter σ_x is a specified constant and represents the inverse of the cell Reynolds number below which no artificial dissipation is added. The dissipation coefficient d_y is evaluated in an analogous manner and is based on the local cell Reynolds number $Re_{\Delta y}$ and grid spacing Δy for the y-direction and the specified parameter σ_y. It should be noted that recently calculations have been run with artificial dissipation added in the conservative form $\partial(\rho^{n-1} d_x \, \partial\phi/\partial x)/\partial x$ and no significant difference between the forms was noted.

The question arises as to the values of σ_x and σ_y which should be chosen. Based upon the results of Ref. 24, as well as several other investigations for a variety of viscous subsonic and transonic flows it was concluded that setting between 0.1 and 0.025 suppressed non-physical oscillations, gave solutions which were insensitive to the precise value of σ in this range and gave good agreement with data. Therefore, second order damping in the conservative form was used in the present calculations with σ being set in the range between 0.1 and 0.05.

Results

The analysis described previously was applied to the flow about an NACA 0012 airfoil oscillating sinusoidally in pitch. The airfoil was immersed in a stream of Reynolds numbers equal to 2.08×10^6 and Mach number equal to 0.30. The airfoil mean incidence was set at 12° and oscillated with an amplitude of 8° at a reduced frequency based upon semichord of 0.125. These conditions correspond to Run 51.005 of the data of St. Hilaire and Carta[2,3]. The calculation was run for slightly more than one cycle using a highly stretched grid with the first point away from the airfoil being 0.32×10^{-5} chords from the airfoil. Approximately 950 time steps were required to proceed through a cycle for this reduced frequency. Higher reduced frequencies required fewer time steps. The calculation was initiated from a converged steady solution at 4° incidence. The calculation was begun with the artificial dissipation parameter, σ, being set to 0.05. During the high incidence downstroke portion of the calculation numerical problems appeared at $\alpha \approx 19.7°$, which required temporarily increasing artificial dissipation by raising the artificial dissipation factor, σ, to 0.5. It was kept at this value until $\alpha = 19°$ when it was dropped to 0.1. The numerical difficulties are believed related to mesh resolution and the temporary increase in artificial dissipation was adopted rather than adding more grid points simply due to economic necessity.

Comparisons between calculated and measured pressure distributions are given in Figs. 1-5 where the pressure coefficient, C_p, is defined as $(p-p_\infty)/(\frac{1}{2}\rho_\infty q_\infty^2)$. As can be seen in Figs. 1 and 2, the agreement during much of the upstroke is very good. The excellent comparisons shown in Figs. 1 and 2 give evidence to the time-accuracy of the calculation for the surface pressure. Further examination of the data and calculation shows the data to indicate stall at approximately 18°, whereas the calcu-

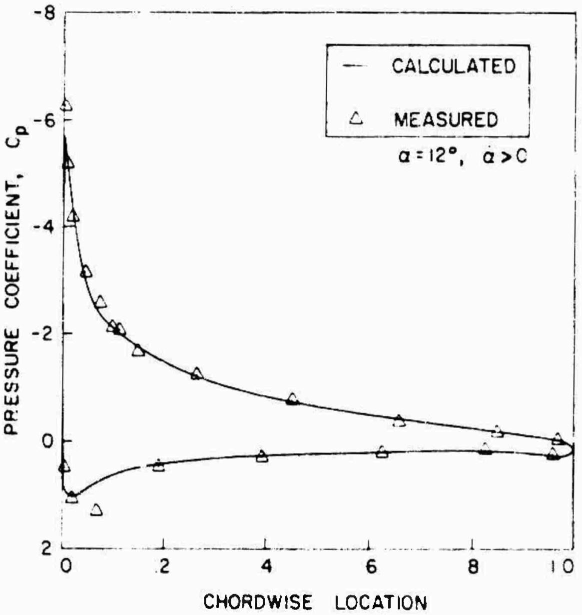

Fig. 1 - Calculated and measured pressure coefficient, $\alpha = 12°$.

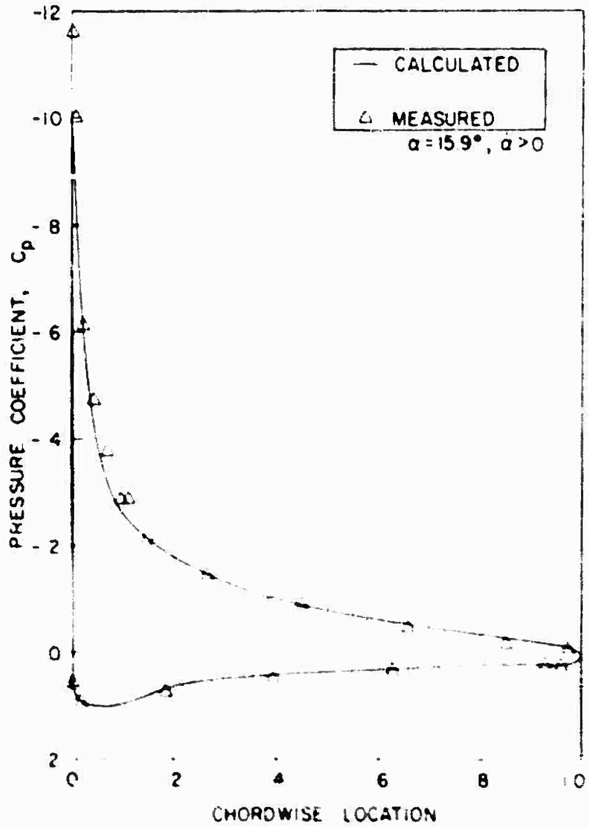

Fig. 2 - Calculated and measured pressure distribution, $\alpha = 15.9°$.

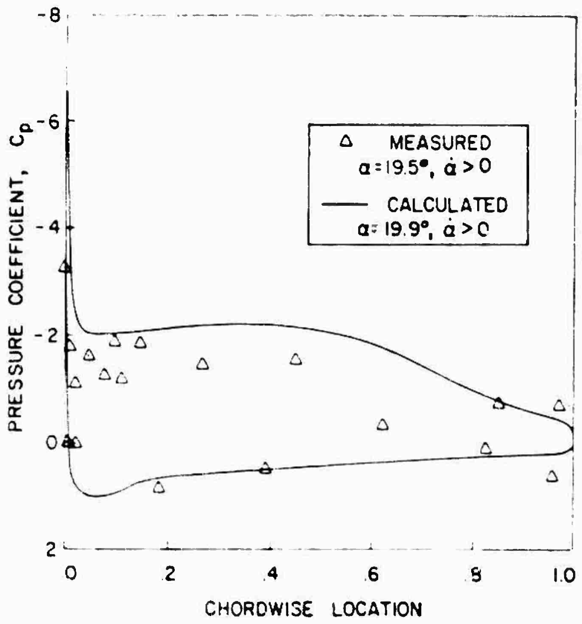

Fig. 3 - Calculated and measured pressure distribution, α = 19.7°.

lation indicated stall at 19.5°. Therefore, at incidence values greater than 17.5° the excellent quantitative agreement shown in Figs. 1 and 2 no longer was found. However, a strong qualitative agreement remained. For example, the data at 19.5° is presented with the calculation at α = 19.9°, $\dot{\alpha} > 0$ in Fig. 3. Although these are at different values of α, they represent pressure distributions at approximately the same incremental time after stall is initiated; the distributions are remarkably similar. Fig. 3, as well as figures not presented here due to space limitations, indicate that although the calculation predicts stall to occur after the measured incidence, once stall occurs, when referenced to the time of stall, the calculated and measured pressure distributions become quite similar. The major discrepancy in the calculated and measured values appear to lie in the prediction of vortex initiation. This, in turn, is likely to be dependent on turbulence and transition modeling. Comparisons over the downstroke are given in Figs. 4 and 5. As shown in Fig. 5 by α = 8.5°, $\dot{\alpha} < 0$, both measured data and calculation indicate the flow to be nearly recovered from the stall process. Obviously, the basic trends are in agreement as a strong qualitative comparison is shown between the calculation and the measured data. Overall, the detailed pressure distributions show good agreement with data.

Comparisons between measured and calculated lift and moment coefficient are given in Figs. 6 and 7. In viewing these figures it should be noted that lift and moment coefficient are integrated quantities. Relatively small differences in pressure distributions can lead to significant differences in lift coefficient and large differences in moment coefficients. Likewise, correspondence of the coefficients does not necessarily mean correspondence of surface pressure distribution. The predicted normal force coefficient is compared to the measured normal force coefficient in Fig. 6. As can be seen, the results are in good agreement over the upstroke. However, the measured lift begins to decrease at $\alpha \approx 18°$,

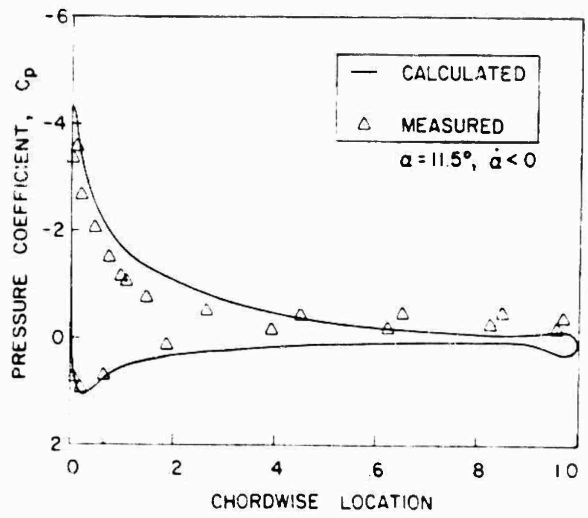

Fig. 4 - Calculated and measured pressure distribution, α = 11.5°.

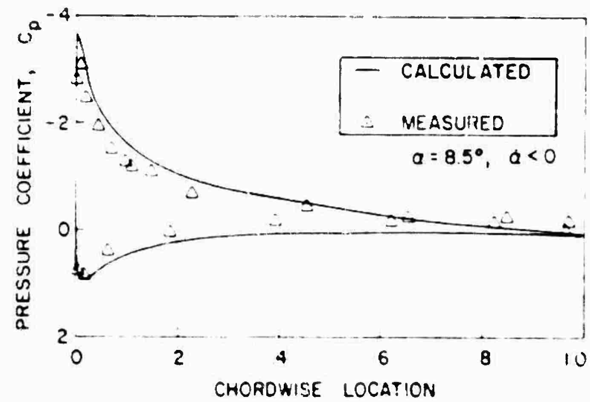

Fig. 5 - Calculated and measured pressure distribution, α = 8.5°.

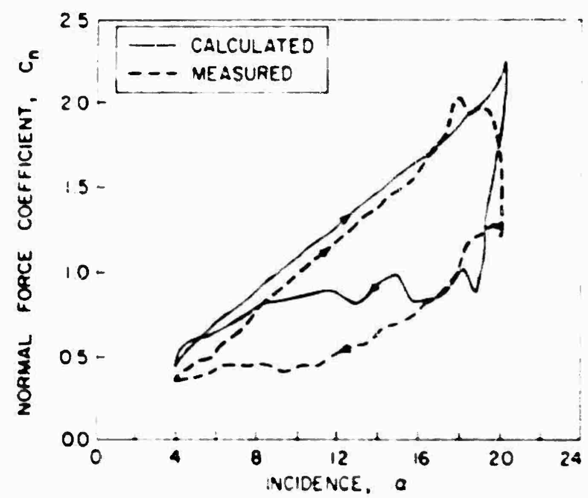

Fig. 6 - Normal force coefficient comparison.

whereas the calculated lift continues to increase until 20°. Both measurement and calculation show a precipitous drop near the maximum incidence. The major disagreement in the measured and calculated lift coefficient is over the low incidence half of the downstroke. The measured coefficient continued to decrease until α = 12°, whereas the calculated coefficient plateaued at $\alpha \approx 16°$, indicating a somewhat more rapid recovery from stall. This agreement is regarded as reasonable with the major difference occurring at low incidence during stall recovery. A comparison between calculated and measured moment coefficient is shown in Fig. 7. As can be seen in Fig. 7, the current comparison shows good qualitative agreement, the major difference being the larger negative moment coefficient calculated than measured near α_{max}. Overall the agreement is quite good.

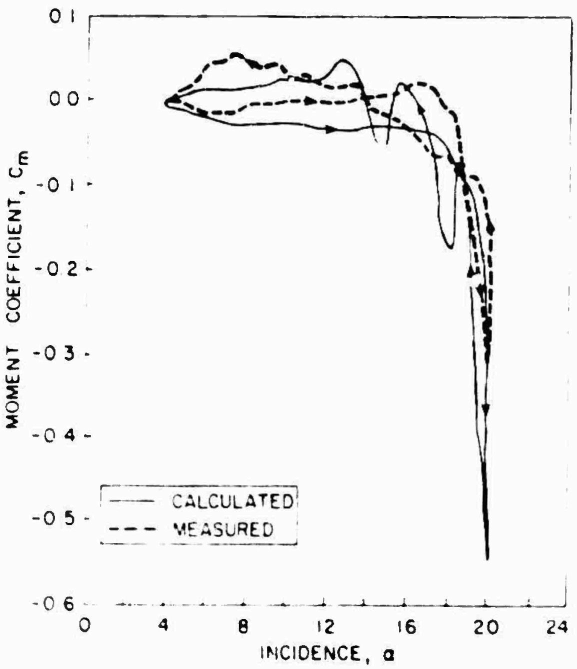

Fig. 7 - Moment coefficient comparison.

In addition to the surface pressure, plots of velocity vectors and vorticity contours were obtained at various times throughout the cycle. A detailed study of the plots and results show a clear pattern of the calculated stall process. During the initial portion of the upstroke the flow remains fully attached. At approximately 15.5° incidence both small leading edge and trailing edge separation bubbles appear on the suction surface. With increasing incidence the trailing edge separation point moves rapidly forward while the leading edge separation bubble remains small. By 18.5° the bubbles merge; however, they remain very thin and have only minimal effect on the outer nominally inviscid flow. The separated zone remains very thin until a dramatic change occurs at approximately α = 19.7°; at this incidence a leading edge vortex is shed and the stall process commences. Selected plots are shown in Figs. 8 and 9. The breakdown of the suction side flow is evident in both the vector plot Fig. 8 and the vorticity plot, Fig. 9. Also note

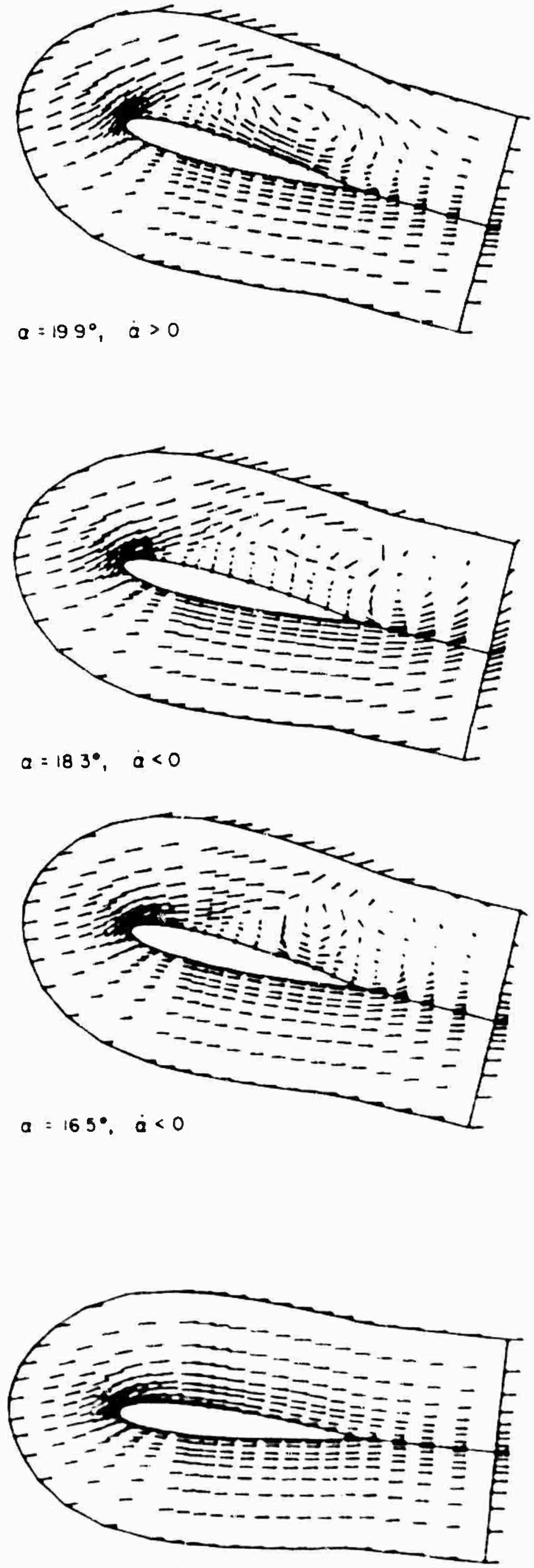

Fig. 8 - Velocity vector plots.

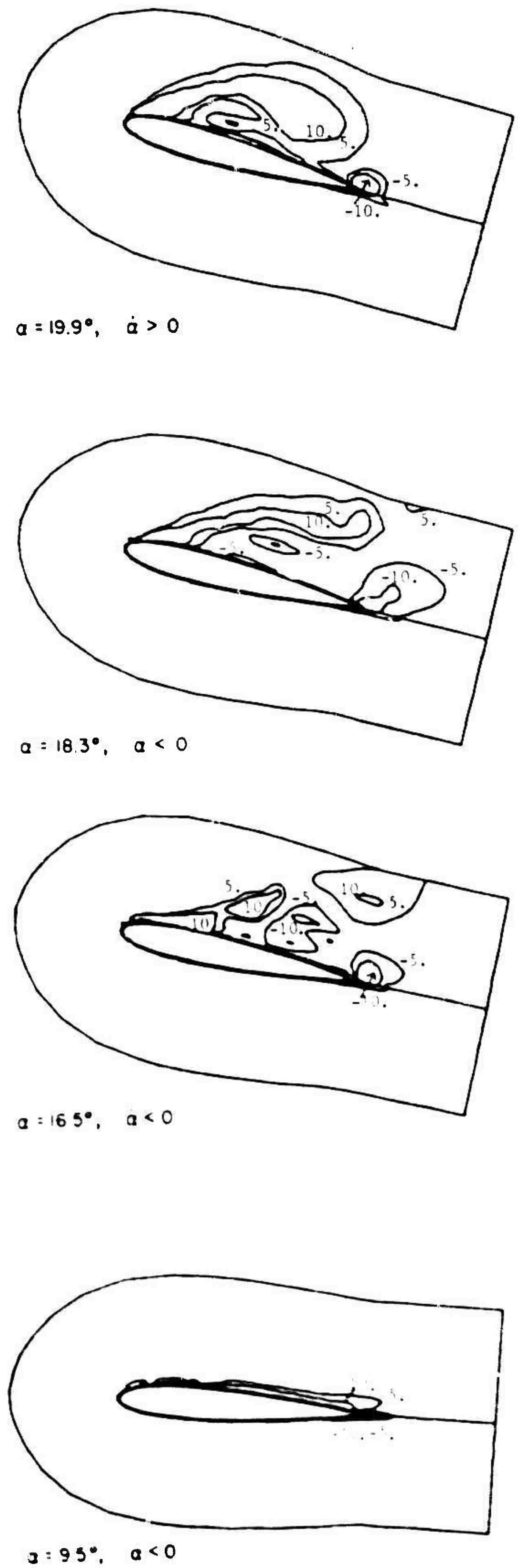

Fig. 9 - Vorticity contour plots.

the appearance of the trailing edge counterclockwise vorticity appears to arise from two sources. The first source is the pressure surface boundary layer being convected around the trailing edge and up the suction surface by the large clockwise leading edge separation zone. The second source of this negative vorticity is a secondary boundary layer arising as the large clockwise separated zone is brought to a no-slip condition at the airfoil surface. By $\alpha = 18.3°$, $\dot{\alpha} < 0$ the leading edge vortex has clearly broken away and the trailing edge vortex of opposite sign has increased in size and is moving somewhat upstream. This is demonstrated more clearly in the vorticity contour plot. By $\alpha = 16.5°$, $\dot{\alpha} < 0$ the vortices are tending to interact and begin to move downstream. This process also has been discussed by Robinson and Luttges.[25] Finally by $\alpha = 9.5°$, $\dot{\alpha} < 0$ the flow has fully recovered.

Concluding Remarks

A Navier-Stokes calculation procedure has been applied to the problem of an isolated airfoil oscillating sinusoidally in pitch. The calculation procedure has solved the governing equations by an implicit technique with turbulence represented via a mixing length model. A highly stretched grid was used to resolve the turbulent boundary layer. Although further effort remains in regard to the turbulence model, boundary conditions, etc., the resulting calculation showed many of the observed flow field features, including the vortex shedding and separation processes. In addition, comparisons between predicted and measured surface pressure distribution showed strong qualitative agreement.

Acknowledgment

This work was supported under a joint NASA/Army program between the Structures Laboratory, U.S. Army Research and Technology Laboratory (AVRADCOM) and NASA Langley Research Center under Contract NAS1-15214.

References

1. Carta, F.O.: "A Comparison of the Pitching and Plunging Response of an Oscillating Airfoil," NASA CR-3172, 1979.

2. St. Hilaire, A.O. and Carta, F.O.: "Analysis of Unswept and Swept Wing Chordwise Pressure Data from an Oscillating NACA 0012 Airfoil Experiment, Vol. I - Technical Report," NASA CR-3567, 1983.

3. St. Hilaire, A.O. and Carta, F.O.: "Analysis of Unswept and Swept Wing Chordwise Pressure Data from an Oscillating NACA 0012 Airfoil Experiment, Vol. II - Data Report," NASA CR-165927, 1983.

4. McAlister, K.W., Pucci, S.L., McCroskey, W.J. and Carr, L.W.: "An Experimental Study of Dynamic Stall in Advanced Airfoil Sections, Vol. 2, Pressure and Force Data," NASA TM 84245, USAAVRADCOM TR-82-A-8, 1982.

5. Fukushima, T. and Dadone, L.U.: "Comparison of Dynamic Stall Phenomena for Pitching and Vertical Translation Motions," NASA CR-2793, 1977.

6. McAlister, K.W., Carr, L.W. and McCroskey, W.J.: "Dynamic Stall Experiments on the NACA 0012 Airfoil," NASA Tech. Report 1100, 1978.

7. Young, W.H., Meyers, J.F., and Hoad, D.R.: "A Laser Velocimeter Flow Survey Above a Stalled Wing," NASA Tech. Paper 1266, 1978.

8. Shamroth, S.J. and Gibeling, H.J.: "Analysis of Turbulent Flow About an Isolated Airfoil Using a Time-Dependent Navier-Stokes Procedure," Boundary Layer Effects on Unsteady Airloads, AGARD-CP-296, 1980.

9. Mehta, U.B.: "Dynamic Stall of an Oscillating Airfoil," Unsteady Aerodynamics, AGARD-CP-277, 1977, pp. 23-1, 23-32.

10. Wu, J.C., Sampath, S. and Sankar, N.L.: "A Numerical Study of Unsteady Viscous Flow Around Airfoils," Unsteady Aerodynamics, AGARD-CP-277, 1977, pp. 24-1, 24-18.

11. Shamroth, S.J.: "A Turbulent Flow Navier-Stokes Analysis for an Airfoil Oscillating in Pitch," Unsteady Turbulent Shear Flows, Springer-Verlag, New York, 1981, pp. 185-196.

12. Tassa, Y. and Sankar, N.L.: "Dynamic Stall of an Oscillating Airfoil in Turbulent Flow Using Time-Dependent Navier-Stokes Solver, Unsteady Turbulent Shear Flows, Springer-Verlag, New York, 1981, pp. 207-220.

13. Thompson, J.F., Ed., Numerical Grid Generation, North Holland, New York, 1982.

14. Gibeling, H.J., Shamroth, S.J. and Eiseman, P.R.: "Analysis of Strong Interaction Dynamic Stall for Laminar Flow in Airfoils," NASA CR-2969, 1978.

15. Steger, J.L.: "Implicit Finite Difference Solution of Flow about Arbitrary Two-Dimensional Geometries," AIAA Journal, Vol. 16, 1978, pp. 679-686.

16. Hindman, R.G.: "Generalized Coordinate Forms of Governing Fluid Equations and Associated Geometrically Induced Errors," AIAA Journal, Vol. 20, 1982, pp. 1359-1367.

17. Thomas, P.D. and Lombard, C.K.: "Geometric Conservation Law and Its Application to Flow Computations in Moving Grids," AIAA Journal, Vol. 17, 1979, pp. 1030-1037.

18. Shamroth, S.J., McDonald, H. and Briley, W.R.: "Prediction of Cascade Flow Fields Using the Averaged Navier-Stokes Equations," to be published in ASME Journal of Engineering for Power.

19. Briley, W.R. and McDonald, H.: "Solution of the Multidimensional Compressible Navier-Stokes Equations by a Generalized Implicit Method," J. Comp. Phys., Vol. 24, 1973, pp. 372- .

20. Briley, W.R. and McDonald, H.: "On the Structure and Use of Linearized Block Implicit Schemes," J. Comp. Phys., Vol. 34, 1980, pp. 54-73.

21. Moretti, G. and Pandolfi, M.: "Critical Study of Calculations of Subsonic Flow in Ducts," AIAA Journal, Vol. 19, 1981, pp. 449-457.

22. Briley, W.R. and McDonald, H.: "Computation of Three-Dimensional Horseshoe Vortex Flow Using the Navier-Stokes Equations," Seventh International Conference on Numerical Methods in Fluid Dynamics, 198[illegible].

23. Numerical Boundary Condition Proceedings, NASA Conference Publication 2201, 1981.

24. Shamroth, S.J., McDonald, H. and Briley, W.R.: "A Navier-Stokes Solution for Transonic Flow Through a Cascade," SRA Rpt. 81-920007-F, 1982.

25. Robinson, M.C. and Luttges, M.W.: "Unsteady Flow Separation and Attachment Induced by Pitching Airfoils," AIAA Paper 83-0131, 1983.

AD-P004 164

SOME STRUCTURAL FEATURES OF UNSTEADY SEPARATING TURBULENT SHEAR FLOWS

Roger L. Simpson*
Southern Methodist University
Dallas, Texas 75275

ABSTRACT

Some physical features of unsteady separating turbulent boundary layers are presented for practical Reynolds numbers and reduced frequencies for helicopter and turbomachinery flows. Upstream of detachment in moderate amplitude flows, the flow is quasi-steady, i.e., the phase-averaged flow is described by the steady free-stream flow structure. Results presented here show that oscillation waveform and amplitude strongly influence the detached flow behavior.

I. INTRODUCTION

Unsteady turbulent boundary layers are of considerable interest because of unsteady aerodynamic phenomena associated with blades in compressors and turbines and with helicopter rotors in translating motion. They are particularly important during high lift or loading conditions when separation may be present during a portion of the oscillation cycle. Under such conditions there is significant interaction between the thick turbulent shear layer and the inviscid flow. Thus, information on the structure of separating unsteady turbulent shear layers is necessary for the understanding and proper calculation of these practical flows.

An unsteady flow experimental facility[1] with a multi-velocity component laser anemometer has been developed and used for measurements on two steady freestream separating flow cases[2,3] and two unsteady cases.[4,5,6] The unsteady cases had moderate amplitude sinusoidal velocity variations at reduced frequencies ($\omega L/U_\infty$) of 0.61 and 0.90. Other measurements at SMU, which are presented here, show that oscillation waveform and amplitude strongly influence the detached flow behavior. This is an important result since some practical unsteady flows have non-sinusoidal waveforms.

In spite of its importance, relatively little fundamental work has been done to describe the structure of unsteady separating turbulent shear layers. To this writer's knowledge, measurements of turbulent Reynolds stresses in an unsteady separating turbulent shear flow have been made only at SMU and by Cousteix et al.[7] at O.N.E.R.A. in France. Parikh et al.[8] and Jayaraman et al.[9] at Stanford examined some cases with small amounts of near-wall reversed flow during part of a cycle, but with no flow detachment. The amplitude to mean free-stream velocity ratio was about 0.3, 0.15, and 0.3 in these investigations, respectively. Direct measurements of the oscillating Reynolds shearing and normal stresses, surface shearing stress, and fraction of time backflow was present were made at practical Reynolds numbers and reduced frequencies by the SMU group.

As background for this paper, a brief summary is given in section II of the nature of a steady freestream separating turbulent boundary layer as determined by the work of Simpson et al.[2,3] and Shiloh et al.[10] at SMU. The results from the sinusoidally unsteady separating turbulent shear layer of Simpson et al.[4,5] are discussed in section III. Section IV presents the results from recent work that indicate that the oscillation waveform and amplitude strongly determine the behavior of a detaching turbulent shear layer.

II. SUMMARY OF THE NATURE OF A STEADY-FREESTREAM SEPARATING TURBULENT BOUNDARY LAYER

The fraction of time with forward flow near the wall γ_{pu} is a descriptive parameter of the flow detachment state.[11] Incipient detachment (ID) occurs with backflow 1% of the time; inter-

* Professor of Mechanical Engineering.

mittent transitory detachment (ITD) occurs with backflow 20% of the time; transitory detachment (TD) occurs with backflow 50% of the time; and detachment (D) occurs where the time-average wall shear stress is zero.

Figure 1 shows a qualitative sketch of the second steady-freestream bottom wall turbulent separated flow studies at SMU and the locations of ID, ITD, and D when determined 1 mm from the wall. The mean flow upstream of ID obeys the "law of the wall" and the "law of the wake" as long as the maximum shearing stress $-\rho\overline{uv}_{max}$ is less than 1.5 τ_w, where τ_w is the local wall shearing stress. When $-\rho\overline{uv}_{max} > 1.5\ \tau_w$, the Perry and Schofield[12] mean velocity profile correlation and the law of the wall apply upstream of ITD. Up to one-third of the turbulence energy production in the outer region is due to normal stresses effects, which modifies the relations between dissipation rate, turbulence energy, and turbulent shear stress that are observed farther upstream.

Downstream of detachment, the mean backflow profile scales on the maximum negative mean velocity U_N and its distance from the wall N.[13] A U^+ vs. y^+ law of the wall is not consistent with this result since U_N and N increase with streamwise distance while $u_\tau = (\tau/\rho)_w^{1/2}$ varies inversely with $(\tau)_w^{1/2}$. High turbulence levels exist in the backflow, with u and v fluctuations of the same order as U_N. $-\overline{uv}/u'v'$ becomes lower with increasing backflow and is about 25% lower in the outer region than for the upstream attached flow. Mixing length and eddy viscosity models are adequate upstream of detachment and in the outer region, but are physically meaningless in the backflow. γ_{pu} never reaches zero, indicating that there is no location with backflow all of the time. Normal and shear stress turbulence energy production in the outer region supply turbulence energy to the backflow by turbulence diffusion where it is dissipated. Negligible turbulence energy production occurs in the backflow.

This turbulence energy diffusion and the small mean backflow are supplied intermittently by large-scale structures as they pass through the detached flow as suggested by Figure 1. Space-time correlations obtained by a rapidly scanning laser anemometer reveal a relatively coherent structure of the large eddies.[14] The backflow does not come from far downstream. The frequency of passage n of these large-scale structures varies as U_e/δ and is about an order of magnitude smaller than the frequency far upstream of detachment. Reynolds shearing stresses in the backflow must be modeled by relating them to the turbulence structure and not to local mean velocity gradients. The mean velocity profiles in the backflow are a result of time-averaging of the large fluctuations and are not related to the cause of the turbulence.

Commonly used turbulence models for attached flows do not work well for separated flows. Eaton[15] discussed computations of the Simpson et al.[3] flow that were made for the 1980-1981 AFOSR-HTTM-Stanford Conferences on Complex Turbulent Flows. The integral, eddy viscosity, and mixing length methods that were used were essentially attached boundary layer methods with some ad hoc change that would make the detached flow mean velocity profiles look good. Unfortunately, the calculated Reynolds shearing stresses were much lower than the data. One 5 equation model was used that better predicted the shearing stress, but overpredicted the growth rate of the shear layer. Collins and Simpson[16] also showed that when attached flow mixing length models are imposed on detached flows, low mixing lengths and low shear stresses must be used in order to get good mean velocity profiles.

III. SUMMARY OF THE NATURE OF A SEPARATING TURBULENT FLOW WITH MODERATE AMPLITUDE SINUSOIDAL UNSTEADINESS

The experiments of Simpson et al.[5] show that a periodic unsteady separating turbulent boundary layer at a streamwise distance Reynolds number of 4.7×10^6, a practical reduced frequency of 0.61, and a ratio of the amplitude of the first harmonic to mean velocity outside the shear layer $u_{1e}/\bar{U}_e \approx 0.3$ has both similarities and differences with a steady freestream separating turbulent boundary layer at the same mean free-stream conditions (Figure [illegible]). (Note that a tilde denotes a periodic quantity, while a caret denotes an ensemble average obtained at a given phase ωt of a cycle.) Figure 3 shows the sinusoidal waveform $\tilde{U}_e/\bar{U}_e$. Upstream of where intermittent backflow begins ($\bar{\gamma}_{pu} < 1$), the flow and turbulence structure behave in a quasi-steady manner.

After the beginning of detachment, large amplitude and phase variations develop through each flow and the structure is not quasi-steady. Unsteady effects produce hysteresis in relationships between flow parameters. As the free-stream velocity during a cycle begins to increase, the fraction of time that the flow moves downstream $\tilde{\gamma}_{pu}$ at a given phase of the cycle increases as backflow fluid is washed downstream. As the free-stream velocity nears the maximum value in a cycle, the increasingly adverse pressure gradient causes progressively greater near wall backflow at downstream locations while γ_{pu} remains high at the upstream part of the detached flow. After the free-stream velocity begins to decelerate, the location where flow reversal begins moves upstream. This cycle is repeated as the free-stream velocity again increases.

Near the wall in the backflow region, the ensemble-averaged velocity leads the free-stream velocity by a large amount. The phase angle of the periodic backflow velocity and $\tilde{U}_1/\bar{U}$ are nearly independent of y near the wall. The mean backflow profile in terms of $\bar{U}/\bar{U}_N$ and y/N are approximately the same as for the comparable steady free-stream case. Thus, it appears that the ensemble-averaged backflow near the wall behaves like a quasi-steady flow when normalized with U_N and N.

Downstream of detachment $\overline{u^2}$ and $\overline{v^2}$ are slightly higher for the unsteady flow than the steady flow, especially near the wall where mean backflow occurs. The phase angle for $\tilde{u}_1$ in the backflow is progressively greater than the free-stream velocity phase angle as the flow moves downstream. The turbulence structure progressively lags the ensemble-averaged flow oscillation with $-\tilde{uv}_1$ lagging $\tilde{U}_1$ in the backflow by about 20°. The ratio $-\tilde{uv}_1/-\overline{uv}$ increases from about 0.[illegible] upstream of detachment to about 0.[illegible] downstream.

Near the wall $\hat{\gamma}_{pu}$ is nearly in phase with $\tilde{U}_1$, but since [illegible] negative the ensemble-averaged backflow is greatest when $\hat{\gamma}_{pu}$ is low and when $\widehat{u^2}$ and $\widehat{v^2}$ are near maximum values. In other words, $\hat{U}$ in the backflow is nearly in phase with $\widehat{u^2}$ and $\widehat{v^2}$. This is consistent with the general observation from the steady flow that $\overline{u^2}$ and $\overline{v^2}$ are greater when there is more mean backflow.

The steady flow results show that $-\overline{uv}/\sqrt{\overline{u^2}\,\overline{v^2}}$ decreases with decreasing $\bar{\gamma}_{pu}$. In the steady flow $-\widehat{uv}$ is greater with less ensemble-averaged backflow or greater $\hat{\gamma}_{pu}$. In other words, $\hat{U}$ is lower and $\tilde{U}_1$ is nearly in phase with $-\tilde{uv}_1$. As in the steady free-stream flow, $-\widehat{uv}/\sqrt{\widehat{u^2}\,\widehat{v^2}}$ decreases with decreasing $\hat{\gamma}_{pu}$, although there is some hysteresis and phase lag for the unsteady flow.

Simpson and Shivaprasad[6] reported measurements for a reduced frequency of 0.90 also with $\tilde{U}_{1e}/\bar{U}_e = 0.3$. The 0.90 reduced frequency has the same qualitative behavior as the 0.60 reduced frequency case. Downstream of detachment in both flows, the free-stream velocity and the pressure gradient are in phase. In both sinusoidally unsteady flows, the ensemble-averaged detached flow velocity profiles agree with steady freestream profiles for the same $\hat{\gamma}_{pumin}$ value near the wall when ωt_{pumin} at ~ 0. However, the higher reduced frequency flow has much larger hysteresis in ensemble-averaged velocity profile shapes when ωt_{pumin} at ≥ 0 than the lower reduced frequency. Larger and [illegible] values of the ensemble-averaged velocity profile shape factor $\hat{H}$ occur for this flow during phases when the nondimensional backflow is greater and $\hat{\gamma}_{pumin}$ = [illegible].

IV. THE EFFECT OF OSCILLATING VELOCITY WAVEFORM AND AMPLITUDE ON AN UNSTEADY SEPARATING TURBULENT SHEAR FLOW

The flows discussed in Section III have a sinusoidal variation of the free-stream velocity. Because practical unsteady flows in turbomachines often have a non-sinusoidal waveform with a large amplitude oscillation, it is useful to determine how these effects influence an unsteady turbulent shear flow. Figure [illegible] shows the sinusoidal waveform used in the experiments discussed above, an axial-compressor-type waveform, and a large amplitude oscillation, which were produced in the SMU wind tunnel. The parameter $R = (U_{e\,max} - U_{e\,min})/2\bar{U}_e$ is 0.3, 0.238, and 0.752 for these cases, respectively. In each case examined the mean free-stream velocity $\bar{U}_e$ was the same near the test-section throat (1.62m).

To survey the influence of waveform and amplitude on the flow, the surface skin friction at the wind tunnel throat and $\bar{\gamma}_{pumin}$ near the wall in the detaching flow zone were measured for these cases. Upstream of the strong adverse pressure gradient region, the mean unsteady friction factor C_{f_u} was found to be independent of waveform shape and amplitude:

$$C_{f_u} = [illegible]$$

Note that $\overline{U_e^2}$ is the mean square of the free-stream velocity and, thus, includes the non-linear contributions of the oscillatory flow to the mean dynamic pressure. Skin-friction measurements were made by a Rubesin-type surface hot-wire gauge described by Simpson et al.[3] This behavior is not totally surprising since the sinusoidal waveform flows well upstream of detachment behave in a quasi-steady manner at practical reduced frequencies.

Figure 4 shows $\bar{\gamma}_{pumin}$ vs. X at various ωt for the axial-compressor-type waveform. The interpretation of this diagram is similar to that discussed in Section III, but with significant differences. Like the [illegible] sinusoidal waveform cases, the backflow is washed downstream and the detached shear layer thickness decreases as the free-stream flow accelerates during [illegible] < ωt < 60°. For [illegible] < ωt < [illegible], U_e continues to increase and $\bar{\gamma}_{pumin}$ remains high. Higher harmonic oscillations of $\bar{\gamma}_{pumin}$ vs. ωt, such as shown in Figure 4, cause $\bar{\gamma}_{pumin}$ to be [illegible] downstream than upstream. For [illegible] < ωt < 300°, U_e is nearly constant and the variation of $\bar{\gamma}_{pumin}$ with X is primarily due to second harmonic effects. As U_e decreases for ωt > 300°, $\bar{\gamma}_{pumin}$ decreases.

Figure 6 shows $\bar{\gamma}_{pumin}$ vs. X at various ωt for the large amplitude oscillatory flow. During 20° < ωt < 120°, the backflow is completely washed out with $\bar{\gamma}_{pumin}$ becoming unity. As the freestream velocity reaches the maximum velocity, $\bar{\gamma}_{pumin}$ decreases in the downstream zone. Some second harmonic effects are evident for 120° < ωt < 240°. At larger ωt, $\bar{\gamma}_{pumin}$ drops to very low values in the downstream zone and backflow occurs as far upstream as the test-section throat (1.62m). The quantitative differences between Figures 4 and 6 indicate that the oscillation amplitude influences the detached flow behavior.

Some mean velocity profiles for the large amplitude flow are shown in Figure 7. These profiles are much different in shape than those of the lower amplitude sinusoidal cases since large variations of the detached shear flow occur and the shapes of the ensemble-averaged profiles for each phase of the cycle are much different than those of the lower amplitude flows. Figure 8 shows profiles of the mean fraction of time that the flow moves downstream, $\bar{\gamma}_{pu}$. Figure 9 shows profiles of the phase angle of the first harmonic. Unlike the lower amplitude sinusoidal waveform flows, there is little variation of this phase angle through the detached shear layer. This does not mean that this detached flow is quasi-steady because higher harmonics and non-linear effects are important.

CONCLUSIONS

New data for non-sinusoidal waveform unsteady separating flows have been presented. The waveform and amplitude of the unsteadiness strongly influence the detached flow behavior. In order to improve understanding of unsteady, detached flows, measurements of velocity [illegible] and the turbulence structure need to be made for these cases. These data would also [illegible] the [illegible] and [illegible] modeling of these flows.

ACKNOWLEDGMENTS

This work was supported by NASA, Ames Research Center, Experimental Fluid Dynamics Branch, under Grant NSG-2354, monitored by J.G. Marvin.

REFERENCES

1. Simpson, R.L., Sallas, J.J., and Nasburg, R.E., "Tailoring the Waveform of a Periodic Flow with a Programmable Damper," J. Fluids Engrg., 100, pp. 287-290, 1978.

2. Simpson, R.L., Strickland, J.H., and Barr, P.W., "Features of a Separating Turbulent Boundary Layer in the Vicinity of Separation," J. Fluid Mech., 79, pp. 553-594, 1977.

3. Simpson, R.L., Shivaprasad, B.G., and Chew, Y.-T., "The Structure of a Separating Turbulent Boundary Layer: Part 1, Mean Flow and Reynolds Stresses; Part 2, Higher Order Turbulence Results," J. Fluid Mech., 113, pp. 23-74, 1981.

4. Simpson, R.L., Shivaprasad, B.G., and Chew, Y.-T., "Measurements of Unsteady Turbulent Boundary Layers with Pressure Gradients," Rept. WT-6, SMU Dept. of Civil and Mechanical Engrg., August, 1980, NTIS AD-A090 585/1, 1980.

5. Simpson, R.L., Shivaprasad, B.G., and Chew, Y.-T., "The Structure of a Separating Turbulent Boundary: Part 4, Effects of Periodic Free-Stream Unsteadiness," J. Fluid Mech., 127, pp. 219-261, 1983.

6. Simpson, R.L. and Shivaprasad, B.G., "The Structure of a Separating Turbulent Boundary Layer: Part 5, Frequency Effects on Periodic Unsteady Freestream Flows," J. Fluid Mech., 131, pp. 319-339, 1983.

7. Cousteix, J., Houdeville, R., and Raynaud, M., "Oscillating Turbulent Boundary Layer with a Strong Mean Pressure Gradient" NASA TM, [illegible], 1979.

8. Parikh, P.G., Reynolds, W.C., Jayaraman, R., and Carr, L.W., "Dynamic Behavior of an Unsteady Turbulent Boundary Layer," pp. 35-36, Unsteady Turbulent Shear Flows, R. Michel et al. editors, Springer-Verlag, 1981.

9. Jayaraman, R., Parikh, P., and Reynolds, W.C., "An Experimental Study of the Dynamics of an Unsteady Turbulent Boundary Layer," Tech. Rept. TF-18, Thermosciences Div., Dept. Mech. Engrg., Stanford, CA., 1982.

10. Shiloh, K., Shivaprasad, B.G., and Simpson, R.L., "The Structure of a Separating Turbulent Boundary Layer: Part 3, Transverse Velocity Measurements," J. Fluid Mech., 113, pp. 75-90, 1981.

11. Simpson, R.L., "A Review of Some Phenomena in Turbulent Flow Separation," J. Fluid Engrg, 103, pp. 520-533, 1981.

12. Perry, A.E. and Schofield, W.H., "Mean Velocity and Shear Stress Distribution in Turbulent Boundary Layers," Physics Fluids, 16, pp. 2068-74, 1973.

13. Simpson, R.L., "A Model for the Backflow Mean Velocity Profile," AIAA J., 21, pp. 142-143, 1983.

14. Chehroudi, B. and Simpson, R.L., "The Structure of a Separating Turbulent Boundary Layer: Part 7, Space-Time Correlations from a Rapidly Scanning Laser Anemometer," submitted to J. Fluid Mech., 1983.

15. Eaton, J.K., "Incompressible Separated Flows- Internal Flows," pp. 886-895, Vol. II, The 1980-81 AFOSR-HTTM-Stanford Conference on Complex Turbulent Flows: Comparison of Computation and Experiment, edited by S.J. Kline, B.J. Cantwell, and G.M. Lilley; Stanford Univ. Dept. Mech. Engrg., 1982.

16. Collins, M.A. and Simpson, R.L., "Flowfield Prediction of Separating Turbulent Shear Layers," AIAA Journal, 16, pp. 291-292, 1978.

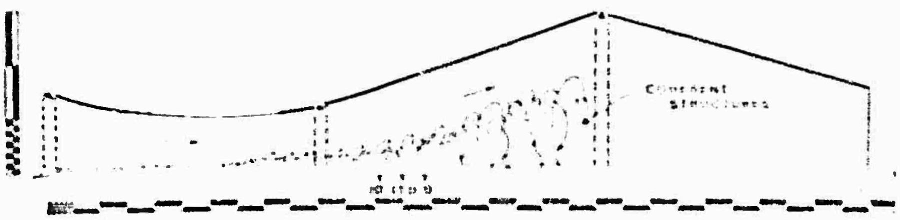

Figure 1. Sideview schematic diagram of the test section with the steady freestream separating turbulent boundary layer (Simpson et al. 1981a) on the bottom wall. The major divisions on the scales are 10 in. Note the baffle plate upstream from the blunt leading edge on the bottom test wall and side- and upper-wall set boundary-layer controls.

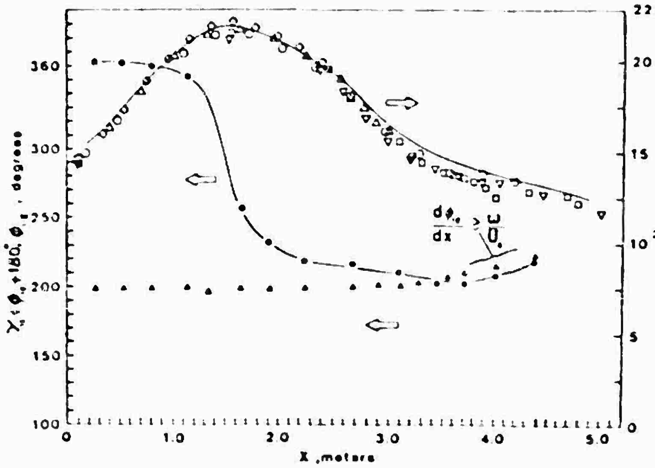

Figure 2. Freestream flow conditions for the steady free-stream flow of Simpson et al. (1981a) and the sinusoidal unsteady flow of Simpson et al. (1983). U_e, solid line, steady flow, open symbols, sinusoidal unsteady flow on different days. Phase angles of first harmonics: ▲, ϕ_{1e}, free-stream velocity; ●, $\phi_{1e} + 180 + \gamma_{1e}$, pressure gradient (dashed line for visual aid).

$$\hat{U}_e = \bar{U}_e \left\{ 1 + \sum_{n=1}^{\infty} \left[\frac{\bar{U}_{ne}}{\bar{U}_e} \cos(\omega nt - \phi_{ne}) \right] \right\}$$

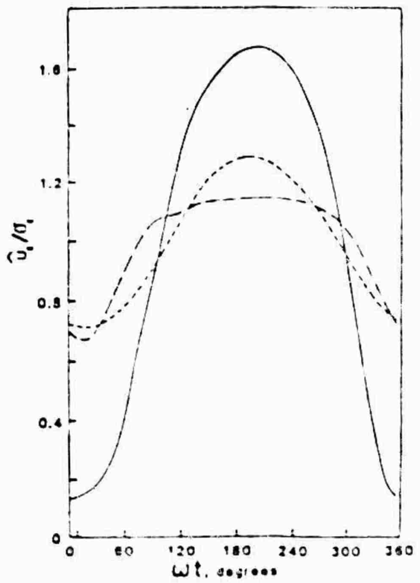

Figure 3. Velocity waveform shapes: dashed line, sinusoidal case; — - - -, compressor-type case; solid line, large amplitude case.

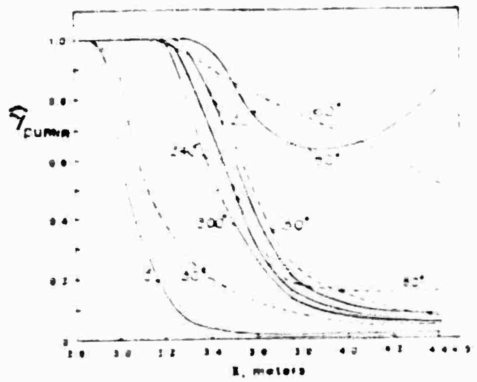

Figure 4. Phase-averaged γ_{min} vs. X for different ωt phases of a cycle for the compressor-type waveform.

Figure 5. $\hat{\gamma}_{min}$ or phase-averaged γ_{min} from thermal tuft measurements for the compressor-type waveform flow shown in Figure 4.

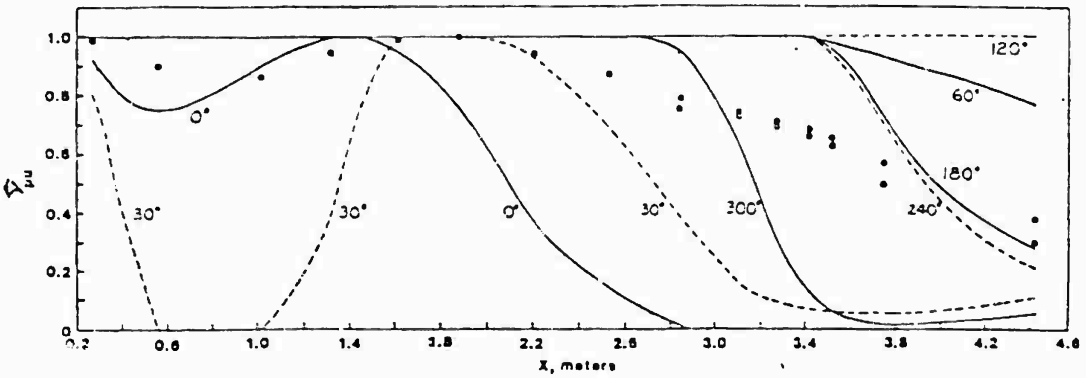

Figure 6. Phase-averaged Υ_{pumin} vs. X for different ωt phases of a cycle for the large amplitude waveform.

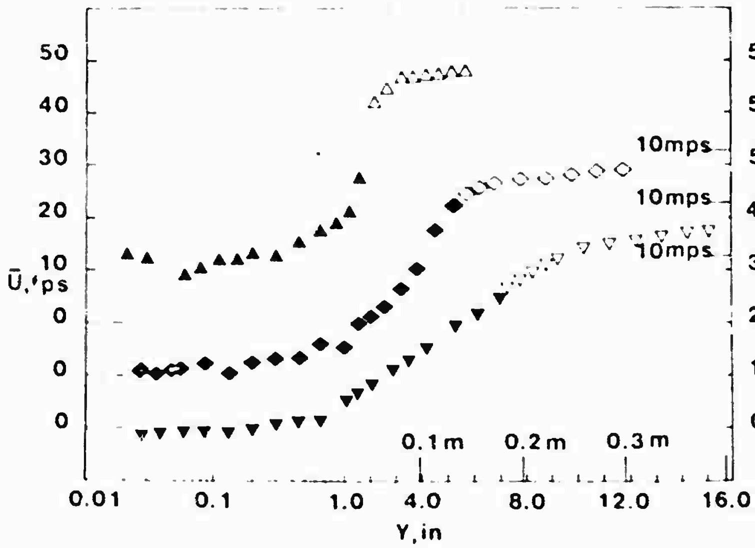

Figure 7. Mean velocity profiles U vs. y for the large-amplitude flow: Δ, 3.00 m; $\Diamond$, 3.66 m; ∇, 4.34 m. Closed symbols: directionally-sensitive laser anemometer data; open symbols: hot-wire anemometer data.

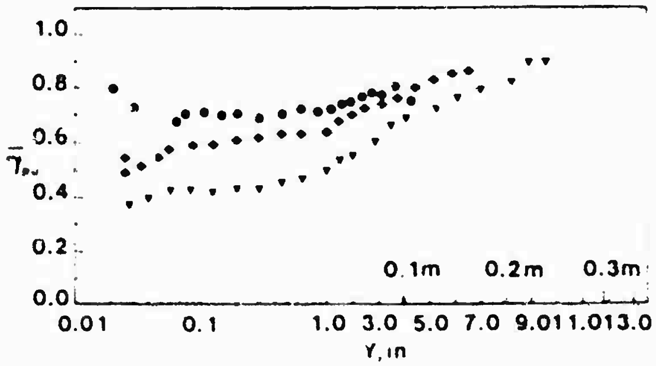

Figure [illegible]. $\bar{\Upsilon}_{pu}$ vs. [illegible] profiles for the large amplitude flow. Legend same as for figure 7.

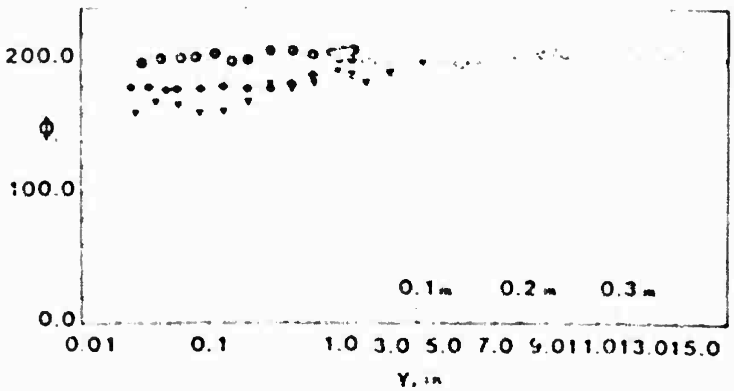

Figure 9. ϕ_i vs. [illegible] profiles for the large amplitude flow. Legend same as in figure 7.

CAN THE SINGULARITY BE REMOVED IN TIME-DEPENDENT FLOWS?

Tuncer Cebeci*, A. A. Khattab** and S.M. Schimke***
Aerodynamics Research and Technology Department
Douglas Aircraft Company
Long Beach, California 90846

AD-P004 165

Abstract

The evolution of unsteady boundary layers on oscillating airfoils is studied. The computational difficulties associated with the movement of the stagnation point as a function of space and time are solved by using a novel numerical scheme. Calculations are performed for pressure distributions typical of those found near the leading edge of airfoils. Results are presented for two cases. In the first, solutions are obtained for a flow with separation and with prescribed pressure distribution; they infer that a singularity develops and is of the same type as that observed on a circular cylinder started impulsively from rest. In the second, results are obtained for the same flow and the viscous flow solutions are interacted with the external flow by using an inverse boundary-layer method. The interaction seems to remove the singularity, however, these results are preliminary and need to be checked and improved upon.

1.0 Introduction

In recent years some important developments have occurred in the theory of two-dimensional laminar boundary-layer flows. The crucial discovery, due to van Dommelen and Shen, is that the solution of the boundary-layer equations with boundary conditions corresponding to a circular cylinder started impulsively from rest develops a singularity. This, with u_∞ denoting the velocity of the cylinder and a its radius, occurs at a time $u_\infty t/a = 3.0$ and at an angular distance $\phi = 111°$ from the forward stagnation point. At this time the position of zero skin friction is at $\phi = 106°$ close to, but not coincident with, the singularity. This discovery was made by solving the governing boundary-layer equations in Lagrangian form; subsequently, the existence of the singularity was confirmed by Cebeci using the Eulerian form and by Cowley using the method of series truncation. The importance of this result is two-fold. First, it is of importance to the fundamental theory of high-Reynolds number flows in indicating that an interactive theory is necessary to understand the evolution of the flow field at a finite time after the motion starts rather than only after a long time. Secondly, it is clear that significant changes will then occur in the flow field and these may be related to the phenomenon of vortex shedding. The physical processes which take place during the oscillation of the angle of attack of the airfoil are complicated and depend on a large number of parameters. For example, an important characteristic is a large vortex that is formed near the surface at some stage in the cycle and causes stall to occur shortly afterwards. The occurrence of the vortex is probably associated with a breakdown of the unsteady boundary layer.

The purposes of the present research are to determine the relationship between unsteady separation and singularities in the solution, and to explore the possibilities of removing this singularity by interaction of the viscous and inviscid equations. In this paper we outline the current status of the work, report our progress and describe the problems which remain to be solved. So far we have examined the evolution of the boundary layer near the nose of an oscillating airfoil and found that, when the reduced frequency is of the same order as in the experiments on dynamic stall, the unsteady boundary layer ceases to behave in a smooth manner just downstream of separation and before one cycle has been completed; as with the impulsively started circular cylinder, this irregular behavior signals the onset of a singularity in the solution of the boundary-layer equations. The equations and solution procedures used in the present study are described in Sections 2 and 3, respectively, and the results are presented and discussed in Section 4.

At present we are in the process of examining the link between this singularity and the external flow. Previous studies of steady interactive boundary layers have been reported for the leading-edge region of thin airfoils of the type considered here. If α is the angle of attack, it was observed that the boundary layer near the nose is well behaved and unseparated if $\alpha \le \alpha_s$ = 1.15 and although there is significant adverse pressure gradient. At higher values of α, however, separation occurred with an associated singularity which required the use of an interactive theory. With such a theory, calculation of flows with small separation presented no difficulties, but at higher values of α the solutions failed to converge, providing no steady-state solution. An important objective of our study of interactive unsteady flows is to determine whether a similar breakdown will occur. The equations and the solution procedures are similar to those of Sections 2 and 3 and the progress so far is described in Section 5.

2.0 Equations, Initial and Boundary Conditions

The boundary-layer equations for unsteady incompressible laminar flows on oscillating airfoils can be written as

$$\frac{\partial u}{\partial x} + \frac{\partial v}{\partial y} = 0$$

$$\frac{\partial u}{\partial t} + u\frac{\partial u}{\partial x} + v\frac{\partial u}{\partial y} = \frac{\partial u_e}{\partial t} + u_e\frac{\partial u_e}{\partial x} + \nu\frac{\partial^2 u}{\partial y^2}$$

*Staff Director, Research and Technology.
**Senior Engineer Scientist.
***Engineer-Scientist Specialist.

Usually the boundary-layer calculations for the above equations are performed for prescribed boundary conditions given by

$$u(s,0,t) = 0,\ v(s,0,t) = 0,\ u(s,n_e,t) = u_e(s,t) \quad (3)$$

and we shall refer to this as the standard problem. In the interactive problem we determine $u_e(s,t)$ partly from inviscid theory and partly from the pressure distribution resulting from the blowing velocity $d/ds\ (u_e\delta^*)$ induced by the boundary layer. Thus we write

$$u_e(s,t) = u_e^0(s,t) + u_c(s,t) \quad (4)$$

where $u_e^0(s,t)$ is the slip velocity at the airfoil according to inviscid theory and $u_c(s,t)$ is related to the blowing velocity by a variation of the Hilbert integral

$$u_c(s,t) = \frac{1}{\pi}\int_{-\infty}^{\infty} \frac{d}{ds}(u_e\delta^*)\frac{d\sigma}{s-\sigma} \quad (5)$$

Strictly, Eq. (5) is valid only for straight walls but it can be generalized for any airfoil shape as discussed by Cebeci and Clark[8]. For unseparated boundary layers the effect of $u_c(s,t)$ is generally weak but once separation occurs, its effect is enhanced significantly in the neighborhood of separation. That this must be so may be seen by noting that otherwise the integrand in Eq. (5) would develop a strong singularity at separation and cause the solutions to break down further downstream. As discussed in Refs. 7 and 8, it is sufficient to replace Eq. (5) by

$$u_c(s,t) = \frac{1}{\pi}\int_{s_a}^{s_b} \frac{(u_e\delta^*)'}{s-\sigma}\, d\sigma \quad (6)$$

where the prime denotes differentiation with respect to s.

In the standard problem, the solution of boundary-layer equations requires that the external velocity distribution be specified. Since the present effort is directed toward solutions near the leading edge of the airfoil, a local model for the potential flow has been chosen in the place of a full-potential-flow code. We consider an ellipse with major axis 2a and minor axis $2a\tau(\tau \ll 1)$ at an angle of attack $\alpha(t)$. The surface of the body is defined by

$$x = -a\cos\theta,\quad y = a\tau\sin\theta \quad -\pi \le \theta \le \pi$$

and with these definitions and to a first approximation, the external velocity around the ellipse can be deduced from inviscid flow theory to be

$$\bar{u}_e^0(s,t) = \frac{\xi + \xi_0}{\sqrt{1+\xi^2}} \quad (7)$$

Here $\bar{u}_e^0(s,t)$ denotes a dimensionless velocity, $u_e^0/u_\infty(1+\tau)$, the parameter ξ denotes a dimensionless distance related to the x- and y-coordinates of the ellipse by $x = 1/2\, a\tau^2\xi^2$, $y = a\tau^2\xi$ measured from the nose, and $\xi_0\ (\equiv\alpha/\tau)$ represents a dimensionless angle of attack. The parameter ξ is also related to the surface distance s by

$$s = a\tau^2\int_0^{\xi}(1+\xi^2)^{1/2}d\xi \quad (8)$$

We next define a dimensionless distance η by

$$\eta = \left[\frac{R(1+\tau)}{2\tau^2(1+\xi^2)}\right]^{1/2}\frac{n}{a} \quad (9a)$$

with $R = 2au_\infty/\nu$, and a dimensionless stream function f by

$$f(\xi,\eta,t) = [(1+\tau)au_\infty\nu\tau^2]^{-1/2}\psi(s,n,t) \quad (9b)$$

Introducing these relations together with Eq. (8) into Eqs. (1) and (2), it can be shown that the continuity and momentum equations can be written as

$$f''' + \frac{\xi}{1+\xi^2}f'^2 + (1+\xi^2)\bar{u}_e\frac{\partial\bar{u}_e}{\partial\xi} + (1+\xi^2)^{3/2}\frac{\partial\bar{u}_e}{\partial t_1} = f'\frac{\partial f'}{\partial\xi} - f''\frac{\partial f}{\partial\xi} + (1+\xi^2)\frac{\partial f'}{\partial t_1} \quad (10)$$

Here primes denote differentiation with respect to η and $t_1 = (1+\tau)u_\infty t/a\tau^2$.

The boundary conditions for f and f' become

$$f = f' = 0 \quad \text{at} \quad \eta = 0,$$

$$f' \to (1+\xi^2)^{1/2}\,\bar{u}_e(\xi,t_1) \quad \text{as} \quad \eta \to \infty \quad (11)$$

The definition of $\bar{u}_e(\xi,t_1)$ is given by

$$\bar{u}_e(\xi,t) = \frac{u_e(\xi,t)}{u_\infty(1+\tau)} = \frac{\xi + \xi_0(t_1)}{\sqrt{1+\xi^2}} + \frac{u_c}{u_\infty} \quad (12)$$

where with a prime denoting differentiation with respect to ξ,

$$\frac{u_c}{u_\infty} = \frac{2^{1/2}}{\pi R^{1/2}}\frac{(1+\tau)^{1/2}}{(1+\xi^2)^{1/2}}\int_a^b\frac{\Delta'(\xi,t_1)}{\xi-\bar{\xi}}\,d\bar{\xi} \quad (13)$$

and the dimensionless displacement thickness is given by

$$\Delta(\xi,t_1) = \lim_{\eta\to\infty}\,[\eta f_e'(\xi,\eta,t_1) - f(\xi,\eta,t_1)] \quad (14)$$

Substituting Eq. (14) into Eq. (13), and using Eq. (12), the edge boundary condition in Eq. (11) can be written as

$$f' + \xi + \xi_o(t_1) + \varepsilon \int_{\xi_a}^{\xi_b} \frac{\Delta'(\bar{\xi},t_1)}{\xi - \bar{\xi}} d\bar{\xi} \tag{15}$$

where

$$\varepsilon = \frac{1}{\pi\tau}\left[\frac{2(1+t)}{R}\right]^{1/2} \tag{16}$$

To complete the formulation of the problem, initial conditions must be specified in the (t,n) plane at some $s = s_0$, either on the lower or upper surface of the airfoil as well as initial conditions in the plane on both surfaces of the airfoil. In the latter case, if we assume that steady-flow conditions prevail at $t = 0$, then the initial conditions in the (s,n)-plane can easily be generated for both surfaces by solving the governing equations for steady flow, which in this case, are given by Eq. (1) and by

$$u\frac{\partial u}{\partial s} + v\frac{\partial u}{\partial n} = u_e\frac{du_e}{ds} + \nu\frac{\partial^2 u}{\partial n^2} \tag{17}$$

There is no problem with the initial conditions for Eqs. (1) and (17) since the calculations start at the stagnation point.

The generation of the initial conditions in the (t,n)-plane are not so straightforward to obtain as is discussed in Section 3.1.

3.0 Solution Procedure

The solution procedure for the set of equations and boundary and initial conditions given in Section 2 can be achieved in two parts concerned, respectively, with the leading edge and downstream region. These two parts are considered in the following two subsections. In both cases the solution procedure makes use of Keller's box method, which is a two-point finite-difference scheme extensively used for the solution of parabolic partial-differential equations, as discussed by Bradshaw et al.[9].

3.1 Leading-Edge Region

The generation of the initial conditions in the (t,n)-plane at $s = s_0$ requires a special numerical procedure. Given, as we are, the complete velocity profile distribution on the previous time line, there is, in principle, no difficulty in computing values on the next time line by an explicit method, but if we wish to avoid the stability problems associated with such a method by using an implicit method, we are immediately faced with the problem of generating a starting profile on the new time line.

In order to explain the problem further, it is instructive to see what happens to the stagnation point as a function of time. For this purpose let us consider Eq. (7). If we choose $\xi_o(t_1)$ to be of the form $\xi_o(1 + A \sin\bar{\omega} t_1)$, and let $\bar{u}_e^o = u_e^o/u_\infty(1+\tau)$, then Eq. (7) becomes

$$\bar{u}_e^o(\xi,t_1) = \frac{\xi + \xi_o(1 + A\sin\bar{\omega} t_1)}{\sqrt{1+\xi^2}} \tag{18}$$

where $\bar{\omega}$ is related to the dimensional frequency by

$$\bar{\omega} = \frac{a\tau^2}{(1+\tau)u_\infty}\omega$$

Here ξ_o and A denote parameters that need to be specified. Since by definition $\bar{u}_e^o = 0$ at the stagnation point, its location, ξ_s, is given by

$$\xi_s = -\xi_o(1 + A\sin\bar{\omega} t_1) \tag{19}$$

and so the upper and lower surfaces of the airfoil as functions of time are defined, in particular, by $\xi > \xi_s$ and $\xi < \xi_s$. For example, let us take $A = 1$, $\bar{\omega} = \pi/4$ and plot ξ_s/ξ_o in the (t,ξ)-plane, as shown in Figure 1 for one cycle $(0 \leq t_1 \leq 8)$.

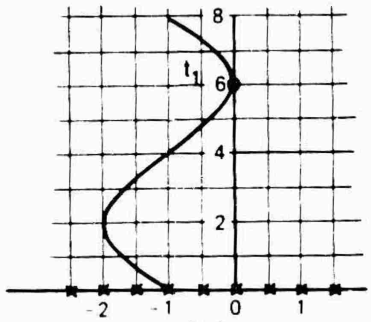

Fig. 1. Variation of stagnation point with time for one cycle according to Eq. (19), with $\bar{\omega} = \pi/4$, $A = 1$.

When $t_1 = 2$, the stagnation point ξ_s is at $-2\xi_o$, when $t_1 = 6$ is at 0, etc. If ξ_s were fixed, we could assume that $u = 0$ at $\xi = \xi_o$ for all time and all η, but this is not the case. It is also possible to assume that the stagnation point is coincident with zero u-velocity for a prescribed time. However, we should note that the stagnation point given by Eq. (19) is based on the vanishing of the external velocity. For a time-dependent flow, this does not necessarily imply that the u-velocity is zero across the layer for a given ξ-location and specified time. This point is substantiated by the results shown in Figure 2 taken from Ref. 10 and obtained with a novel numerical procedure called the characteristic box scheme. It is also evident from Figure 2 that flow reversals do occur due to the movement of the locus of zero u-velocity across the layer. This causes numerical instabilities which can be avoided by using either the zig-zag box or the characteristic box finite-difference scheme. The details of these numerical schemes have been reported in Ref. 9 and, with special reference to oscillating airfoils, in Ref. 10.

3.2 Downstream Region

A solution to the leading-edge region, obtained by the procedure of Section 3.1, may be used as initial conditions for the solution of the system of equations given by Eqs. (11) and (15) both with either standard or inverse procedures. In

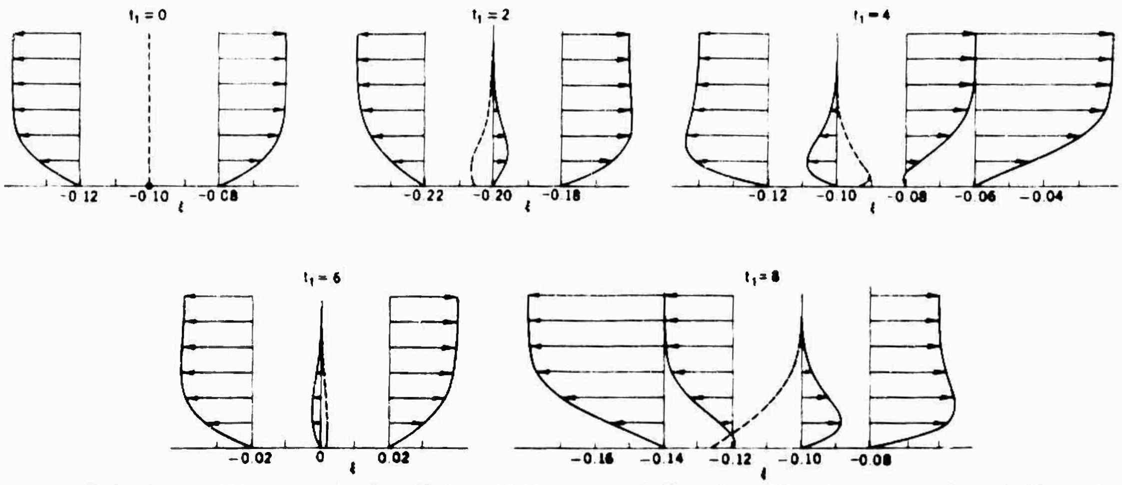

Fig. 2. Velocity profiles in the immediate neighborhood of the stagnation line at different times for $\bar{\omega} = \pi/4$ and A = 1. The dashed lines indicate the locus of zero u-velocity across the layer.

practice a standard procedure is used up to a specified ξ-location after which the calculations may proceed by either standard or inverse procedures. For example, to study the evolution of the boundary layer on an oscillating airfoil with prescribed pressure distribution, we use the standard procedure and where the inviscid and viscous flow equations are solved interactively, the inverse procedure is used after a short distance from the leading-edge region.

To solve the equations for both standard and inverse problems we use modified forms of Keller's box scheme. In the latter case we use the Mechul function formulation[9] which treats the external velocity as an unknown.

The box scheme reduces Eq. (10) to a first-order system. With $\bar{u}_e$, f' and f" represented by w, r and v, respectively, we write

$$f' = r \qquad (20a)$$

$$r' = v \qquad (20b)$$

$$w' = 0 \qquad (20c)$$

and obtain

$$v' + \frac{\xi}{1+\xi^2} r^2 + (1+\xi^2) w \frac{\partial w}{\partial \xi} + (1+\xi^2)^{3/2} \frac{\partial w}{\partial t_1}$$

$$= r\frac{\partial r}{\partial \xi} - v\frac{\partial f}{\partial \xi} + (1+\xi^2)\frac{\partial r}{\partial t_1} \qquad (20d)$$

With this notation, the boundary conditions given by Eq. (11) can be written as

$$f = r = 0 \quad \text{at} \quad \eta = 0 \qquad (21a)$$

$$r_e = (1+\xi^2)^{1/2} w_e \quad \text{at} \quad \eta = \eta_e \qquad (21b)$$

For the standard problem w_e is known and is given by Eq. (18). A fourth boundary condition is required for the inverse problem and is obtained from Eq. (15). Introducing a discrete approximation to Eq. (15), it can be written in the form

$$r_e(\xi_i) - c_{ii}\varepsilon\Delta(\xi_i) = g_i \qquad (22)$$

where c_{ij} is the matrix of interaction coefficients defining the relationship between the displacement thickness and external flow and the parameter g_i represents terms whose values are assumed to be known. It is given by

$$g_i = \xi_i + \xi_0 + \varepsilon \sum_{k=1}^{i-1} c_{ik}\Delta(\xi_k) + \varepsilon \sum_{k=i+1} c_{ik}\Delta(\xi_k) \qquad (23)$$

The system of Eqs. (20) to (22) has been solved by the numerical procedure of ref. 9 for the standard and inverse formulations.

4.0 Nature of the Singularity for an Oscillating Airfoil

One phase of the calculations for the oscillating airfoil was carried out by choosing $\alpha_0 = 1$, A = -1/2 and $\bar{\omega} = 0.1$. With these choices the maximum value of α_{eff}, defined by

$$\alpha_{eff} = \alpha_0(1 + A\sin\bar{\omega}t_1) \qquad (24)$$

is sufficient to provoke separation with a strong singularity if the boundary layer were steady. At present α_0, A, $\bar{\omega}$ are being varied to examine their effect on the nature of singularity.

The unsteady flow calculations displayed in Fig. 3 show that the boundary layer eventually separates, the flow remaining smooth. However, just downstream of separation, it is evident that a singularity develops in the solution in the neighborhood of ξ = 2.12 and $\bar{\omega}t_1$ = 308.75° and that it is not possible to continue the solution beyond this time without conceptual changes in the mathematical and physical formulation of the problem. While this is a satisfying conclusion, and may be interpreted as giving theoretical support to experimental observations of dynamic stall, it should be

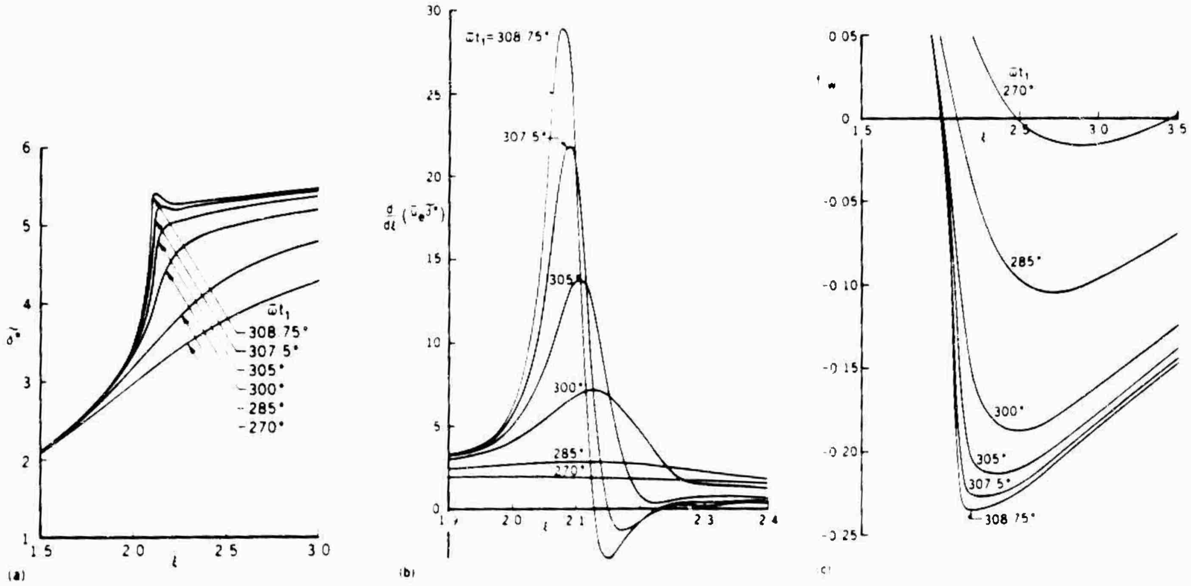

Fig. 3. Computed results for the oscillating airfoil, A = -1/2, $\bar{\omega}$ = 0.1. (a) Displacement thickness $\bar{\delta}^*$. (b) Displacement velocity, $d/d\xi\ (\bar{u}_e\bar{\delta}^*)$. (c) Wall shear parameter, f_w''.

treated with some caution. Boundary-layer singularities have been the subject of much controversy in recent years and it is clearly important to make sure that any irregularities in a computed solution are not creatures of the numerical method used. We, however, feel confident that the calculations reported here are accurate and that the singularity is real.

Figure 3a shows that the variation of the displacement thickness

$$\bar{\delta}^* = \frac{\delta^*}{a}\left(\frac{1+\tau}{\tau}\right)\frac{1}{\zeta\eta} \qquad (25)$$

is generally smooth except in the neighborhood of ξ = 2.12 and for $\bar{\omega}t_1$ = 308.75°. The first sign of irregularity is the steepening of the slope of $\bar{\delta}^*$ when $\bar{\omega}t_1$ = 300°. A local maximum of $\bar{\delta}^*$ occurs at ξ = 2.12 when $\bar{\omega}t_1$ = 308.75°. When the same results are plotted for a displacement velocity, $(d/d\xi)(u_e\bar{\delta}^*)$, (Fig. 3b), we observe that the steepening of the displacement velocity near ξ = 2.12 is dramatic. For example, for $\bar{\omega}t_1$ = 300°, the peak is at ξ = 2.125, for $\bar{\omega}t_1$ = 305°, it is at ξ = 2.105, for $\bar{\omega}t_1$ = 307.5°, it is at ξ = 2.09 and finally for $\bar{\omega}t_1$ = 308.75°, the peak moves to ξ = 2.08. It should be noted that the maximum value of displacement velocity moves towards the separation point with increasing $\bar{\omega}t_1$; the same behavior will be shown to occur for the circular cylinder discussed below.

As shown in Fig. 3c, the wall shear parameter f_w'' shows no signs of irregularity for $\bar{\omega}t_1 \leq$ 308.75° but a deep minimum in f_w'' occurs near ξ = 2.15, i.e. near the peak of $\bar{\delta}^*$.

It is interesting and useful to compare the results presented in Fig. 3 for an oscillating airfoil with those obtained for a circular cylinder started impulsively from rest. This comparison lends support to the accuracy of the present calculation method and at the same time enables us to compare the characteristics of two distinctly different unsteady flows near the singularity location. The circular cylinder problem has been extensively studied as reported in Refs. 11 and 12 and the present results shown below are in close agreement with those of previous authors, but with subtle differences which may have important implications.

Figure 4 shows the results obtained by Cebeci[2] for the circular cylinder problem. As in the case of the oscillating airfoil, the flow separates and remains smooth up to the separation point. However, just downstream of separation with increasing time, a singularity develops in the neighborhood of θ = 112° and t ≈ 3.0 and it was not possible to continue the boundary-layer calculations beyond this time and angular location. From Fig. 4a we see that while the variation of displacement thickness is smooth for values of θ less than 108°, it begins to steepen dramatically thereafter. The same results are plotted in Fig. 4b to demonstrate that, as in Fig. 3b, the displacement velocity exhibits a maximum which increases rapidly with time. Again the maximum shift towards the location of separation with increasing time.

The results of local skin-friction coefficient calculations in Fig. 4c follow similar trends to those obtained for the oscillating airfoil. In both cases, the distributions pass through zero with no signs of irregularity and do not exhibit any breakdown before the time corresponding to the singularity.

The very careful calculations of van Dommelen and Shen are reproduced on Figures 5 and 6 for displacement thickness and velocity profiles, respectively. The corresponding displacement thickness results of Cebeci[2] together with the new calculations of the velocity profiles are reproduced for

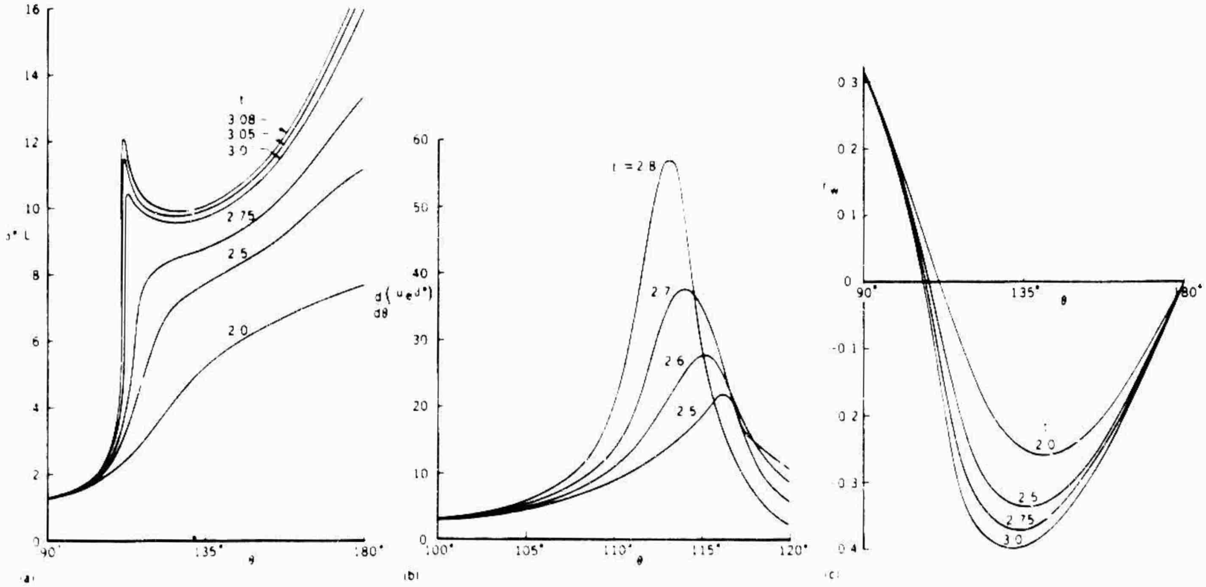

Fig. 4. Computed results of Cebeci[2] for the circular cylinder. (a) Displacement thickness δ^*/L. (b) Displacement velocity, $d/d\theta(u_e\delta^*)$. (c) Wall shear parameter, f''_w.

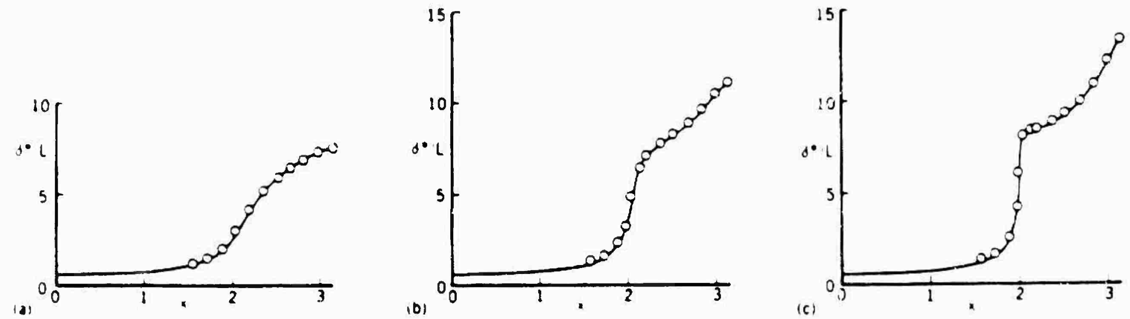

Fig. 5. Comparison between the displacement thickness values obtained by van Dommelen and Shen[1] (circles) and by Cebeci[2] (solid line) for the circular cylinder. (a) t = 2.0, (b) t = 2.5, (c) t = 2.75. (x is in radians.)

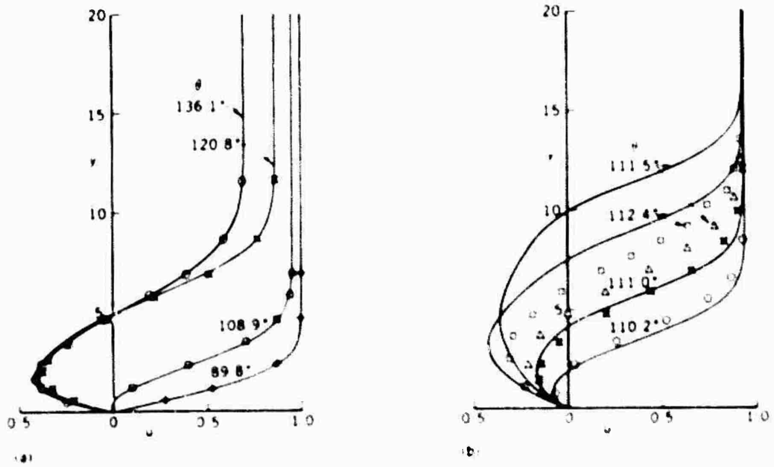

Fig. 6. Comparison between the velocity profiles obtained by van Dommelen and Shen[1] (solid lines) and by Cebeci[2] (symbols). (a) 2.75, (b) t = 2.984375 (van Dommelen and Shen) and t = 2.9875 (present calculations).

comparison purposes. As can be seen from Fig. 5, the agreement between the sets of calculations for three values of t = 2, 2.5 and 2.75 is excellent. The velocity profiles of Fig. 6a, which correspond to a time t = 2.75 as in Fig. 5, are also in excellent agreement for various angular locations. In contrast, the calculated velocity profiles of van Dommelen and Shen[13] at t = 2.984375 show differences from the present results obtained at t = 2.9875. The figure confirms the expected close agreement of the two sets of results at the two smallest angular locations, but significant differences at the two highest values. The trend is different in that the present results show that the location and the magnitude of the maximum negative velocity increases with angular location. Also the tendency for flattening of the velocity profiles in the vicinity of the singularity is not confirmed by the present results.

Figure 7 shows the velocity profiles obtained by Cebeci[2] for two values of t as a function of angular location. It is clear that the magnitude of negative velocity increases with angular location and suggests that as the singularity is approached, the magnitude of the negative velocity will tend to infinity.

Figure 8 allows comparison of the displacement velocities obtained by Cowley[3] and by the present method for four values of time. We would expect, from the previous comparisons that the two sets of results would be in close accord at least for times

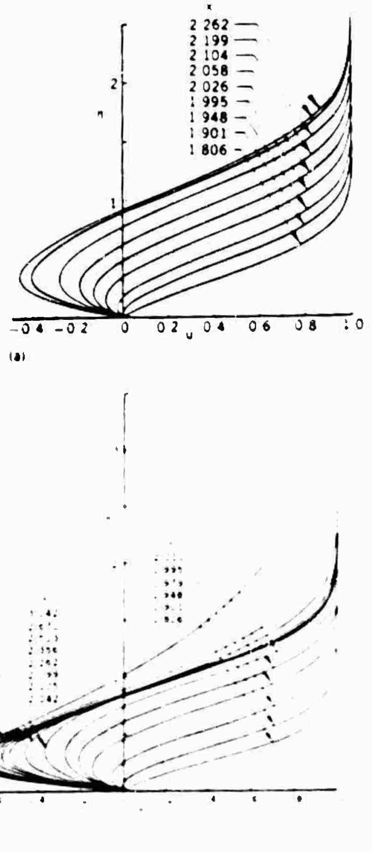

Fig. 7. Computed velocity profiles for the circular cylinder according to the calculations of Cebeci[2]. (a) t = 2.5, (b) t = 2.75. (x is in radians.)

up to 2.75. The figure shows the expected close agreement until the maximum value is approached. The discrepancies apparent at higher values of θ cannot readily be explained, and it should be noted that the location and time of singularity occur at different values of θ; the results of Cowley and van Dommelen and Shen appear to agree in this respect. The reasons for these discrepancies are presently under investigation.

4.0 Effect of Interaction on the Singularity

The interaction procedure discussed in Section 3 has been applied to the flow problem previously examined in Section 4 with the standard method. The results are shown in Fig. 9 and are discussed below. In contrast to the standard problem which makes the implicit assumption of infinite Reynolds number, the interaction requires the specification of a finite Reynolds number. In addition, a thickness ratio τ has to be specified and, since the definition of ε involves R and τ, the calculations are performed for a specific value of ε, ($\equiv 4.5 \times 10^{-3}$) for the present results. Other values of ε are being examined to determine the effect of combinations of Reynolds number and thickness ratio.

The present calculations were performed in the following way. For all values of time with $\overline{\omega t_1}$ ranging from 0 to 360°, the standard method with the leading-edge region procedure of Section 3 was used to generate the initial conditions at a short distance from the leading edge, ξ = 0.5. With these initial conditions and for each value of $\overline{\omega t_1}$, the inverse method was used to calculate the unsteady flow from ξ = 0.5 to ξ = 5.5, for the specified value of ε. Since the system of equations is now elliptic, several sweeps in the ξ-direction were necessary to achieve a converged solution. Where flow reversal was encountered, as happens for values of $\overline{\omega t_1} > 270°$ and ξ > 2, up to three sweeps are required; where separation did not exist, a single sweep was sufficient. It is to be expected that the value of ε will influence the number of sweeps and, since it is linked to physical parameters, will affect the singularity and the size of the bubble.

Figure 9a shows the variation of displacement thickness δ^* and Fig. 9b the wall shear parameter f_w'' as a function of nondimensional distance ξ and time. It is evident that for values of ξ < 2.5, the solutions are well behaved. As expected, the displacement thickness δ^* increases with ξ for all values of time and reaches a maximum around $\overline{\omega t_1}$ = 300° as a consequence of the change in the angle of attack. In the same range of ξ, the shear stress parameter decreases for all values of $\overline{\omega t_1}$ and reaches a minimum corresponding to the maximum in displacement thickness.

For values of ξ > 2.5, the solutions remain well behaved until around $\overline{\omega t_1}$ = 290°. The general trends are in accord with the expectations and there is negligible difference between the results obtained with the standard and interactive methods for values of $\overline{\omega t_1}$ up to the maximum for which the standard method allowed solutions. The wiggles apparent in the solutions for high values of $\overline{\omega t_1}$ remain to be explained. In particular, the influence of numerical parameters such as Δξ and Δt spacing together with the assigned value of ε need to be systematically explored. Nevertheless, it is important to note that the singularity no longer

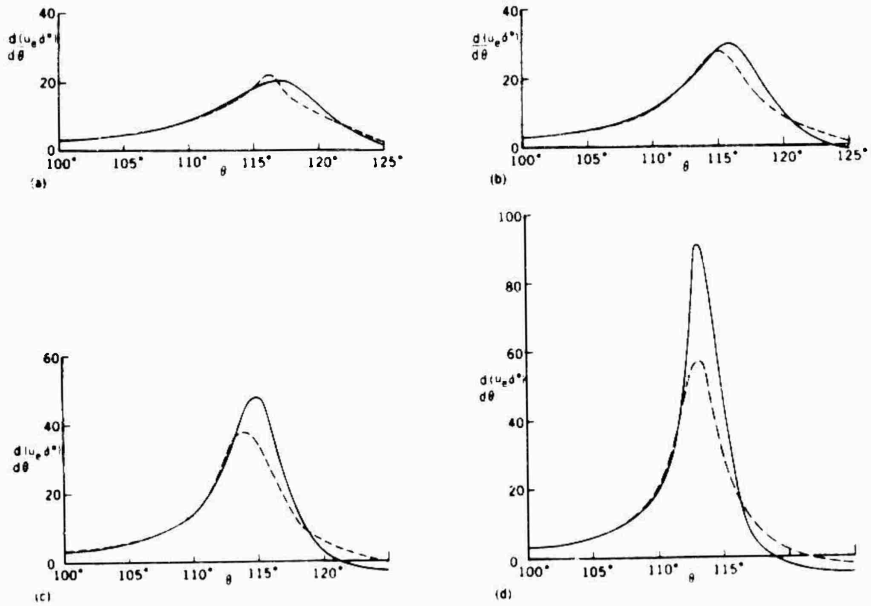

Fig. 8. Comparison between the displacement velocity values obtained by Cowley[3] (solid lines) and by the present method (dashed lines)for the circular cylinder. (a) t = 2.5, (b) t = 2.6, (c) t = 2.7, (d) t = 2.8.

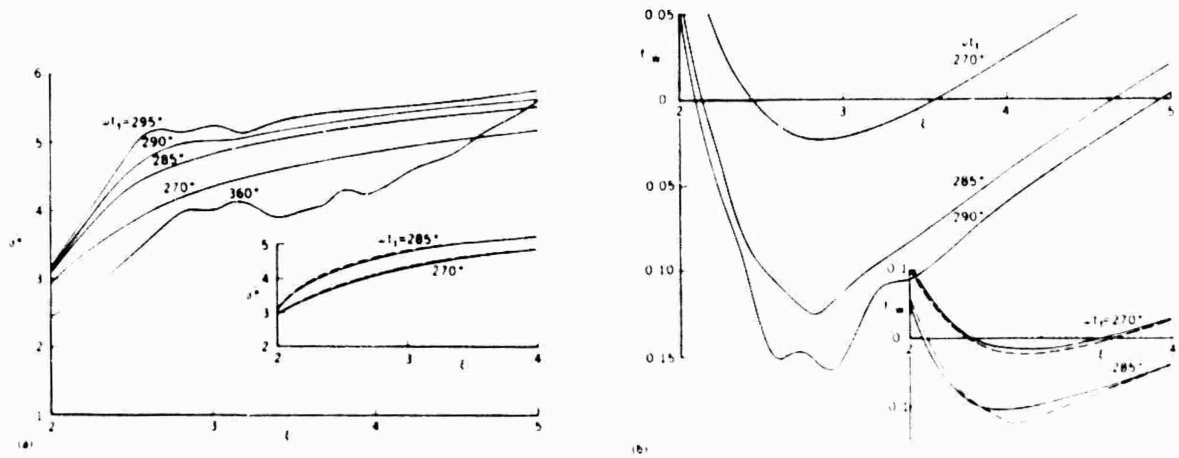

Fig. 9. Effect of interaction on the variation of (a) displacement thickness δ^*, (b) wall shear parameter f_w'' for an oscillating airfoil with ϵ = 4.5 x 10^{-3}. Solid lines in the insert represent the results obtained by the standard method and dashed lines those by the inverse method.

exists and, in contrast to the standard method which allowed the solutions to be performed up to ωt_1 = 308.85°, the calculations with the inverse method were performed for a complete cycle. It is also important to note that the chosen value of ϵ implies a high Reynolds number ($\sim 10^6$) for a thickness ratio of τ = 0.1. Since typical leading-edge bubbles are associated with lower values of Reynolds number, we expect that interactive calculations can be performed over a wide range of angle of attack without problems associated with the singularity.

6.0 Acknowledgment

This research was supported under Air Force Office of Scientific Research contract F496720-82-C-0055.

7.0 References

1. van Dommelen, L.L. and Shen, S.F.: The Genesis of Separation. In Numerical and Physical Aspects of Aerodynamic Flows (ed. T. Cebeci), Springer-Verlag, NY, 1982.

2. Cebeci, T.: Unsteady Separation. In Numerical and Physical Aspects of Aerodynamic Flows (ed. T. Cebeci), Springer-Verlag, NY, 1982.

3. Cowley, S.: Private communication.

4. McCroskey, W.J. and Pucci, S.L.: Viscous-Inviscid Interaction on Oscillating Airfoils in Subsonic Flow. AIAA J., 20, 167-174, 1982.

5. Carr, L.W., McCroskey, W.J., McAlister, K.W., Pucci, S.L. and Lambert, O.: An Experimental Study of Dynamic Stall on Advanced Airfoil Sections. Vol. 3. Hot-Wire and Hot-Film Measurements. NASA TM 84245, 1982.

6. Carr, L.W., McAlister, K.W. and McCroskey, W.J.: Analysis of the Development of Dynamic Stall Based on Oscillating Airfoil Experiments. NASA TN D-8382, 1977.

7. Cebeci, T., Stewartson, K. and Williams, P.G.: Separation and Reattachment Near the Leading Edge of a Thin Airfoil at Incidence. AGARD CP 291, Paper 20, 1981.

8. Cebeci, T. and Clark, R.W.: An Interactive Approach to Subsonic Flows with Separation. In Numerical and Physical Aspects of Aerodynamic Flows II, (ed. T. Cebeci) Springer-Verlag, NY, 1983.

9. Bradshaw, P., Cebeci, T. and Whitelaw, J.H.: Engineering Calculation Methods for Turbulent Flows. Academic Press, London, 1981.

10. Cebeci, T. and Carr, L.W.: Prediction of Boundary-Layer Characteristics of an Oscillating Airfoil. In Unsteady Turbulent Shear Flows, Proc. Symp. (ed. R. Michel, J. Cousteix and R. Houdeville), Toulouse, France, 1981.

11. Cebeci, T. (ed.): Singularities in Unsteady Boundary Layers. In Numerical and Physical Aspects of Aerodynamic Flows, Springer-Verlag, NY, 1982.

12. Smith, F.T.: On the High Reynolds Number Theory of Laminar Flows. IMA J. Appl. Mech. 28, 207-281, 1982.

13. van Dommelen, L.L and Shen, S.F.: Private communication.

AD-P004 166

ON THE SHEDDING OF VORTICITY AT SEPARATION

by

D. P. Telionis and D. Mathioulakis
Department of Engineering Science and Mechanics
Virginia Polytechnic Institute and State University
Blacksburg, Virginia 24061

Abstract

Steady and unsteady velocity components over a backward-facing circular arc are measured by Laser-Doppler Velocimetry. A periodic disturbance is added to the mean flow and the response of unsteady separation is investigated. Special attention is given to the distribution and the flux of vorticity.

1. Introduction

Aerodynamicists are interested in the phenomenon of separation because it controls the behavior of separated flows and therefore the loading of airfoils and phenomena like steady or unsteady stall. The study of unsteady separation has generated some controversies, mostly because of the widely varied tools of investigation and quite often because of confusing terminology. The significance of the phenomenon lies in its interaction with the entire flow field. Its local properties may explain the detailed structure of the flow but these should only be viewed as a step towards the understanding and eventually prediction of the global effects. In this paper we discuss our initial experimental efforts in this direction. We study how the vorticity generated in the boundary layer is convected and shed in the free stream. Moreover, we are interested in the interaction of the separated free-shear layer with the dead water and the rigid wall.

Experimental work on unsteady separation has been initiated in the past few decades following the pioneering work of Sears[1], Moore[2] and Rott[3]. The experimental work of Vidal[4] and Ludwig[5] pertains only to steady flow, and the work of Despard and Miller[6] is confined to high frequency oscillatory flow. Our knowledge at the beginning of the 1970's about this complex phenomenon was therefore remarkably narrow and seriously in need of more intensive experimental investigation. Some progress was achieved by methods of flow visualization and by hot-wire anemometer techniques. Such methods have already been employed by Schraub et al[7], Werle[8], Ruiter, Nagib and Fejer[9] and McCroskey[10] to study unsteady viscous flow phenomena, but the specific cases considered and the scale of the models were designed for a study of the whole flow field. In all these studies the boundary layers were so thin that it was essentially impossible to study the features of the unsteady boundary-layer and in particular, separation. In a most recent effort Carr, McAlister and McCroskey[11] employed a variety of sensing devices, ranging from flow visualization methods (tufts, smoke) to pressure or velocity measuring methods (pressure transducers, hot wire anemometers, etc.) to study the phenomenon of unsteady stall. In this study pressure and velocity signatures throughout a period of oscillation are given for different stations on the airfoil and compared with flow visualization data.

The present group attempted to examine more closely the immediate neighborhood of unsteady laminar separation. In the first phase of the work (Telionis and Koromilas[12], Koromilas and Telionis[13]) emphasis was given to the qualitative aspects of the flow. This was accomplished by flow visualization methods and water-glycerin mixtures to achieve thick boundary layers with not so small velocities. Steady flows over moving surfaces were first examined in an open channel. Unsteady effects, transient and oscilatory were later conducted in a closed water tunnel designed and constructed for this purpose, with two different systems of pressure disturbance generators.

More recently, Mezaris and Telionis[14] obtained detailed LDV measurements over a rearward facing circular arc. In the work of Ref. 14, unsteadiness is introduced by a flap pulsating over the circular arc. The model employed in the present study is the same with the model of Mezaris and Telionis and will be described in the main body of the paper.

It is well known that the amplitude ratio is scaled for a flat plate by the frequency parameter $k = \omega x/U_\infty$ where ω, x and U_∞ are the frequency, the distance along the wall and the free stream velocity respectively (Lightnill[15]). With increasing x, or equivalently ω, the amplitude profiles have been proved analytically and experimentally (Telionis[16]) to have smaller overshoots which approach the wall. The oscillatory part of the flow tends to become plug flow and the Stokes layer is confined closer and closer to the wall. This is not the case if the adverse pressure gradient increases with x (Ref. 14). In fact, the data of Mezaris and Telionis[14] indicate overshoots about 10 times larger than the amplitude of the outer flow.

In the present paper we introduce the disturbance in the oncoming stream rather than through a pulsating flap. We then examine more carefully the flow in the vicinity of separation by a more powerful data acquisition system which permits frequency domain analysis as well as Fourier series expansions of all wave forms. Moreover, the vorticity field is examined carefully. What is unique about the problem considered here is that the effects being studied are due exclusively to viscosity. It is well known that separation and the wake formation process is independent of the level of the outer velocity for a good range of the Reynolds number. In other words, as long as the geometry of the solid body and hence the potential flow does not change, the location of separation is fixed. In our case, for all steady cases corresponding to instantaneous values of the free stream, the flows are identical. Periodic response of the wake is then due exclusively to viscous effects. This is not the case in flows over oscillating airfoils, since to each angle of attack correspond entirely different flow fields.

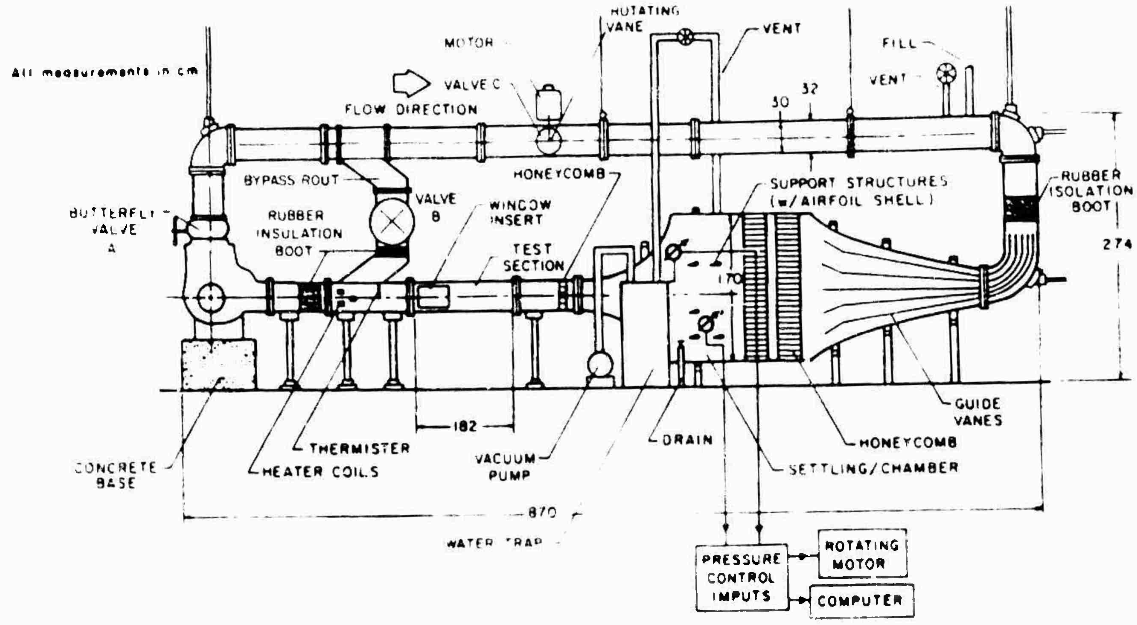

Fig. 1 The VPI water tunnel showing the recent modifications: (a) A rotating vane driven by a variable speed motor and (b) a by-pass system with a control valve.

2. Facilities and the Model

To conduct the research reported in this paper, some modifications and additions were necessary. The basic task was to convert the tunnel to an unsteady water tunnel. Disturbances were introduced upstream of the settling chamber by a rotating vane (Fig. 1). For the past 6 years, our experimental work on unsteady aerodynamics was performed with a steady stream. Unsteadiness was introduced by dynamic motion of the model or part of it. Modifications were proposed and carried out to convert the tunnel to an oscillating tunnel. This, of course, required extra efforts to reduce the turbulence in the tunnel and recalibrate the facility. To control the mean flow, a rotating vane was installed immediately above the test section as shown in Fig. 1. This vane was coupled to a HELLER DC motor with variable speed control. The unit controls automatically the speed to within ± 0.5% of the set value. It is also equipped with an optical encoder which can be interfaced directly with the laboratory computer.

A very significant factor in studies of unsteady aerodynamics is the amplitude of oscillation. To the knowledge of the present authors, in all facilities employing some mechanical method for control of the frequency of oscillation, the amplitude ends up being a function of the frequency. A separate system is necessary if one desires to control independently both the amplitude and the frequency of the oscillation. In our case this was accomplished by a by-pass pipe and a by-pass valve as shown in Fig. 1. The position of this valve controls the efficiency of the rotating vane. Charts of the performance of these controls have been constructed and will be included in an engineering report (Ref. 17).

Any periodicity externally added to a tunnel generates free-stream turbulence. Many existing unsteady flow facilities operate with turbulence levels of the order of 1%. Careful studies require much lower turbulence levels. To quiet the flow in our tunnel we studied the literature on honeycombs and screens[18-22] and contacted personally an expert in the field (Nagib[23]). As a result of our investigations, we installed in the settling chamber a second set of finer honeycombs and 3 sets of fine screens.

Typical results are shown in Tables 1 and 2, obtained with an LDV tracker and counter respectively. In this table, the tunnel speed and the by-pass valve are controlled independently. It is surprising that the by-pass system influences greatly the turbulence level, even though it is far upstream of the test section. We have also performed an exhaustive study of turbulence frequency spectra examples of which are included in Ref. 16.

The acceleration and deceleration of large masses of water induce fluctuations of pressure that may exceed the strength of the plexiglass structure. Moreover, the efficient operation of hydrogen bubbles require pressure levels lower than the atmosphere. To control the pressure level in the tunnel, we have installed a water trap and piping which connects the system to a vacuum pump.

Experiments are conducted on a model similar to the model of Mezaris and Telionis[24]. A convergence of the test section leads the flow between two slightly diverging flat plates to account for the two growing boundary layers. At the entrance of the convergence, the boundary layers growing on the walls of the tunnel are sucked. New boundary layers start developing on the flat portion of the model. A very short distance downstream of the

Speed of Pump	By Pass Closed fo (kHz)	RMS (mV)	TU (%)	By Pass at 2 fo (kHz)	RMS (mV)	TU %	By Pass at 4 fo (kHz)	RMS (mV)	TU (%)	By Pass Open fo (kHz)	RMS (mV)	TU (%)
0.5	107	12	0.16[a]	94	25	0.39	64	351	0.82	55	30	0.81
0.5*	115	5	0.07	104	12	0.17	70	40	0.85	60	35	0.87
1	145	17	0.62	122	17	0.69	83	80	1.44	72	48	1
2	220	30	0.63	180	25	0.63	130	25	0.96	115	20	0.26[c]
3	290	40	0.68	255	38	0.76	140	35	1.028	160		
4	350	8[d]	0.11[e]	240	35	0.6	212	50	1.17	195	55	1.41
4*	360	7	0.09	310	20	0.32	230	50	1.08	210	60	1.42
5	420	15	0.53	360	[illegible]	0.09	261	50	0.96	225	60	1.33
5*	410	2[g]	0.015[f]	350	9	0.12	251	60	1.2	230	60	1.30

Table 1: The effect of the bypass system and the tunnel speed on the turbulence level. The speed of the tunnel is represented by the speed of the driving pump in control system values which correspond here roughly to speeds of up to 3m/sec. In the vertical columns f_0 is the mean Doppler frequency, RMS is the root mean square of the signal and TU is the turbulence level. The by-pass opening is also marked in values of the control system. The starred rows correspond to tests with no extra honeycomb at the entrance of the test section. Data were obtained with a DISA tracker. This instrument displays large discrepancies if the reading is not within a narrow band of the scale. The readings marked by a letter were repeated with a different scale and resulted in the following values of the turbulence level: (a) TU = 0.56%, (b) RMS = 25 mV, (c) TU = 10.8%, (d) RMS = 12 mV, (e) TU = 0.5%, (f) RMS = 15 mV, (g) TU = 0.53%.

Speed of Pump	By Pass Closed fo (kHz)	RMS (mV)	TU %	By Pass at 2 fo (kHz)	RMS (mV)	TU %	By Pass at 4 fo (kHz)	RMS (mV)	TU %	By Pass Open fo (kHz)	RMS (mV)	TU %
0.5	n=9) (v=2.44) 40	11	1.37	n=4) v=2.36) [illegible]	[illegible]	[illegible]	n=4) v=1.61) 40	15	1.43	n=4) (v=1.442) 44	15	1.34
1	n=8) v=2.714) 135	[illegible]	1.63	n=8) v=1.46) [illegible]	[illegible]	[illegible]	[illegible] v=1.244) [illegible]	[illegible]	[illegible]	n=4) v=1.104 67	15	1.35
[illegible]	n=8) v=3.22) [illegible]	[illegible]	[illegible]	[illegible]	[illegible]	[illegible]	[illegible]	[illegible]	[illegible]	n=4 v=1.134) [illegible]	[illegible]	1.34
[illegible]	n=4 v=4.4) [illegible]	[illegible]	[illegible]	[illegible]	[illegible]	[illegible]	[illegible]	[illegible]	[illegible]	[illegible] v=1.35) 144	35	1.4
[illegible]	n=8) v=5.5) [illegible]	[illegible]	[illegible]	[illegible]	[illegible]	[illegible]	[illegible]	[illegible]	[illegible]	[illegible]	[illegible]	[illegible]
[illegible]	[illegible]	[illegible]	[illegible]	[illegible]	[illegible]	[illegible]	[illegible]	[illegible]	[illegible]	[illegible]	[illegible]	[illegible]

Table 2: [illegible] as Table 1 except that data were [illegible] by a [illegible] counter. In all cases, a honeycomb was positioned at the entrance of the test section.

convergence, the boundary layer developes like a flat plate Blasius layer (Mezaris and Telionis[14]). Further downstream, the top surface diverges to generate a region of adverse pressure gradient. However, the bottom plate is continued further downstream. In this way the separated region is not affected by mirror image separation. It is recalled that flows about symmetric bodies, as for example a circular cylinder are controlled by the interaction of two shear layers with opposite signs of vorticity, which eventually results into periodic shedding of large scale vortices. The situation is different in the case of an airfoil at an angle of attack, whereby the separating flow over the suction side develops with little or no influence of the trailing edge vorticity. This is exactly the situation which is simulated by our rig. Measurements are conducted on the diverging section which has the shape of a circular arc as shown schematically in Fig. 2.

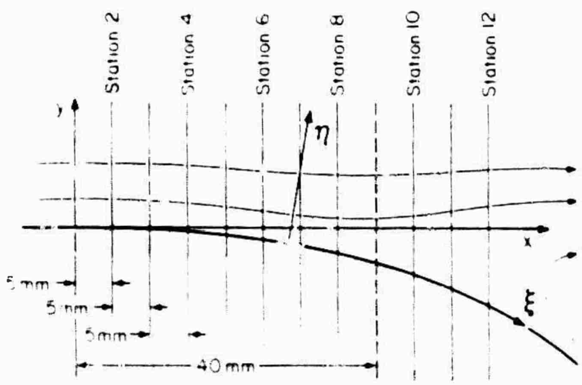

Fig. 2 The model and coordinates defining the mesh of measurements.

3. Instrumentation and Data Acquisition

Our plans to measure vorticity by shifting the beams can be implemented much easier in the backward scatter mode. However, the most significant advantage of backward scatter is the convenience and precision of traversing mechanisms. A special system was designed and constructed for traversing the measuring volume via mirrors. Such a system should meet some basic requirements: (i) it should allow very accurately controlled displacements, (ii) it should permit the displacement of the measuring volume in two directions, parallel and perpendicular to the flow, (iii) it should be controlled directly by the laboratory computer, (iv) it should be free of vibrations and finally, (v) it should allow the rotation of the beams about their bisector, so that components of the velocity in any direction can be measured.

The system we designed and constructed is shown schematically in Fig. 3. The train of TSI optics is mounted on a linear translator which allows the entire system to move in the x-direction. The parallel beams are then reflected twice from mirrors as shown in the figure and pass through a lens to converge at the measuring

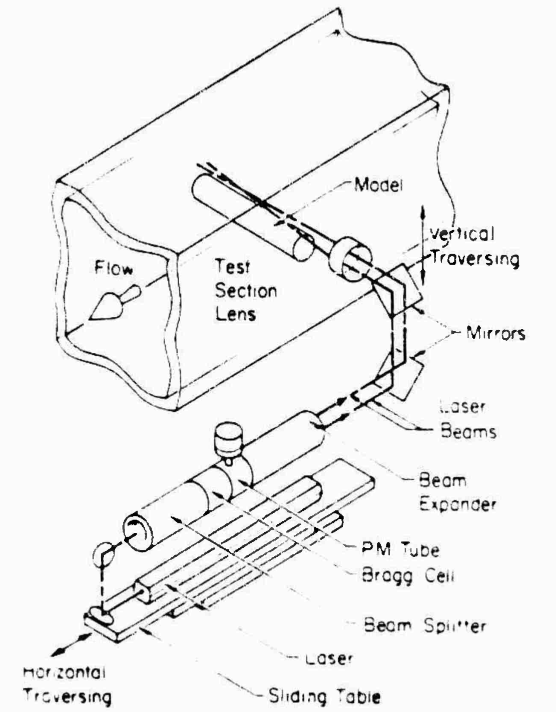

Fig. 3 The LDV System in a backward scattering mode showing the traversing mirrors.

volume. The upper mirror together with the lens translates in the vertical direction to facilitate motion of the measuring volume along the y-axis. Details of the mirror tower are shown in Fig. 4.

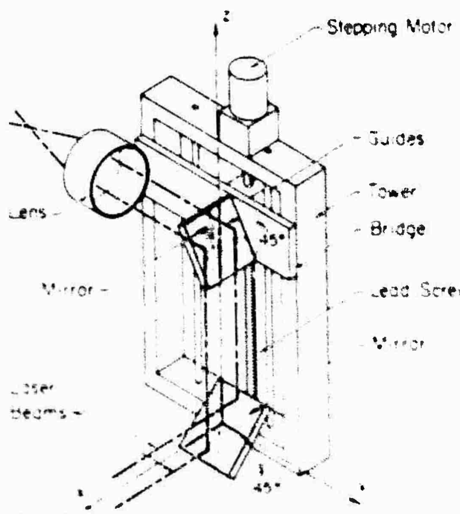

Fig. 4 The traversing mechanism.

Both motions are controlled by stepping motors interfaced with the laboratory computer. In this way steps as small as 1/100 mm can be implemented easily. Moreover, successive steps in x and then in y may displace the measuring volume along any inclined straight line. The LDV signals we process now with TSI counters. Our two counters are equipped with a master and a slave interface respectively, to allow them to talk directly to our laboratory computer. This is another serious advantage of the present system. The signals from the photomultipliers are processed digitally and

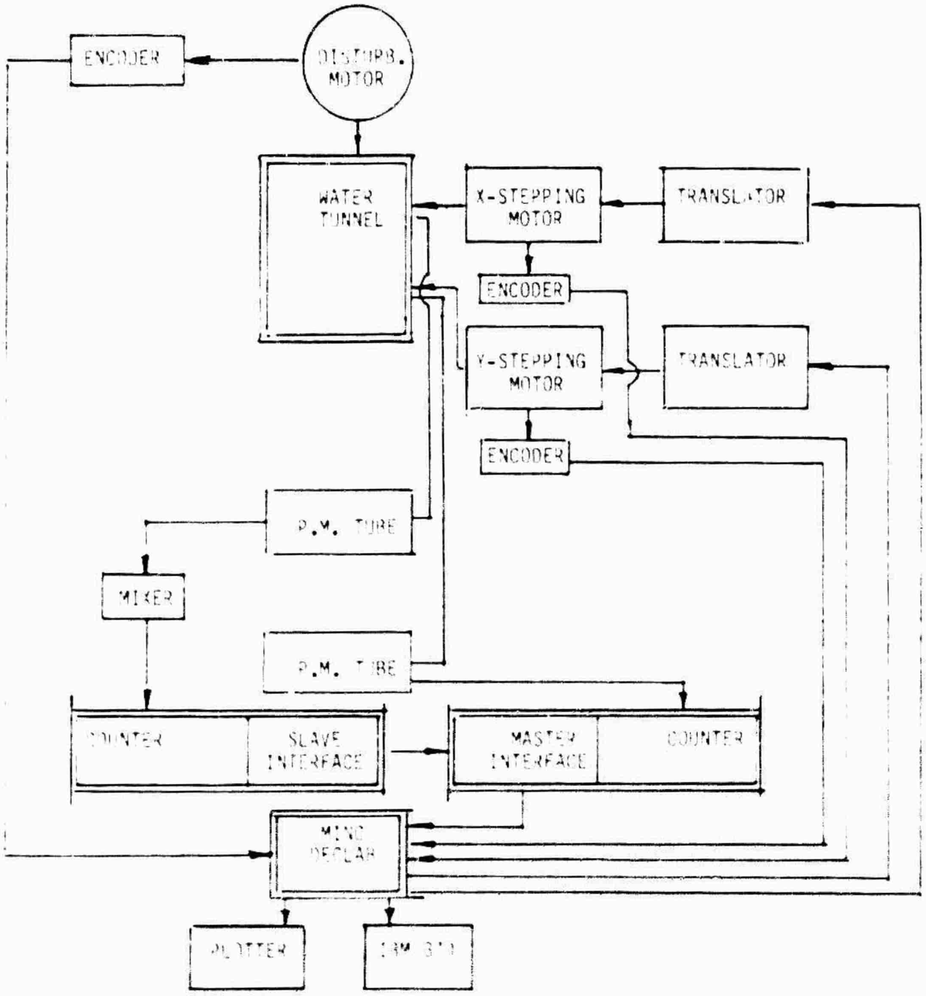

Fig. 5 Data Acquisition System.

the information is fed directly to the computer without the interference of digital to analog and analog to digital converters.

A major improvement in our experimental facilities has been the acquisition of a MINC-11 computer with all the necessary boards (D/A and A/D converters, digital or analog output, multiplexer, etc.). We have already prepared and tested software for all the necessary operations in our laboratory. Many of these tasks were performed before by an HP5420 which of course is still available. However now we have the flexibility to control and define the way of manipulating our data on line. Moreover, we can dump our raw data directly to an IBM 370 for further processing.

The laboratory computer is the heart of the entire system. It controls all other instruments, it displaces the measuring volume, it checks continuously for the quality of the signal, it receives the data, it manipulates them on the line and it stores them. The particular arrangement for the present project is shown schematically in Fig. 5. An outline of the flow chart of this operation is shown in Fig. 6. The computer performs conditional averaging of the periodic signal at a point and then orders the stepping motors to proceed to the next position. According to the specific application, the LDV counters are interrogated by the computer to insure proper operation of the system. The software provides for input from encoders which would insure that the micropositioning commands have been executed properly. Moreover, the general condition of the tunnel will be recorded, namely speed, temperature of the medium, and frequency of the imposed oscillation.

4. Results & Conclusions

Data were obtained along a mesh aligned with the coordinate systems x,y (Fig. 2). A total of 16 vertical stations were thus defined at a distance of 5mm apart. Along each x station the vertical increments varied between Δy = 0.2 mm and 1.5 mm. Data obtained in this way do not correspond to velocity profiles traditionally discussed in boundary layer investigations since the y coordinate is not perpendicular to the surface of the body. However we found that the system x,y as defined in Fig. 2 is more convenient for the study of separating flows since it is more or less aligned with the separating free shear layer. Since both velocity components are obtained, one can always convert the data in a more traditional

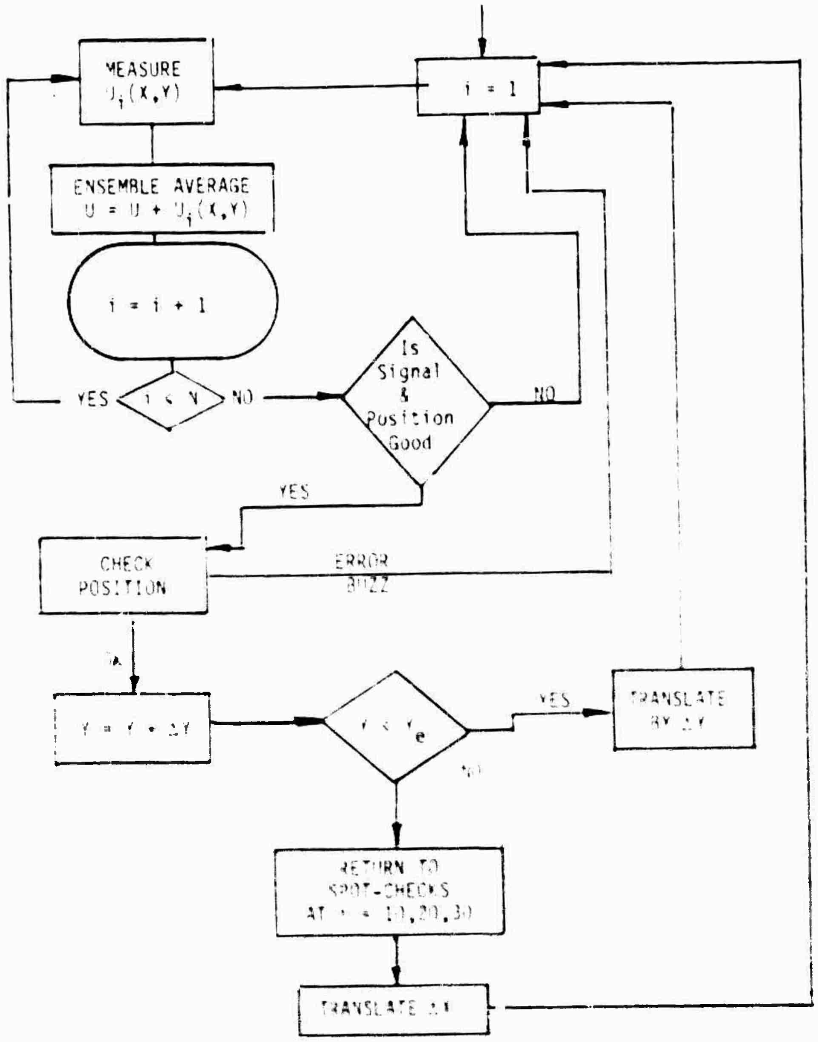

Fig. 6 Flow-chart for data acquisition.

coordinate system. Raw and reduced data are presented plotted over a portion of the circular arc drawn to scale. Attention is focused on the region between x = 30 and 80 mm, downstream of the origin. Profiles are plotted against a y coordinate stretched by a factor of 5 with respect to the x-coordinate. All quantities plotted are reduced by the value corresponding to the maximum y at the first station. All the raw data are available on tape for any investigator who would care to request them.

The LDV signals were averaged over 10 samples to smooth out the small amounts of hydrodynamic and electronic noise. For a speed of 15cm/sec, the velocity profiles of the u-component of the velocity are displayed in Fig. 7. It was estimated that the point of zero skin friction for this case is approximately at x = 55mm. A good number of downstream stations were now obtained beyond separation as shown in this figure. This was possible only with shifting of the Doppler frequency which was not successful when the data of Ref. 11 were obtained.

Evidence was presented in Ref. 14 that, even for steady flow, the boundary layer remains attached for some distance beyond the point of skin friction. Our present investigation seems to corroborate this finding as documented in Fig. 8. In this figure we display the turbulence level profiles reduced by the free-stream turbulence. The turbulence level apparently stays low and in fact decreases in the small recirculating region which extends from the point of zero skin friction at x = 55mm until x = 70mm.

Unsteady data were obtained for a driving frequency of 0.2 Hz. A signal from the rotating vane was used to provide a trigger for ensemble averaging of the data. Information obtained in this way was stored in the form of waveforms. An example is shown in Fig. 9. These waveforms were Fourier analyzed to generate the mean value and the amplitudes of all harmonics at each point in space in the form

$$f(x,y,t) = a_0(x,y) + a_{11}(x,y)\cos\omega t$$

$$+ b_{11}(x,y)\sin\omega t + a_{12}(x,y)\cos 2\omega t + b_{12}(x,y)\sin 2\omega t + \ldots$$

profiles of the u-component of the velocity, mean and amplitudes respectively.

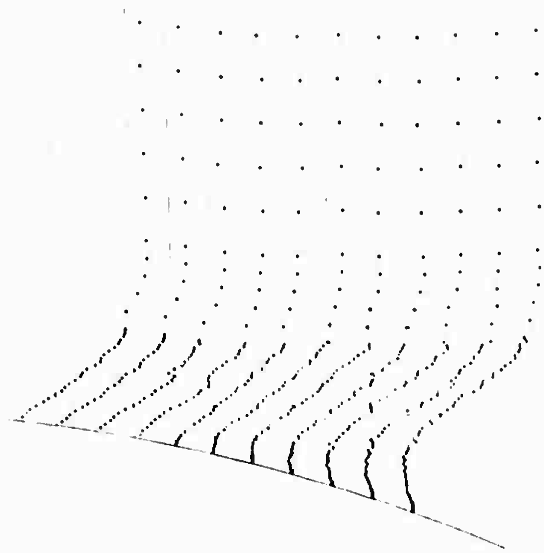

Fig. 7 Reduced velocity profiles at stations x = 30mm to 80mm. Vertical lines corresponds to stations spaced 5mm apart.

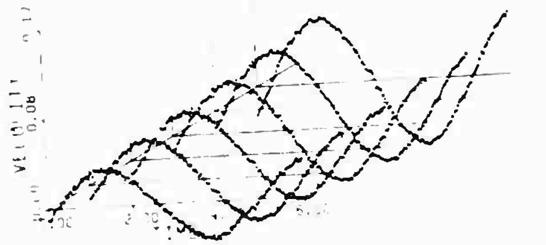

Fig. 9 Selected velocity waveforms at x = 50mm. Front to back corresond to y = 6, 5.2, 4.8, 4.2, 3.8 and 2.8mm.

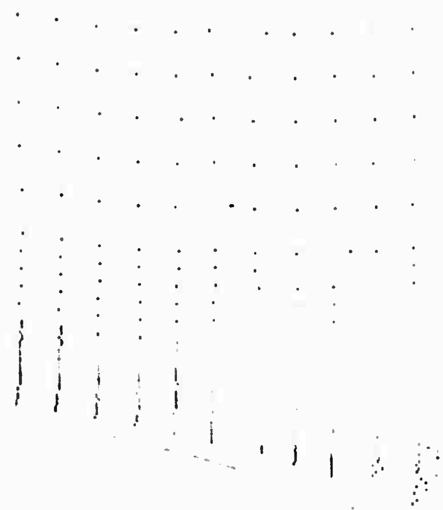

Fig. 8 Reduced turbulence level profiles at stations x = 30mm to 80mm.

where q(x,y,t) is any measured velocity component. The amplitudes of higher harmonics for the u-component proved to be not more than 5% of the amplitude of the first harmonic which is an indication that the waveforms are nearly sinusoidal. However, our data contain a lot more information which can be retrieved later if necessary. In this paper we will refer to q_0 and $q_1 = \sqrt{a_1^2 + b_1^2}$ as the mean and the amplitude of a quantity respectively. In Figs. 10 and 11 we plot

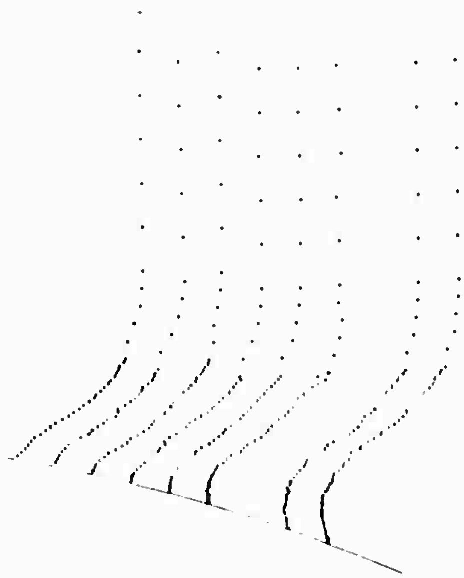

Fig. 10 Reduced mean velocity profiles at stations x = 40 through 80mm.

Instantaneous profiles at each station and for any of the phase points for which data are stored have been plotted and studied. We selected to display here in Fig. 12 sixteen profiles equispaced within a period at the first upstream station, x = 45mm, at which the point of zero skin friction vanishes. At this station, the skin friction is always positive and its minimum value is zero. Another station of significance for the variation of zero skin friction is the location at which the skin friction is always negative but its maximum is equal to zero. This occurs approximately at the station, x = 65mm (Fig. 13). Incidentally, according to the definition of Despard and Miller[6], this is the location of separation. However, this is valid for high enough frequencies for which the point of separation does not respond to the periodic fluctuations of the velocity.

To determine the normal component of the velocity, the component in a direction inclined by 20° with respect to the x-axis, say u', was measured. In terms of u and u' then the normal component v can be calculated by a simple algebraic formula.

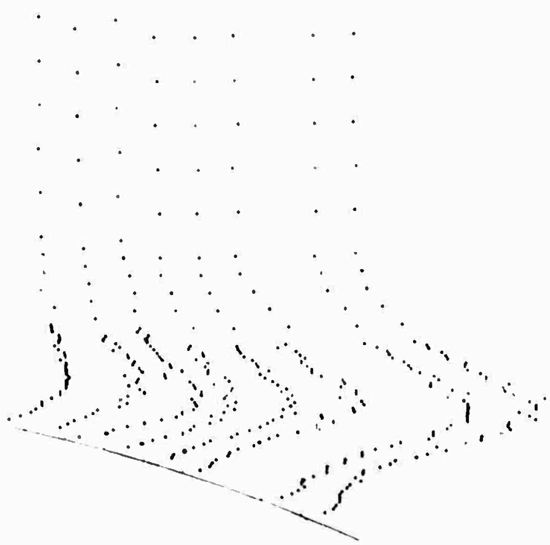

Fig. 11 Reduced velocity amplitude profiles at stations x = 40 through 80mm.

Of great interest for separating flows is the behavior of displacement thickness. In a large number of unsteady separation problems studied so far by other investigators, the separated region is confined in the axial direction. As a result, the displacement thickness goes through a maximum but then drops again. In our case the displacement thickness grows continuously with the axial distance, until it becomes meaningless to define such a quantity. The waveforms of the displacement thickness for the stations x = 40m to 80mm we show in Fig. 14. For the first station this quantity is about 180 out of phase with the free

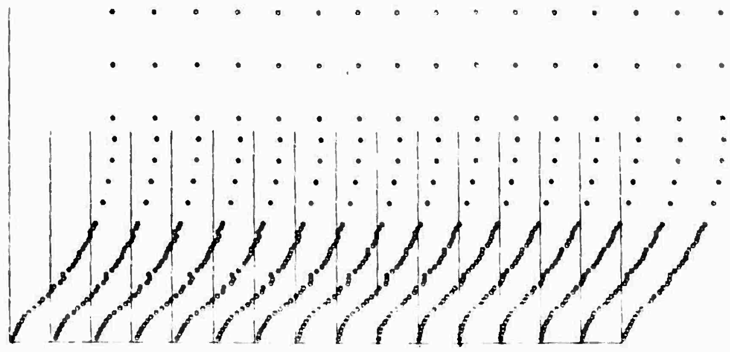

Fig. 12 Velocity profiles at x = 45mm for 16 values of the period.

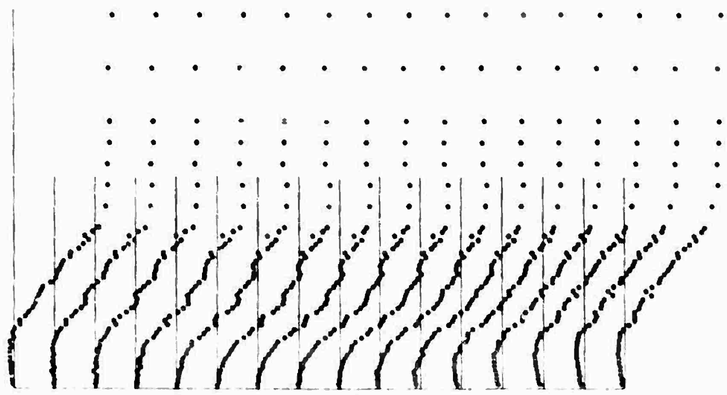

Fig. 13 Velocity profiles at x = 65mm for 16 values of the period.

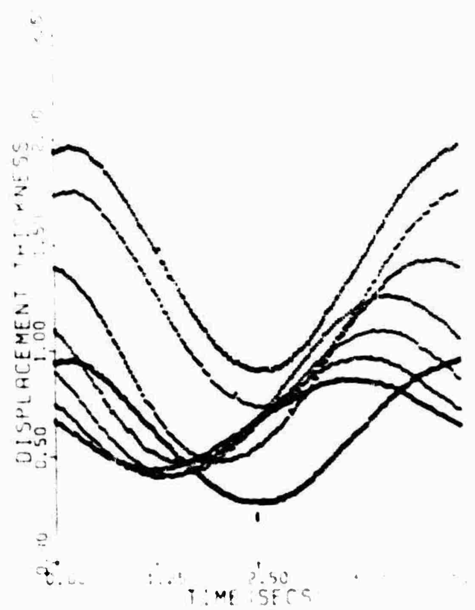

Fig. 14 The waveforms of displacement thickness. The symbols ◻, ○, △, +, x, ◇, ✢, X correspond to stations 9 through 15 in this order. The period of oscillation is 5 sec.

stream. This is the well known property of boundary layers whereby outer flow decelerations result in thickening of the boundary layer. However, further downstream a peculiar behavior is observed. The minimum of the displacement thickness shifts upstream to about the quarter point of the period until x = 45mm. Downstream of this station the minimum and therefore the entire waveform of the almost sinusoidal signal shifts again towards the midpoint in the phase. This suggests that the station x = 45mm is the origin of a wavelike phenomenon which propagates periodically in both directions, upstream and downstream. Incidentally, this station is the station of the uppermost position of zero skin friction. This phenomenon is more clearly illustrated in Figs. 15 and 16 where the displacement thickness is plotted versus the axial distance, with the period appearing as a parameter.

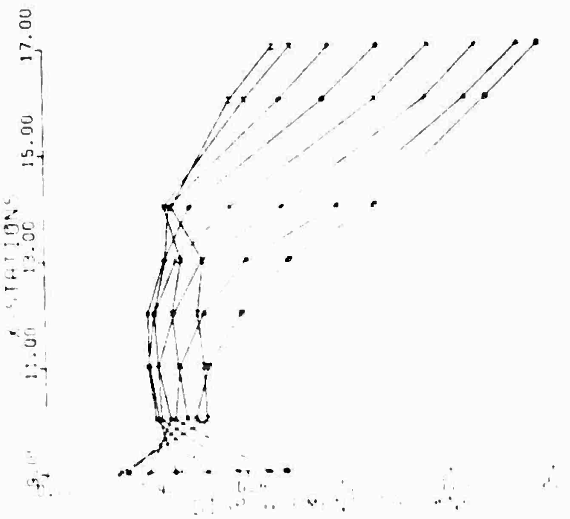

Fig. 15 Axial variation of displacement. The symbols [illegible], ◇, ✢, X, Z correspond to times T/16 through 8T/16 in this order.

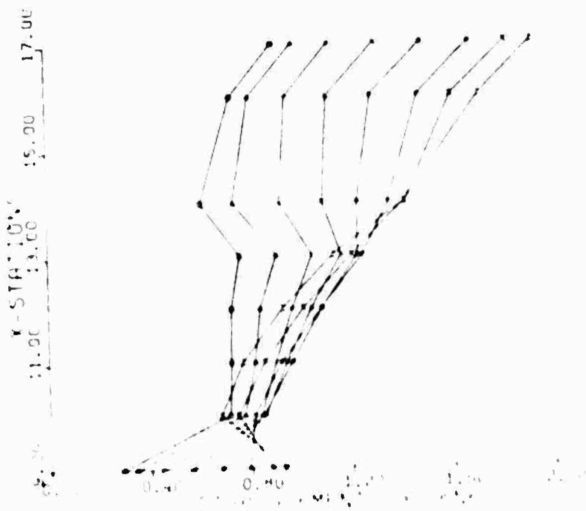

Fig. 16 Axial variation of displacement. The symbols [illegible], ◇, ✢, X, Z correspond to times 9T/16 through 15T/16 in this order.

5. The Shedding of Vorticity

A classical relationship between circulation, Γ, and vorticity, Ω, dictates that

$$\Gamma = \iint \Omega dA \tag{2}$$

where A is the area contained by the contour of integration of the circulation integral. Howarth (see discussion in Ref. 24) has demonstrated that if the area is chosen appropriately, the rate of shedding of vorticity at separation becomes

$$\frac{d\Gamma}{dt} = \int_0^\delta \Omega u dy \tag{3}$$

which within the boundary layer approximation yields

$$\frac{d\Gamma}{dt} = \frac{1}{2} U_e^2 \tag{4}$$

where U_e is the edge velocity at separation. This simple formula has been used extensively in the literature of discrete vortex dynamics. The validity of this formula and its possible improvement and extension to unsteady flow is the topic of an on-going investigation at VPI & SU.

In all the attempts to calculate the strength of the discrete vortex via Eq. (4), the position and initial velocity of the vortex are arbitrarily assigned. The present group is working on an interactive approach which will allow the calculation of this necessary information. In the present paper we have made the first steps towards measuring the flux of vorticity.

Our data have been employed so far to calculate the quantity $\partial u/\partial y$ which is equal to vorticity within the boundary-layer approximation. Instantaneous profiles of this quantity have been calculated and are plotted in Fig. 17 for 4 phases of the flow. A lot more phase values have been plotted but are omitted here due to space limitations. A careful inspection of Fig. 17 indicates the periodic lift-off of the shear layer. However, it is known that the second term of vorticity, the quantity $\partial v/\partial x$ may not be negligible in the neighborhood of separation.

In the continuation of our research we plan to calculate the combined effect of the terms $\partial u/\partial y$ and $\partial v/\partial x$. Moreover we intend to calculate the instantaneous moments of vorticity, namely the center of gravity of the vorticity and the vorticity flux which will generate information on the position, y_c, magnitude, Γ_c, and convective velocity U_c, V_c of a discrete vortex equivalent to the total vorticity shed by the boundary layer. These quantities can be calculated by the formulas

$$\Gamma_c = \int_0^\delta \Omega dy \tag{5}$$

$$y_c \Gamma_c = \int_0^\delta \Omega y dy \tag{6}$$

$$U_c \Gamma_c = \int_0^\delta \Omega u dy \tag{7}$$

$$V_c \Gamma_c = \int_0^\delta \Omega v dy \tag{8}$$

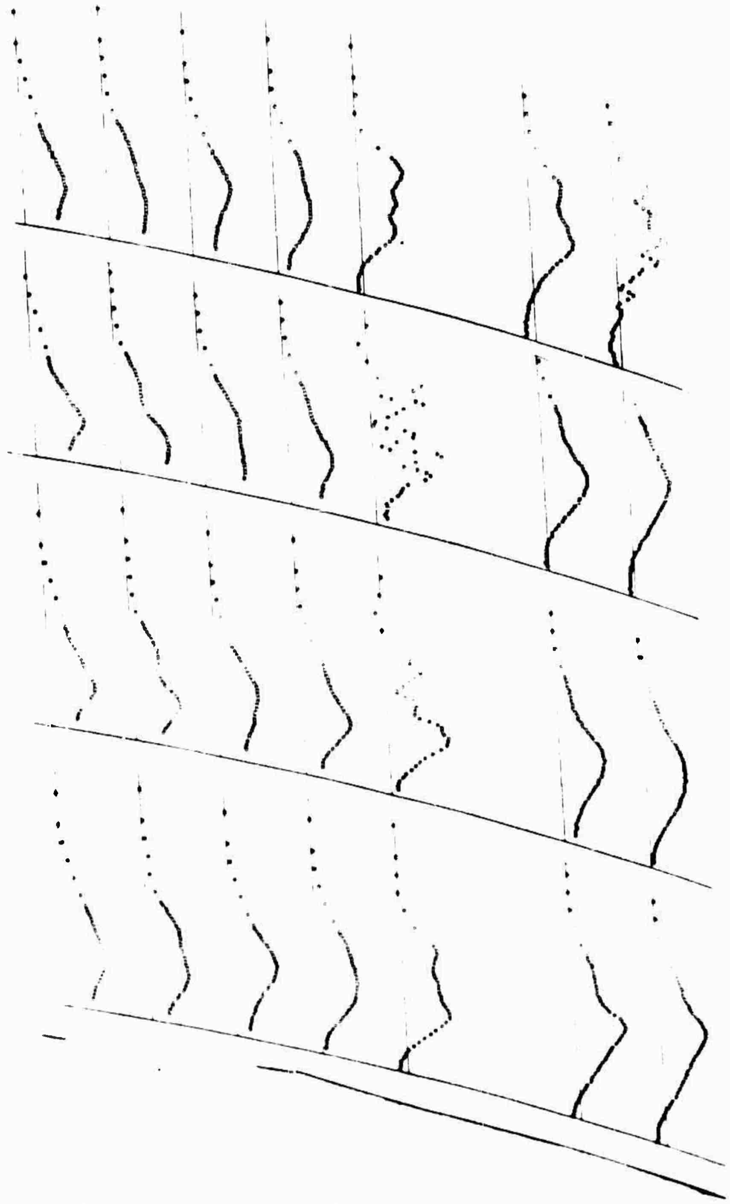

Fig. 17 Vorticity profiles for 4 phases of the periodic oscillation. Top to bottom, T/16, 5T/16, 9T/16 and 13T/16.

It is proposed here that the nascent vorticies and their initial motion in discrete vortex dynamics should be determined in this way to eliminate the arbitrary assumption commonly employed in this theory. The present authors intend to calculate the instantaneous values of these quantities and compare with interacting boundary-layer calculations.

5. Conclusions

The data obtained so far in this investigation and presented here display some important trends in the developing of unsteady separating flows. Most interesting is the fact that the amplitude of oscillations increases further along the separating free shear layer. Vorticity is therefore guided away from the wall but it is pulsating with a much higher amplitude than within the attached boundary layer. Work on this problem is currently being continued. More data are obtained, but the data already stored and presented here in raw form can be used to generate useful information. In an expanded version of this paper we intend to present data on the flux of vorticity and circulation and its ultimate fate once separated from the solid boundary.

Acknowledgement

This work is supported by AFOSR Grant No. 82-0223 and is monitored by Captain Michael S. Francis.

References

1. Sears, W. R., 1956, "Some Recent Developments in Airfoil Theory", Journal Aero. Sciences, 23, 490-499.

2. Moore, F. K., 1958, "On the Separation of the Unsteady Boundary Layer", Boundary Layer Research, H. Gortler, ed., Springer, Berlin, 296.

3. Rott, N., 1956, Unsteady Viscous Flow in the Vicinity of a Stagnation Point, Quart. Appl. Math., 13, 444.

4. Vidal, J. R., 1959, "Research on Rotating Stall in Axial-Flow Compressors, Part III", WADC TR-59-75.

5. Ludwig, G. R., 1964, "An Experimental Investigation of Laminar Separation from a Moving Wall", AIAA Paper 64-6.

6. Despard, R. A. and Miller, J. A., 1971, "Separation in Oscillating Boundary-Layer Flows", Journal Fluid Mechanics, 47, 21-31.

7. Schraub, F. A., Kline, S. J., Henry, J., Runstadler, P. W. and Littel, A., 1965, "Use of Hydrogen Bubbles for Quantitative Determination of Time Dependent Velocity Fields in Low-Speed Water Flows", Journal of Basic Eng., 87, 429-444.

8. Werle, H., 1973, "Hydrodynamic Flow Visualization" in Annual Review of Fluid Mechanics, Van Dyke, M., Vincenti, W. G. and Wehausen, J. V., eds., 5, 361-382.

9. Ruiter, G. H., Nagib, H. M. and Fejer, A. A., 1971, "Unsteady Boundary-Layer Separation Over Oscillating Airfoils", Proceedings of SQUID Workshop, Atlanta, ed., Marshall, F. J., 423-425.

10. McCroskey, W. J., 1971, "Dynamic Stall on a Helicopter Rotor Blade", Proceedings of SQUID Workshop, Atlanta, ed., Marshall, F. J., 346-350.

11. McCroskey, W. J., 1977, "Some Current Research in Unsteady Fluid Dynamics - The 1976 FREEMAN SCHOLAR LECTURE", J. Fluids Eng., 99, 8-38.

12. Telionis, D. P. and Koromilas, C. P., 1978, "Flow Visualization of Transient and Oscillatory Separating Laminar Flows", in Nonsteady Fluid Dynamics, eds., D. E. Crow and J. A. Miller, 21-32.

13. Koromilas, C. A. and Telionis, D. P., 1980, "Unsteady Laminar Separation - An Experimental Study", Journal of Fluid Mechanics, 95, 347-384.

14. Mezaris, T. B. and Telionis, D. P., 1980, "Visualization and Measurement of Separating Oscillatory Laminar Flow", AIAA Paper No. 80-1420.

15. Lighthill, M. J., 1954, "The Response of Laminar Skin Friction and Heat Transfer to Fluctuations in the Stresm Velocity", Proc. Roy. Soc., 224A, 1-23.

16. Telionis, D. P., 1979, "Review - Unsteady Boundary Layers, Separated and Attached", Journal Fluids Eng., 101, 29-43.

17. Telionis, D. P., Mathioulakis, D. and Kim, B. K., 1983, "Calibration of the ESM Water Tunnel", VPI&SU Engineering Report, to appear.

18. Schubauer, G. B., Spangenberg, W. G. and Klebanoff, P. S., 1948, "Aerodynamic Characteristics of Damping Screens", NASA TN 2001.

19. Dryden, H. L. and Abbott, I. H., 1948, "The Design of Low-Turbulence Windd Tunels", NACA TN 1755.

20. Loehrke, R. I. and Nagib, H. M., 1976, "Control of Free-Stream Turbulence by Means of Honeycombs: A Balance Between Suppression and Generation", Journal of Fluids Engineering, Vol. 98, pp. 343-353.

21. Tan-Atichat, J., Nagib, H. M. and Loehrke, R. I., 1982, "Interaction of Free-Stream Turbulence, with Screens and Grids: A Balance Between Turbulence Scales", Journal of Fluid Mechanics, Vol. 114, pp. 501-528.

22. Wigeland, R. A., Ahmed, M. and Nagib, H. M., 1978, "Management of Swirling Flows with Application to Wind Tunnel Design", AIAA Journal, Vol. 16, pp. 1125-1131.

23. Nagib, H., 1983, private communication.

Unsteady Separated Flow: Forced and Common Vorticity About Oscillating Airfoils

Michael C. Robinson and Marvin W. Luttges
Department of Aerospace Engineering Sciences
University of Colorado
Boulder, Colorado 80309

AD-P004 167

ABSTRACT

Flow perturbations induced through dynamic sinusoidal oscillations of an NACA 0015, NACA 0012, and flat plate were examined across a wide range of test conditions. Phase-locked multiple exposure flow visualization in conjunction with corroborative hotwire anemometry documented the development of temporally and spatially synchronus leading and trailing edge vortices induced through unsteady flow separation. Airfoil oscillation dynamics directly influenced vortex initiation, development and traversing velocities. The results suggest the existence of optimal combinations of variables for maximizing both vortex strength and residence time over the airfoil.

INTRODUCTION

Much of the new impetus for research into unsteady separated flows has resulted from the potential use of large scale vortices for improving aerodynamic performance (McCroskey 1982, et al). The possible exploitation of large scale vortices as an additional energy source has already been demonstrated. Current research activities (Carr et al. 1977, McCroskey et al. 1975) have shown that the unsteady lift and moment coefficients produced via dynamic airfoil oscillations can be four to five times greater than steady state counterparts.

However, before a realistic utilization of such unsteady vortical structures is possible, many fundamental questions regarding the physics of vortex development in a temporally dependent flow field must be answered. The dependence of vortex initiation, development, strength and interaction with the airfoil are required as a function of airfoil geometry and oscillation dynamics in order to determine both the physics of development as well as defining the control and repeatability of vortex production. The present study focuses on the relations between the forcing variables (airfoil geometry and oscillation dynamics) and the resultant vortex developmental behavior.

METHODS

Experiments were conducted on an NACA 0012, NACA 0015 and flat plate in the low turbulence 2' x 2' wind tunnel at the University of Colorado. Flow field measurements were obtained via flow visualization in conjunction with hotwire anemometry.

A solid aluminum NACA 0012 with 10" chord, a hollow-core aluminum NACA 0015 with six inch chord, and a 6-inch and 12-inch chord by 0.25 inch thick solid aluminum flat plate were used for the experiment. Stiffeners were placed along the span of the 12" flat plate to minimize flexing of the plate during rapid oscillation. The airoils were driven with a 1/3 H.P. D.C. motor using a 6 to 1 gear reduction connected to a variable displacement scotch yoke. Sinusoidal oscillation rate could be held constant while the magnitude of the oscillation angle was changed by a radial bearing adjustment on the fly wheel of the D.C. motor. A rotating potentiometer on the fly wheel was used to determine the oscillation period and specific airfoil attitude during any portion of the rotation cycle.

Flow visualization was obtained using a smoke rake constructed of a NACA 0015 airfoil with 1/8-inch diameter tubes inserted in the trailing edge. The smoke rake was located in the settling chamber of the 2' x 2' wind tunnel in order to minimize disturbances to the test section. The rake could be moved vertically to optimize the position of the smokelines. Dense smoke generated from heated Rosco fog juice was stored in a 55-gallon drum and delivered to the rake at modest pressure. The pressure and ensuing flow rates were adjusted to prevent smoke from being emitted as a turbulent jet.

Synchronization of data acquisition with the arifoil angle during oscillation was accomplished using a 0 to 5 volt ramp output from the potentiometer on the fly wheel which corresponded to the 0 to 2π oscillation of the airfoil. Voltage discrimination levels from 0 to 5 volts could be preset on the electronic trigger. When the selected voltage level was reached, a pulse was generated to trigger both the stroboscopic lamp for flow visualization and LSI 11/23 microprocessor for velocity measurements. All angle-dependent data collection could be synchronized with the proper phase angle of the airfoil. Synchronization signals were checked regularly by stroboscopic examination of airfoil position relative to a fixed micrometer scale.

Single and multiple phase locked stroboscopic (7μ sec duration, point source) pictures were taken of the flow field, using a 35 mm SLR camera and ASA 400 TRI-X film developed at ASA 800. The phase-locked multiple exposure photographs highlighted the repetitiveness of flow field disturbances.

Velocity measurements were made using a conventional constant temperature 2-needle hotwire probe constructed of 0.0001-inch Wollaston wire. Using various linearizing circuits referenced elsewhere (Francis, et al., 1978), a 0 to 5 volt, full scale output was preset for the velocity of the mean flow. The hotwire probe was mounted on an orthogonally driven traverse mechanism in the wind tunnel test section.

Hotwire data acquisition and subsequent reduction were accomplished with an LSI 11/23 microprocessor. Upon receipt of the phase-locked trigger signal, the analog signal was digitized and stored at a sampling frequency of 1000 Hz. Data were collected over two complete oscillation cycles for each data sample and ten successive data samples runs were averaged.

RESULTS

The unsteady flow field produced by an airfoil driven through sinusoidal pitch oscillations was extremely complex due to the temporal and spatial interdependence on oscillation dynamics. Changes in any independent parameters altered the flow field. Such complexity did not prohibit highly reproducible flow structure synchronized with the airfoil oscillation. The most prominent structures were the (1) initiation and growth of a leading edge vortex, (2) the interaction between the leading edge vortex and the upper airfoil surface, and (3) the development of a trailing edge vortex. These structures were stable enough to permit repeatable visualizations using multiple exposure photographs and to permit averaged velocity histories using hot-wire anemometry when both were synchronized with specific phase angles of the oscillation cycle. The initiation, development, and shedding characteristics of these flow structures were studied in detail.

The general patterns of vortex formation remained quite constant over the extensive range of test conditions and airfoil geometries examined. Figure 1 depicts the vortex formation over an oscillating flat plate. As the flat plate approached the maximum angle of attack, a small structure was visualized about the flat plate leading edge at approximately 0.2 chord (Fig. 1A). Further into the oscillation cycle, this small structure rapidly grew in size and was readily identified as a leading edge vortex. Superimposed smokelines from successive phase-locked, multiple exposure photographs attested to the reproducible appearance and growth of this leading edge vortex. The presence of the leading edge vortex over the airfoil surface reattached what otherwise would have been separated flow under static test conditions. As the clockwise rotating vortex was about to shed into the wake (Fig. 1I), a vortex exhibiting counterclockwise circulation was initiated around the trailing edge from beneath to above the airfoil. Whereas the presence of the leading edge vortex had reattached separated flow, the initiation and rapid growth of the trailing edge vortex resulted in complete 'cataclysmic' flow separation from the airfoil leading edge (Fig. 1I). In the wake, the leading and trailing edge vortices combined

Fig. 1 – Vortex development over an oscillating 12" flat plate; Re 87,000; $\alpha = 15^{\circ} \pm 5^{\circ}\cos(\omega T)$; osc pt. 0.75 c; K = 1.0; A-J correspond to 1/10 increments of the oscillation cycle

to form a tandem structure which remained coherent for many chord diameters downstream. Though Fig. 1 depicts vortex development for a single set of conditions, similar development sequences have been observed across a wide range of flow conditions and airfoil geometries. Critical differences in vortex initiation, development, repeatability and convecting velocity did emerge. Alterations in these characteristics were examined in detail and are presented later.

The use of short duration, multiple exposure photographs permitted documentation of vortex reproducibility. Whereas superimposed smokelines from successive phase-locked exposures (Fig. 1) identify repeatable vortex characteristics, spatially disparate or diffuse smokelines indicate oscillation-independent flows. The latter structures are evident in the diffuse smokelines about the circumference of the leading edge vortex in the wake where viscous diffusion has started the breakdown into turbulence. Similarly, diffuse patterns also were evident near the airfoil leading edge where turbulent separation had occurred.

VORTEX STRUCTURE

Flow visualization and hot-wire anemometry provided insight into the structure of the leading edge vortex. Multiple-exposure visualizations of a single vortex initiated over a flat plate (Fig. 2) indicate an almost laminar

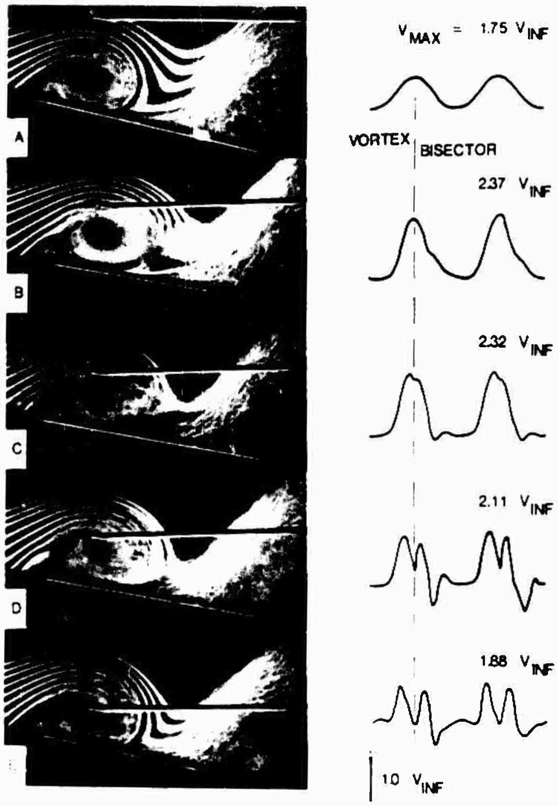

Fig. 2 - Velocities induced by a traversing vortex over an oscillating flat plat; Re 38,000; α = 15° ± 5°; K 1.5;osc pt. 0.75c; vortex located over 0.2c; A-E correspond to probe positions of 3.01, 3.51, 3.77, 4.20 and 5.58 inches above the airfoil surface.

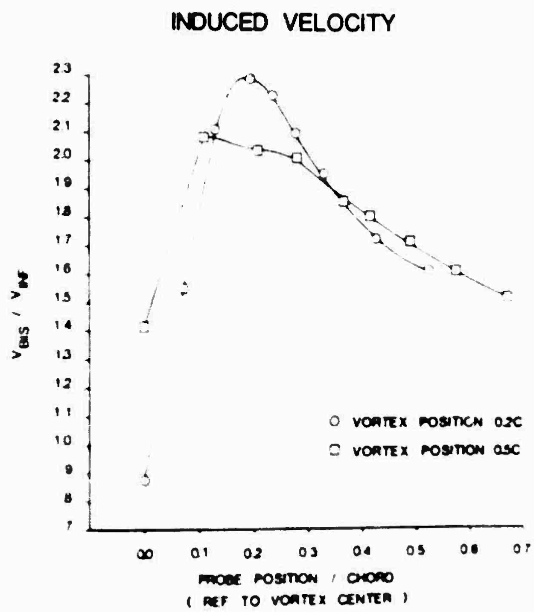

Fig. 2a - Instantaneous peak velocities on a perpendicular bisector through the vortex center; vortex located over 0.2 chord and 0.5 chord; same conditions as Fig. 2.

rotation of outlying streamlines down and around a turbulent vortex circumference. The absence of smoke from the vortex core created a striking contrast between the turbulent vortex circumference and the laminar rotation induced in the potential field. The visualizations suggested the existence of a strong shear layer between the inner core and the vortex circumference. In addition, growth of the vortex from a separation tongue (see Freymuth, these proceedings) emanating from the boundary layer would have little smoke. Diffusion at the turbulent circumference of the vortex into the potential field suggests that a decrease in the induced velocity would correspond to an increase in radius away from the vortex core.

Anemometric measurements which give a time-dependent profile of the velocities of the vortex substantiated visualizations. A hot-wire probe positioned at various chord locations above and normal to the airfoil surface yielded velocity profiles at each location over successive oscillation cycles. Two representative cycles are indicated in the data of Fig. 2. The velocity perturbations increased as the probe was immersed first in the potential flow field (Fig. 2A) and later in the vortex. A peak velocity maximum was obtained with the probe located tangent to the vortex circumference (Fig. 2B). Further movement toward the vortex center produced a velocity minimum. The probe recorded the passage of the high velocity region of the vortex circumference and entered the slow moving inner core. The two maxima on either side of the velocity minima indicated the passage of the vortex as the probe entered and exited the inner core. Though only two oscillation cycles are shown, profiles at any location were quite reproducible when phase-locked to airfoil oscillation.

Multiple exposure photographs in Fig. 2 indicate the relative positions of the hot-wire probe and vortex which produced velocity maxima and minima peaks. In the far field, outside the vortex core (Fig. 2A), the velocity maxima occurred with the probe tangent to the vortex diameter. Similarly, inside the vortex core (Fig. 2E), the minima between the two velocity maxima was observed with the probe again tangent to the diameter and on a perpendicular bisector through the vortex center. A plot of these instantaneous peak velocities along this bisector line (Fig. 2a) shows the instantaneous velocity field induced by the passing vortex. Inside the core (Fig. 2a, 0.0 to 0.15c), the vortex behaves as a solid body rotation. Outside the viscous core, the velocity induced in the potential field diminishes as 1/R with R being the effective vortex radius. This result agrees with the classic solutions derived by Oseen (1911) and Hamel (1916) as reviewed by Schlichting (1979) for the velocities induced by a vortex filament as a function of radial distance.

Repeated measurements across most test conditions and airfoil geometries indicated similar structures for any leading edge vortex. This similarity permitted a characterization to be made of the leading edge vortices based upon relative diameter and circulation velocity. The circumference diameter and the peak velocity obtained there were selected as measures to be used across various test conditions. These

Fig. 3 - Mean angle of attack effects on vortex development; 6" NACA 0015 airfoil; Re 60,000; α_m 15°; osc. pt. 0.25c; K 0.5; F-J correspond to mean angles of 0, 5, 10, 20 and 30 degrees respectively.

characteristic values as well as vortex initiation point in the oscillation cycle, and the average convecting velocity of the vortex center over the airfoil surface provides for a rather complete comparison of unsteady flow structures elicited in the following tests.

MEAN ANGLE OF ATTACK

To create a leading edge vortex, it was necessary to oscillate airfoils or plates such that the critical stall angle was exceeded during some portion of the oscillation cycle. Thus, the static stall angle provided a good reference angle for determining whether or not a leading edge vortex would be produced. Figure 3 shows the dependence of vortex development on mean angle of attack. For α_m up to 5° (Fig. 3 F & G), the multiple exposure photographs indicated no leading edge vortices had been generated. A further increase in mean angle (Fig. 3 H, α_m 10°) produced small leading and trailing edge vortices most evident in the wake. Leading edge vortex diameter increased 25% as the mean angle of attack was increased from 10° to 15°. For α_m increments between 15° to 30°, vortex size remained unchanged.

Vortex characteristics became quite sensitive to other test parameters at higher mean angles (α_m > 20°). With an oscillation angle of ± 5° at a reduced frequency of K = 0.25, the leading edge vortex separated from the airfoil at approximately 30% chord. The detachment was not totally dependent upon the mean angle of attack. Duplication of the same geometric conditions but at a higher oscillation rate (K = 1.0) produced a vortex which remained attached shedding into the wake only at the airfoil trailing edge.

OSCILLATION ANGLE

The magnitude of the oscillation angle provided another reference condition for the production of synchronous vortices. Small oscillation angles ($\alpha_\omega \leq 0.5$) at rapid oscillation rates ($K \geq 2.0$) were shown to effectively attach modestly separated flow. Instantaneous (< 7μ sec duration) single exposure photographs documented the presence of vortex development similar to that shown in Fig. 1. Multiple exposure phase-locked photographs, however, showed no spatially and temporally synchronous vortices. Oscillation angles up to α_ω ± 3 at K values < 0.25 similarly produced little evidence of synchronus flow structures. However, further increases in either the reduced frequency parameter or oscillation amplitude produced repeatable disturbances. Hence, a threshold condition existed requiring a combination of dynamic parameters of sufficient strength to elicit repeatable flow structure.

REDUCED FREQUENCY

The reduced frequency parameter, oscillation angles, and oscillation axes directly affected the size, velocity profile and repeatability of vortex formation. Of these dynamic parameters, the reduced frequency (K) provided the most predictable alteration of the flow fields. From a series of multiple exposure photographs (12/cycle), the location of the vortex center was tracked as a function of time and fraction of the oscillation cycle. Across the Reynolds numbers (60,000 - 140,000) and oscillation angles (3-5°) examined (Fig. 4), K provided an accurate index of the vortex convection velocity. The straight line drawn through the data points established the average traversing speed across the airfoil at 30 to 40% of the free stream velocity.

The individual vortex positions (Re = 60,000, K = 0.5, and K = 0.75) reveal instances of momentary delays. These delays were most prominent as the airfoil reversed direction from the maximum angle of attack and pitched downward. The characteristic circulation velocity of the vortex circumference showed that maximum delays were obtained from vortices exhibiting the

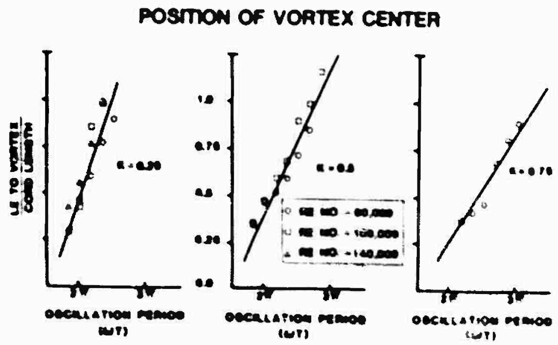

Fig. 4 - Vortex position as a function of oscillation cycle over an NACA [illegible]; [illegible] pt. [illegible]

largest reference profile velocity maxima. As the airfoil approached the lowest positions, a rapid acceleration in traversing velocity ensued. Though the reduced frequency was a good measure of the average vortex position, it did not adequately predict either vortex delay or acceleration characteristics. All dynamic parameters as well as airfoil geometry were observed to affect vortex motion.

The flow field structures related to K changes ranged from weak, poorly synchronized vortices at low K values (Fig. 5A K=0.25), to a succession of compact, intense, and closely spaced leading edge vortices well synchronized to airfoil oscillation at high K values (Fig. 5E K=1.75).

Fig. 5 - Reduced frequency effects on vortex development; NACA 0012; Re 75,000; α $15^{\circ} \pm 5^{\circ}$; osc. pt. 0.25c; A-E correspond to K = 0.25, 0.5, 1.0, 1.5 and 1.75 respectively.

At K values greater than 1.5, significant alterations in the developmental pattern of trailing edge vorticity occurred. The presence of multiple leading edge vortices over the airfoil surface displaced the formation of trailing edge vortices into the wake. The trailing edge vortex which had produced complete flow separation over the airfoil at lower K values ($K \lesssim 1.25$) generated no observable separation at high K values (Fig. 5 D & E). Thus, attached flow over the airfoil resulted throughout the entire oscillation cycle at elevated values of $K \gtrsim 1.5$ across the other conditions tested.

Velocity measurements at three chord locations over the airfoil (Fig. 6) indicated a

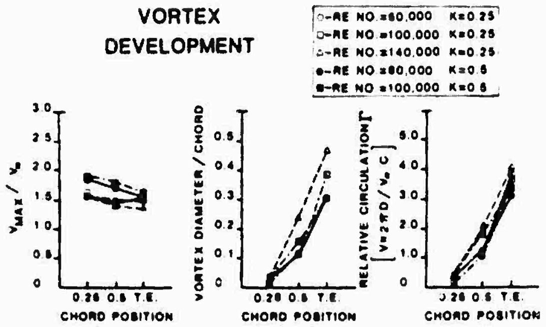

Fig. 6 - Vortex magnitude, diameter and relative circulation based upon the peak velocity obtained at various chord locations; NACA 0012; α $15^{\circ} \pm 5^{\circ}$; osc. pt. 0.25.

peak circulation velocity increase of 16% as the reduced frequency was changed from 0.25 to 0.5. At these low K values, the vortex diameter changed slightly across test conditions with larger diameters occurring at a Reynolds number of 140,000. Both the characteristic circulation velocity and diameter were combined to obtain a realtive circulation index Γ. Though the characteristic maximum vortex velocity decreased in almost linear fashion across the airfoil chord, vortex diameter increased rapidly from 0.25 chord to the trailing edge. The net effect was a continual increase in relative circulation as the vortex passed from the leading to the trailing edge.

OSCILLATION AXIS

Similar to the reduced frequency parameter, the oscillation axis location directly affected the velocity magnitudes and repeatability of vortex development. In order to minimize the effects of airfoil geometry, a flat plate was oscillated about two different axis locations; 0.25 and 0.75 C. Figure 7 contrasts the vortex development between the two oscillation positions for otherwise duplicate test conditions. The diffuse smokelines in Fig. 7, plates A - E do not exhibit the highly repeatable characteristics observed with oscillations about 0.75c. Both plates A and F were taken at the same position in the oscillation cycle, $\omega T = 2\pi$ or the maximum angle of attack 20°. The leading edge vortex in plate A (oscillation axis 0.25C) appears much larger and further down the chord than in plate F (oscillation axis 0.75C). A better match between conditions based upon vortex diameter and placement over the airfoil occurs between A and G at 20% further into the oscillation cycle. This 20% phase shift produced a vortex size and location match plate for plate throughout the entire oscillation cycle. Changing the oscillation axis from 0.25C to 0.75C would appear to have delayed the development of the leading edge vortex by 20% of the oscillation period. A detailed analysis of vortex initiation and traversing velocity as a function of the dynamic parameters is presented later.

Velocity measurements (Fig. 8) showed dynamic alterations in both the circulation

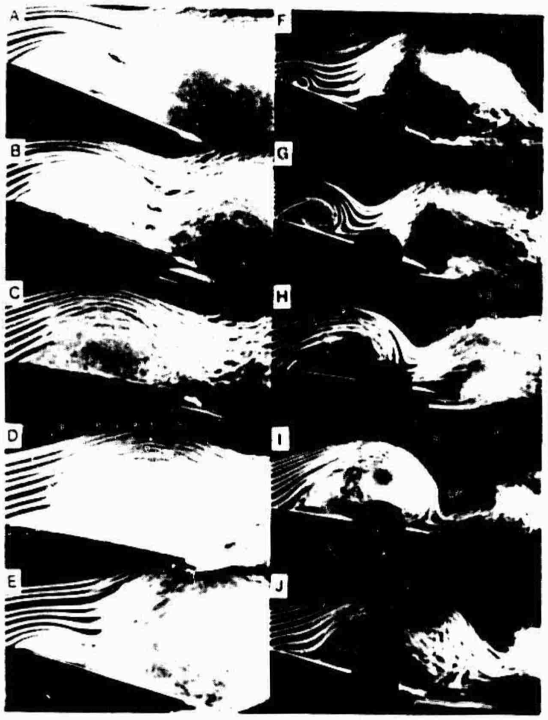

Fig. 7 - Oscillation axes effect on vortex development; 12" flat plate; Re 70,000; α 15° $\pm$ 5° cos(ωT); K 2.5; A-E and F-J correspond to 1/5 increments of the oscillation cycle

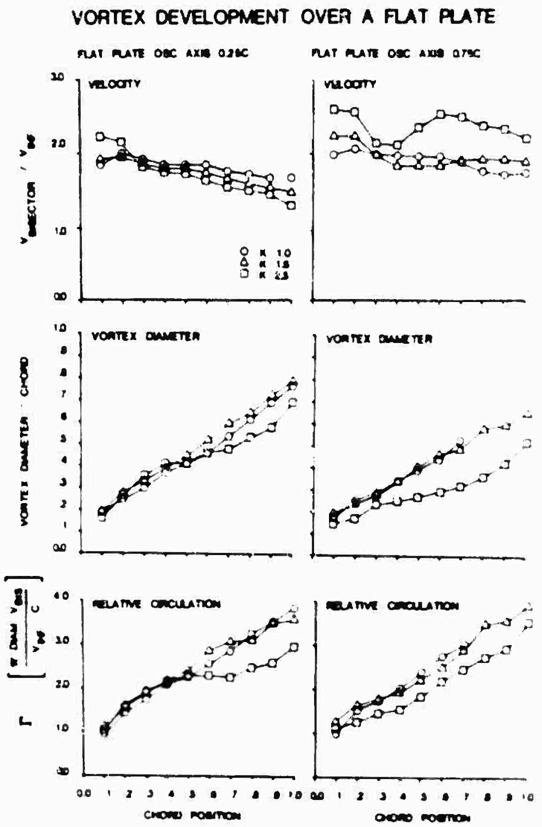

Fig. 8 - Vortex magnitude, diameter and relative circulation based upon the peak velocity obtained at 0.1 chord increments; 12" flat plate; Re 70,000; α 15° $\pm$ 5°; osc. pt. 0.25 and 0.75 c.

velocities and vortex diameters with changes in oscillation axes and K. An average circulation velocity increase of 15% was obtained for reduced frequencies of 1.0, 1.5, and 2.5 by relocating the oscillation axis from 0.25 to 0.75 C. The vortex diameter decreased an average value of 10 to 15%. Circulation velocities increased 30% between K values of 1.0 and 2.5 for a fixed oscillation position. Also, average vortex diameters decreased 40 to 50% with elevated values of K. Whereas the magnitude of the circulation velocities were directly proportional to increases in the oscillation axis and K, the size of the vortex diameter was inversely related.

A direct correlation existed between the magnitude of the circulation velocity and the repeatability of vortex generation. Flow visualizations which produced the most concise, temporally repeatable vortices also possessed the strongest circulation velocities. The combination of circulation velocity and vortex diameter to obtain relative circulation produced results similar to those obtained with the NACA 0012 airfoil (Fig. 6). The average circulation of the leading edge vortex increased as the vortex passed from the leading to the trailing edge of the flat plate used in these tests.

Sinusoidal oscillations of the flat plate about 0.75 C at elevated values of K ($\geq$ 1.5) failed to produce the linear decay in velocity across the airfoil chord. A 25% decrease in velocity occurred from the leading edge to 0.3 C. A linear increase in vortex diameter was also indicated. The decrease was followed by a rapid acceleration of the circulation velocity at 0.5 C with a corresponding decrease in vortex diameter. Velocity decay commenced again from 0.7 C to the trailing edge. The velocity reduction followed by the rapid acceleration of the vortex over midchord was commensurate with the formation of a second vortex over the leading edge. Thus, it appears that strong interaction between successively generated vortices at high K values altered the normal vortex velocity decays.

AIRFOIL GEOMETRY

Airfoil geometry altered the development of both leading and trailing edge vortices. Under static conditions, the flat plate exhibited flow separation at slightly lower mean angles of attack (α_m 10°) than the NACA 0012 and 0015 airfoils (α_m 10.9° & 11.4°, respectively). With an oscillation angle fixed at $\pm$ 5°, the flat plate produced leading edge vortices at lower mean angles of attack than the two conventional airfoils. This result was not unexpected as it had been shown earlier that the static stall angle had to be exceeded in order to generate a leading edge vortex.

Under duplicate test conditions, the sharp leading edge of the oscillating flat plate produced better temporal and spatial cohesiveness than either the NACA 0012 and 0015 airfoils. At least part of the key to this difference appeared to be the sharp leading edge of the oscillating flat plate. When either the NACA 0012 or 0015 airfoils were rotated 180° and oscillated about 0.75C with the sharp trailing edge forward, the leading edge vortices produced were qualitatively the same as those generated from a flat plate oscillated about 0.75C. The most intense, cohesive, and repeatable vortex structures were observed from the flat plate and reversed NACA 0012 and 0015 airfoils oscillated about 0.75C at the maximum limiting frequency of the oscillatory mechanism (~15 Hz).

Significant differences were observed, however, in trailing edge vortex development between the flat plate and reversed NACA airfoils. Passage of the leading edge vortex over the rounded trailing edge of the NACA 0012 airfoil always triggered a trailing edge vortex independent of reduced frequency. In contrast, the sharp trailing edge of both the flat plate and a conventionally oriented NACA 0012 airfoil produced trailing edge vortices at different positions in the oscillation cycle, relatively independent of the leading edge vortex location. For either the normal or reversed geometry, development of the trailing edge vortex at $K < 1.25$ produced flow separation whereas K values in excess of 1.5 resulted in attached flow through the entire oscillation cycle.

VORTEX INITIATION

The identification of leading edge vortex initiation using flow visualization and hot-wire anemometry presents a unique problem. Though flow visualization may not necessarily indicate the initial build-up of vorticity, it is crucial in identifying a developed vortex structure. All test conditions which produced synchronized leading edge vortices revealed fully developed vortices by 0.1 to 0.2 chord. For analysis purposes, therefore, the 0.2 chord location of the leading edge vortex was selected as a spatial reference for vortex initiation. The composite Figure 9 cites the contribution of oscillation angle (α_w, mean angle (α_m), and the reduced frequency parameter (K) to the initiation of a leading edge vortex relative to the oscillation cycle. All data points were obtained from flow visualization and hot-wire anemometry using a 12 in. C flat plate and reversed NACA 0015 airfoil with 5 in. C. Oscillation of both devices was about 0.75 C at $\alpha_m \pm \alpha_w$.

In Figure 9, it is clear that with low values of α_w a vortex formed during the upstroke of the oscillation cycle and increasing values of α_w delayed the appearance of a vortex until or even beyond 2.0 π. It is notable that this relation was asymptotic, further excursions beyond $\alpha_w = 6°$ provided little additional delay in vortex initiation.

Also in Figure 9, increasing α_m's were correlated with the increasingly early appearance of vortices. At α_m of 10°, a leading edge vortex was identified over 0.2 chord when both test devices were well into the downstroke portion of the oscillatory cycle. As α_m approached 30°, the vortices appeared during the upstroke portion. Hence, the effects of α_w and α_m are opposite of each other with both generating

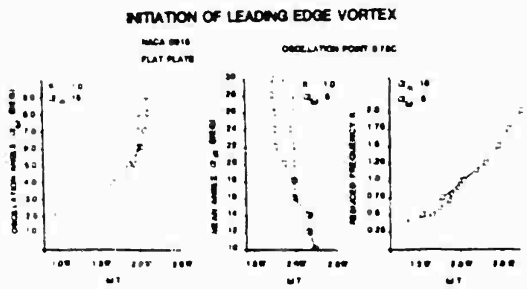

Fig. 9 - Vortex initiation over a 12" flat plate and a reversed NACA 0015 airfoil; osc. pt. 0.75c.

asymptotic limits. Somewhat surprisingly, α_m seems a somewhat less effective variable than α_w across the values tested.

Variations in reduced frequency parameter also produced the large alterations in vortex initiation. The index of initiation shows that increases in K delayed the appearance of leading edge vortices in almost linear fashion. The delay increased through K values of 1.25 with more modest delays occurring at higher K values.

TRAVERSING OR CONVECTING VELOCITY

It was noted earlier (Fig. 4) that momentary delays occurred in the traversing motion of the leading edge vortex passing from the leading to the trailing edge. Hot-wire measurements at 0.1 C increments over an oscillating flat plate for two different oscillating axes (0.25 and 0.75C) and three different values of K (1.0, 1.5, and 2.5) showed similar results (Fig. 10). The leading edge vortex did not traverse the airfoil surface with a uniform velocity after initiation. Vortices accelerated over the airfoil surface at different rates dependent upon the test conditions.

Plotting the vortex position as a function of the oscillation cycle may distort the dependence of vortex development on airfoil oscillation. When the same position data were plotted in real time (Fig. 11), the dynamics of vortex initiation and traversing velocity were observed independent of oscillation dynamics. The time required to complete one oscillation cycle for each of the three K values is indicated above the time scale in Fig. 11. Though the oscillation rate differed by a factor of 2.5, vortex initiation and position as a function of real time remained quite similar across conditions. In contrast, Fig. 10 skews the position data to oscillation cycle phases. The actual dependence of vortex initiation and position on real time seem to indicate a characteristic initiation and development time that is somewhat independent of the airfoil oscillation dynamics.

Other characteristics of vortex initiation and position, however, were observed to be dependent upon the airfoil oscillation dynamics. Regardless of oscillation axes (Fig. 11), increases in the reduced frequency parameter resulted in vortex traversing velocity

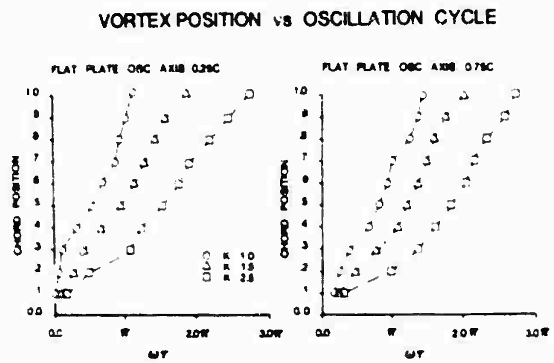

Fig. 10 - Vortex position as a function of oscillation cycle; 12" flat plate; Re 70,000; α $15^{\circ} \pm 5^{\circ}$; osc. pt. 0.25 and 0.75 c.

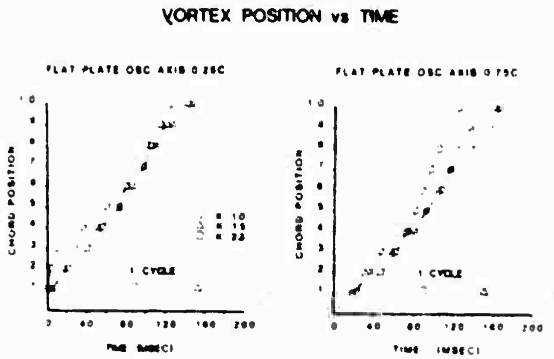

Fig. 11 - Vortex position as a function of time; 12" flat plate; Re 70,000; α $15^{\circ} \pm 5^{\circ}$; osc. pt. 0.25 and 0.75 c.

increments. This effect was previously noted in the flow visualization study (Fig. 4). At reduced frequencies where the leading edge vortex remained over the airfoil surface through one complete oscillation cycle ($K \leq 0.75$), the vortex experienced convection acceleration immediately after initiation (Fig. 11 T = 0-40 msec).

For all the conditions tested, the convection movements remained sufficiently linear to approximate "average" traversing velocities between 0.2 and 0.9 C (Fig. 12). Flow visualization of the leading edge vortex centered over these points permitted a rapid assessment of traversing velocity across a wide parameter range. The average traversing velocity obtained with this technique agreed with anemometric tests to within 2%. Although a direct correlation existed between the reduced frequency and traversing velocity (Fig. 12), a change in the slope of this correlation occurs at approximately K = 1.0. Interestingly, at the same K value cataclysmic flow separation due to the trailing edge vortex ceases. Mean angle of attack (α_m) shows an inverse correlation to traversing velocity such that high angles of attack result in a slower vortex convection. Similar results were obtained for both the reversed NACA 0015 and oscillating flat plate despite the differences in geometry and chord length.

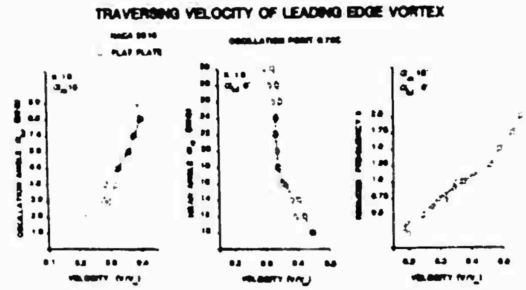

Fig. 12 - Vortex traversing velocity over a 12" flat plate and a reversed NACA 0015 airfoil; osc. pt. 0.75c.

DISCUSSION

The observations made in the previously described tests may be organized into two general categories: (1) initiation, development and convection velocities of vortices and (2) inherent vortex characteristics. As will be noted later, vortex characteristics appear to relate to the convection velocities.

INITIATION:

Assuming that the static stall angle is exceeded at some time in the sinusoidal oscillation cycle, α_m increments are related directly to earlier vortex occurrence during upward pitching of the lifting surface: the larger the α_m, the earlier in the cycle a vortex is initiated. Both α_ω and K value increments delay the appearance of a vortex to later portions of the oscillation cycle. When the oscillation axis is moved back from 0.25 to 0.75 chord locations, vortex initiation is similarly delayed. Thus, earlier vortex initiation derives from $\alpha_m - \alpha_{stall}$ while later vortex initiation derives from any test condition which increases α values. Across the tests done in the present series of studies, vortex appearance occurred as early as midway through the upward pitching and as late as midway through the downward pitching of the oscillation cycle.

TRAVERSING OR CONVECTING VELOCITY:

The traversing velocity (V/V_∞) of the leading edge vortex was affected in a manner analagous to the initiation. Increments in both the reduced frequency parameter (K) and oscillation amplitude increased the vortex traversing velocity. Over the conditions tested, increased K resulted in linear changes, but oscillation amplitude produced velocities which approached an asymptotic limit of 0.4 V_∞ for $\alpha_\omega \geq 6^{\circ}$. A similar asymptotic condition probably exists at higher reduced frequencies as well; for it is doubtful that the traversing velocity would exceed the local free stream velocity value. The traversing velocity was inversely related to increments in the mean angle of attack. A decrease of 33% in traversing velocity resulted from increasing the mean angle of attack from 10° to 30° for both the flat plate and reversed NACA 0015 airfoil. Hence, it appears that the reduction in vortex traversing can be directly attributed to an airfoil blockage effect. Conditions which produced greater blockage of the free stream flow (greater α_m) for longer periods of time (reduced K values) resulted in slower traversing velocities. Vortices developing in the shadowed wake of the airfoil remained for longer periods over the airfoil.

RELATIVE CIRCULATION:

The size, strength and repeatability of leading edge vortices were directly altered by changes in the oscillation axes and varying the oscillation rate. Higher peak circulation velocities with simultaneous decreases in vortex diameters were realized with either increased reduced frequency parameter or rearward movements of the oscillation axes. Through multiple exposure flow visualization and ensemble averaged hotwire signals, the concise, energetic and extremely coherent vortices (axis 0.75C, K > 1.0) were repeatable to within 2% variation of induced velocity over 30 consecutive oscillation cycles.

When the peak velocity was combined with the corresponding vortex diameter, the relative circulation estimate remained relatively unchanged across conditions. The initial formation (vortex over 0.2 chord) value of the circulation appeared constant across K values and oscillation positions for the flat plate. As the vortex traversed the airfoil surface from leading to trailing edge, the relative circulation increased by a factor of 2.5. Hence, the vorticity appeared to build with time over the airfoil rather than decay with time after initiation. The magnitude of the relative circulation was inversely related to the oscillation rate. Though the peak velocity increased with K, the decrease in the vortex diameter resulted in an overall decrease in the relative circulation at higher K values. For the flat plate oscillated about 0.75C, decreased approximately 25% as the reduced frequency was increased from 1.0 to 2.5. Although each vortex possessed a reduced circulation at higher K values, the total overall vortex influence about the airfoil was higher since multiple vortices resided over the airfoil at all times during an oscillation cycle.

The "temporal" component of this sinusoidally forced unsteady flow seems to provide a common thread between vortex initiation, size, strength and traversing velocity. Increasing the reduced frequency parameter decreases the amount of time available for vortex initiation and development. Since the initial formation of a leading edge vortex is delayed at increased K values, a characteristic time of vortex initiation and formation was suggested and must be caught. Similarly, these high oscillation rates produce initial vortices with relatively high circulation velocities but smaller diameters and relatively constant circulation indices. These concise, energetic vortices tend to move across the airfoil at significantly higher traversing speeds. A characteristic development time as well as a vortex-vortex interaction was suggested. Lower reduced frequencies permit the airfoil to remain at increased angles of attack for longer periods of time. The duration of this blockage effect as described previously, directly affected vortex size and traversing speeds. Lower reduced frequencies permitted a greater period of time for the vortex to grow in size and remain over the airfoil surface in the wake region of the blocked flow. Since the relative circulation indices were quite constant, higher reduced frequencies resulted in vortices with higher circulation velocities and smaller diameters. Less time was available for the development of the vortex in the shadowed wake; hence, the vortices remained concentrated.

CONCLUSION

Harmonic oscillation of airfoils at angles of attack in excess of static stall were observed to produce complex interactive flow field structures. The most predominate of these were the formation of both a leading and trailing vortex which were temporally and spatially dependent upon the airfoil oscillation dynamics. These structures were sufficiently reproducible to permit multiple exposure flow visualizations and ensemble averaged hotwire anemometer profiles to be made phase locked to the airfoil oscillation. The presence of the leading edge vortex was observed to reattach otherwise separated flow at angles of attack which produced complete flow separation under non-oscillating conditions.

The dynamics of the airfoil oscillation directly influenced vortex initiation, development and traversing velocity. The oscillation rate (reduced frequency), mean angle of attack, oscillation angle, oscillation axes as well as the airfoil geometry were shown to directly alter the vortex circulation velocity and size, yet, left the relative circulation index quite constant. Optimal selection of the airfoil geometry and oscillatory parameters should permit maximal lift enhancement through increasing vortex residence time and circulation velocity over the airfoil surface. Much additional work remains to be done in two areas: (1) measuring the total vorticity field during airfoil oscillation and (2) examining the interaction of multiple vortices over the airfoil at elevated values of K. Both these approaches have readily apparent explanatory and technical exploitation values.

NOMENCLATURE

- c — airfoil chord
- K — reduced frequency [illegible]
- Re — Reynolds number, [illegible]
- t — time
- U_∞ — freestream velocity
- α — angle of attack [illegible]
- α_m — mean angle of attack
- α_o — oscillation amplitude
- ν — kinematic viscosity
- ω — rotational frequency, rad/sec

ACKNOWLEDGEMENT

This work has been sponsored, in part, by the U.S. Air Force Office of Scientific Research, Grant [illegible], Dr. M[illegible] Program Manager. The technical assistance of [illegible] was appreciated. The manuscript was prepared by [illegible].

BIBLIOGRAPHY

Adler, J.N., Robinson, M.C., Luttges, M.W., and Kennedy, D.A., "Visualizing Unsteady Separated Flows," Third International Symposium on Flow Visualization, Sept. 6-9, Ann Arbor, Michigan, Proceedings, Vol. III, 1983, pp. 806-811.

Carr, L.W., McAlister, K.W., and McCroskey, W.S., "Analysis of the Development of Dynamic Stall Based on Oscillating Airfoil Experiments," NASA TN D-8382, Jan. 1977.

Francis, M.S., Kennedy, D.A., and Butler, G.A., "Technique for the Measurement of Spatial Vorticity Distributions," Review of Scientific Instruments, Vol. 49, May 1978, pp. 617-623.

Francis, M.S., Keesee, J.E., Land, J.D., Sparks, G.W., and Sisson, G.E., "Aerodynamic Characteristics of an Unsteady Separated Flow," AIAA Journal, Vol. 17, No. 12, Dec. 1979, pp. 1332-1339.

Freymuth, P., Bank, W., and Palmer, M., "Visualization of Accelerating Flow Around an Airfoil at Angles of Attack 0° - 30°," 8th Biennial Symposium on Turbulence, Rolla, Mo., Sept. 26-28, 1983.

Hamel, G., "Spiralformige Bewegung Zahler Flussigkeiten," Jahresber, Dr. Mathematiker-Vereinigung 25, 1916, pp. 34-60.

Keese, J.E., Francis, M.S., and Lang, J.D., "A Technique for the Measurement of Spatial Vorticity Distributions," Review of Scientific Instruments, Vol. 49, May 1978, pp. 617-623.

McCrosky, W.M., Carr, L.W., and McAllister, K.W., "Dynamic Stall Experiments on Oscillating Airfoils," AIAA Paper No. 75-125, Jan. 1975.

Oseen, C.W., "Ark.f.Math.Astron.och.Fys.7" 1911; Hydromechanik, Leipzig, 1927, p.82.

Robinson, M.C. and Luttges, M.W., "Unsteady Flow Separation & Reattachment Induced by Pitching Airfoils," AIAA Paper No. 83-0131, Jan. 1983, pp. 1-14.

Robinson, M.C. and Luttges, M.W., "Vortex Generation Induced by Oscillating Airfoils: Maximizing Flow Attachment," 8th Biennial Symposium on Turbulence, Rolla, Mo., Sept. 26-28, 1983, pp. 13.1-13.10.

Schlichting, H., "Boundary-Layer Theory," J. Kestin translation, 7th Ed., McGraw-Hill, New York, 1979, pp. 89-90.

UNSTEADY SEPARATED FLOWS: GENERATION AND USE BY INSECTS

M. W. Luttges, C. Somps, M. Kliss, and M. Robinson
Aerospace Engineering Sciences
University of Colorado
Boulder, Colorado 80309

AD-P004 168

Abstract

The novel lift generation mechanism postulated by Weis-Fogh (1973) and evaluated by Lighthill (1973) in regard to hovering insects provided graphic evidence for the possible utility of unsteady flows. The present report summarizes flight mechanisms in dragonflies that appear to exploit unsteady flows to achieve rather remarkable aerodynamics. We envision that such studies may provide a means of identifying crucial combinations of unsteady variables that are effective in both generating and using unsteady flows.

Dragonfly flight was studied both in unrestrained, normal specimens and in tethered, laboratory-tested specimens. In both instances, high speed photography permitted the characterization of wing motions including stroke length, stroke angles, stroke frequency, angles of attack and phase angles for the tandem pair of wings. In the laboratory such observations were coupled with force balance measures such that instantaneous correlations of wing motion and lift were obtained. Flow visualization also was obtained for tethered insects during elicited flight episodes. Simple oscillating plate models were used in a zero flow test to simulate at least some aspects of observed dragonfly aerodynamics.

The flight modes of a dragonfly include (1) high-speed forward and upward maneuvers, (2) gliding or soaring maneuvers, and (3) hovering or slow maneuvers in any direction. Combined modes and rapid transitions from one mode to another are observed often without major changes in body attitude or wing dynamics. The wing geometries are simple and static except for passive deformations produced by interactions with nearby energized fluid. Wing dynamics include wing beat frequencies of 25-36 Hz, wing stroke angles of 35° forward and 20° behind the root attachment as well as angles of 40° beneath and 60° above the horizontal, angles of attack of 1 to 50° and phase angles for the tandem wings of near 0 to 30°.

In tethered insects a well-defined point of maximum lift generation occurred once during each wing beat cycle of the tandem wings. The maximum lift generated at this point was approximately 20 times body weight. In contrast, unrestrained dragonflies routinely exhibit very stable hovering indicative of more continuous lift generation. Photographs of dragonflies exhibiting both modes of flight revealed no remarkable changes in wing motion despite the obvious differences in lift generation.

Flow visualization in the vicinity of tethered dragonflies revealed two major types of structure. During episodes of high lift generation, smoke moves rapidly from ahead of the insects to form 45° angle wakes behind them. The structure of the wakes is commonly dominated by vortices that appear to unfold as the wake travels downstream. In conditions of more modest lift generation, the smoke is pulled into large stationary vortices surrounding the upper wing stroke quadrant.

As a working model of dragonfly flight mechanisms, summarizes the observed wing positions, angles of attack, flow fields and lift peaks we have been able to characterize. In essence, it appears that high angles of attack of the wings generate a local circulation exploitable to provide relatively high lift under hovering conditions. Angles of attack appear smaller if thrust is to be provided and if net flow is to be achieved.

In view of these observations, vertically-oriented flat plates of varying thicknesses were driven back and forth in a zero flow test condition to evaluate the effects of stroke length and stroke frequency. The results of these studies were quite clear. For very thin plates, stroke length dictated vortex size and stroke frequency had little effect other than a modest enhancement of flow structure cohesiveness. The addition of angularity to the flat plates resulted in net flows dominated by vortices. These observations are consistent with the notion that flow structure may be initiated by a wing and can be expected to persevere. This preserved local flow structure could be exploited by another wing or by the same wing on a later stroke.

Overall, these experiments indicate that unsteady flows may be used to support quite sophisticated insect flight maneuvers. No significant change in wing geometry is needed to achieve such flight and only modest alterations in dynamic wing stroke variables are required. The observations made here indicate that dragonflies use mechanisms quite different from those used by the Chalcid wasp, as described by Weis-Fogh. Other means of exploiting unsteady separated flows may exist also within the insect world. Many of these possibilities remain to be examined and to be analyzed in regard to generation, control and use.

Introduction

The publication of two papers concerned with hovering in the Chalcid wasp, Encarsia formosa, (Weis-Fogh, 1973; Lighthill, 1973) signaled a renewed interest in biological models of flight. Weis-Fogh had suggested the existence of a novel lift generation mechanism to explain hovering in the Chalcid wasp as well as other insects. Lighthill showed that such a novel mechanism could, in principle, account for the required levels of lift generation during hovering. More recently, Maxworthy (1979) has shown that the postulated flows elicited by the wasp could be simulated by a simplified physical model. The impetus for most of these studies has grown out of an interest [illegible] by fluid mechanicists.

Flight, [illegible] represents a more useful model for examination than flight in mammals and birds. Lifting surface configurations are often more simple in insects and muscle-elicited changes in configuration during various flight modes are more limited. Unlike birds, for example, many insects achieve excellent aerodynamics and maneuverability in the absence of a variety of deployable wing devices. Also, insects are able to accomplish a wide range of flight behaviors without the aid of an elaborate set of neural controls. Thus, attempts to understand biological flight are best focused upon these accomplished, but simple, flight practitioners.

Work focused upon the Chalcid wasp is limited by several considerations. First, the wasp is extremely small (~ 0.5 cm) and exhibits flight in a very low Reynold's number range. To do so, wing beat frequencies approach 300 Hz. Also, this wasp has not received much attention in regard to either flight musculature or neural flight control mechanisms.

Because of these limitations with the Chalcid wasp, we have elected to study flight in the dragonfly. Weis-Fogh (1973) cited this insect as one which most probably had to utilize novel lift generation mechanisms. More recently, Norberg (1975) and Savage et al. (1979) have provided evidence that these insects produce higher amounts of lift than can be anticipated using usual steady state aerodynamic principles. Work on underlying neural control mechanisms (Pringle, 1968; Neville, 1960) indicates that these insects use central pattern generators to drive wing movements. These movements are subject to only minor (Alexander, 1982; Olberg, 1983) feedback modifications. Thus, the dragonfly appears to achieve excellent aerodynamics not using standard steady state mechanisms and not depending upon elaborate wing control. The wing motions exhibited by dragonflies reveal highly stereotyped kinematics and fluid-wing interactions. So dedicated are the wing motions, the wing musculature has but two cardinal motions: elevation and depression. Flexion and extension, characteristics of insects which retract or fold the wings when not in use, are omitted from both the control and musculature of the dragonfly (Clark, 1940).

As an aside, it is notable that fossil records indicate dragonflies have survived since the time of dinosaurs, essentially unchanged except for a modest decrease in size. Presumably these insects which mate and eat while airborne have engaged in innumerable life and death aerodynamic struggles in the approximately 250 million years of existence. Obviously, these highly skilled flyers have, as a species, prevailed through this test of time. Humbled by this remarkable record of survival, we set out to investigate the inherent flight wisdom of the dragonfly.

Our studies were designed to determine (1) what quantities of lift the dragonfly generates, (2) how this lift related to wing kinematics, and (3) whether specific fluid interactions occurred about the wings.

Methods

In beginning our studies it was necessary to perform a number of pilot investigations. Dragonflies (Odonata, anisoptera) were netted from nearby habitats in the early morning. This was readily accomplished since dragonfly escape flight from a stationary reed or twig was highly predictable. These insects inevitably depart rapidly at a 45° angle from the horizon and in the direction of body orientation. The insect net was simply moved to an intercept position. Within an hour of capture, the insects were in the laboratory being subjected to cooling (for next day testing) or to chloroform anesthetization (for handling purposes). Each insect was weighed, fully measured and then tethered to a small wood beam using cyanoacrylate. A variety of tests ensued as described below.

To relate laboratory observations with natural flight behavior in the dragonfly, unrestrained flight of the dragonfly was observed in the habitat from which they were collected. Flight modes were recorded and simple aerodynamic values were estimated. In addition, the wing kinematics were recorded using telescopic photography (35 mm camera; 1/1000 shutter speed; 250 mm lens; 1000 ASA color film). Most photographs were taken as the dragonflies hovered near favorite reed-top perches.

Lift measurements and simultaneous wing motion analyses were achieved with tethered dragonflies mounted to a one-dimensional strain-gauge force balance. The amplified force balance output was displayed on one channel of a CRT oscilloscope and a photodiode output was displayed on the second channel. As the stroboscopic (~ 0.5 msec) illumination was triggered for photographing wing motion, the diode signal on the oscilloscope marked related instantaneous lift values. Alternatively, continuous Strobotach (Gen. Radio) output provided diode marking of lift values associated with videotaped, phase-related wing motions. From a large number of elicited flight episodes visualized for 21 dragonflies, it was possible to describe both the wing kinematics and the associated, phase-related lift values. In many instances, it was necessary to place a mark on the rear wings of the dragonflies to assure subsequent discrimination of the front from the rear wings. In some instances, the cyanoacrylic cement used for tethering spread to legs of the insects or to other thoracic structures. These specimens were not used since the spread might have altered flight patterns and lift generation. In general, the insects could be tested over numerous flight episodes for periods of at least two hours. Altered wing motions and decreased lift generation were used as indicators of deteriorating flight behavior.

Flow visualization was achieved during dragonfly flight episodes. Heated kerosene smoke was delivered (< 10 cm sec^{-1}) from a 1 cm diameter tube approximately 10 cm in front of the test specimens. The laminar smoke stream was positioned to intercept the median wing position approximately mid-span. All testing and photography was done in a 60 x 60 x 80 cm zero flow box constructed of clear cast acrylic (Plexiglas). At about the middle of a flight episode lasting 3-5 secs, a stroboscopic photograph was taken. This procedure was repeated many times to produce a composite model of flow (smoke stream) -wing interactions.

Based upon the above observations, an empirical model of wing motion and flow interactions was constructed to relate to the observed amounts of lift generation. Also, a few simplified experiments with an oscillating flat plate were pursued to simulate some of the flow-wing interactions observed during dragonfly testing. Finally, a novel means of testing dragonflies was developed to permit more detailed flow-wing visualizations. This novel procedure is described together with a projection of its potential in model studies of insect flight.

Results

Before turning our attention to the laboratory studies, a few of our observations on natural flight will be summarized (Table 1). After spending much of its development as a predatory water nymph, the dragonfly emerges as the flying adult form from a metamorphosis that takes place on a twig or reed that grows out of the water habitat of the nymph. As the wings are unfolding and drying, the adult, itself, is subject to predation by birds. Thereafter, dragonflies are not subject to heavy predation because both color and maneuverability provide excellent survival probability.

Flight in the adult dragonfly serves several biological functions and roles. During feeding, the dragonfly alternates between gliding, powered flight and aerobatics. During territory patrols, a prelude to mating, the dragonfly glides with an occasional powered wingbeat sequence to maintain altitude. In instances of startle or predation threat, episodes of escape behavior consist of powered flight upward at 45° angles mixed with dramatic aerobatics. Mating consists of male and female dragonflies flying in tandem with constant, albeit poorly coordinated, wing motion exhibited by one or both members of the union. In all of the above circumstances, periods of hovering occur. Hovering also occurs as a prelude to a dragonfly returning to a favored perch atop a reed.

Reduced to flight modes, the dragonfly exhibits escape, gliding and hovering. Escape consists of short duration (1-5 secs) episodes of high amplitude, high frequency (~ 30 Hz) wingbeat cycles that propel the insect at speeds estimated at > 5 m sec^{-1}. Gliding is a forward, low angle flight rarely interrupted by wing motion. This mode continues for periods of 10 or more seconds. A relatively moderate speed of 1 m sec^{-1} is estimated. Hovering is stationary flight that shows remarkable spatial stability (<0.5 cm) and durations of > 10 sec. Slow spatial corrections occur with movements in all planes and with backwards movements, as well. We judged that transitions from one flight mode to another occurred in approximately 100 msec. During most flight modes, the dragonfly body remains oriented along the flight path and during hovering this horizon-oriented body position does not change regardless of upward, downward, sideward or backward movements.

During all of our dragonfly observations, only one flight instability appeared to occur--a roll instability. In hovering, the dragonfly maintained its position in space relative to a fixed landing site atop a reed, but often the spatial stability gave way to a rotation of the body about its long horizontal axis. The net result, of course, was that the legs were sometimes rolled away from the landing site and further flight corrections were required.

Using high speed film and natural lighting, we photographed many dragonflies during hovering. This photography provided a basis for comparing the wing kinematics of tethered dragonflies to those of dragonflies exhibiting natural flight. A few of these photographs are shown in Fig. 1. The wing positions are quite similar to those photographed previously (Dalton, 1975; Norberg, 1975). Also, the same wing motion characteristics are seen in our laboratory tests. This comparison is important since the lift generation measured in tethered specimens (whether using normal wing kinematics or not) was quite high. Undoubtedly, the wing-fluid interactions supporting such high lift are of prime importance but, in addition, it seems biologically unlikely that highly disturbed wing motions would be capable of high lift generation. In any event, the photographs of natural flight clearly show that the tethered dragonflies exhibit, at our present level of analysis, normal wing kinematics.

The _Libellula luctuosa_ specimens tested in the laboratory for simultaneous wing motion and

Flight Characteristics of Unrestrained Dragonflies

Modes	Duration	Speed	Maneuvering
1) Escape	<5 sec	>5m sec^{-1}	modest; upward, forward @ 45° angle from body axis
2) Gliding	>10 sec	~1m sec^{-1}	little; low negative angle glide path; occasional wing use to regain altitude
3) Hovering	>10 sec	---	excellent but slow movement in virtually any direction in any plane

i) feeding on the wing consists of brief bursts of directions, sharp turns and rapid reversals of direction; similar aerobatic displays observed in dragonfly disputes over territory

ii) roll instabilities seem prominent

iii) aerobatic displays appear to be comprised of rapid (<100 msec) changes from one flight mode to another

Table 1. Observed natural flight behaviors of dragonflies. Based upon observed major flight characteristics exhibited during feeding, patroling, territory displays, mating and predation avoidance, these general categories summarize the most reliably observed flight modes.

Fig. 1 Examples of wing positions photographed for hovering dragonflies. The photographs were taken with a 1 msec shutter speed using a telephoto lens and natural light. Over 120 such photographs were used to document the similarities in wing kinematics between free flying and tethered dragonflies.

Lift generation measured had an average weight of [illegible] ± 36 mg. The area of the four wings averaged 1[illegible] ± 1 cm^2 so the typical wing loading was [illegible] ± [illegible] mg/cm^2. Aspect ratios of the front wings were 8-[illegible] and of the rear wings were 6-7. The dragonfly wing exhibits relatively thick venation that provides both structural reinforcement as well as local cambering or roughness. The leading edge venation or spar is comparatively thick, also, but behind the 1/4 chord location, the venation thins out. The trailing edges of the wings are much more delicate and flexible than the leading edge - 1/4 chord components of the wings. At the [illegible] chord, the wings narrow to the point of thoracic attachment. Wing thickness to chord ratios range from [illegible] 1-2%. A representative photograph of front and rear wings is provided in Fig. 2.

The test specimens were attached to the [illegible] force balance in the [illegible]

Fig. 2 A silhouette of a dragonfly [illegible] wing geometry, venation and form relative to the body. The lighting used in this photograph "washed-out" [illegible]

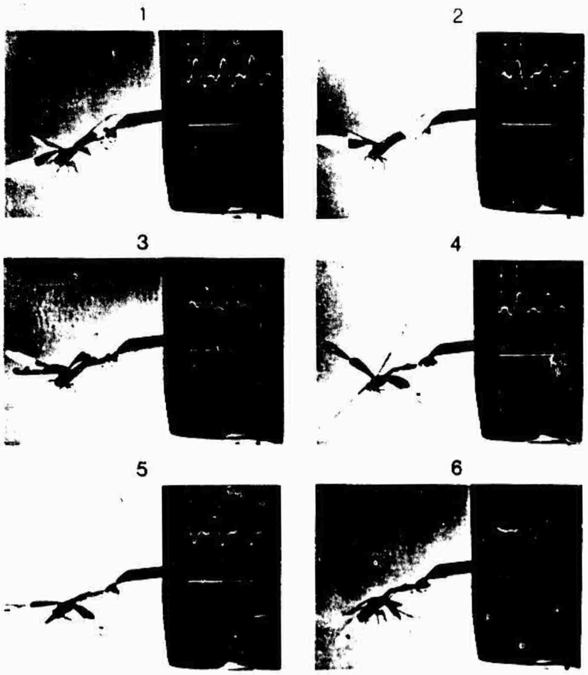

Fig. 3 Simultaneous photographs of dragonfly wing motions and photodiode marked, lift generation. These frontal views of the dragonfly revealed wing stroke angles while side views (not shown) revealed caudal-rostral angles as well as the geometric angle of attack of the wings. In these photographs, the rear wings were marked to allow easier differentiation of front and rear wing angles.

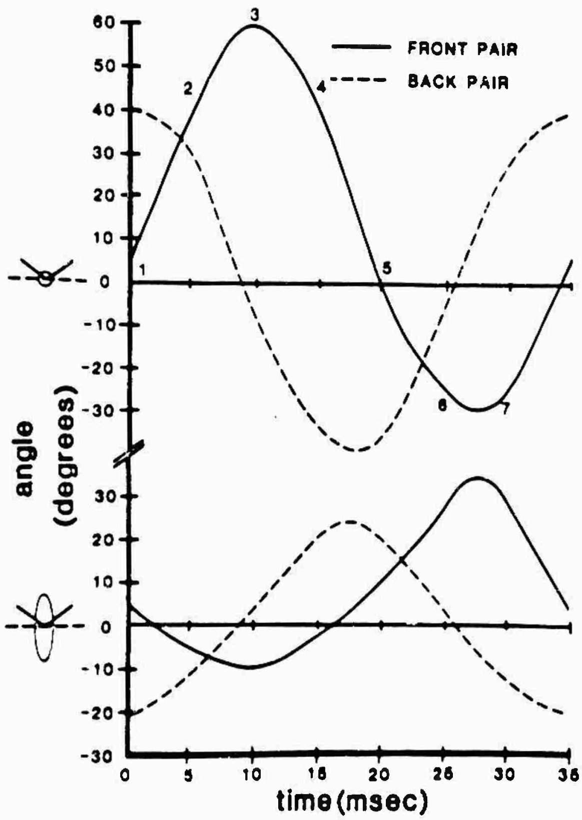

Fig. 4 Summary of two dimensions of the wing motions. Using video tapes and 35mm photographs, the typical wing angles are indicated across a full wingbeat cycle. Both front and rear wing motions are indicated such that phase angles between them can be determined. These motions can be summarized as a wing tip motion which traces out an ovoid path slanted downward and forward then upward and backward through a complete wingbeat.

box both wing motions and oscillographic records could be photographed simultaneously. A typical series of wing positions and associated lift traces are provided in Fig. 3. Using these photographs and Strobotach illuminated video tapes, it was possible to construct the summary of wing kinematics as shown in Fig. 4. As may be seen, the wing tips trace out an oval during each cycle. Beginning at the top of this oval, the wing tips move downward and forward, then upon reaching the bottom of the oval they twist upward while moving backward to return to the top of the oval. Both the front and rear wing of the tandem pair show similar motions, although the rear wing can lead the front one by as much as 150° in some instances, the wings are clearly 180° out of phase with each other, so it is difficult to determine which wing leads through a typical wingbeat cycle. The frequency of wingbeat cycle is approximately 25-35 Hz and at any instant is the same for both wings. Average wing tip velocities were about 40% larger during upstrokes (~ 370 cm sec^{-1}) than during downstrokes (~260 cm sec^{-1}).

The model of wing tip motion in Fig. 5 summarizes approximate angles of attack associated with various phases of a typical wingbeat cycle. The angles indicated are shown for increments of time of about 5 msec so fewer angles are depicted on the upstroke than the downstroke. In these summaries, no attempt has been made to represent wing twisting along the span; however, a modest amount of twisting propagates from the root to the wing tip each time the wing changes direction from upstrokes to downstrokes and vice versa.

The lift generation recorded across all 21 specimens and over a dozen elicited flight episodes each revealed an instantaneous peak once during each complete wingbeat cycle (Fig. 6). The average amplitudes of such lift peaks was approximately 7 gf (1 gf = 9.81 x 10^{-3} N). Thus, at one instance during each wingbeat cycle, the tethered dragonflies produced lift forces of about 20 times the average body weight. Both Norberg (1975) and Weis-Fogh (1973) had estimated that dragonflies must have a minimum lift

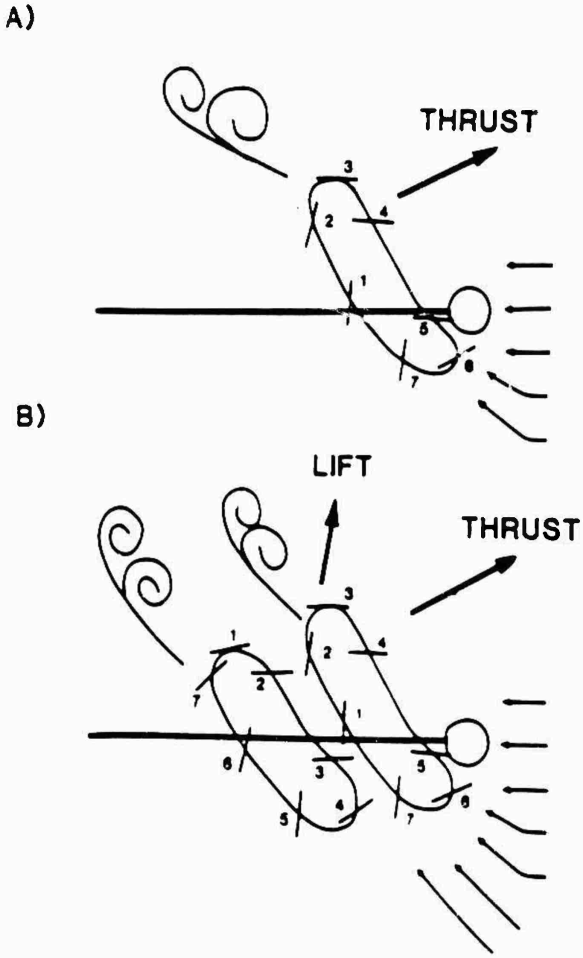

Fig. 5 Summary of geometric angles of attack throughout a wingbeat. These angles are indicative of wing tip characteristics and do not indicate a small amount of spanwise twisting. Hypothesized flow and thrust vectors are also indicated. The angle representations are indicated over a typical 40 msec wingbeat cycle duration at approximately 5 msec intervals.

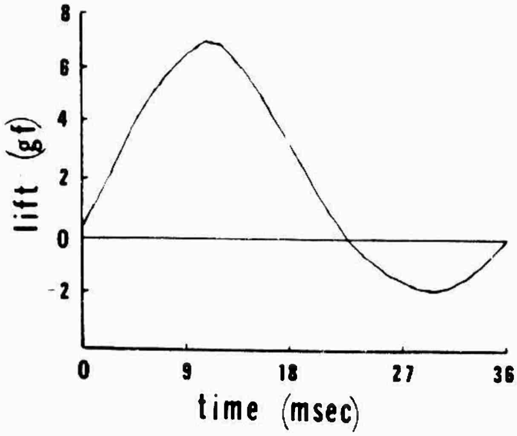

Fig. 6 Summary of lift generation during a typical wingbeat cycle. All wingbeat cycles have been normalized to the indicated time scale to correct for variations in wingbeat frequency. As indicated, lift peaks of approximately 7 gf are generated once during each wingbeat cycle. Such peaks give rise to inordinately high apparent C_L values.

coefficient, C_L, of 2.3 to counteract gravity and that these lift coefficients were not possible using appropriate low Reynold's number, steady-state aerodynamic calculations. To compare measured lift with these estimates, the average sustained lift was obtained from the force balance measures over complete wingbeat cycles. Still, the average sustained lift exceeded twice the dragonfly body weight. Thus, we estimate that the tethered dragonflies tested in our studies must be exhibiting $\bar{C}_L$ values of approximately 4.6; and instantaneous lift values almost 10 times larger!

As a first step in understanding how such large lift values are generated, we examined the wing positions and motions peculiar to the lift peaks. As the rear wing begins the downstroke and is followed into the downstroke by the front wing maximum lift was recorded in all test episodes. Sometimes the lift peak even exhibited two components which we speculate might reflect the peak lift contribution of the two wings moving through the maximum lift production portion of the wingbeat cycle at slightly different times. Also, throughout a typical test episode variations in peak lift amplitudes occurred. Such variations appeared to relate to wingbeat stroke amplitudes but these relationships remain to be more carefully measured. The effect of wingbeat frequency was negligible in terms of instantaneous lift peaks but did, of course, have a direct impact on total amount of lift generated per unit time.

Anxious to determine how these wing kinematics produce such high lift, we arranged a flow visualization test for tethered dragonflies. Thick kerosene smoke delivered a short distance ahead of the dragonflies in the zero flow apparatus was rapidly drawn toward the insect, passed through the tandem wings and appeared as two discernable wakes behind the insect. With ambient illumination, the laminar stream of smoke appears to run into an eggbeater and to emerge as a split, turbulent wake. With stroboscopic illumination, however, the smoke shows a considerable amount of identifiable structure (Fig. 7). The upper wake shows the effects of vortices which seem to be decaying while the lower wake shows rather homogeneous smoke distributions as might be expected from a fully turbulent flow. Video tape records suggested the presence of vortex structures near the wing surface but due to the changing wingbeat frequencies typically shown by tethered dragonflies, it was not possible to document such flow structures photographically. What was quite clear in the photographs was the distinction

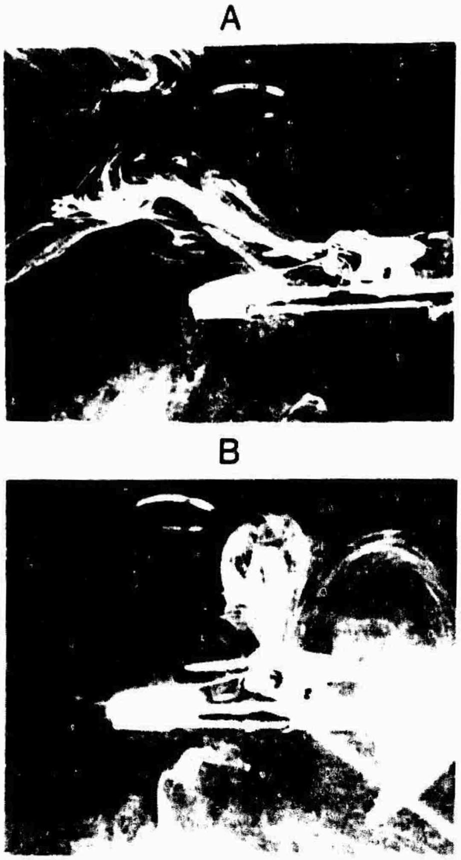

Fig. 7 Stroboscopic flow visualizations of wake structures about a dragonfly during a tethered flight episode. Smoke was delivered immediately ahead of the dragonfly wing at a low velocity.

Fig. 8 Multiple exposure flow visualizations about an automaton model of the tethered dragonfly. All but one forward wing have been removed. The vortex formation is clearly documented for a variety of wing-flow interactions throughout a portion of the wing stroke cycle. The driven wing kinematics are quite similar to those of the unrestrained and tethered (nondriven) dragonflies.

between the source of the wake vortex structures and possible wing tip vortices. The latter moved into the lower turbulent wake and were quite lateral compared to the former. Thus, we were able to document at least the residual evidence of a novel fluid-wing interaction.

Encouraged by these findings, we sought a way to better understand the flow-wing interactions employed by the dragonfly to achieve high lift. Two approaches were tried: (1) the dragonfly was exploited to become an automation model of its flight kinematics and (2) an oscillating flat plate model was used for didactic flow visualization. Both approaches are in their infancy but both appear to have good potential.

The automaton dragonfly approach employs electrical stimuli delivered directly to thoracic neuromuscular systems to elicit flight kinematics. Appropriately placed electrodes can yield stimulus amplitude-dependent control of wingbeat amplitude and frequency-dependent control of wingbeat frequency. Thus, the crucial parameters of the wing kinematics can be made to operate in a quite mechanical fashion. Interestingly, the dragonfly may at any time override the electrical stimuli and initiate flight kinematics of varying frequencies. The dragonflies tested to date rarely elect to disrupt our automaton procedures in this way. The result is a reproducible visualization of wing-fluid interactions at any phase, in what appears to be, a rather normal wingbeat cycle. The preliminary results of this approach are encouraging. As may be seen in Fig. 8, the single front wing (others removed to provide flow simplicity) elicits reproducible vortices during certain portions of the driven wingbeat cycle. Since the visualizations represent 4-5 stroboscopic exposures taken at the same time delay between a stimulus pulse and the onset of illumination, both the automaton characteristics of the wing motion and the reproducible structures of the flow are evident. We have not analysed the wing-flow interactions fully but we can definitely cite the presence of unsteady energized flows produced by dragonfly wing kinematics. Such flows are characteristically seen in the complete four wing automaton model as well. The size, shape and position of these structures, as suggested by the visualizations, make it clear that the flow-wing interactions are remarkably different from those postulated for the Weis-Fogh lift generation mechanism (cf., Weis-Fogh, 1973; Maxworthy, 1979; Maxworthy, 1981).

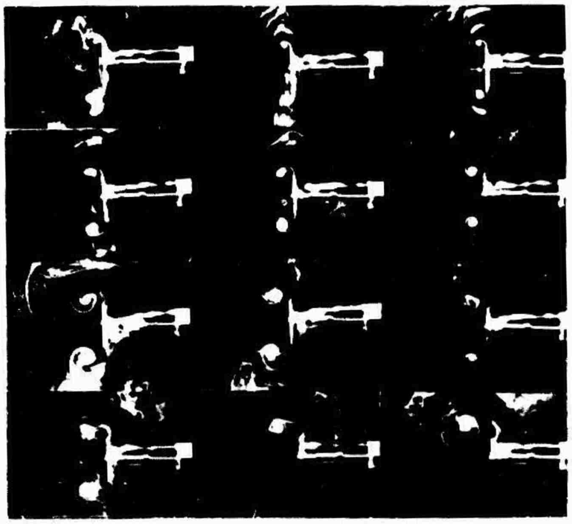

Fig. 9 Flow visualization for an oscillating flat plate. In these photographs the vortex structures elicited by a thin (~ 0.5 mm) plate are shown for a variety of stroke lengths and oscillation frequencies.

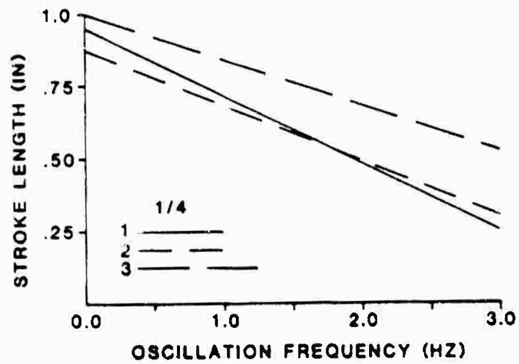

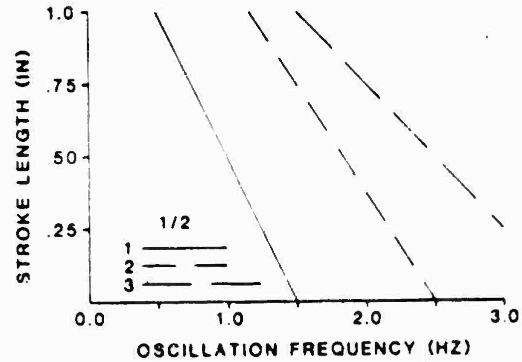

Fig. 10 Summary of stroke length and oscillation frequency effects on vortex formation by an oscillating flat plate. Approximately 160 test conditions were evaluated for flow structure cohesiveness prior to a quantification (ordinal scaling) of the relations depicted here.

In our second model approach employing an oscillating flat plate, we simply sought a didactic indication of flow-plate interactions using a variety of thin plates. In these tests the effects of oscillation amplitude, oscillation rate and plate thickness were visualized. Anemometry data were collected in a single dimension using an overheated miniature thermister. The experimental parameters were quickly reduced to those which produced cohesive vortex structures. Within this parameter range vortex cohesiveness was rated from the flow visualizations and then plotted in regard to the appropriate production parameters. The results were strikingly consistent (Fig. 9). Very cohesive structures occurred with extremely thin plates (~ 0.5mm). As plate thickness increased, both oscillation frequency and oscillation amplitude improved flow cohesiveness. As plate thickness decreased, oscillation frequency had a large effect on flow cohesiveness but stroke length had little effect (Fig. 10). The addition of small amounts of angularity to the oscillating plate did not change this relation. But in instances of angularity that exceeded 20-25°, a definite net flow was induced in the flowfield.

Overall, these observations substantiate an informal bias obtained from flow visualizations about dragonfly wings. First, the flow structure is exceedingly cohesive and, secondly, wingbeat amplitude has little effect upon such structures. The use of plate angles indicates that the oscillating dynamics (that induce an increased or decreased angle relative to flow) can enhance vortex production and cohesiveness. It appears that dragonflies may be able to use similar flow control mechanisms. Other characteristics of this model system will be presented elsewhere (Ellis and Luttges, in preparation). Some of the nondimensional relationships are intriguing in and of themselves.

Discussion

The relationships between dragonfly lift generation and wing kinematics have shown the presence of high lift once during each wingbeat cycle. Also, the total amount of lift generation measured was quite large. These observations are inconsistent with steady-state aerodynamics and indicate that the dragonfly must employ unsteady or energized separated flows to achieve lift. Such direct empirical verification of the need to employ alternative lift generation mechanisms has not been achieved for other hovering insects.

The wing kinematics of the dragonfly differ significantly from those reported for the Chalcid wasp (Weis-Fogh, 1973). Also, the front and rear wings operate independently in an "unlatched" configuration and the dragonfly body remains horizontal throughout different flight modes:

hovering, escape and gliding. These facts suggest that the dragonfly must utilize unsteady flows and related lift generation mechanisms which differ substantially from those of the Chalcid wasp. The flow visualization studies corroborate such a difference. Visualized vortex-dominated flows are immediately adjacent to the wing's mid-span. They persist in this spatial relation to the wing over an appreciable amount of the wingbeat cycle. And, these flows are lateralized such that each side of the insect interacts with a local flowfield that is somewhat independent of the flowfield on the other side. It is tempting to speculate that the lateralization of flowfields underlies the roll instabilities seen in the natural flight of dragonflies.

One major conclusion may be drawn from the above observations: dragonflies use unsteady mechanisms that differ in many ways from those used by the Chalcid wasp. Further, it now appears likely that other biological organisms could utilize yet other unsteady flow characteristics to achieve lift and flight behaviors. This is not a deterrent to attempting to understand and, perhaps, emulate the use of such flows. Rather, it is encouraging that many exploitation possibilities may exist: each optimized for a range of different aerodynamic needs.

For us, our work has just begun. Given the data at hand, we must determine how the dragonfly produces the unsteady separated flows we have visualized. We must determine how these flows are controlled. And, we must determine how such flows interact with the dragonfly wings to produce the remarkable lift values we have documented.

References

1. Adler, J.N., Robinson, M.C., Luttges, M.W., and Kennedy, D.A., "Visualizing unsteady separated flows," Third International Symposium on Flow Visualization, Sept. 6-9, Ann Arbor, Michigan, Proceedings, Vol. III, 1983, pp. 806-811.

2. Alexander, D.E., "Studies on flight control and aerodynamics in dragonflies," Dissert. Abs. Intntl., [illegible], 1983.

3. Bacon, J. and Mohl, B., "Activity of an identified wind interneurone in a flying locust," Nature, 278, 638-640, 1979.

4. Chadwick, L.E., "The wing motion of the dragonfly," Bull. Brooklyn Ent. Soc., 35, 109-112, 1940.

5. Clark, H.W., "The adult musculature of the Anisoptera dragonfly thorax (Odonata, Anisoptera)," J. Morph., 67, 523-565 (1940).

6. Dalton, S., Borne on the Wind, Readers Digest Press, New York: 1975.

7. Furber, S.B. and Ffowcs-Williams, J.E., "Is the Weis-Fogh principle exploitable in turbomachinery?" J. Fluid Mech., [illegible], [illegible], 1979.

8. Lighthill, M.J., "On the Weis-Fogh mechanism of lift generation," J. Fluid Mech., 60, 1-17, 1973.

9. Lighthill, M.J., "Aerodynamic aspects of animal flight," In Swimming and Flying in Nature, Chu, T., Brokaw, C. and Brenner, C. (eds.), Plenum Press, New York; 1975.

10. Luttges, M.W., Somps, C., Kliss, M. and Robinson, M., "Unsteady separated flows: Generation and use by insects," Workshop on Unsteady Separated Flows, Aug. 10-11, 1983, U.S. Air Force Academy. Abstracts, 93-97.

11. Maxworthy, T., "Experiments on the Weis-Fogh mechanism of lift generation by insects in hovering flight. Pt. 1, Dynamics of the fling," J. Fluid Mech., 93, 47-63, 1979.

12. Maxworthy, T., "The fluid dynamics of insect flight," Ann. Rev. Fluid Mech., 13, 329-350 (1981).

13. McCroskey, W., Carr, L. and McAlister, K., "Dynamic stall experiments on oscillating airfoils," AIAA Paper No. 75-125, 1975.

14. Nachtigall, W. and Mohl, B. (eds.), The Biophysics and Physiology of Insect Flight, Biona Reports, Stuttgart, 1982.

15. Neville, A.C., "Aspects of flight mechanics in anisopterous dragonflies," J. Exp. Biol., 37, 631-656, 1960.

16. Newman, B.G., Savage, S.B., and Schonella, D., "Model tests on a wing section of an Aeschna dragonfly," In Scale Effects in Animal Locomotion, Pedley, T. (ed.), Academic Press, New York, 1977.

17. Norberg, R.A., "Hovering flight of the dragonfly Aeschna Juncea L.: Kinematics and aerodynamics," In Swimming and Flying in Nature, Wu, Y., Brokaw, C. and Brennen, C. (eds.), Plenum Press, New York, 1975.

18. Olberg, R., "Identified interneurons steer flight in the dragonfly," Neuroscience Abstracts, Pt. 1, 98.13, 326, 1983.

19. Pringle, J.W.S., "Comparative physiology of the flight motor," Adv. Insect. Physiol., 5, 163-223, 1968.

20. Robinson, M. and Luttges, M.W., "Vortex generation induced by oscillating airfoils: Maximizing flow attachment," VIII Biennial Symposium on Turbulence, Rolla, Mo., pp. 13.1-13.10, 1983.

21. Robinson, M. and Luttges, M.W., "Unsteady flow separation and attachment induced by pitching airfoils," AIAA Paper No. 83-0131, 1983.

22. Savage, S., Newman, B. and Wong, D., "The role of vortices and unsteady effects during the hovering flight of dragonflies," J. Exp. Biol., 83, 59-77, 1979.

23. Somps, C., "Lift generation mechanisms of the dragonfly," AIAA Student Paper Competition, St. Louis, MO., 1982.

24. Weis-Fogh, T., "Quick estimates of flight fitness in hovering animals, including novel mechanisms for lift production," J. Exp. Biol., 59, 169-230, 1973.

25. Wendler, G., "The influence of proprioceptive feedback on Locust flight coordinations," J. Comp. Physiol., 88, 173-200, 1974.

26. Wilson, D.M., "The central nervous control of flight in a locust," J. Exp. Biol., 38, 471-490, 1961.

THEORETICAL STUDY OF NON-LINEAR UNSTEADY AERODYNAMICS OF A NON-RIGID LIFTING BODY

J. C. Wu*, N. L. Sankar**, and H. Hu Chen†
School of Aerospace Engineering
Georgia Institute of Technology
Atlanta, Georgia 30332

AD-P004 169

Abstract

A recently developed general theory of aerodynamics is utilized in an investigation of non-linear unsteady flow problems involving a non-rigid lifting body. It is shown that this theory, developed on the basis of viscous flow equations, permits the important interactive fluid dynamic elements dominating the aerodynamics of non-linear unsteady flows to be identified and their contributions evaluated individually. Closed form expressions for the lift, the drag, and the power expenditure of the Weis-Fogh problem, considered as a special case of flexible lifting bodies, are presented and discussed.

I. Introduction

The subject of unsteady aerodynamics has been, for more than half a century, an active field of fluid dynamics research. Previous theoretical and experimental efforts have demonstrated that, under certain restrictive circumstances, unsteady flows can be approximated by small departures from steady or uniform behavior. The addition of unsteady phenomena to steady ones reasonably describe such flows. The resulting linearized equations describing the flows are often amenable to mathematical treatment. A large body of valuable literature has been developed over the years dealing with various aspects of linear unsteady flows. Most of the fundamental concepts of unsteady flows that are adequately described by the linear theory are now well-understood. In contrast, in the domain of non-linear unsteady flows, where strong unsteady effects invalidate the linear simplifications, the mathematical and experimental difficulties attendant to a rigorous treatment of unsteady aerodynamic problems are immense. Many of the essential and unique features of the non-linear unsteady flows are not well-understood today[1].

In recent years, there has been a rapid growth of research activity in non-linear unsteady aerodynamics. Most of the current research topics in non-linear unsteady aerodynamics are motivated by applications in turbo-machines, marine propellers, helicopter rotors, etc., where strong flow unsteadiness is an intrinsic part of the overall behavior. The minimization or alleviation of large adverse effects caused by flow unsteadiness is of primary concern in these applications. A number of researchers have, however, undertaken research efforts with the aspiration of employing unsteady aerodynamic forces advantageously in the design of future airborne vehicles. It is worthy of note that the design of aircraft of the past and present generations are conceptualized mainly within the context of steady and quasi-steady aerodynamics. Since the production of large unsteady forces is invariably associated with flows in the non-linear domain, an improved understanding of non-linear unsteady aerodynamic phenomena is a prerequisite to the advantageous utilization of such forces.

---

* Professor.

** Senior Research Engineer.

† Graduate Research Assistant.

The present paper describes some of the recent efforts of the present authors in establishing an adequate understanding of the various inviscid and viscous mechanisms of generating unsteady aerodynamic forces. The work described here is a part of a long range research program, underway since early 1970s, in computational aerodynamics and in theoretical aerodynamics. This research program has progressed through several stages. During its initial stages, computational and theoretical approaches designed specifically for non-linear unsteady flow problems were conceived, developed, calibrated, and thoroughly tested through analyses and numerical illustrations. Most recently, these approaches have been utilized in studies of several important problems of non-linear unsteady aerodynamics. These studies demonstrated that a general theory for aerodynamic forces and moments in viscous flows, developed previously by the first author of the present paper, is ideally-suited for non-linear unsteady aerodynamic problems.

In previous papers[2,3], detailed and rigorous derivations of the general aerodynamic theory and preliminary results of a theoretical study of the vortex/airfoil interaction problem have been presented. In the present paper, important concepts related to the application of this general theory are reviewed. In particular, it is shown that, with this general theory, the total air load on a solid body can be divided into several components, each representing the contribution of a distinct physical process. This distinguishing feature of the general theory can be utilized in the establishment of a reasonable understanding of the detailed mechanism of production of aerodynamic forces. It is anticipated that such an understanding will in time provide a rational basis for the alleviation, control, or utilization of large non-linear aerodynamic forces in various applications.

The contents of the present paper are centered upon the theoretical treatment of the Weis-Fogh problem. Extensive computational efforts, however, are being carried out concurrently with theoretical studies. In fact, computational results have provided in the past and are continually providing important physical insights to unsteady aerodynamic problems. Numerical procedures utilized in the present research program emphasize integral-representation formulations of the viscous flow equations[4]. This formulation permits the solution field to be confined to the vortical region of the flow. However, once the vorticity distribution is computed, then the evaluation of the co-flowing potential flow surrounding the vortical region is straightforward. The resulting numerical procedure is particularly well-suited for computing high Reynolds number external flows. For these flows, the vortical region, which may encompass boundary layers, recirculating flows and wakes, comprises only a small part of the total flowfield. The integral-representation formulation, by confining the solution field, leads to extremely efficient numerical procedures. Furthermore, the integral representation approach permits the boundary layer portion and the detached portion of the vortical region to be computed individually[5], thus eliminating the difficulties of simultaneously accommodating the diverse length scales present in the two portions of the vortical flow. At present, parametric studies of two-dimensional flows can be performed economically using widely available computers such as the CDC-6600 computer. Three-dimensional computations have been carried out for several flows involving simple boundary geometries. The amounts of computation required for these flows are not unreasonable. Computed results for the unsteady flow problems discussed in this paper and in Reference 3 will be presented in future articles. In this connection, it is worthy of note that the general viscous theory of aerodynamics used in the present study relates the aerodynamic forces and moments acting on lifting bodies to their vortical environments. The general theory and the integral-representation approach are therefore ideally suited for one another in a combined theoretical and computational research program.

Previous applications[2,3] of the general viscous theory of aerodynamics are concerned with flows past rigid lifting bodies. The Weis-Fogh motion considered in this paper, however, involves two wings attached and yet moving relative to one another. The present study is, in this context, a precursor to a more comprehensive study of the unsteady aerodynamics of flexible (non-rigid) lifting bodies. It has been recognized for a number of years that unsteady aerodynamics of flexible lifting bodies is inherent to aquatic propulsion and flight of animals. Obviously, a reasonable understanding of the physical mechanisms of generation of unsteady aerodynamic forces accompanying large amplitude motions of flexible lifting surfaces is, beyond its biological significances, of decisive import to novel designs of airborne vehicles utilizing large unsteady forces.

2. Vorticity Dynamics

Unsteady incompressible motions of viscous fluid are governed by the law of mass conservation and Newton's laws of motion. The mathematical statements of these laws are familiarly expressed, in terms of the velocity vector $\vec{v}$ and the pressure p, as the continuity and the Navier-Stokes equations. It is however, advantageous to introduce the concept of vorticity vector $\vec{\omega}$ defined by

$$\nabla \times \vec{v} = \vec{\omega} \tag{1}$$

and to consider the vorticity transport equation

$$\frac{\partial \vec{\omega}}{\partial t} = (\vec{\omega} \cdot \nabla)\vec{v} - (\vec{v} \cdot \nabla)\vec{\omega} + \nu \nabla^2 \vec{\omega} \tag{2}$$

There are several major advantages in the use of the concept of vorticity. In the first place, the remarkable success of the well-known circulation theory in predicting the lift force implies that the vorticity of the flow, which ultimately should be responsible for the circulation, is accountable for forces exerted by the fluid on aerodynamic surfaces. Secondly, it is well known that viscous effects are present only in the vortical part of the flow. This fact suggests that it is possible, in studying flows about solid body, to confine the solution to the viscous region of the flow through the use of the vorticity concept. Thirdly, the concept of vorticity permits the overall flow problem to be decomposed into a kinematic aspect and a kinetic aspect. This decomposition facilitates the identification of important physical processes associated with various types of flows. These major advantages offered by the use of the vorticity concepts have been employed by the present authors in studies of unsteady aerodynamic problems. In particular, the first advantage has yielded the general viscous theory of aerodynamics[2] and the second advantage the integral representation approach for computing viscous flows. The third advantage has been utilized previously in studies of various steady and time-dependent flow problems. This advantage is briefly reviewed below.

The kinematic aspect of the viscous flow problem is described by Eq. (1) and the continuity equation. This aspect expresses the instantaneous relationship between the velocity field and the vorticity field. The kinetic aspect of the problem is described by Eq. (2). This aspect is concerned with the redistribution of vorticity in the fluid through various kinetic processes. In studies of unsteady flows, it is convenient to follow the kinetic development of the vorticity field in the fluid. A knowledge of the velocity field is needed in the solution of the vorticity transport equation. This velocity field is kinematically a function of the vorticity field. The vorticity transport equation is non-linear and its mathematical analysis presents great difficulties. It is, however, possible to obtain a significant amount of understanding about the kinetic processes involved in unsteady flows without detailed mathematical analyses.

Consider a finite solid body immersed in an infinite incompressible fluid with uniform viscosity. The solid body is initially at rest in the fluid which is also at rest. Subsequent prescribed motion of the solid body induces a corresponding unsteady motion of the fluid. It has been shown that vorticity is neither created nor destroyed in the interior of the fluid domain[4]. Vorticity, however, is continually being generated at the solid boundary in contact with the fluid following the initiation of the solid motion. This vorticity spreads into the interior of the fluid by the process of viscous diffusion and, once there, is transported away from the solid surface by both convection and diffusion. Since the transport of vorticity by convection is a finite rate process and that by diffusion is effectively finite rate, the vortical region of the flow is of finite extent at any finite time level after the initiation of the solid motion. Outside the vortical region, the flow is irrotational and therefore inviscid. If the flow Reynolds number is not small, then the effective rate of viscous diffusion is much smaller than that of convection. Therefore, a large region of the fluid, ahead and to the side of the solid, is free of vorticity and is inviscid.

The general pattern of unsteady flow development can be briefly described as follows. As a consequence of the solid motion relative to the fluid, vorticity is generated continually at the fluid/solid interface. Once generated, the vorticity moves along the solid surface as long as the flow remains attached. That is, since the effective rate of viscous diffusion is much smaller than that of convection, the vorticity, generated on the solid surface, cannot penetrate far into the interior of the fluid domain before being carried downstream by the fluid motion. A thin layer of vorticity adjacent to the solid boundary is therefore present. This layer is simply the well-known boundary layer. The vorticity within the boundary layer continually moves downstream with the fluid and, at the same time, is continually being replenished through the generation of vorticity on the solid surface. This process of replenishment is present in both steady and unsteady flows. In steady flows, the replenishment process and the vorticity transport process balance one another and the vorticity distribution in the boundary layer is independent of time in a reference frame attached to the solid. In unsteady flows, the replenishment and transport processes do not balance one another and vorticity distribution in the boundary layer is time-dependent. In both steady and unsteady flows, because the boundary layers are thin, it is often convenient to represent the vorticity in the layers by vortex sheets.

The representation of a boundary layer by a vortex sheet in the present context does not imply an inviscid fluid assumption. Rather, this representation approximates the location of the vorticity across the boundary layer by a given point adjacent to the solid surface. The strength of the concentrated vortex sheet is simply the integrated vorticity across the boundary layer. The vortex sheet moves along the solid surface. The distinction between the inviscid assumption and the present approximation is not merely a matter of semantics. While the two concepts often lead to the same conveniences in analyses and computation, the present approximation is based on a viscous flow viewpoint and experiences no conceptual difficulties associated with previous inviscid theories.

The vorticity in the boundary layer eventually leaves the vicinity of the solid surface through several possible avenues. If no massive separation of the flow occurs on the solid surface, then the vorticity in the boundary layer eventually feeds into a wake layer. This occurs, for example, in the case of a thin airfoil at a small angle of attack. The two boundary layers at the two sides of the airfoil in this case merge at the trailing edge, with both layers feeding vorticity into the wake layer. In steady flows, the total flux of vorticity entering the wake is zero. In unsteady flows, a net flux of vorticity enters the wake. Since the boundary layers are thin, the wake layer, which is a continuation of the boundary layers, is also thin initially. As the vorticity layer moves away from the solid through the convective process, viscous diffusion produces only a slow growth in the thickness of the wake layer. In consequence, it is reasonable in many applications to represent the wake layer also by a vortex sheet. The wake layer is usually unstable. The velocity field associated with the vorticity in the wake layer causes the wake layer to "roll-up"[illegible]. If the roll-up process occurs at a large distance from the solid, then it is reasonable to represent the rolled-up vorticity by a single vortex filament in analyzing the flow near the solid. If the roll-up process occurs near the solid, however, then detailed structure of the rolled-up vorticity may be necessary. In any event, the total strength of the rolled-up vorticity needs to be known in order to determine correctly the aerodynamic forces acting on the solid. For three-dimensional flows, the vorticity in the boundary layer leaves the vicinity of the solid surfaces also through the formation of tip vortices which usually roll up.

In applications where flow separation is an important feature, the representation of the vorticity in the boundary layer part of the flow by a vortex sheet is still permissible. Quantitatively accurate solution to the flow problem in this case requires a knowledge of the detailed vorticity distribution in the separated (recirculating) part of the flow. This distributed vorticity is not accurately represented by concentrated vortex sheets or vortex filaments. It is well known, however, that in unsteady flows vortex assemblies often move more or less as an entity. In consequence, considerable physical insight can be gained through a vortex sheet/filament representation even in cases of flows containing massive separated regions.

3. Aerodynamic Theory for Viscous Flows

Aerodynamic forces and moments acting on solid bodies immersed and moving in viscous fluids can be determined, in principle, through a quantitative knowledge of the detailed fluid motion around the bodies. The acquisition of detailed information about the real flowfield associated with lifting surfaces, however, presents immense, often insurmountable, mathematical and experimental difficulties. Historically, therefore, the most remarkable advances in aerodynamics were brought about by aerodynamicists who perceived approaches for the prediction of aerodynamic forces and moments that avoid, as much as possible, entanglement with the details of the fluid motion. In particular, the circulation theory is known to predict the lift force accurately for certain types of lifting surfaces, e.g., thin airfoils with sharp trailing edges, under certain flow environments, e.g., small angles of attack.

The circulation theory is today, as it was fifty years ago, the foundation of accepted theories of aerodynamics. Considerable uncertainties and conceptual difficulties, however, exist regarding the application of the circulation theory in cases where the lifting surface does not possess a sharp trailing edge or where more than one trailing edge is present, where massive flow separation occurs, and where the lifting surface is three-dimensional and its motion is time-dependent. These uncertainties arise mainly because of the perfect-fluid assumption in the mathematical development of the theory. The viscous origin of circulation has been long recognized and several well-known works, e.g., by Von Karman and Millikan[7] by Howarth[8], and by Sears[9], have dealt with certain aspects of viscous phenomena that produce circulation. A thorough understanding of the viscous mechanisms of generation of steady and time-dependent aerodynamic forces, however, is not available and it is usually difficult to interpret the application of the circulation theory as an approximation of the viscous flow phenomena.

A general theory[2] for aerodynamic forces and moments in viscous flows was rigorously established recently on the basis of the Navier-Stokes and continuity equations. No simplifying assumptions, other than those contained in the Navier-Stokes equations, were introduced in the derivation of this theory.

The general theory comprises the following three mathematical statements:

$$\int_{R_\infty} \vec{\omega}\, dR = 0 \tag{3}$$

$$\vec{F} = -\frac{\rho}{d-1}\frac{d}{dt}\int_{R_\infty} \vec{r}\times\vec{\omega}\, dR + \rho\frac{d}{dt}\int_{R_s} \vec{v}\, dR \tag{4}$$

$$\vec{M} = \frac{\rho}{2}\frac{d}{dt}\int_{R_\infty} r^2\vec{\omega}\, dR + \rho\frac{d}{dt}\int_{R_s} \vec{r}\times\vec{v}\, dR \tag{5}$$

where R_∞ is the infinite unlimited region jointly occupied by the fluid and the solid bodies; $\vec{F}$ is the aerodynamic force acting on the solid bodies; d is the dimensionality of the problem, i.e., d = 2 for two-dimensional flows and d = 3 for three-dimensional flows, $\vec{r}$ is a position vector; R_s is the region occupied by the solid bodies, and $\vec{M}$ is the moment of aerodynamic force acting on the solid bodies.

Equations (3), (4) and (5) are valid for the incompressible motion of an infinite fluid with uniform viscosity and with one or more solid bodies immersed in the fluid. The motions are considered to start from rest and are generally time-dependent. Steady flows, when they exist, are considered to be approached asymptotically at large time levels after the onset of the motion. Equation (3) states that the combined total vorticity of the fluid and the solid bodies is zero. The vorticity in the solid bodies, as defined by Eq. (1), is simply twice the angular velocity of the solid bodies. In cases where the region occupied by the solid bodies is negligibly small, or where the solid bodies undergo only translational motions, the vorticity in the solid vanishes and the total vorticity in the fluid is zero. For these cases, existing inviscid aerodynamic theories correctly require the total circulation of the whole system, including the bound vortex, the starting vortex and the wake vortices, to be zero. The effects of rotation of the solid bodies and of distributed vorticity, correctly given by Eqs. (3) are generally not included in inviscid analyses.

Equation (4) states that the aerodynamic force acting on the solid bodies is composed of two contributions. The first term on the right side of Eq. (4) gives the contribution of the time variation of the first moment of the vorticity. The second term gives the contribution of the inertia force of the fluid displaced by the solid bodies. Equation (5) states that the moment of aerodynamic force is composed of two contributions, a contribution of the total second moment of the vorticity field and a contribution of the moment of inertia. The inertia terms in Eqs. (6) and (7) of course vanish in cases where the solid region is negligibly small or where the solid bodies experience no acceleration.

As discussed earlier, it is convenient to divide the overall unsteady flow problem into its kinetic and kinematic aspects. The general theory described here relates the unsteady aerodynamic forces and moments acting on the solid bodies to the kinetic development of the vorticity field. The task of analyzing the kinetics and the kinematics of the flow remains.

It is clear from the general theory, that all the information about aerodynamic forces and moments are contained in the time-dependent vorticity environment of the lifting body. No information about the potential field surrounding the vortical region is needed in the theory. Under certain restrictive circumstances, it is possible to specify the vorticity field approximately without actually solving the vorticity transport equation. The general theory described above then permits the unsteady aerodynamic forces and moments to be determined in a straightforward manner.

It needs to be emphasized, even at the risk of appearing repetitive, that the general theory described above is exact in that it is an exact consequence of the viscous flow equations. This fact, however, does not inhibit the introduction of approximations to the equations given in this section. As discussed in Section 2 of this paper, the word "approximation" is used here to indicate that the precise distribution of the vorticity in the fluid is compromised in exchange for convenience in the evaluation of unsteady aerodynamic forces and moments. Through this approximation, the general theory offers an opportunity of establishing important physical insight to the mechanisms of generation of large unsteady aerodynamic forces. This opportunity is available even with relatively imprecise approximations of the vorticity distribution. Under circumstances where the vorticity distributions can be accurately approximated, the general theory leads to accurate predictions of unsteady aerodynamic forces and moments in both the linear and the non-linear domains.

The approximations to the general theory, are conceptually different from the inviscid fluid assumption which is the basis of classical theories. Since a truly inviscid fluid does not exist in nature and since the limit of vanishingly small viscosity is distinct from a zero viscosity, the success of the inviscid theories must depend upon the auspicious circumstance that inviscid conclusions coincide with certain approximations of viscous conclusions. The general viscous theory has been shown, indeed, to yield, at various levels of approximation, well-known conclusions of classical inviscid theories.

For high Reynolds number external flows containing no appreciable regions of separation, as that described in Section 2, the vorticity distribution in the fluid is accurately represented by vortex sheets and vortex filaments. The integrals in Eqs. (3), (4), and (5) over the region R_f then reduces to integrals over surfaces in three-dimensional flows and over lines in two-dimensional flows. Under these circumstances, the analyses become considerably simpler. To determine the aerodynamic force, the following approximation of Eq. (4) may be used:

$$\vec{F} = -\frac{\rho}{d-1}\frac{d}{dt}\int_{S^{+}+W} \vec{r} \times \vec{\gamma}\, dB + \rho\frac{d}{dt}\int_{R_s} \vec{v}\, dR \quad (6)$$

where W is the wake surfaces (or lines) including tip vortex sheets and starting vortex where they exist, and S^+ is a surface enveloping the solid surface S and at infinitesimal distance from S. The distinction between S and S^+ is conceptually important. With the approximation discussed, the vortex sheet represents the boundary layer vorticity which is in the fluid domain. The velocity of the vortex sheet is different from the solid surface velocity.

In Eq. (6), the vortex sheet on S approximates the boundary layer adjacent to the solid surface. The vortex strength γ on S is therefore the integrated vorticity across the thickness of the boundary layer[5]. To the accuracy of the boundary layer approximation, the vorticity is the negative of the normal derivative of the velocity component in the direction tangent to the solid surface. One therefore obtains, upon integrating the vorticity along the normal direction,

$$\gamma(s) = -v_s(s, \delta) + v_s(s, 0) \qquad (7)$$

where s in the boundary layer coordinate tangential to the solid surface, v_s is the tangential velocity component, δ is the normal coordinate at the edge of the boundary layer and 0 is the normal coordinate on the solid surface. If $v_s(s, 0) = 0$, then γ is simply the negative of the boundary layer edge velocity.

Equation (7) is easily generalized to three-dimensional applications. According to Eq. (7), the vortex sheet on the solid surface represents a discontinuity in tangential velocity between the solid and the inviscid flow surrounding the boundary layer. This discontinuity is consistent with the approximation of the boundary layer, which possesses a finite albeit small thickness, by a sheet. This approximation of course is not suitable for the computation of the kinetic transport of vorticity within the boundary layer. The approximation, nevertheless, is well-suited for the computation of aerodynamic forces. In many applications, distribution of the vortex strength on the solid can be computed without actually performing boundary layer calculations. For example, if the vorticity distribution in the detached part of the flow is known, then the strength of the vortex sheet on S is uniquely determined, as discussed in Ref. 5, without computing the detailed flow within the boundary layer. It is mentioned in passing that the concept described in Ref. 5 is similar to that used in the panel/vortex lattice methods currently receiving a great deal of attention within the aerodynamics community. In many existing panel codes, fictitious source-sink distributions over S are used. It is not difficult to show[10], however, that these source-sink distributions are equivalent to vortex distributions over S. The vortex distributions over S, as discussed earlier, are approximations of real vorticity in the boundary layer. Computationally, the use of vortex distributions over S is as convenient as the use of source-sink distributions[10]. Also, in vortex lattice methods, the vortices in the interior of the fluid domain are usually allowed to convect but not to diffuse. This restriction, however, is not necessary and can be removed in viscous computations.

Once the vortex distributions over S and W are computed, Eq. (6) immediately gives the aerodynamic force $\vec{F}$. The use of Eq. (6) clearly offers distinctive advantages over the prevailing surface pressure-shear stress integration method since, with Eq. (6), both the unsteady drag and the lift can be evaluated in a straightforward manner directly from the vortex distributions.

In general, the vortical region in the fluid is composed of a vortical system near the solid bodies and a vortical system trailing the solid bodies. The near vortical system in general contains attached boundary layers and detached recirculating flows. The vorticity in the trailing vortical system represents the vorticity shed from the near vortical system at previous time levels. Shortly after the initiation of the motion of a solid body, the vorticity region is confined to thin layers near the solid body. In the case of a lifting body, a concentrated dose of vorticity, i.e., a starting vortex, leaves the vicinity of the body shortly after the motion's onset. The average velocity of this starting vortex is initially one half of the freestream velocity. This fact is consistent with the well-known Wagner's effect and can be shown by analyzing the vorticity distribution in the boundary layer as it leaves the solid body's trailing edge. With increasing time, the starting vortex moves in the general downstream direction, becomes diffused, and approaches the velocity of the freestream. Between the starting vortex and the near vortical system is stretched the remainder of the trailing vortical system which, for convenience, is called the vortical wake. The line of demarcation between the near vortical system and the wake need not be delineated precisely. The division of the overall vortical system into its several components is extremely useful since, with the general viscous aerodynamic theory, the contributions of each of these components to the aerodynamic force and moment can be considered individually. For example, with Eq. (4), the integral over R_f can be written as the sum of four integrals over, respectively, the unsteady boundary layers, the recirculating regions, the vortical wake, and the starting vortex. By separating the overall aerodynamic force into contributions by the several flow components, considerable physical insights can be developed.

In the case of a high Reynolds number flow containing no appreciable recirculating regions, Eq. (6) shows that the overall aerodynamic force is composed of four contributions. The first contribution, represented by the vortex moment integral over S^+, is due to the development of the unsteady boundary layer. The second and third contributions are due to, respectively, the movements of the wake and the starting vortex, and are represented by the vortex moment integral over W. The fourth contribution is due to the solid body acceleration.

The preceding discussion concerning the aerodynamic force is applicable also to the moment of aerodynamic force. In the case of a high Reynolds number flow containing no appreciable recirculating regions, Eq. (5) yields an equation expressing M in terms of vortex sheet strengths over S^+ and W and the effects of solid body acceleration.

4. Weis-Fogh Mechanism

It is well-known that, according to inviscid theories, steady lift force acting on an airfoil is proportional to the circulation around the airfoil. For an airfoil initially at rest and is set into motion impulsively, the circulation is developed through the shedding of a starting vortex. That is, because of the need to conserve total vorticity, the acquisition of a circulation around an airfoil is accompanied by the release of a starting vortex. The circulation around the starting vortex is equal in magnitude and opposite in sense to the circulation acquired by the airfoil. The process of vortex shedding is not difficult to understand in the context of viscous flow. Indeed, the starting vortex is a direct consequence of the unsteady boundary layer activities around the airfoil. There exist, however, conceptual difficulties in understanding the process of vortex shedding in the context of an inviscid fluid, i.e., a fluid with a zero viscosity rather than a vanishingly small viscosity.

Weis-Fogh[11] observed that certain types of insects, e.g., Encarsia Formosa, with a pair of wings pivoted together at their trailing edge, rotate their wings individually in opposite directions. The rotation generates a circulation about each wing. If the two wings are identical in shape and their rotational speed is identical, then the circulation magnitude of each wing is equal to that of the other wing. The senses of the circulations of the two wings are opposite to one another. Because of symmetry, no trailing edge shedding of vortices occurs. In fact, if vortices were shed from the trailing edges of the two wings, they would annihilate one another because they are of opposite senses.

Weis-Fogh described the above mentioned mechanism of generating circulation as the "fling" phase of a fling-clap cycle. At the beginning of the cycle, the two wings are close to each other. The wings' leading edges separate from one another as the wings fling apart, i.e., rotate about their trailing edges and open up into a V shape. After reaching a certain opening angle, the two wings break apart and move in opposite directions around the body of the insect. The wings eventually flip and return to their initial position through a clap motion. In this paper, the fling, or opening, phase of the motion is examined. The analyses presented, however, is obviously also applicable directly to the clap phase of the motion.

The two-dimensional definition of the Weis-Fogh motion is given in detail by Lighthill[12]. The fling phase of the motion is shown schematically in Figure 1, where the wing pair is modeled by a pair of flat plates of chord c. The points A_1 and A_2 are stationary and are the junctures of the two wings, with A_2 on the upper surfaces and A_1 on the lower surfaces of the wings. During the fling phase, the wings rotate about the points A_1 and A_2 with a angular velocity

$$\Omega = \dot{\alpha} \tag{8}$$

where α is the half angle of the opening of the wing pair. The motion is symmetric about the line EF. The fluid infinitely far from the wing pair is stationary. Each of the two wings acquires a circulation during the fling phase. Since the two circulations of the two wings are equal in magnitude and opposite in sense, the total circulation about the two wings is zero. At the moment of breaking apart of the wings, each wing possesses a circulation suitable for generating lift during its subsequent motion. It is easy to see that if the range $0 < \alpha < \frac{\pi}{2}$ corresponds to the fling phase, then the range $\frac{\pi}{2} < \alpha < \pi$ corresponds to the clap phase of the Weis-Fogh motion.

Lighthill[12] emphasized the absence of the trailing-edge shedding of vortices in the Weis-Fogh motion. He indicated that it is remarkable that the Weis-Fogh mechanism works "for a fluid of zero viscosity; not simply in the limit of vanishing viscosity". He presented a two-dimensional inviscid analyses which showed that the circulation around each wing during the fling phase is proportional to the wings' angular velocity Ω and to a function of the opening angle α of the wings. He expressed this function in the form of an integral and presented computed results for this function. Edwards and Cheng[13] recently extended Lighthill's work and presented a closed form expression for the wing's circulation during the fling phase.

Although vortices are not expected to be shed at the trailing edges of the two wings during the fling phase, the rotation of the wings may cause leading edge shedding of vortices. Lighthill[12] examined this leading edge separation phenomenon and concluded that its effect on the wing's circulation is weak. Subsequent experiments by Maxworthy[14], however, showed a substantial effect of the leading-edge separation. Results of a recent study by Edwards and Cheng[13] are in general agreement with Maxworthy's observation[14].

Weis-Fogh suggested that the opening of the wing pair causes the necessary circulation to be generated immediately and thus avoiding any delays in the build-up of the maximum lift required by the well-known Wagner's effect. Also, in the case of the conventional wing, substantial work must be done by the wing on the fluid to provide the kinetic energy associated with the starting vortex. In consequence, the wing experiences a large unsteady drag immediately after the start of its motion. Since the starting vortex is absent, the Weis-Fogh wing is not expected to experience a large drag immediately after the breakup of the wing pair. To the present authors' knowledge, although the problem of generation of circulation on the wing pair has received the attention of previous investigators, the questions of unsteady lift force, unsteady drag force, and power expenditure experienced by the wings during the fling phase of the Weis-Fogh motion have not been resolved. Answers to these questions are important in establishing a comprehensive understanding of non-linear unsteady aerodynamics and in future utilization of large unsteady aerodynamic forces.

For the problem under consideration, the processes of generation and transport of vorticity described in Section 2 of this paper lead to an unsteady boundary layer wherever the flow near the solid surface is essentially tangential to the surface. The thickness of this boundary layer is comparable to the diffusion length $(\nu\tau)^{\frac{1}{2}}$, where τ is the time duration of the fling phase of the Weis-Fogh motion. If this diffusion length is much smaller than the chord of the wings, then the boundary layer vorticity is accurately approximated by a vortex sheet. For the present problem, flow near the lower surface of the wing is expected to remain attached throughout the fling phase. The flow is, however, expected to separate from the leading edge, resulting in leading-edge vortex shedding.

Following Lighthill[12], the problem is reformulated in a conformally mapped plane, $\zeta = \xi + i\,\eta$, through the use of a Schwarz-Christoffel transformation. A closed form expression for the transformation function presented by Edwards and Cheng[13] is used. The transformation function is

$$z = i\,k(1+\zeta)^{1-\alpha/\pi}(\zeta-1)^{\alpha/\pi} \qquad (9)$$

where $z = x + i\,y$ is the physical plane described in Figure 1, and k is a constant given by

$$k = \frac{1}{2}c\left(\frac{\alpha}{\pi}\right)^{-\alpha/\pi}\left(1-\frac{\alpha}{\pi}\right)^{-1+\frac{\alpha}{\pi}} \qquad (10)$$

The transformation (9) maps the wing pair onto the straight line segment lying on the ξ-axis in the range $-1 < \xi < 1$ as shown in Fig. 2, with the two wings, A_1BA_2 and A_1CA_2, mapped respectively onto the lower and upper surfaces of the segment. The y-axis EF is mapped onto the remaining parts of the ξ-axis, as shown in Fig. 2.

During the fling phase, the line EF remains to be a line of symmetry. It is therefore necessary only to consider the left half complex z-plane, which is mapped onto the upper half complex ζ-plane. The normal velocity of the wing A_1BA_2 during the fling phase is $\Omega|z|$. The impermeable boundary condition on the wing A_1BA_2 therefore gives the following boundary condition for the stream function ψ.

$$\psi = -\frac{1}{2}\Omega|z|^2 \qquad (11)$$

The stream function vanishes on the line of symmetry $EA_1 - A_2F$ and also infinitely far from the wing.

It is simple to show that, with the potential function ϕ, the complex potential, $W_1 = \phi_1 + i\,\psi_1$, expressed in terms of ζ below satisfies these conditions for the stream function:

$$W_1 = -\frac{\Omega k^2}{2\sin 2\alpha}\left[(\zeta+1)^{2-2\alpha/\pi}(\zeta-1)^{2\alpha/\pi} - \zeta^2 - 2\left(1-\frac{2\alpha}{\pi}\right)\zeta\right] \qquad (12)$$

In Eqs. (12) and the following equations, the subscript 1 is used to indicate the omission of the leading-edge vortex shedding phenomena. The complex velocity in the ζ-plane, $V_\zeta = dW/d\zeta$, is given by

$$V_{\zeta 1} = -\frac{\Omega k^2}{\sin 2\alpha}\left[\left(\zeta - 1 + \frac{2\alpha}{\pi}\right)(\zeta+1)^{1-2\alpha/\pi}(\zeta-1)^{-1+2\alpha/\pi} - \left(\zeta + 1 - \frac{2\alpha}{\pi}\right)\right] \qquad (13)$$

The complex velocity in the z-plane is given by the right side of Eq. (13) divided by the derivative $dz/d\zeta$. It is, however, more convenient to use a transformed version of Eq. (6) in studies of aerodynamic forces acting on the wings.

In the present problem, the wing's cross-sectional area is negligibly small. The last integral in Eq. (6) therefore vanishes. The contributions of the unsteady boundary layer and the wake can be treated individually. One has therefore, with the wake, i.e., the shed vortices, omitted,

$$F_{1x} + i\,F_{1y} = i\,\rho\,\frac{d}{dt}\int_{S^+} z\,\gamma_1\,ds \qquad (14)$$

where F_{1x} and F_{1y} are respectively the horizontal and the vertical components of aerodynamic force acting on the wing pair due to the motion of the wing pair.

Because of symmetry, the vortex strength on the right wing is equal in magnitude and opposite in sense to the vortex strength on the left wing. The lift force L_1 acting on each wing is therefore one half of the total vertical force F_y and is given by the time variation of the vortex moment on a single wing. One therefore has

$$L_1 = \rho\,\frac{d}{dt}\int_{A_1BA_2} x\,\gamma_1\,ds \qquad (15)$$

where the integration is over both the upper and the lower surfaces of the left wing.

Since the wing has no tangential velocity on its surface, the last term in Eq. (7) vanishes. The vortex strength γ is therefore simply the negative of the tangential velocity at the fluid side of the vortex sheet. Since $dz = d\zeta\,(dz/d\zeta)$, Eq. (20) can be rewritten as

$$L_1 = \rho\,\frac{d}{dt}\int_{-1}^{1} x\,\gamma_\xi\,d\xi \qquad (16)$$

where γ_ξ is the negative of the ξ-component of velocity, given by Eq. (13), on the ξ-axis.

On the ξ-axis, for the interval $-1<\xi<1$, one obtains from Eqs. (9) and (13) the following expressions

$$x = -\sin\alpha\,k(1+\xi)^{1-\alpha/\pi}(1-\xi)^{\alpha/\pi} \qquad (17)$$

and

$$\gamma_{\xi 1} = -\frac{\Omega k^2}{\sin 2\alpha}\left[\left(\xi - 1 + \frac{2\alpha}{\pi}\right)(1+\xi)^{1-2\alpha/\pi}(1-\xi)^{-1+2\alpha/\pi}\cos 2\alpha + \left(\xi + 1 - \frac{2\alpha}{\pi}\right)\right] \qquad (18)$$

Placing Eqs. (17) and (18) into Eq. (16), one obtains, after performing the integration,

$$L_1 = \rho c^3 \frac{d}{dt}[\Omega\, f_1(\alpha)] \qquad (19)$$

where

$$f_1(\alpha) = \frac{\pi}{3}\left(\frac{\alpha}{\pi}\right)^{1-3\alpha/\pi}\left(1-\frac{\alpha}{\pi}\right)^{-2+3\alpha/\pi}\left(1-\frac{2\alpha}{\pi}\right)\csc 2\alpha \qquad (20)$$

Equation (21) can be rewritten as

$$\frac{L_1}{\rho c^3} = \dot{\Omega}\, f_1 + \Omega^2 \frac{df_1}{d\alpha} \qquad (21)$$

where $\dot{\Omega}$ is the angular acceleration of the wing.

Equation (21) states that the unsteady lift component L_1 has two contributions. One contributor is the angular acceleration of the wing, its effect being directly proportional to the angular acceleration. The other contributor is the angular velocity of the wing, its effect being proportional to the square of the angular velocity. Both contributions are functions of the opening angle, α , of the wing pair, as given by $f_1(\alpha)$ and its derivative.

For convenience, the horizontal force acting on the wing A_1BA_2 is designated as an unsteady drag. This drag cannot be determined from the vorticity moment on a single wing alone. The total horizontal force acting on the wing pair is zero because of symmetry. The two wings are hinged together at their trailing edges. In Fig. 3 is shown a free body diagram for the wing, with N_1 and S_1 representing respectively the normal and tangential components of the unsteady aerodynamic force acting on the wing. H_1 is the reaction at the hinge, i.e., the force exerted by the wing A_1CA_2 on the wing A_1BA_2. Because of symmetry, this reaction is directed horizontally. The free body diagram shows that the unsteady lift L_1 is the sum of the vertical components of S_1 and N_1. The unsteady drag is the sum of the horizontal components of S_1 and N_1 and is the negative of H_1.

The unsteady normal force N_1 acting on each wing is given by

$$N_1 = \int_{A_1}^{B} p_1\, ds - \int_{B}^{A_2} p_1\, ds \qquad (22)$$

where p_1 is the pressure acting on the wing. Since the boundary layer cannot support a significant pressure difference across the layer, it is permissible to let this pressure p be the pressure at the boundary layer's outer edge, where the vorticity is negligibly small and the flow is potential. From the inviscid momentum equation, one obtains

$$\nabla\left(\rho \frac{\partial \phi}{\partial t} + p + \rho \frac{v^2}{2}\right) = 0 \qquad (23)$$

At the edge of the boundary layer, the normal velocity of the flow is negligibly small compared to the tangential velocity. The tangential velocity magnitude is equal to the strength γ of the vortex sheet representing the boundary layer. Using this information, one obtains from Eqs. (22) and (23),

$$N_1 = -\rho \frac{d}{dt}\int_{-1}^{1} \phi_1 \frac{dr}{d\xi}\, d\xi - \frac{\rho}{2}\int_{-1}^{1} \gamma_{\xi 1}^{2} \frac{dr}{d\xi}\, d\xi \qquad (24)$$

where r is the distance from the origin in the z-plane.

Using Eqs. (12) and (18), it can be shown that

$$\frac{N_1}{\rho c^3} = \frac{d}{dt}[\Omega f_1(\alpha)]\csc\alpha - \Omega^2 g_1(\alpha)\,\mathrm{ctn}\,\alpha \qquad (25)$$

where

$$g_1(\alpha) = -\frac{\pi}{2}\csc^2(2\alpha)\left(\frac{\alpha}{\pi}\right)^{1-4\alpha/\pi}\left(1-\frac{\alpha}{\pi}\right)^{-3+4\alpha/\pi}\left(1-\frac{2\alpha}{\pi}\right)^2 \qquad (26)$$

Equations (21) and (25) gives the following expressions for the unsteady tangential force and the unsteady drag

$$\frac{S_1}{\rho c^3} = \Omega^2 g_1(\alpha) \qquad (27)$$

and

$$\frac{D_1}{\rho c^3} = \frac{d}{dt}\Big[\Omega f_1(\alpha)\Big]\mathrm{ctn}\,\alpha - \Omega^2 g_1(\alpha)\csc\alpha \qquad (28)$$

The normal forces can be expressed in the form

$$\frac{N_1}{\rho c^3} = \dot{\Omega} f_{n1}(\alpha) + \Omega^2 g_{n1}(\alpha) \qquad (29)$$

where the subscript n indicates the fact that the functions $f_{n1}(\alpha)$ and $g_{n1}(\alpha)$ are related to contributions to N.

The forces L_1 and D_1 are easily expressed in forms similar to Eq. (29). The tangential force S_1 is independent of the angular acceleration and is proportional to the angular velocity, as is shown in Eq. (27). The physical significance of this rather remarkable feature of the tangential force is not yet explained. It is clear, however, that this tangential force is due to the well-known leading edge suction effect which is also present in steady flows past airfoils at non-zero angles of attack. In the case of a thin airfoil represented by a infinitesimally thin flat plate, this suction force can be determined through a limiting process. The procedure just described for the Weis-Fogh problem when applied to the flat plate, at an angle of attack and a free stream velocity u_∞, gives a suction force value of $-\rho u_\infty \Gamma \sin\alpha$, where Γ is the circulation (boundary layer vorticity) around the plate. This suction force corresponds to a zero drag as is expected for steady inviscid flows.

The functions $f_{\ell 1}$, $g_{\ell 1}$, f_{d1}, etc. are represented graphically in Figures 4, 5, 6 and 7. It is worthy of note that all these functions are easily expressible in terms of the two functions f_1 and g_1 and the derivatives of these two functions.

It is of interest to determine the power expenditure needed to maintain a prescribed motion of the wing. The power requirement P_1 for the case of no leading-edge vortex shedding is given by

$$P_1 = \int_{A_1}^{B} p_1 v_n\, ds - \int_{B}^{A_2} p_1 v_n\, ds \qquad (30)$$

Since, on the wing, $v_n = \Omega r$, where r is the distance from the origin, one has, in the ζ-plane,

$$P_1 = -\rho\Omega \frac{d}{dt}\left[\Omega\int_{-1}^{1} \phi_1 r \frac{dr}{d\xi}\, d\xi\right] - \frac{\rho\Omega}{2}\int_{-1}^{1} \gamma_{\xi 1}^{2}\, r/\left(\frac{dr}{d\xi}\right) d\xi \qquad (31)$$

Placing Eqs. (9), (12), and (18) into Eq. (31), one obtains, after considerable manipulations,

$$\frac{P_1}{\rho c^4} = \frac{d}{dt}\left[\Omega^2 f_{p1}(\alpha)\right] \qquad (32)$$

where

$$f_{pl}(\alpha) = \frac{\pi}{8}\left(\frac{\alpha}{\pi}\right)^{1-4\alpha/\pi}\left(1-\frac{\alpha}{\pi}\right)^{-3+4\alpha/\pi}\left(1-\frac{2\alpha}{\pi}\right)^2 \csc^2 2\alpha \tag{33}$$

Equation (33) can be expressed as

$$\frac{P_1}{\rho c^4} = 2\,\dot{\Omega}\Omega f_{pl}(\alpha) + \Omega^3 g_{pl}(\alpha) \tag{34}$$

where g_{pl} is the derivative of f_{pl} with respect to α.

The functions of f_{pl} and g_{pl} are shown graphically in Figure 8. The function f_{pl} is positive, as expected. The function g_{pl} is always negative. This suggests that, during the fling phase of the Weis-Fogh motion, if the wing is moving at a constant velocity, then the fluid performs work on the wing and not the other way around! It is likely that this apparent paradox is a consequence of the omission of the leading-edge vortex shedding phenomena.

5. Leading-Edge Vortex Shedding

The analyses of the preceding section omits the presence of vortices shed from the wing's leading edge. Using the present general viscous theory of aerodynamics, the effects of the shed vortices on the aerodynamic forces, moments, and power requirement can all be expressed as functions of the distribution (location and strength) of shed vortices.

To demonstrate the use of the general theory, consider a distribution of shed vorticity $\omega_\zeta(\zeta)$ in the ζ-plane. Because of symmetry, one has $\omega_\zeta(\bar{\zeta}) = -\omega_\zeta(\zeta)$. A complex potential W_2 associated with this vorticity distribution exists in the region free of shed vorticity. This complex potential is

$$W_2 = -\frac{i}{2\pi}\int_{R_w} \ln\left(\frac{\zeta-\zeta_o}{\zeta-\bar{\zeta}_o}\right)\omega_\zeta(\zeta_o)\, dR_{\zeta_o} \tag{35}$$

where R_w is the region occupied by the shed vorticity in the upper complex ζ-plane.

It is easy to show that the imaginary part of W_2 vanishes on the ξ-axis. The complex potential $W = W_1 + W_2$ therefore satisfies the boundary conditions for ψ stated in Section 4. This complex potential W therefore is the correct complex potential for the fling phase of the Weis-Fogh motion, with vorticity shed from the leading edge of wings taken into account. The complex potential is invariant under a conformal transformation. The distribution of the vorticity field in the z-plane corresponding to ω_ζ is obtainable through the transformation relation, Eq. (9).

Equation (35) states that the effects of the shed vortices can be considered in a piecewise manner. That is, the region of integration R_w can be divided into segments and the effects of vorticity within each segment studied individually and the results summed. To illustrate this process, consider the effects of vorticity in a small region, say δR_w, around the point $\zeta = \zeta_o$. The total vorticity in this small region is designated $\delta\Gamma$. Consider this total vorticity to be a vortex located at $\zeta = \zeta_o$. By reason of symmetry, there exists a vortex of strength $-\delta\Gamma$ at $\zeta = \bar{\zeta}_o$ as shown in Fig. 2. The complex potential δW for this vortex pair is

$$\delta W = -\frac{i\,\delta\Gamma}{2\pi}\ln\left(\frac{\zeta-\zeta_o}{\zeta-\bar{\zeta}_o}\right) \tag{36}$$

It is easy to show that the strengths of the corresponding pair of vortices in the z-plane are also respectively $\delta\Gamma$ and $-\delta\Gamma$. The location of the vortex pair in the z-plane, as sketched in Fig. 1, are expressible in terms of ζ_o and $\bar{\zeta}_o$ through Eq. (9).

The vortex strength $\delta\gamma_\zeta$ on the wing in the ζ-plane is simply the negative of the ξ component of velocity on the ξ-axis for $-1<\xi<1$. This velocity component is easily obtained from Eq. (36). The increment lift δL due to the vortex pair $\delta\Gamma$ and $-\delta\Gamma$ is related to $\delta\gamma_\zeta$ through

$$\delta L = \rho\frac{d}{dt}\int_{-1}^{1} x\,\delta\gamma_\zeta\, d\xi \tag{37}$$

It can be shown that

$$\int_{-1}^{1} x\,\delta\gamma_\zeta d\xi = k\,\eta_o\,\delta\Gamma \tag{38}$$

where η_o is the η coordinate of the vortex $\delta\Gamma$ and k is a function of α defined by Eq. (10). It is clear from Eqs. (37) and (38) that the increment lift δL_2 is dependent upon the vortex strength $\delta\Gamma$, the movement of $\delta\Gamma$ in the η direction, and the opening angle of the wing pair through k. If all the shed vorticity in the flow is reasonably represented by a single pair of vortices with known strength and location, then Eqs. (37) and (38) permit the lift due to shed vorticity to be evaluated simply. In general, it is possible to represent the shed vorticity by a series of pairs of vortices. The lift increment due to each pair of vortices can be determined using Eqs. (37) and (38). The sum of all the lift increments and L_1, given by Eq. (19) is the total lift acting on a Weis-Fogh wing during the fling phase. Indeed, with a distribution of shed vorticity, the total lift L is obviously the sum of L_1 and L_2, the contribution of the shed vorticity to the lift is given by

$$L_2 = \rho\frac{d}{dt}\left[k\int_{R_w}\eta_o\,\omega(\zeta_o)\,dR_{\zeta_o}\right] \tag{39}$$

The total normal force N and the total power requirements P are expressible in terms of the potential function and vortex strength in forms identical to Eqs. (24) and (31), with the subscripts "1" removed. In these equations, the potential function ϕ is the sum of ϕ_1 and ϕ_2, the real part of W_2. The form of Eqs. (24) and (31) states that the contributions of ϕ_1 and ϕ_2 to the normal force and the power can be individually evaluated and added together to give the contribution of ϕ. The total vortex sheet strength γ is the sum of γ_1 and γ_2, the vortex sheet strength due to W_2. The vortex sheet strength, however, appears in Eqs. (24) and (31) as squared terms. In consequence, the contribution of the vortex sheet γ, which represents the unsteady boundary layer on the wing, is not simply the sum of the contributions of γ_1 and γ_2. If one let, for example,

$$N_2 = -\rho\frac{d}{dt}\int_{-1}^{1}\phi_2\frac{dr}{d\xi}\,d\xi - \frac{\rho}{2}\int_{-1}^{1}\gamma_{\xi 2}^2/\frac{dr}{d\xi}\,d\xi \tag{40}$$

then

$$N = N_1 + N_2 - \rho\int_{-1}^{1}\gamma_{\xi 1}\gamma_{\xi 2}/\frac{dr}{d\xi}\,d\xi \tag{41}$$

Similarly, one has

$$P = P_1 + P_2 - \rho\Omega\int_{-1}^{1}\gamma_{\xi 1}\gamma_{\xi 2}\,r/\left(\frac{dr}{d\xi}\right)d\xi \tag{42}$$

Closed form expressions for N and P have been obtained by the present authors. Expressions for S and D are easily obtainable from those for L and N. Because of the length limitation of the present paper, discussions of these results are postponed for the future.

6. Concluding Remarks

The present work has yielded useful results for the lift and the drag acting on a wing undergoing the fling and the clasp phases of the Weis-Fogh motion. Closed form expressions have been obtained for the unsteady lift, the drag, and the power expenditure of the Weis-Fogh wing. These results have led to the identification of major contributors to unsteady aerodynamic forces acting on the wing and the power requirement to sustain prescribed wing motions.

It should be pointed out that, compared with aerodynamics of rigid lifting bodies, the Weis-Fogh problem is substantially more difficult to treat. For the rigid body problem, the use of the general viscous theory, as stated as Eqs. (3), (4) and (5) in this paper, is particularly convenient since the overall vortical system can be divided into components and the contribution of each component to airloads can be studied individually. Even though the unsteady flow may be in the non-linear domain, the linear addition of the individual contributions gives the correct total aerodynamic force and moment acting on the rigid body. The line of action of the aerodynamic force and consequently the power expenditure are easily obtainable from the total force and moment. For the Weis-Fogh motion, the total force and moment acting on the wing pair can be determined also in a manner similar to that for the rigid body problem. The force and moment acting on each individual wing, however, cannot be evaluated using Eqs. (4) and (5), excepting that the lift on each wing, because of symmetry, happens to be one half of the total lift on the wing pair. In the present paper, the unsteady total normal force acting on the wing and the power expenditure of the wing are determined from the pressure distribution on the wing. The drag force and the leading-edge suction force are determined from the lift and the normal force. Since the pressure field is not a linear function of the voticity field, the total unsteady force and the power expenditure for each wing is not a simple sum of individual contributions of the several vortical flow components. Eqs. (41), for example, shows that the total normal force is composed of three terms. The terms N_1 and N_2 are respectively the individual contributions of the wing motion and the shed vorticity (wake). In addition to these two contributions, there is a third contribution due to the "interaction" of the first two contributors. This third contribution is expressed in the form of an integral in Eq. (42). The integrand of this integral contains the product of γ_1 and γ_2. γ_1 and γ_2 are the vortex sheets representing the vorticity in unsteady boundary layers resulting from, respectively, the wing motion and the shed vorticity. From Eqs. (42), it is clear that the wing motion and the shed vorticity both contribute to the power expenditure of the wing. In addition, there is a third contribution to the power expenditure due to the interaction of the first two contributors.

The Weis-Fogh problem is a special case of the problem of non-linear unsteady aerodynamics of non-rigid lifting bodies. The present study is, in this context, a precursor to a more comprehensive study of unsteady aerodynamics of flexible lifting bodies. It is anticipated that the development of a routine capability for predicting unsteady aerodynamic behavior in the non-linear domain will require extensive and persistent efforts over a number of years. The work described in this article represents only a few initial steps in search of this capability. In that context, the results of the present study are encouraging in that the recently developed general viscous theory of aerodynamics is shown to be well suited for the theoretical study of unsteady aerodynamic problems, including those associated with flexible lifting bodies.

Acknowledgements

This research is supported by the Air Force Office of Scientific Research under Grant # 82-0108.

References

1. McCroskey, W.J., "Some Current Research in Unsteady Fluid Dynamics," Jour. of Fluid Engng. 1977, pp. 8-39.

2. Wu, J.C., "Theory for Aerodynamic Force and Moment in Viscous Flows," AIAA Jour., Vol. 19, 1981, pp. 432-431.

3. Wu, J.C., Sankar, N.L., and Hsu, T.M., "Some Applications of Generalized Aerodynamic Forces and Moments Theory," AIAA Paper No. 83-0543, 1983.

4. Wu, J.C., "Problems of General Viscous Flows," Chapter 4 of Developments in Boundary Element Methods, Banerjee, P.K. and Shaw, R.P., Editors, Applied Science Publishers, Ltd., Essex, England, 1983.

5. Wu, J.C. and Gulcat, U., "Separate Treatment of Attached and Detached Flow Regions in General Viscous Flow Problems," AIAA Jour., Vol. 19, 1981, pp. 20-27.

6. Thompson, J.F., Shanks, S.P. and Wu, J.C., "Numerical Solution of Three-Dimensional Navier-Stokes Equations Showing Trailing Tip Vortices," AIAA Jour., Vol. 12, 1974, pp. 787-794.

7. von Karman, Th. and Millikan, C.B., "A Theoretical Investigation of the Maximum Lift Coefficient," Jour. of Applied Mechanics, Vol. 57, 1935, pp. A21-25.

8. Howarth, L., "The Theoretical Determination of the Lift Coefficient for a Thin Elliptic Cylinder," Proc. Royal Soc. of London, Vol. A-149, 1935, pp. 558-586.

9. Sears, W.R., "Some Recent Developments in Airfoil Theory," Jour. Aero. Sci., Vol. 23, 1956, pp. 490-499.

10. Wu, J.C., "Fundamental Solutions and Numerical Methods for Flow Problems," Int'l. Jour. for Numerical Methods in Fluids, Vol. 3, 1983 in print.

11. Weis-Fogh, T., "Quick Estimates of Flight Fitness in Hovering Animals, Including Novel Mechanisms for Lift Production," Jour. Exp. Biol., Vol. 59, 1973, pp. 169-230.

12. Lighthill, J., "Mathematical Biofluid-Dynamics," SIAM, 1975, 281 pages.

13. Edwards, R.H. and Cheng, H.K., "The Separation Vortex in the Weis-Fogh Circulation-Generation Mechanism," J. Fluid Mech., Vol. 20, 1982, pp. 463-473.

14. Maxworthy, T., "Experiments on Weis-Fogh Mechanism of Lift Generation by Insects in Hovering Flight. Part I. Dynamics of the Fling," Jour. Fluid Mech., Vol. 93, 1979, pp. 47-63.

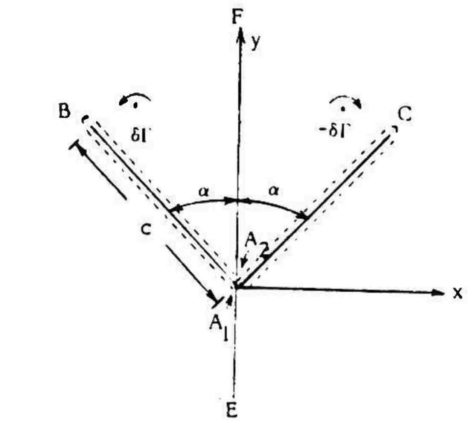

Figure 1. Weis-Fogh Motion

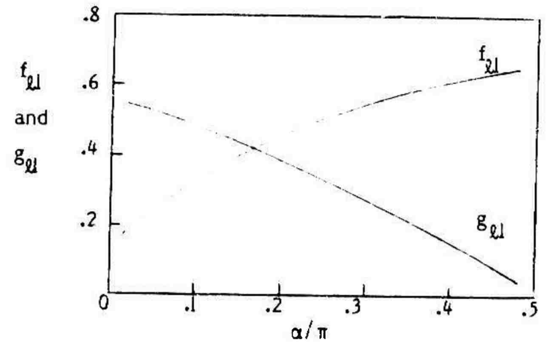

Figure 4. Weis-Fogh Lift Functions

$$\frac{L_1}{\rho c^3} = \dot{\Omega} f_{\ell 1} + \Omega^2 g_{\ell 1}$$

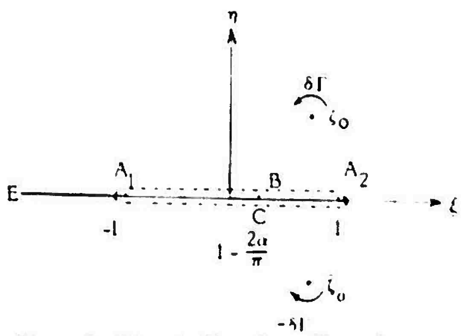

Figure 2. Wings in Transform Plane ζ

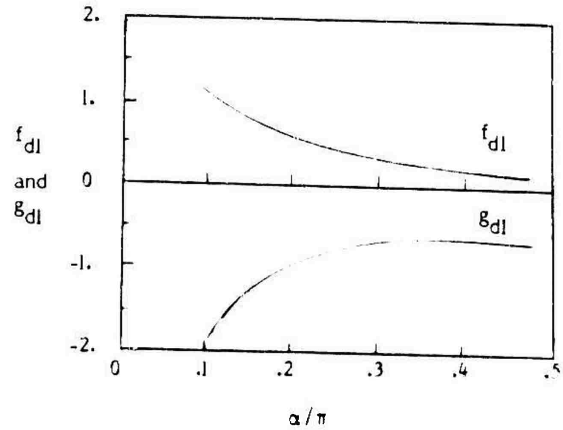

Figure 5. Weis-Fogh Drag Functions

$$\frac{D_1}{\rho c^3} = \dot{\Omega} f_{d1} + \Omega^2 g_{d1}$$

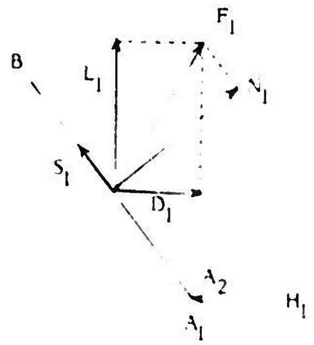

Figure 3. Free Body Diagram

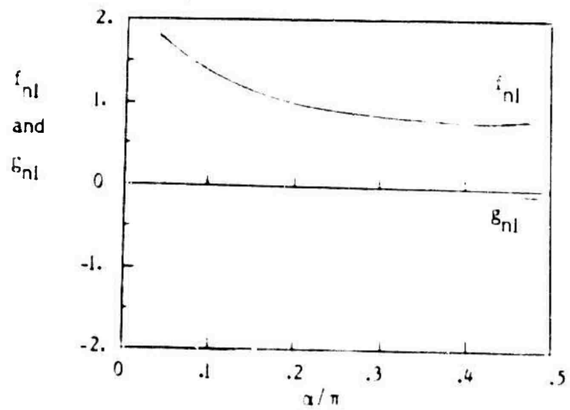

Figure 6. Weis-Fogh Normal Force Functions

$$\frac{N_1}{\rho c^3} = \dot{\Omega} f_{n1} + \Omega^2 g_{n1}$$

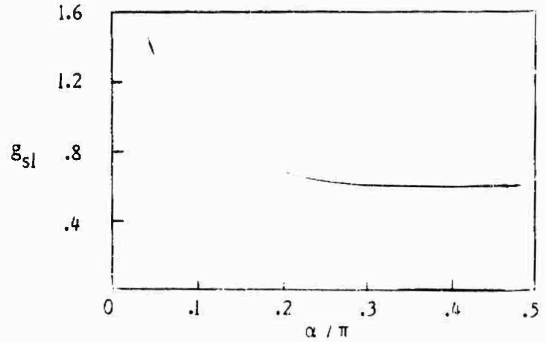

Figure 7. Weis-Fogh Leading-Edge Suction Functions

$$\frac{S}{\rho c^3} = \Omega^2 g_{sl}$$

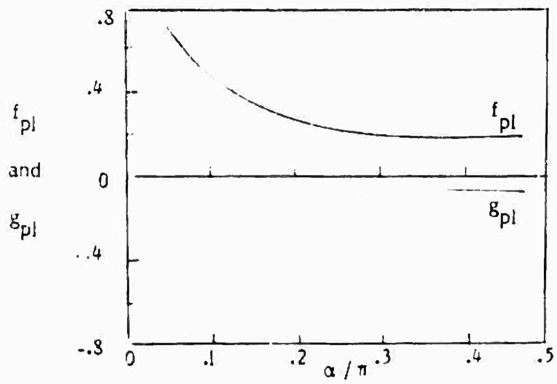

Figure 8. Weis-Fogh Power Functions

$$\frac{p_l}{\rho c^4} = 2\,\dot{\Omega}\Omega f_{pl}(\alpha) + \Omega^3 g_{pl}(\alpha)$$

AD-P004 170

THEORETICAL INVESTIGATION OF DYNAMIC STALL USING A MOMENTUM INTEGRAL METHOD

E.J. Jumper
and
J.E. Hitchcock
Air Force Institute of Technology
Wright-Patterson AFB, Ohio

Abstract

An analytical study into the gust response of an airfoil is presented. The momentum-integral equation for steady flow is extended into the unsteady flow regime to predict the behavior of an airfoil that experiences a constant-rate-of-change of angle-of-attack gust. The von Karman-Pohlhausen method of integration is successfully modified to incorporate the additional transient flow terms; the equation of closure necessary to do this is also presented. Finally, computation of the flow about a Joukowski airfoil using the new equations is performed and the results are presented and discussed. It will be shown that these results are in agreement with existing experimental data.

I. Introduction

In 1932, Max von Kramer published the results of wind-tunnel experiments simulating a wing encountering a constant-rate-of-change of angle-of-attack, $\dot{\alpha}$, gust. His results demonstrated that the wing encountered stall at higher angles of attack than in the static-stall case and the maximum coefficient of lift, $C_{l_{max}}$, was increased a proportionate amount to the increased stall angle of attack[1]. Since that time, a number of empirical studies have been undertaken in the general area of unsteady flow now referred to as dynamic stall. Few, however, have concentrated on the constant-$\dot{\alpha}$ case. One of these few is the work of Deekens and Kuebler[2], which was a flow visualization study and more recently by Daley which was a combination flow visualization-pressure measurement study[3]. These studies quantified only the stall angle of attack as a function of the flow and the constant $\dot{\alpha}$. A summary of the results of references 2 and 3 is shown in Figure 1. It is interesting that the Kramer results and the results of references 2 and 3, while agreeing in trend, do not agree in the extent to the dynamic-stall effect; the effect exhibited in references 2 and 3 is approximately ten times that of the Kramer experiments. It is important to note that these two experiments differ in what is probably a critical way. The Kramer experiment had the wing fixed in Newtonian space with a rotating free stream, while the Deekens and Kuebler and Daley experiments used a rotating wing in a constant velocity free stream.

Little analytic work has been performed on understanding the physics of the phenomena. That which has, has been in the area of full Navier-Stokes solutions[4] which amount to numerical experiments. Such numerical experiments lead to information which is similar to that obtained from experiments like those mentioned above, but because of inclusion of all possible effects, the solutions are of limited use in understanding the interplay of the physical phenomena that may be causing the effect.

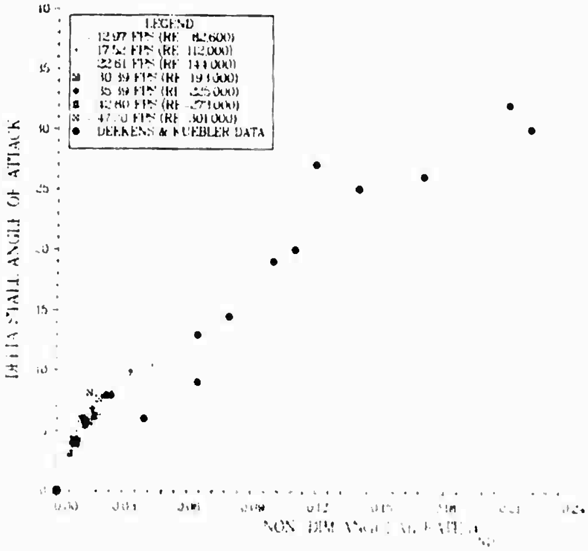

Fig. 1 - Summary of data for increase in α_{stall} vs reduced angular rate, $\dot{\alpha}$ (taken from reference 3)

Because of their simplicity, integral methods have been helpful in understanding the interplay of the physical phenomena leading to stall. Until now, however, these methods could not be applied to unsteady flow because the closure equation necessary to perform the integrations was not available. This paper presents an extension of the integral method to unsteady flow. Also presented are the results of a study using the method to analyze a Joukowski airfoil for the case equivalent to that of the Kramer experiment where the wing remains fixed in Newtonian space[1].

II. Integral-Method Extension to Unsteady Flow

It can be shown that the momentum-integral equation for the boundary layer in unsteady flow is given by[5]

[illegible]

where U_e is the potential flow just outside the boundary layer, x is the direction along the wall, t is the time, τ_w is the shear stress at the wall, ρ is the density, and δ^* and θ are the displacement and momentum thicknesses respectively, defined in the usual way as

[illegible]

$$\delta_2 = \int_0^{\delta} \left(1-\frac{u}{U_e}\right) \frac{u}{U_e}\, dy \qquad (3)$$

The introduction of the transient terms into the momentum-integral equation requires an additional equation which, until now, has not been known. This closure equation, however, may be arrived at as follows for the case in which transients are not too severe. First the observation is made that the displacement thickness is releated to the boundary layer thickness by

$$\delta_1 = C_1 \delta \qquad (4)$$

Assuming C_1 is slowly varying in time,

$$\frac{\partial \delta_1}{\partial t} = C_1 \frac{\partial \delta}{\partial t} \qquad (5)$$

Further, for all laminar flows the boundary layer thickness is related to the potential flow by

$$\delta = C_2 \sqrt{\frac{\nu}{U_e x}} \qquad (6)$$

so that,

$$\frac{\partial \delta_1}{\partial t} = C_1 C_2 \sqrt{\frac{\nu}{x}}\ \frac{\partial}{\partial t}(U_e)^{-\frac{1}{2}} = C_1 C_2 \sqrt{\frac{\nu}{U_e x}} \left(\frac{-1}{2U_e} \frac{\partial U_e}{\partial t} \right) \qquad (7)$$

substituting Eq (6) and Eq (4) into Eq (7) yields

$$\frac{\partial \delta_1}{\partial t} = - \frac{\delta_1}{2U_e} \frac{\partial U_e}{\partial t} \qquad (8)$$

With the help of Eq (8), Eq (1) becomes

$$[illegible] \qquad (9)$$

The solution of Eq (9) may now proceed similar to the technique used by Holstein and Bohlen[5] for the steady momentum-integral equation.

Following Pohlhausen[?], the velocity profile is now assumed to be a polynomial of fourth degree in $\eta = [y/\delta(x,t)]$

$$\frac{u}{U_e} = A + B\eta + C\eta^2 + D\eta^3 + E\eta^4 \qquad (10)$$

The coefficients A, B, C, D, and E may be found by applying the boundary conditions

$$[illegible] \qquad (11)$$

Further, we introduce the modified dimensionless Pohlhausen parameter

$$\Lambda = \frac{\delta^2}{\nu} \left(\frac{\partial U_e}{\partial x} + \frac{1}{U_e} \frac{\partial U_e}{\partial t}\right) \qquad (12)$$

such that the velocity profile is

$$\frac{u}{U_e} = (2\eta - 2\eta^3 + \eta^4) + \frac{\Lambda}{6}(\eta - 3\eta^2 + 3\eta^3 - \eta^4) \qquad (13)$$

Eq (13) may now be used to evaluate δ_1 and δ_2 from Eqs (2) and (3)

$$\frac{\delta_1}{\delta} = \frac{3}{10} - \frac{\Lambda}{120} \qquad (14)$$

and

$$\frac{\delta_2}{\delta} = \frac{37}{315} - \frac{\Lambda}{945} - \frac{\Lambda^2}{9072} \qquad (15)$$

These equations, Eqs (14) and (15) may be combined to yield

$$\frac{\delta_1}{\delta_2} = \left(\frac{3}{10} - \frac{\Lambda}{120}\right) \left(\frac{37}{315} - \frac{\Lambda}{945} - \frac{\Lambda^2}{9072}\right)^{-1} = g_1(\Lambda) \qquad (16)$$

Further, Eq (13) may be used to evaluate the right hand side of Eq (9)

$$[illegible] \left(2 + \frac{\Lambda}{6}\right) \left(\frac{37}{315} - \frac{\Lambda}{945} - \frac{\Lambda^2}{9072}\right) = g_2(\Lambda) \qquad (17)$$

The functions g_1 and g_2 may be written in terms of a new parameter, K, which is an explicit function of Λ

$$K = \frac{\delta_2^2}{\nu} \left(\frac{\partial U_e}{\partial x} + \frac{1}{U_e} \frac{\partial U_e}{\partial t}\right) = \Lambda \left(\frac{37}{315} - \frac{\Lambda}{945} - \frac{\Lambda^2}{9072}\right)^2 \qquad (18)$$

such that

$$f_1(K) = g_1 \qquad (19)$$

and

$$f_2(K) = g_2 \qquad (20)$$

Eq (9) may now be written in terms of these new functions as

$$[illegible] \qquad (21)$$

where $Z = \delta_2^2/\nu$. If we further define a function $F(K)$ as

$$[illegible] \qquad (22)$$

Eq (21) may be rearranged such that

$$[illegible] \qquad (23)$$

and

$$K = Z\left(\frac{\partial U_e}{\partial x} + \frac{1}{U_e}\frac{\partial U_e}{\partial t}\right) \tag{24}$$

Eqs (12), (18), (19), (20), (22), (23), and (24) now constitute a modified set of equations similar to the steady state equations which may be step-wise numerically integrated in a manner equivalent to the von Karman-Pohlhausen method[6].

III. Application to Constant-$\dot{\alpha}$ Gust

The method outlined above was applied to the case of an 15% thick symmetrical Joukowski airfoil undergoing a constant-$\dot{\alpha}$ gust. The unsteady potential flow field was solved for the Joukowski airfoil to provide the flow parameters U_e, $\partial U_e/\partial x$, and $\partial U_e/\partial t$ needed for the momentum-integral-method solution of the boundary layer. The transient potential field was approximated as pseudo-steady by neglecting the starting vortices, an effect which we suspect is small but which is the subject of a separate investigation to be published at a future date[7].

In order to determine the stall angle, separation at the quarter chord was defined as stall for the purposes of this investigation. The angle of attack at stall was determined for a number of flow conditions and constant $\dot{\alpha}$'s, and the results plotted as $\Delta\alpha_{stall}$ vs the reduced angular rate, where $\Delta\alpha_{stall}$ was determined as the new α_{stall} minus that for the steady state case and the reduced angular rate, $\dot{\bar{\alpha}}$, is given by

$$\dot{\bar{\alpha}} = \frac{\frac{1}{2}C\dot{\alpha}}{U_\infty} \tag{25}$$

where C is the chord. The results are shown in Figure 2.

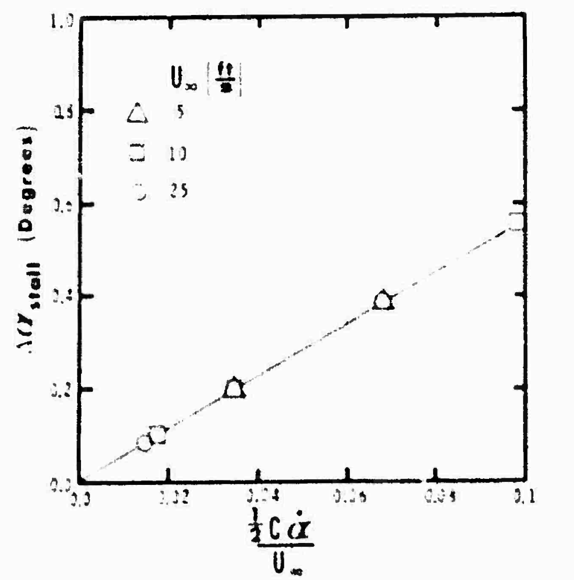

Fig. 2 – Theoretical prediction of $\Delta\alpha_{stall}$ vs reduced angular rate.

IV. Comparison to Experiment

Although the Kramer experiment used a different airfoil, the similarity of the leading edge geometries leads one to suspect that the results should be generally comparable. The effect shown in Figure 2 was compared to the results of reference 1 as follows. Kramer's result may be written as

$$C_{l_{max\ dyn}} = C_{l_{max\ st}} + 0.36\,\frac{C\dot{\alpha}}{U_\infty} \tag{26}$$

where $\dot{\alpha}$ is in radians per second. The results of Figure 2 may be written as

$$\alpha_{stall\ dyn} = \alpha_{stall\ st} + 0.096\,\frac{\frac{1}{2}C\dot{\alpha}}{U_\infty} \tag{27}$$

if written for $\dot{\alpha}$ in radians per seconds. Since these results are not in terms of $C_{l_{max}}$ they are not directly comparable to Eq (26); however, if we assume that the effect of increasing α_{stall} is to simply displace the C_l vs α curve by a comparable amount (see Figure 3), then $C_{l_{max}}$ may be arrived at by simply multiplying by the slope of the unstalled C_l vs α curve. This assumption is similar to that of the pseudo-steady-state assumption in that the effect of the starting vortices is assumed negligible. If the theoretical slope is used (i.e., 2π per radian), Eq (27) predicts a $C_{l_{max}}$ relationship of

$$C_{l_{max\ dyn}} = C_{l_{max\ st}} + 0.301\,\frac{C\dot{\alpha}}{U_\infty} \tag{28}$$

The comparison to Kramer's result, Eq (26), is remarkable.

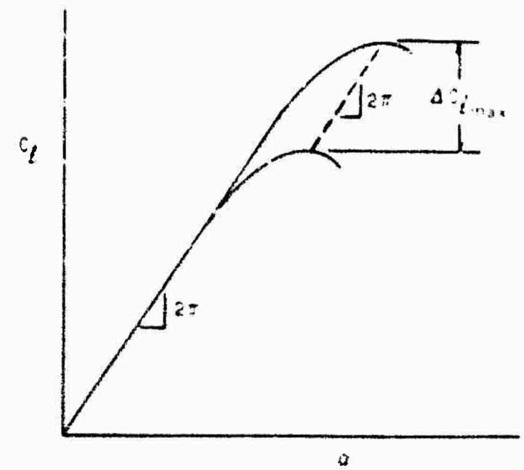

Fig. 3 – Rationale for computing the displacement of $C_{l_{max}}$.

V. Conclusions

This paper makes two contributions which are noteworthy. First, the momentum integral method for a transient boundary layer has been extended to unsteady flow, and second, the case of a wing in a constant-$\dot{\alpha}$ gust has apparently been matched.

In regard to the first, there is still work to be done in establishing the limits to the applicability of the assumptions leading to Eq (8), but the tools for such a study are available in the solution itself, and work in this direction is already underway[9]. Sensitivity studies carried out to date have shown that the worst case errors incurred from these assumptions change the slope of the curve of Figure 2 by less than 10%. In regard to the second, we now have available in the unsteady momentum-integral method a tool to help understand the pieces of physics which are at play in delaying the stall, and although not detailed here, it is clear from plotting the various modified Pohlhausen parameters from the solution that the transient term in the external flow is balancing the unfavorable pressure gradient to delay separation. Much more is to be learned from further exploitation of the unsteady method because of the fact that our solution is not at all limited to constant-$\dot{\alpha}$ cases.

Finally, it should be mentioned that we have also begun work on trying to adapt the method to a non-Newtonian boundary[7]. It is too early to say whether this work will be successful, but the intention is to address the discrepancies in the experiments so graphically demonstrated by a comparision of Figures 1 and 2.

References

1. Karmer, von M., "Die Zunahme des Maximalauftriebes von Tragflügeln bei plötzlicher Anstellwinkelvergroßerung (Böeneffekt)," Zeitschrift für Flugtechnik und Motorluftschiffahrt, 7, 14 April 1932, pp. 185-189.

2. Deekens, A.C. and Kuebler, Jr., W.R., "A Smoke Tunnel Investigation of Dynamic Separation," Aeronautics Digest, Fall 1978, USAFA-TR-79-1, Air Force Academy, CO, Feb 1979, pp. 2-16.

3. Daley, D.C., "The Experimental Investigation of Dynamic Stall," Thesis, AFIT/GAE/AA/82D-6, Air Force Institute of Technology, WPAFB, OH, 1983.

4. Hegna, H.A., "Numerical Prediction of Dynamic Forces on Arbitrarily Pitched Airfoils," AIAA Journal, 21, Feb 1983, pp 161-162.

5. Docken, R.G., Jr., "Gust Response Prediction of an Airfoil using a Modified von Karman-Pohlhausen Technique," Thesis, AFIT/GAE/AA/82D-9, Air Force Institute of Technology, WPAFB, OH, 1982.

6. Schlichting, H., Boundary-Layer Theory, 7th ed., McGraw -Hill Book Comp. NY., 1979.

7. Pohlhausen, K., "Zur naherungsweisen Integration der Differentialgleichung der laminaren Reibungsschicht," Zeitschrigt fur angewandte Mathematik und Mechanik, 1, 1921, pp. 252-268.

8. Tupper, K.W. and Jumper, E.J., work in progress.

9. Lawrence, J.S. and Jumper, E.J., work in progress.

PRELIMINARY RESULTS FROM THE UNSTEADY AIRFOIL MODEL USTAR2

J. H. Strickland*
J. W. Oler**
B. J. Im‡
Texas Tech University
Lubbock, Texas 79409

AD-P004 171

Abstract

Preliminary results from an UnSTeady AiRfoil analysis in 2 dimensions have been obtained from a computer code (USTAR2) developed by the present authors. This computer code is based upon an analysis which utilizes a doublet panel method to model the airfoil surface, an integral unsteady boundary layer scheme to model the viscous attached flow, and discrete vortices to model the detached boundary layers which form the airfoil wake region. This model has been used to successfully predict steady lift and drag coefficients as well as pressure distributions for several airfoils with both attached and detached boundary layers. In addition, calculations have been made for a limited number of cases for both attached and detached unsteady flow situations. These calculations are compared in a cursory way with experimental data to point out some of the strengths and weaknesses of the present formulation.

Introduction

Unsteady aerodynamics is an important phenomenom which has been studied more intensively in recent years. These studies have been made in connection with applications pertaining to helicopters, axial flow turbines and compressors with inlet distortions, vertical axis wind turbines, and missiles and fixed-wing aircraft undergoing rapid maneuvers. Lifting surfaces subjected to time-dependent freestream velocity or time-dependent body motions may, in some cases, also have significant stall regions on their surfaces.

A number of approaches have been taken with regard to the prediction of unsteady stalled airfoils. Most of these approaches have been reviewed by McCroskey[1,2]. In general, these approaches range from empirical models[2,6] to models based on the Navier-Stokes equations[7,8]. The empirical models are generally applicable to small sinusoidal pitch oscillations about some relatively low angle of attack. The Navier-Stokes solutions tend to consume large amounts of computer time and are usually limited to low Reynolds number solutions. Unfortunately, there are few models which can be considered as representing something in between the extreme cases of almost total empiricism and the lengthy more exact solutions of the Navier-Stokes equations. There have been several boundary layer codes developed which can be used to predict some of the behavior associated with unsteady stall[9-11]. There have also been models of the potential flow behavior related to the shedding of leading edge vorticity as typified by the work of Ham[12]. More recently, Katz[13] simulated the unsteady separated flow over a thin cambered airfoil. The models of both Ham and Katz required empirical information regarding the appearance and position of the separation point.

USTAR2 Analysis

Recently, the present authors formulated and began development on an analytical model[14] which is potentially capable of predicting dynamic effects for stalled and unstalled airfoils undergoing arbitrary airfoil motions. This model does not require input of airfoil section data and may thus be used to examine arbitrary airfoil shapes. An UnSTeady AiRfoil model in 2 dimensions based on this analysis has been implemented via a computer code (USTAR2). Execution times for this code are short when compared to Navier-Stokes solutions and little empiricism is required. In order to validate this analysis, however, comparison between USTAR2 predictions and experimental data must be made for a number of cases. This paper presents some of the preliminary comparisons.

The USTAR2 model is a two-dimensional incompressible formulation which is based on state-of-the-art methods with some extensions. The potential flow regions near the airfoil are modeled using the doublet panel analysis of Ashley[15] which consists of a Green's function representation of the potential field resulting from the motion of the airfoil and the presence of associated trailing wakes. This potential flow is based upon the Laplace equation for the velocity potential $\phi(\vec{r},t)$

$$\nabla^2\phi = 0 \tag{1}$$

which is valid for both steady and unsteady flow. By Green's theorem, a solution to (1) may be represented by integrals over the "boundaries" of the flow where those boundaries are replaced by surfaces across which potential jumps occur. These surfaces, as depicted in Figure 1, are represented by the airfoil surfaces and the wake sheets which spring from the trailing edge and any separation point. With Green's theorem, the disturbance potential at any field point $\vec{r}$, due to the airfoil and wake surfaces, may be written as

$$\phi(\vec{r}) = \int_S \phi \frac{\partial}{\partial n}\left[\frac{1}{4\pi R}\right] dS + \int_W \Delta\phi \frac{\partial}{\partial n}\left[\frac{1}{4\pi R}\right] dS \tag{2}$$

*Professor, Dept. Mech. Engr., Member AIAA
**Assist. Prof., Dept. Mech. Engr.
‡Graduate Research Assist., Dept. Mech. Engr.

where μ and $\Delta\phi$ are doublet distributions on the airfoil and wake surfaces S and W respectively, ν is the surface normal at the source point, and R is the distance separating the field point and source point. Boundary conditions include a kinematic surface tangency condition given by

$$\frac{\partial\phi}{\partial n} + (\vec{u}_\infty - \vec{u}_S)\cdot\vec{n} = 0 \qquad \text{on S} \qquad (3)$$

where $\vec{u}_\infty$ and $\vec{u}_S$ are the freestream and airfoil surface velocities respectively and $\hat{n}$ is the outward normal to the airfoil surface. An additional boundary condition is the "trailing edge flow condition" which, in the present model, requires that the flow direction at the trailing edge be along the trailing edge bisector. Equations (2) and (3) are solved for μ and ϕ by first eliminating ϕ to form a single equation in μ. The airfoil and wake surfaces are then discretized to form a set of linear algebraic equations in terms of the unknown μ. The potential ϕ is then obtained from (2). The pressure distribution around the airfoil is obtained from the unsteady Bernoulli equation. Details of this analysis are presented in reference[14].

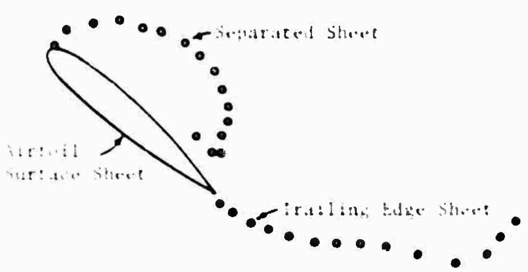

Figure 1. Schematic of Boundary (Vortex) Sheets for Unsteady Pitching Motion with Separation

The primary function of the boundary layer analysis is to predict the presence and location of any boundary separation point on the airfoil surface. The pressure gradient and edge velocity distributions, which are used in boundary layer calculations, are obtained from the potential flow model which may include sheets of vorticity shed from the boundary layer separation point. Therefore, a strong coupling between the boundary layer analysis and potential flow analysis exists for separated flow situations. The turbulent boundary layer analysis used in the present work is essentially that due to Lyrio, Ferziger, and Kline[16]. This unsteady integral technique gives excellent results for the steady flows of Tillman, Herring, and Norbury; Stratford, Samuel and Joubert (see Coles and Hirst, reference 17); Kim[18]; Simpson and Strickland[19]; and Wieghardt (see Kim, reference 18). More importantly, this method predicts the unsteady boundry layer data of Karlson[20] and Houdeville, et al.[21] and compares well with the finite difference methods of McCroskey and Philippe[22] and Singleton and Nash[23] while being an order of magnitude faster. The formulation for the laminar portion of the boundary layer is based upon the author's unsteady extension of Thwaites' method (see Cebecci and Bradshaw[24]. Transition is assumed to occur either due to laminar boundary layer separation or according to a natural transition criteria due to Cebecci and Smith[25].

Experimental Data

An abundance of data for steady flow over airfoils exists and can be used to check the ability of the USTAR2 model to predict such flows. One such case is shown in Figure 2 where the data of Sheldahl and Klimas[26] are compared with USTAR2. Unsteady data are, on the other hand, relatively scarce. In the present paper the unsteady experimental data consists of some recently obtained data for an airfoil undergoing a pitch up motion from zero angle of attack. In each case the pitching rate, $\dot{\alpha}$, remains constant. These data consist of airfoil surface pressure data, flow visualization data, and surface hot-wire data. All data were obtained in the USAF Academy low-speed 2 ft x 3 ft wind tunnel. The experimental arrangements will be briefly described.

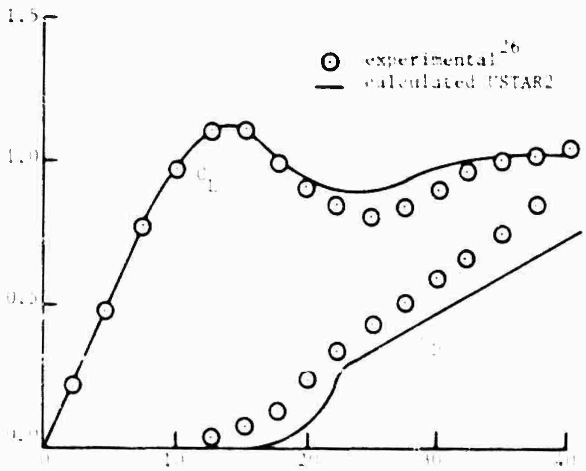

Figure 2. Lift and Drag Coefficients for a NACA 0015 Airfoil with Re = 655,000

Airfoil surface pressure data were obtained by Francis, Keesee, and Retelle[27]. Details of the test setup can be found in that reference. A computer controlled pitch oscillator was used to impart constant $\dot{\alpha}$ pitching to a 6-inch chord NACA 0012 airfoil. Pressure taps were located at 19 positions along the surface of the airfoil. Approximately 25 repetitions of each case were run so as to obtain ensemble averages of the surface pressure coefficients at the pressure ports. These data were then used to obtain lift and drag coefficients for the airfoil as a function of time.

Flow visualization data were obtained by Walker, Helin, and Strickland[28]. In this work, the flow around a 6-inch chord NACA 0015 airfoil was examined using a smoke wire placed across the tunnel upstream of the pitching airfoil. The wire was placed in a plane normal to the axis of rotation of the pitching airfoil. A smoke producing oil (Roscoline) was coated on a 0.005 inch diameter tungsten wire which was in turn heated electrically to produce a large number of smoke streaks in the flow. These streaks have a rather uniform spacing due to the regular spacing of smoke material droplets which are formed when the wire is coated. The smoke was illuminated by a high intensity strobe light placed downstream of the airfoil. The proper sequencing of airfoil pitch commands with strobe light and smoke wire triggering was accomplished by computer control. A 35 mm camera looking along the pitch axis was used to record the visual data.

In the work by Walker, Helin, and Strickland[28], a NACA 0015 airfoil with a 6-inch chord was instrumented with an array of hot-wires. As indicated in Figure 3, seven hot-wires were mounted on the upper surface of the airfoil (suction side). The hot-wire sensing elements (TSI-10 hot films) were soldered to pairs of number 9 sewing needles which protruded above the airfoil surface approximately 0.20 inches. The needle supports in turn were mounted in electrically insulated plugs which were machined flush

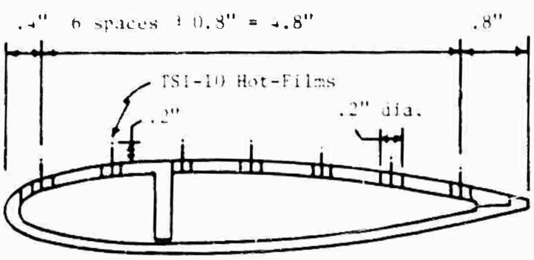

Figure 3. Surface Hot-Wire Configuration

with the airfoil surface. A TSI model 1050 hot-wire anemometer system, along with an in-house linearizer, were used to obtain velocity signals. Approximately 25 repetitions of each case were run to obtain ensemble averages of the velocity signal from each probe.

Discussion of Results

Lift and drag data are shown in Figure 4 for a NACA 0012 airfoil pitching up from a zero angle of attack at a non-dimensional pitching rate K of 0.089. The non-zero lift coefficient at zero angle of attack is due to the so-called "pitch circulation." The slope of the lift curve in this substall region can be seen to be considerably less than for the steady case due to the downwash on the airfoil produced by the vortex sheet springing from the trailing edge. The results from a simple analysis given in Reference 29 are seen to agree with the experimental lift and drag very well up to and a little beyond the stall angle which is approximately 10 degrees

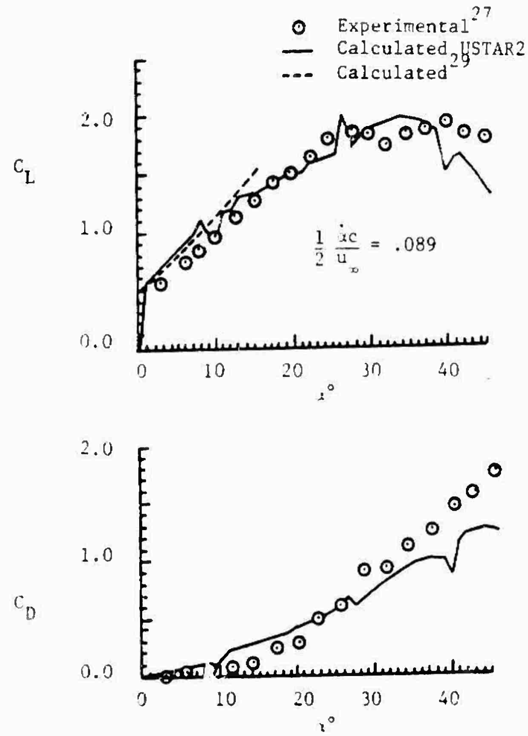

Figure 4. Lift and Drag Coefficient for a NACA 0012 Airfoil Pitching Up at Constant $\dot{\alpha}$ about the 31.7 Percent Chord for Re = 77,700

for the present case. The USTAR2 analysis is seen to predict both lift and drag coefficients reasonably well below an angle of attack equal to about 25-30 degrees. The small, abrupt jumps observed in the USTAR2 results can be attributed to the tendency for the boundary layer separation point to "lock in" on surface panel edges. This problem can be corrected in subsequent versions of USTAR2 by making minor changes in the procedures for introducing "edge velocities" into the boundary layer subroutine. The lack of agreement at high angles of attack is thought to be partially due to discrete wake vortex core growths which are excessively large in the USTAR2 analysis. This reduces the effect of the large scale vortex which grows on the suction side of the airfoil. The core growth parameter was arbitrarily selected in the past and should be reduced to represent more realistic growth rates. Examination of pressure coefficient data bears out the fact that the influence of the vortex moving over the airfoil is too weak in the USTAR2 analysis. The effect on lift for two different pitching rates is shown in Figure 5. Drag coefficients for the cases in Figure 5 are similar to those measured and predicted in Figure 4.

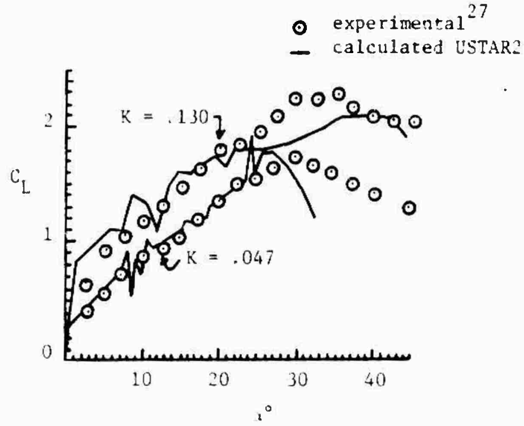

Figure 5. Comparison of Lift Coefficients for a NACA 0012 Airfoil Pitching Up at Constant $\dot{\alpha}$ about the 31.7 Percent Chord for Re = 77,700 ($K = \frac{\dot{\alpha}c}{2u_\infty}$)

The wake geometry obtained from the USTAR2 analysis is compared in Figure 6 to flow visualization data. The vortex sheets obtained in the USTAR2 analysis basically represent "streaklines" in that most of the fluid particles which make up these sheets were either injected into the flow at the leading or trailing edge. While exact comparisons between visual and calculated results are difficult to make, it does apear that the predicted large scale vortex is not as tightly rolled up as that indicated by flow visualization. This again indicates that the discrete wake vortex cores are growing at excessive rates in the USTAR2 analysis.

Velocities obtained from three of the seven surface mounted hot-wire probes are shown for a particular case in Figure 7. Near the nose of the airfoil (7% chord) the velocity measured by the probe rises until the probe becomes immersed in the separated boundary layer which occurs at an angle of attack of about 19°. The probe is located above the airfoil surface about 3% of a chord length. The calculated edge velocity drops much sooner since the separated vortex sheet passes over the 7% chord position almost immediately after the boundary layer separates from the nose. Therefore, agreement between experiment and analysis is at least qualitatively correct at the 7% chord position. For this particular flow situation, the experimental work indicates that a significant region of reversed flow first appears at an angle of attack of about 25 to 30 degrees somewhat downstream of the nose (20% chord). The magnitude of the reversed flow reaches a maximum at about the 60% chord and has a value of about 1.5 times the freestream velocity. Further downstream (87% chord),

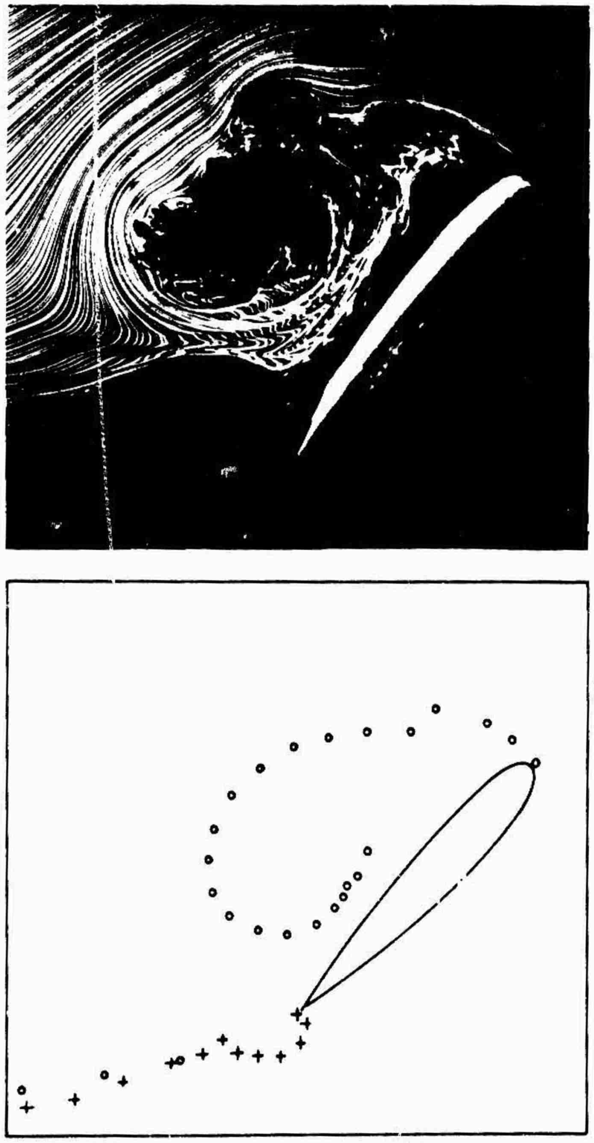

Figure 6. Wake Geometries Obtained from Flow Visualization and USTAR2 (α = 45°, K = 0.109, Re = 62,500, Pivot Point = 0.25 Chord, NACA 0015)

the reverse flow due to the initial large scale vortex passage is reduced and occurs at a higher angle of attack. As can be seen from Figure 7, results obtained from the USTAR2 analysis at 60% chord are in poor agreement with the experimental data above an angle of attack of 25 degrees. The prediction of reversed flow due to the vortex passage lags that of the measured data by a considerable length of time. The immediate reasons for this lag are not clear, but may also be associated with an incorrect discrete vortex core growth rate.

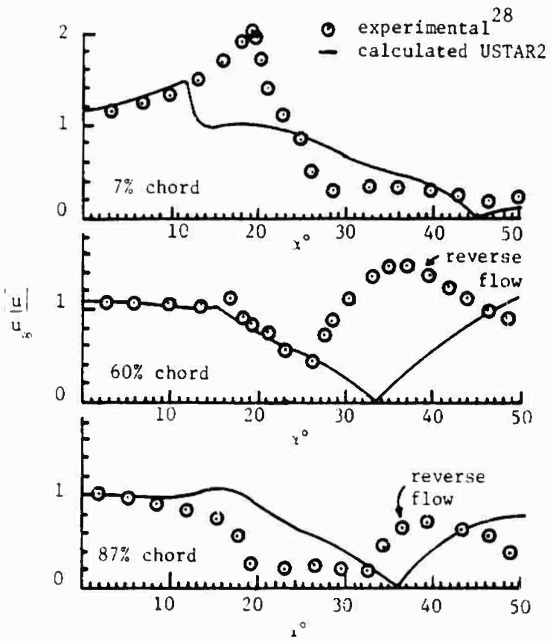

Figure 7. Velocities Obtained from Surface Mounted Hot-Wire Anemometers (K = 0.089, Re = 62,500, Pivot Point = .317 Chord, NACA 0015)

Conclusions

Preliminary results from the USTAR2 analysis are encouraging, but indicate that additional requirements are necessary for satisfactory predictions at large angles of attack for the cases studied. In-depth correlations between the surface pressure data, flow visualization data, and surface velocity data should be made in order to more completely understand the constant ẋ flows used in this paper to test the validity of the USTAR2 analysis.

Acknowledgement

The authors would like to thank Sandia National Laboratory, Albuquerque, New Mexico for their past and present support on contracts 74-1218 and 52-3727 as well as acknowledging the AFOSR support given to one of the authors in the form of an AFOSR/SCEEE Summer Faculty Fellowship.

References

1. McCroskey, W. J., "Recent Developments in Dynamic Stall," Proceedings of a Symposium on Unsteady Aerodynamics, University of Arizona, Vol. 1, pp 1-33, 1975.

2. McCroskey, W. J., "Some Current Research in Unsteady Fluid Dynamics - The 1976 Freeman Scholar Lecture," J. Fluids Engineering, Vol. , pp 8-38, 1977.

3. Ericsson, L. E. and J. P. Reding, "Dynamic Stall Analysis in Light of Recent Numerical and Experimental Results," J. Aircraft Vol. 1, pp 248-255, 1976.

4. Gormont, R. E., "A Mathematical Model of Unsteady Aerodynamics and Radial Flow for Application to Helicopter Rotors," U. S. Army AMRDL Technical Report 72-67, 1973.

5. Carta, F. O., "Unsteady Normal Force on an Airfoil in a Periodically Stalled Inlet Flow," J. Aircraft, Vol. 4, pp 416-421, 1967.

6. Johnson, W., "The Effect of Dynamic Stall on the Response and Airloading of Helicoper Rotor Blades," J. Am. Hel. Soc., Vol. 14, pp 68-79, 1969.

7. Mehta, U., "Dynamic Stall of an Oscillating Airfoil," AGARD Fluid Dynamics Panel Symposium, Ottawa, Paper No. 23, September 1977.

8. Hodge, J. K., A. L. Stone, and T. E. Miller, "Numerical Solution for Airfoils Near Stall in Optimized Boundary-Fitted Curvilinear Coordinates," AIAA Journal, Vol. 17, pp 458-464, 1979.

9. Nash, J. G., L. W. Carr, and R. E. Singleton, "Unsteady Turbulent Boundary Layers in Two-Dimensional Incompressible Flow, AIAA Journal, Vol. 13, pp 167-173, 1975.

10. Dwyer, H. A. and W. J. McCroskey, "Crossflow and Unsteady Boundary Layer Effects on Rotating Blades," AIAA Journal, Vol. 9, pp 1498-1505, 1971.

11. Telionis, D. P., "Calculations of Time-Dependent Boundary Layers," Unsteady Aerodynamics, R. B. Kinney (Ed.), Vol. 1, pp 155, 1975.

12. Ham, N. D., "Aerodynamic Loading on a Two-Dimensional Airfoil During Dynamic Stall", AIAA Journal, Vol. 6, pp 1927-1934, 1968.

13. Katz, J., "A Discrete Vortex Method for the Non-Steady Separated Flow Over an Airfoil," J. Fluid Mech., Vol. 102, pp 315-328, 1981.

14. Oler, J. W., J. H. Strickland, B. J. Im, and G. H. Graham, "Dynamic Stall Regulation of the Darrieus Turbine," Sandia National Laboratory Report SAND83-7209, June 1983.

15. Ashley, H., "Machine Computation of Aerodynamic Loads in Linear and Nonlinear Situations," Report 66-5, AFOSR 66-1440, Fluid Dynamics Research Lab, M.I.T.

16. Lyrio, A. A. and J. Ferziger, "A Method of Predicting Unsteady Turbulent Flows and its Application to Diffusers with Unsteady Inlet Conditions," AIAA Journal, Vol. 21, No. 4, pp 534-540, 1983. See also:
Lyrio, A. A., J. H. Ferziger, and S. J. Kline, "An Integral Method for the Computation of Steady and Unsteady Turbulent Boundary Layer Flows, Including the Transitory Stall Regime in Diffusers," Stanford University Report PD-23, 1981.

17. Coles, D. and E. A. Hirst, Computation of Turbulent Boundary Layers, 1968 AFOSR-RFP, Vol. 2, Stanford University, 1969.

18. Kim, J., S. J. Kline, and J. P. Johnston, "Investigation of Separation and Reattachment of a Turbulent Shear Layer: Flow Over a Backward-Facing Step," Rpt. MD-37, Thermosciences Div., Mech. Engrg. Dept., Stanford University, 1978. See also TASME, J. Fluids Eng., 102, pp 302-308, 1980.

19. Simpson, R. L., J. H. Strickland, and P. W. Barr, "Features of a Separating Turbulent Boundary Layer in the Vicinity of Separation," J. Fluid Mech., Vol. 79, pp 553-594, 1977.

20. Karlson, S.K.F., "An Unsteady Turbulent Boundary Layer," J. Fluid Mech., Vol. 5, 1959.

21. Houdeville, R. and J. Cousteix, "Premiers Resultats D'une Etude sur les Couches Limites Turbulentes en Encoulement Pulse Avec Gradient de Pression Moyen Defavorable," 15E Collogue D'Aerodynamique, AAAF NT-79-05, 1978. Translated into English in NASA TM-75799, 1979.

22. McCroskey, W. J. and J. J. Phillippe, "Unsteady Viscous Flow on Oscillating Airfoils," AIAA Journal, Vol. 13, pp 71-79, 1975.

23. Singleton, R. E. and J. F. Nash, "Method for Calculating Unsteady Turbulent Boundary Layers in Two- and Three-Dimensional Flows," AIAA Journal, Vol. 12, pp 590-595, 1974.

24. Cebecci, T. and P. Bradshaw, Momentum Transfer in Boundary Layers, McGraw-Hill, 1977.

25. Cebecci, T. and A.M.O. Smith, Analysis of Turbulent Boundary Layers, Academic Press, 1974.

26. Shehdahl, R. E. and P. C. Klimas, "Aerodynamic Characteristics of Seven Symmetrical Airfoil Sections Through 180 Degree Angle of Attack for Use in Aerodynamic Analysis of Vertical Axis Wind Turbines," Sandia National Laboratory Report, SAND80-2114, 1981.

27. Francis, M. S., J. E. Keesee, and J. P. Retelle, "An Investigation of Airfoil Dymamic Stall With Large Amplitude Motions," USAF/FJSRL Report (in press).

28. Walker, J., H. Helin, and J. Strickland, "An Experimental Investigation of an Airfoil Undergoing Large Amplitude Pitching Motions." (To be submitted to AIAA Journal).

29. Strickland, J. H., "Dynamic Stall: A Study of the Constant Pitching Rate Case," USAF Summer Faculty Research Program 1983 Report (in press).

EXPERIMENTS ON CONTROLLED, UNSTEADY, SEPARATED TURBULENT BOUNDARY LAYERS

William C. Reynolds
Stanford University

Rangarajan Jayaraman
IBM Scientific Center

Lawrence W. Carr
NASA-Ames Research Center

AD-P004 172

Abstract

Experiments on turbulent boundary layers subjected to controlled unsteadiness have been performed in a special water channel. The flow is steady in the development section upstream of the unsteady test section, where the boundary layer is subjected to an oscillating adverse free-stream velocity gradient sufficient to induce flow reversal near the wall. Measurements of the mean, oscillatory, and turbulence components of the streamwise velocity in the boundary layer indicate that the mean velocity and mean turbulent stresses are unaffected by the oscillation, whereas the periodic components of these quantities are strongly dependent upon frequency. At low frequencies the boundary layer behaves quasistaticly; at intermediate frequencies the boundary layer behavior correlates with the Strouhal number based on the length of the unsteady region; and at high frequencies the outer region of the boundary layer moves as a slug while the sublayer behaves as a Stokes layer described by laminar equations. Reverse flows occur in this Stokes layer, but the boundary layer remains thin and hence attached to the surface. Although the boundary layer would separate from the surface at zero frequency, separation is prevented by rather slow oscillations, and hence unsteadiness can be used as a means for separation control.

Nomenclature

$A_{1,u}$	amplitude of $\tilde{u}$
K	$= (\nu/U_0^2)(dU_E/dx)$, acceleration parameter
L	length of unsteady region, 0.61 m
δ_s	$= \sqrt{2\omega/\nu}$, Stokes layer thickness, m
$P_{1,u}$	phase of $\tilde{u}$
R_θ	$= U_0\theta/\nu$, momentum thickness Reynolds Number
St_x	$\omega(x - x_0)/U_0$
St_δ	$\omega\delta/U_0$
u	streamwise velocity, m/s
$\tilde{u}$	periodic component of u
$\bar{u}$	$= U$, mean component of u
$\langle u \rangle$	$\bar{u} + \tilde{u}$, phase average of u
U_E	local free-stream velocity, m/s
U_0	free-stream velocity at start of the unsteady region, m/s
x	streamwise coordinate, m
x_0	x at start of the unsteady region, m
X'	$= (x - x_0)/L$
Y	distance from surface, m
δ	$= D_c$, boundary layer thickness (Coles), m
ν	kinematic viscosity, m^2/s
ω	frequency, rad/s

Introduction and Objectives

Unsteady turbulent boundary layers have many important applications. Prediction of the behavior of such boundary layers requires models, which need physical insight for their development and sound data for their evaluation. The Stanford unsteady boundary layer research program is designed to meet this need.

The objective of this program is the development of understanding of unsteady turbulent boundary layers and the collection of definitive data for the development and evaluation of predictive models. This paper summarizes results pertinent to this workshop; for full details see Ref. (1).

Experimental System

The experiments are performed in a special water channel shown in Fig. 1. Water was chosen as the working fluid for ease of flow visualization, laser anemometry, and control of unsteadiness over a wide range of pertinent frequencies.

A unique feature of our apparatus is the maintenance of steady flow in the region upstream of the unsteady flow test section. This makes the boundary layer entering the test section a standard, two-dimensional, flat-plate turbulent boundary layer, and gives the modeler a very well known inflow condition. The unsteady flow takes the form of oscillation (or step change) in the free-stream velocity gradient between zero (flat plate) and an adverse condition.

In order to maintain the desired steady flow upstream of the unsteady test section, the channel flow rate must be held constant. This is accomplished by presenting a constant resistance to the flow and by fixing the inlet and discharge pressures. The fixed resistance is provided by slots in the discharge plate (osc. plate in Fig. 1), and a constant-head tank and open sump fix the pressures.

The unsteady behavior in the test section is created by control of the way in which the fluid leaves the test section. A bleed plate on the channel wall opposite the test surface and a similar plate at the end of the recovery section can be used to remove all or part of the flow. By oscillating the slotted flow-control plate back and forth, the relative amounts of flow extracted through these two bleed plates is oscillated, while maintaining the total flow fixed, and this provides the controlled unsteadiness. With a uniform exit bleed from the wall opposite the test boundary layer, the free-stream velocity seen by the test boundary layer decreases linearly in the downstream direction, and with no opposite-wall bleed the free-stream velocity remains uniform. Hence, the (nominal) behavior of the free-stream velocity seen by the test boundary layer is as shown in Fig. 2. The actual variation deviates slightly from this design target, as we shall discuss shortly.

The inlet section was carefully developed to produce a very two-dimensional, quiet inlet flow. Boundary layer suction removes the nozzle boundary layers, and suction from the wall opposite the test surface is used to maintain a uniform free-stream velocity over the test surface in the developing region. The side-wall boundary layers are removed at the entrance to the test section, the intent being to maintain two-dimensionality of the flow in the unsteady test section and downstream recovery region (see Ref. 1 for documentation).

Measurements of the streamwise velocity component have been made using a single-component DISA Laser Doppler Anemometer with tracker. The LDA signals are prefiltered to remove bias noise and then examined in real time with a dedicated MINC microcomputer. The mean, turbulence, and periodic components of the signal are extracted, and then time-averages and phase-averages of these quantities are formed. A shaft position encoder on the oscillating plate provides the timing signals required for phase averaging at 512 points in each cycle.

Great care has been taken to make this a quality experiment. For example, the water temperature is maintained to within 0.5 °F of a set temperature by continuous refrigeration, an important feature that enables stable long-term operation. The water is filtered to 5 microns to control the particle size (important for LDA). Accelerometer measurements and analysis have assured that there are no vibration problems. All measuring equipment has been carefully calibrated and these calibrations have been periodically checked. Degradation of the flow due to algae growth can be detected by appropriate velocity measurements, and has been eliminated by a program of preventative cleaning and water refreshing.

The entire experiment operates under the control of the MINC computer, which sets the frequency of oscillation, positions the LDA, and acquires and processes the data. This enables us to program continuous runs, which is necessary because of the long time of data acquisition, especially at low frequencies. Continuous production operation for a week or two is now common.

Our first major report (Ref. 1) describes the extensive qualification experiments that were made to establish the two-dimensionality of the flow, the steadiness of the upstream region, and the reliability of the unsteady data. These will not be repeated here.

Experiments

To date three groups of experiments have been conducted, two with frequency oscillations and one with step changes. The low-amplitude oscillation and step experiments do not produce flow reversal. The high-amplitude step experiment does show flow reversal, as will a high-amplitude step experiment now in progress. In this paper we shall report only on those aspects of the high-amplitude oscillation experiment of relevance to this workshop and some conclusions that are independent of amplitude. The oscillation experiments are described in full in Ref. 1 and in forthcoming journal publications.

The experiments were run at a number of frequencies over the range 0.1-2.0 Hz. The boundary layer parameters at the entrance to the unsteady region for these experiments were:

Free-stream velocity U_o	0.732 m/s
Coles' boundary layer thickness δ	3.55 cm
Displacement thickness δ^*	0.59 cm
Momentum thickness θ	0.42 cm
Shape factor H	1.42
Momentum thickness Reynolds No. R_θ	2790
Friction coefficient C_f	0.00322
Kinematic viscosity ν	1.09×10^{-6} m²/s

Measurements were made at four streamwise locations designated by X'. The data cover the Strouhal number ranges

$$0.039 < St_\delta < 1.54$$

$$0.22 < St_x < 15.7 .$$

The oscillating plate mechanism produces a free-stream velocity oscillation that is very nearly sinusoidal, and the resulting boundary layer response is essentially sinusoidal, so for purposes of this discussion we shall treat them as such. We decompose the velocity into three components,

$$u = \bar{u} + \tilde{u} + u'$$

where $\bar{u}$ is the time-average, $\tilde{u}$ is the oscillating component, and u' is the turbulence. The time-average is extracted by averaging over a large integer number of cycles, and the oscillating component is extracted by averaging over a large number of cycles at the same phase angle. See Ref. 1 for procedural details.

Ref. 1 and its associated microfiche contain approximately 1000 graphs and tables of data from these experiments. A digital tape for use by modelers is also available.

Free-Stream Dynamics

Figure 3 shows the time-average free-stream velocity in the test region over the range of frequencies. Note that the free-stream velocity gradient is linear as intended and essentially independent of frequency. The acceleration parameter corresponding to this gradient is

$$K = \frac{\nu}{U_o^2}\frac{dU_E}{dx} = -1.95\times10^{-7} .$$

This represents a strong adverse-pressure gradient for which, in a steady flow, one would expect the development of a separation.

An important observation is that the boundary layer remained attached during all of these unsteady experiments. However, when we set the frequency to zero (at the mean free-stream gradient shown in Fig. 3) a separation builds up over a period of a minute or so, and the boundary layer leaves the surface and never reattaches in the test section. Therefore, we could not conduct experiments at zero frequency for this case (we could and did for the lower-amplitude case (see Ref. 1). It is interesting that separation is prevented in our experiment at the lowest operating Strouhal numbers.

Figure 4 shows the amplitude of the unsteady component in the free stream. Note that the amplitude grows linearly from the start of the test section, as per the design target (Fig. 2). However, unlike the design target the phase of this variation is not constant in the streamwise direction. Figure 5 shows the phase lag; note that the lag decreases downstream in the test section, and over the second half of the unsteady region is very small at all frequencies. These phase lags are probably not important in discussing the qualitative aspects of the boundary layer behavior, but probably should be considered by modelers comparing a prediction to the data.

Time-Averaged Behavior

Figure 6 shows the time-average velocity profiles in the boundary layer near the end of the unsteady section. The scales are staggered to prevent confusion; when these data are laid on top of one another, very little difference can be seen, indicating that the mean velocity profile is essentially unaffected by the oscillation frequency.

Figure 7 shows the time-average of the streamwise component of Reynolds stress, normalized on the local free-stream velocity at the outer edge of the boundary layer, near the end of the unsteady section. Again we see that the time-average turbulence profiles are essentially all the same, indicating no significant effect of the oscillation on the time-averaged turbulence.

The observation that the time-average flow is not significantly affected by the oscillation is consistent with other recent observations in unsteady boundary layers. It also explains why prediction methods based on steady flow models often do very well in predicting transitory stall phenomena.

Unsteady Component

Figure 8 shows the amplitude of the unsteady component at the end of the test section, normalized on the free-stream amplitude. Here a significant variation with frequency is seen. Note that at low frequencies the amplitude is greater in the boundary layer than in the free stream, by over a factor of 2 at 0.1 Hz. At high frequencies the amplitude is uniform over most of the layer, indicating a slug-like motion. Note the log-linear region at low frequencies, suggestive of retained law-of-the-wall behavior in this range.

Figure 9 shows the phase of the unsteady component. Note particularly the high-frequency cases, where the outer region of the boundary layer moves in phase with the free stream, and there is a rapid change variation in phase near the surface. The phase lead near the surface approaches 45° as the frequency is increased; it is interesting that this is the theoretical phase lead for a laminar Stokes layer.

The phase-averaged velocity profiles ($\langle u \rangle = \bar{u} + \tilde{u}$) can be computed from the time-average and periodic components at any desired phase angle (or directly by phase-averaging the data). At low frequencies these profiles show no flow reversal near the wall. However, as the frequency is increased the flow near the wall periodically reverses in a thin region near the surface. Figure 10 shows the phase-average profiles at 2 Hz over a portion of the cycle. Note that the lowest three curves display reversed flow near the wall. At this frequency and location the flow reversal occurs from about 130° to 210°, and is greatest at about 165°, consistent with the phase lead shown in Fig. 9.

Flow Regimes

Analysis of the governing equations and the data suggests that there are three regimes of flow in unsteady boundary layers. These can be expressed in terms of the time scale for the oscillation,

$$T_o = 1/\omega$$

the time scale for the unsteady region,

$$T_u = (x - x_o)/U_o$$

and the time scale for the large eddies

$$T_e = \delta/U_o \, .$$

The ratios of these time scales define the two pertinent Strouhal numbers,

$$St_\delta = T_e/T_o \qquad St_x = T_u/T_o \, .$$

When T_o is long compared to T_u and T_e, both the overall flow and the eddies have time to respond to the change, and the flow behaves quasistaticly. Since the zero-frequency flow here is a separated flow, and the oscillating flows are not, it would seem that this regime was not reached in the experiments, and hence that the quasistatic regime requires Strouhal numbers at least as low as

$$St_\delta < 0.04 \qquad St_x < 0.2 \, .$$

When T_o is comparable with T_u but long compared to T_e, the eddies have time to respond and the entire boundary layer should reflect the influence of the oscillation. As a result, integral quantities such as the displacement thickness vary throughout the cycle. The equations (Ref. 1) suggest that the behavior should correlate on St_x. Figure 11 shows the displacement thickness as a function of St_x, normalized by the amplitude of the free-stream fluctuation, for the full set of high-amplitude and low-amplitude oscillations. Note that, for $0.5 < St_x < 3$ the correlation on St_x is excellent, indicating that St_x is indeed the correct correlating parameter for this range of flows (a similar plot vs St_δ does not collapse the data). Note also that at higher frequencies the displacement thickness variation becomes independent of St_x.

When T_o is short compared to T_e, i.e., St_δ is sufficiently high, the eddies do not have time to respond to the oscillation. Our data suggest that this occurs approximately for $St_\delta > 0.5$. It is in this region that the displacement thickness becomes independent of St_x.

Analysis of the equations of motion (Ref. 1) suggest that at high frequencies the laminar Stokes equations should describe the unsteady component in the boundary layer, and we indeed find this to be the case. Figure 12 shows the amplitude of the periodic component, normalized on the free-stream velocity amplitude, plotted vs the dimensionless Stokes coordinate y/δ_s. Note the excellent collapse of the data for a wide range of St_x and the excellent agreement of these data with the analytical solution of the Stokes equation. The same holds for the phase (Fig. 13).

We conclude that the flow reversal encountered at high frequencies is simply the Stokes layer response of the viscous region near the wall, and that the dynamics of this layer is not coupled significantly to the turbulence for $St_\delta > 0.5$.

Concluding Remarks

Three regimes of boundary layer behavior in unsteady flow have been identified, and boundaries for these regimes suggested. Important work remaining to be done includes direct measurement of the turbulent shearing stress in unsteady boundary layers and direct measurement of the wall shear stress. We are now beginning to conduct these measurements at Stanford, and in addition are exploring the interesting case of a sudden step change in more detail. We hope to extend our program to three-dimensional unsteady effects in the future.

Acknowledgements

Dr. Pradip Parikh did the detailed design of the experimental facility and conducted important preliminary experiments, and has provided much helpful advice throughout this program. The work is supported by the Army Research Office and by the Aeromechanics Laboratory, RTL (AVRADCOM); companion work contributing to the facility has been supported by NASA-Ames Research Center and by the National Science Foundation.

Reference

1. Jayaraman, R., P. Parikh, and W.C. Reynolds, "An Experimental Study of the Dynamics of an Unsteady Turbulent Boundary Layer," Rept. TF-18, Thermosciences Division, M.E. Department, Stanford University, December 1982.

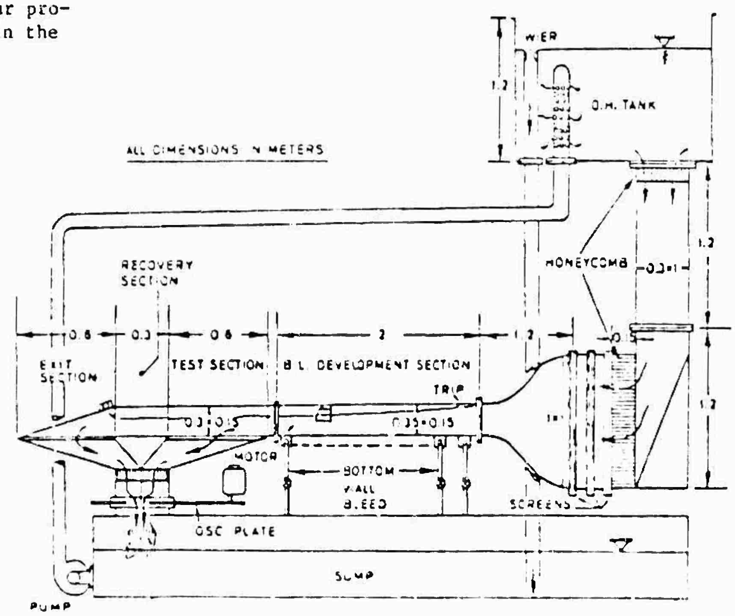

Figure 1. Schematic of the apparatus

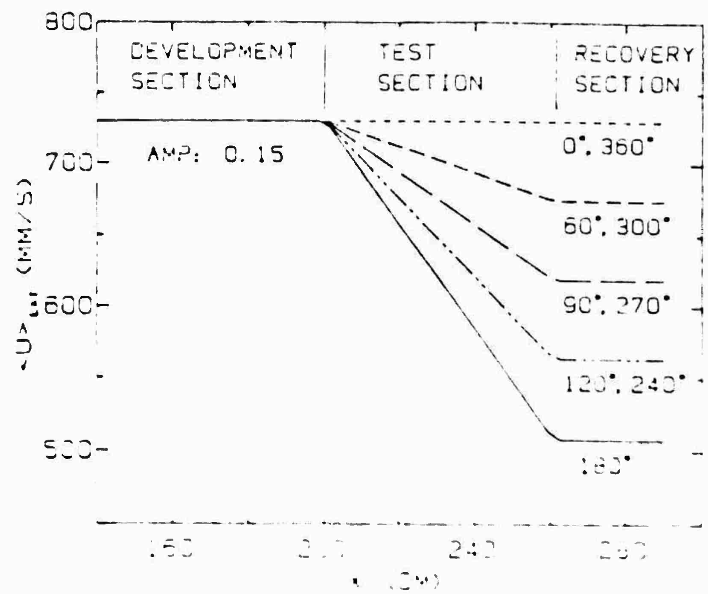

Figure 2.

Design target for free-stream velocity oscillation

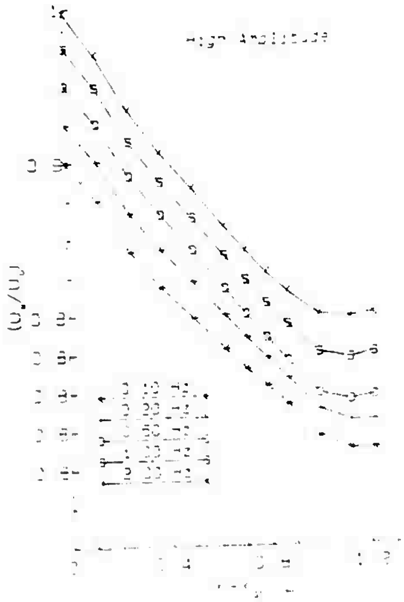

Figure 3.

Time-average free-stream velocity distribution

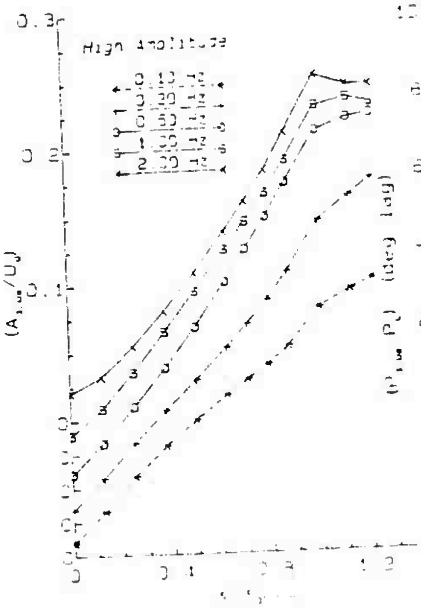

Figure 4.

Amplitude of the periodic component of the free-stream velocity

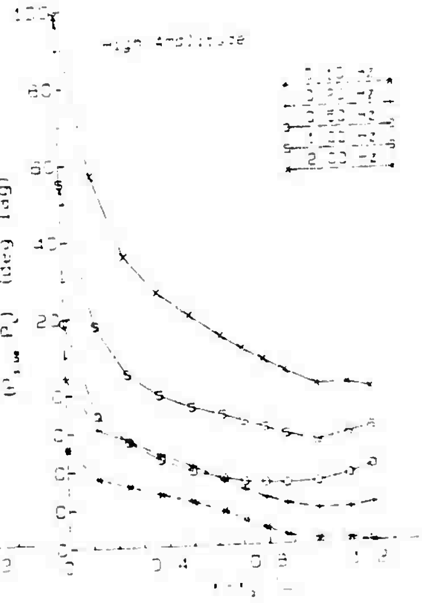

Figure 5.

Phase of the periodic component of the free-stream velocity

Figure 6. Time-averaged velocity profiles in the boundary layer

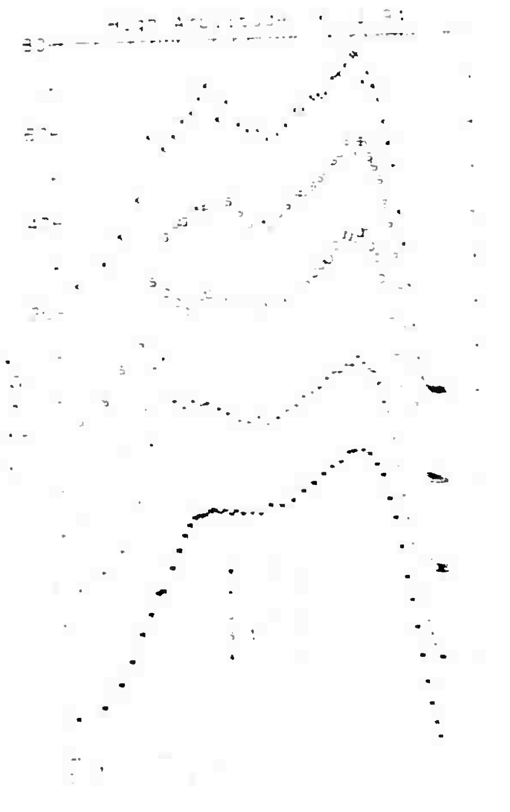

Figure 7. Time-averaged turbulence profiles in the boundary layer

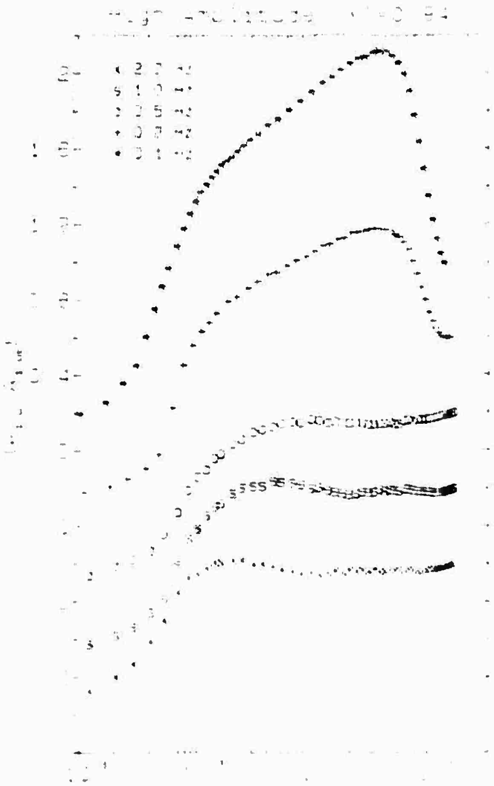

Figure 8. Amplitude of the periodic component of velocity in the boundary layer

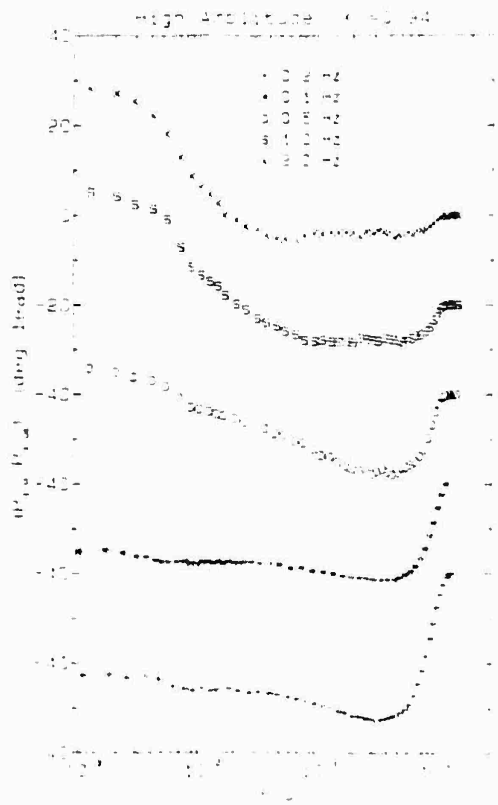

Figure 9. Phase of the periodic component of velocity in the boundary layer

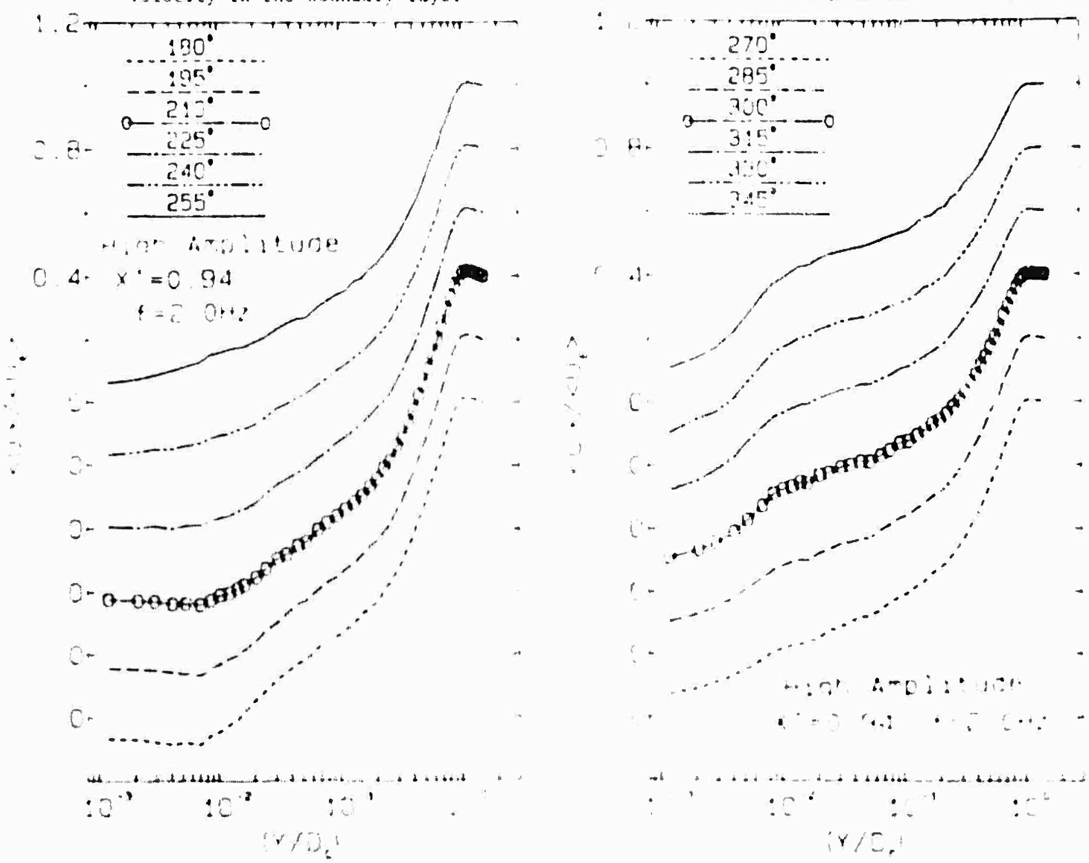

Figure 10. Selected ensemble-average velocity profiles showing reverse flow near the wall

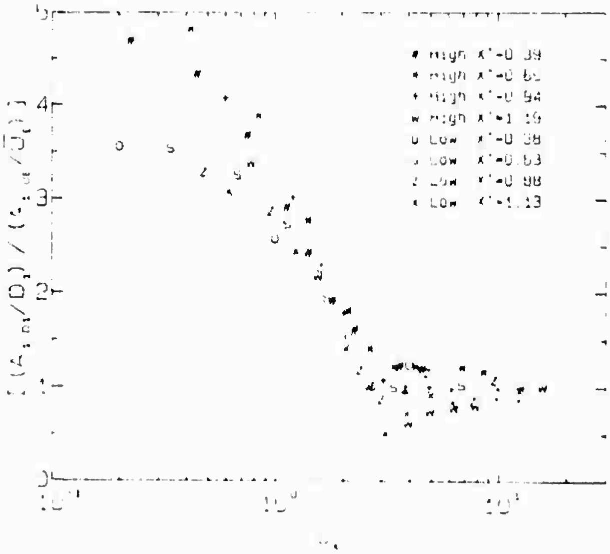

Figure 11. Amplitude of the periodic component of the displacement thickness, normalized on the amplitude of the free-stream velocity oscillation, for all oscillatory experiments

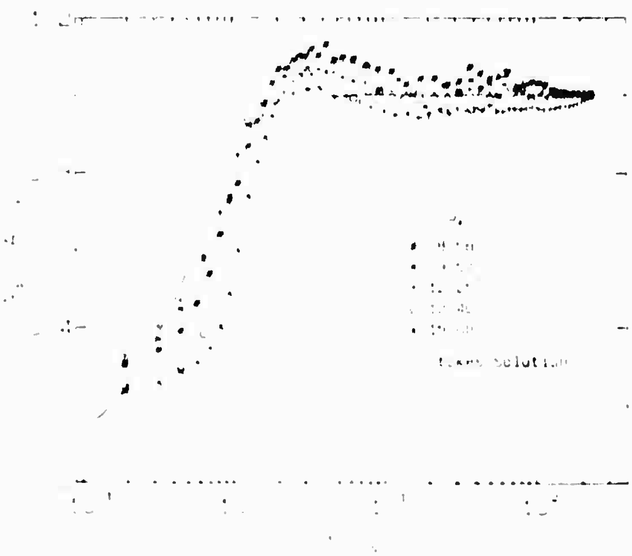

Figure 12. Amplitude of the periodic component in the Stokes layer, normalized on the amplitude of the free-stream velocity oscillation, for all high-frequency oscillatory experiments

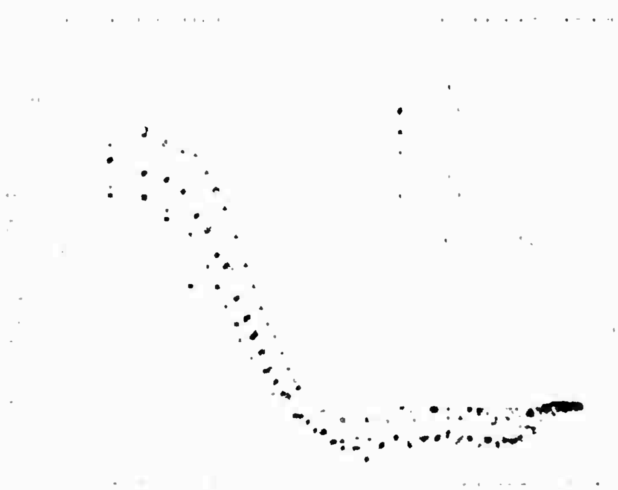

Figure 13. Phase of the periodic component in the Stokes layer, relative to the phase of the free-stream velocity, for all high-frequency oscillatory experiments

GENESIS OF UNSTEADY SEPARATION

AD-P004 173

Ho, Chih-Ming*
University of Southern California
Los Angeles, California 90089-1454

Abstract

Unsteady separation is a problem of great technical importance but with little basic understanding. A very limited amount of experimental data is available because of the difficulties involved in measuring the temporally evolving separated flows. In this presentation we first examine the flow field of a downstream moving separation in detail and then we explore the possibility of applying the learned physical mechanism to the upstream moving separation problems and to the unsteady separation on a lifting surface.

Introduction

The unsteady separation was recognized to be intrinsically different from steady separation in the mid 1950's. Rott[1] Sears[2] and Moore[3] pointed out that the vanishing of the wall shear stress could not be the criterion for unsteady separation. Instead separation should occur at the zero shear stress location in a coordinate system convected with the separation speed. This has been called the MRS criterion since then. The obvious problem in this criterion is that the separation speed is not known a priori. Large amounts of theoretical effort have been spent on this challenging topic. The most complete summary is the monograph by Teleionis.[4] Extensive experimental works are available in studying the effects produced by unsteady separation on lifting surfaces.[5] Experimental investigations on the processes involved in unsteady separation however are very few. The main problem is that the velocity field needs to be well documented but severe limitations exist in measuring the time evolving separated velocity field. Separation usually involves two or even three spatial variables. In the unsteady case, time is an additional variable. Therefore the measurements require the use of many probes as well as large and fast data storage systems. Furthermore, reverse flow occurs in most separations and the well developed hot wire anemometry cannot be used to measure the reverse flow. Therefore the laser Doppler velocimeter is needed. These difficulties significantly hamper the progress in the technically important unsteady separation problem.

In this presentation we will first discuss the unsteady separation which occurs in an impinging flow. In this special situation, the instantaneous velocity and the surface pressure fluctuations were surveyed in detail. The data clarified several important issues. The detachment point in this flow moves downstream. We then attempted to apply the mechanisms learned from the downstream moving detachment point to a case of upstream moving detachment point, e.g. separation on the cylinder or the airfoil. The results are promising.

Unsteady Separation With Downstream Moving Detachment Point

Moore[3] pointed out that the flow reversal will not occur in a situation with the downstream moving detachment point (Fig. 1).

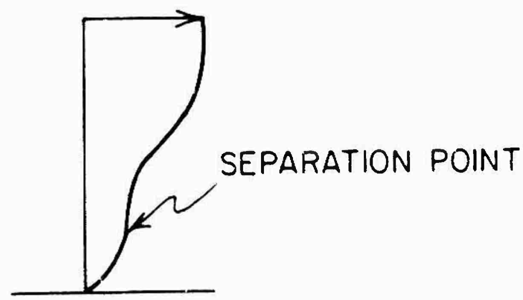

Fig. 1. Separation with downstream moving detachment point (Moore 1958).

This advantageous characteristic allows us to investigate the velocity in great detail by using hot-wire probes. An interesting unsteady separation occurred in the impinging jet case. When the coherent structure in the jet shear layer, the primary vortex, approaches the wall, a counter-rotating secondary vortex inside the viscous region is induced by the perturbations in the inviscid region (Fig. 2). The ejection of the secondary vortex makes the boundary abruptly thicker. After the passing of the vortices the boundary becomes reattached.

From the ensemble averaged velocity measurements, vorticity contours can be constructed. The features of unsteady separation (the ejection of vorticity, thickening of the boundary layer and the MRS criterion) were all observed.[illegible] With the help of the velocity field, the surface pressure signature of the secondary vortex associated with the unsteady separation can be identified by a sharp and high amplitude suction peak (Fig. [illegible]).

*Associate Professor, Department of Aerospace Engineering.

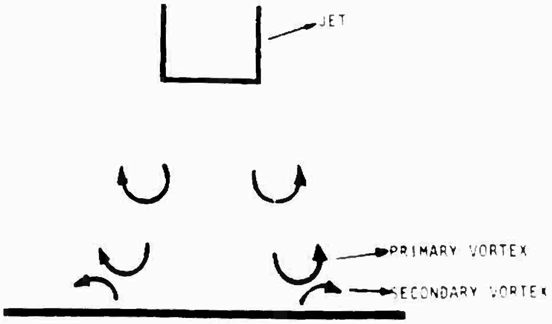

Fig. 2. Unsteady separation in an impinging jet.

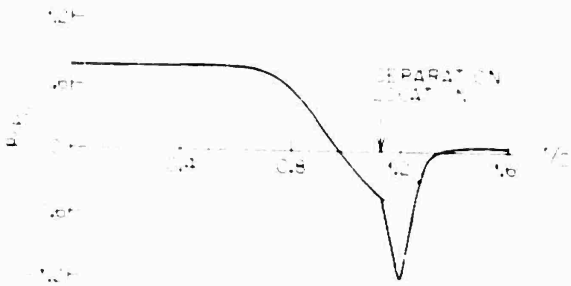

Fig. 3. Normalized ensemble averaged surface pressure traces, [illegible], in an impinging jet with diameter D, t/T = 0.2 where T is the period.

An important characteristic of the pressure data is the existence of an unsteady adverse pressure gradient (Fig. 4).

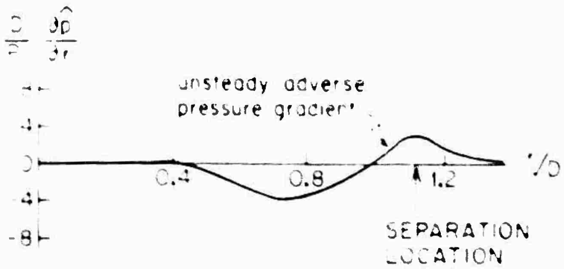

Fig. 4. Unsteady adverse pressure gradient in an impinging jet [illegible]

This is induced by the primary vortex in [illegible]. [illegible] flow near the wall was retarded by the adverse pressure gradient. A shear layer was created at the viscous and inviscid interface. The vorticity in the unstable shear layer was lumped and formed the secondary vortex. Subsequently, the boundary layer thickened and the flow separated.

Unsteady Separation With Upstream Moving Detachment Point

In the impulsively started cylinder the detachment point moves upstream. A local shear layer was also detected. In the initial stage (Fig. 5-a), several vortices similar to those in the free shear layer were observed near the rear side surface of the cylinder. Eventually, two large vortices were formed at each side of the stagnation streamline (Fig. 5-b).

Fig. 5. Separation vortices of an impulsively started cylinder with diameter of D (Bouard and Coutanceau 1980) [illegible]

In another situation, [illegible] et al. [illegible] the flow separated [illegible] vortex shedding and examined the wake [illegible] the separation in the light [illegible] shear layer. The results were similar [illegible] but not exactly the same as the free shear layer. [illegible] surface pressure [illegible] made in either [illegible] experiments. Therefore, the relation between the [illegible] shear layer and the [illegible] separation [illegible].

Fig. 5 b.

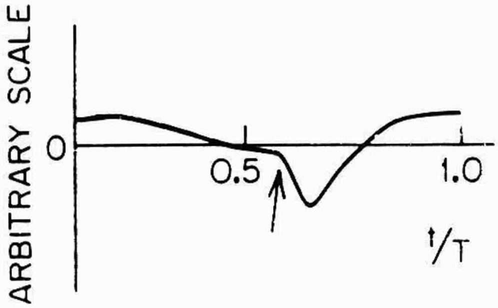

Fig. 6. Ensemble averaged pressure traces of a plunging airfoil

U_o = 18.6 m/sec   x/c = 7.35%

k = 0.27

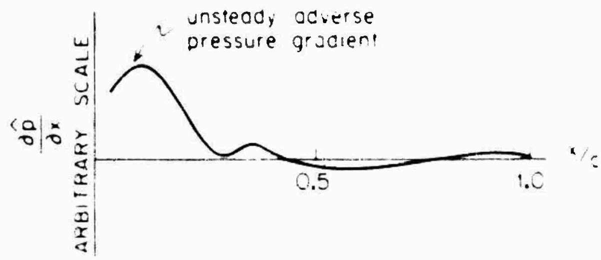

Fig. 7. Unsteady adverse pressure gradient on a plunging airfoil

U_o = 18.6 m/sec   [illegible]

k = 0.27

Unsteady Separation on the Lifting Surface

On the unsteady airfoil a large hysterisis of lift, drag and moment were found during one cycle of oscillation. Well documented visualization and surface pressure measurements showed that the flow near the leading edge was disturbed by the unsteady separation vortex.[9] Due to practical difficulties, information concerning velocity field around the unsteady wing is very limited. It is then difficult to obtain a full picture of the initial stage of the separation. A detailed look at the individual pressure traces on a plunging airfoil[10] indicated the sharp suction peak similar to that in Fig. 1 also appears near the separation (Fig. 6). An even more interesting feature is that the adverse pressure gradient was detected before the occurrence of the unsteady separation (Fig. 7). The visualization on a pitching airfoil had shown that the separation vortex developed from a local shear layer[11] near the surface. Phenomena similar to that in a free shear layer, multiple small vortices and merging of these vortices, also have been observed.

Conclusion

In an unsteady separated flow with a downstream moving detachment point, the separation is developed from a local shear layer produced by an unsteady adverse pressure gradient. On an unsteady airfoil, the mechanism of the separation is not completely understood due to inadequate information of the velocity field. However, the surface pressure measurements indicate that the unsteady pressure gradient could still be the mechanism which produces the separation. The most important implication is that artificial perturbations of the pressure gradient at the proper phase and the proper location could alter the separation.

process and significantly modify the aero dynamic properties of the unsteady airfoils.

Acknowledgment

The author would like to thank N. Didden and S.H. Chen for their great help during the course of this research.

The work is supported by AFOSR Contract No. F49620-82-K-0019.

References

1. Rott, N. Unsteady Viscous Flow in the Vicinity of a Stagnation Point. Q. Appl. Math. 13, 444-451 (1956).

2. Sears, W.R. Some Recent Development in Airfoil Theory. J. Aerosp. Sci. 23, 490-499 (1956).

3. Moore, F.K. On the Separation of the Unsteady Laminar Boundary Layer. Boundary-Layer Research ed. H.G. Gortler, pp. 296-310 Berlin, Springer (1958).

4. Telionis, D.P. Unsteady Viscous Flows, Springer, New York (1981).

5. McCroskey, W.J. Unsteady Airfoils. Ann. Rev. Fluid Mech. 14, 285-311 (1982).

6. Didden, N. and Ho, C.M. Unsteady Separation in the Boundary Layer Produced by an Impinging Jet. In preparation.

7. Bouard, R. and Coutanceau, M. The Early Stage of Development of the Wake Behind an Impulsively Started Cylinder for 40 Re 10^4. J. Fluid Mech. 101, 583-607 (1980).

8. Jones, G.S., Telionis, D.P. and Farhi, C. Separation and Wake Interaction of a Pulsating Laminar Flow. AIAA Paper No. 81-0053 (1981).

9. Ho, C.M. and Huang, L.S. Subharmonics and Vortex Merging in Mixing Layers. J. Fluid Mech. 119, 443-473 (1982).

10. Ho, C.M. and Chen, S.H. Unsteady Separation of a Plunging Airfoil. 1984 AIAA Aerospace Science Meeting.

11. McAlister, K.W. and Carr, L.W. Water Tunnel Visualizations of Dynamic Stall. Nonsteady Fluid Dynamics ed. Crow, D.E., Miller, J.A., pp. 103-110 [illegible]. ASME, New York (1978).